

# Changes in the mineral assemblage of paddy soils upon redox cycles

---

**Dissertation**  
**zur Erlangung des Doktorgrades der Naturwissenschaften**  
**(Dr. rer. nat.)**

der

Naturwissenschaftlichen Fakultät III  
Agrar- und Ernährungswissenschaften,  
Geowissenschaften und Informatik

der Martin-Luther-Universität  
Halle-Wittenberg

vorgelegt von

Frau Vogelsang, Vanessa  
Geb. am 04.03.1980 in Berlin

Tag der öffentlichen Verteidigung: 10.04.2017

Gutachter:

Prof. Dr. Reinhold Jahn  
Prof. Dr. Friederike Lang

## **Danksagung**

Zu allererst danke ich Prof. Reinhold Jahn und Prof. Sabine Fiedler (Universität Mainz) für die Überlassung des Themas, ihren wissenschaftlichen Rat und die stete Unterstützung.

Ein besonderes Dankeschön geht zudem an Dr. Klaus Kaiser für seine unermüdliche Unterstützung in Form von anregenden fachlichen Diskussionen, zahlreichen konstruktiven und wertvollen inhaltlichen Anmerkungen bei der Planung, Auswertung und Verschriftlichung der vorliegenden Arbeit.

Die Durchführung der Feldversuche in China wäre nicht ohne die Hilfe der folgenden Personen möglich gewesen: Dr. Zou Ping und Xi Wu danke ich sowohl für die organisatorische als auch tatkräftige Unterstützung bei der Durchführung der Feldversuche. Ebenso gedankt sei Prof. Fu Jianrong und Prof. Zhihong Cao als Projektpartner vor Ort. Dr. Klaus Kaiser, Prof. Sabine Fiedler und Dr. Yuqin Chen haben mir tatkräftig beim Aufbau der Feldversuche geholfen. Tina Truzschezinski, Maike Sauerwein und Dr. Cordula Vogel haben mit mir bei Wind und Wetter unzählige Daten im Feld erhoben.

Meinen ehemaligen Kollegen von der Professur für Bodenkunde und Bodenschutz möchte ich insbesondere für die Hilfe beim Bau der ‚mineral bags‘ sowie für die gute Zusammenarbeit und angenehme Arbeitsatmosphäre danken. Christine Krenkewitz, Gerlinde Hardt und Gudrun von Koch sei herzlich gedankt für ihre Hilfe und Unterstützung bei den Laboranalysen und der Aufbereitung der Testminerale. Ein besonderes Dankeschön geht auch an Tina Truzschezinski, die sich im Rahmen Ihrer Diplomarbeit der Aufbereitung und Analytik der zahlreichen Bodenlösungen angenommen hat, und an die wissenschaftlichen Hilfskräfte, die bei den Laborarbeiten geholfen haben.

Dr. Thomas Kühn und Dr. Christian Bender Koch (Universität Kopenhagen) danke ich für Einführung in die Röntgendiffraktometrie bzw. in die Mößbauer-Spektroskopie. Für die Durchführung der XRD-Messungen an den Testmineralen danke ich Prof. Hofmeister und Ralf Meffert (Universität Mainz). Bei Prof. Friedrich Wagner (TU München) bedanke ich mich herzlich für die Erstellung der Mößbauer-Spektren, die zahlreichen fachlichen Diskussionen sowie die wertvollen Hinweise bei der Auswertung der komplexen Spektren. Dr. Michael Kastler danke ich für die Einführung in die Welt von R.

Der DFG danke ich für die finanzielle Unterstützung. Meinen Kollegen und Mitdoktoranden der DFG Forschergruppe FOR 995 „Biogeochemistry of Paddy Soil Evolution“ möchte ich für den fachlichen Austausch sowie die schöne Zeit und gute Zusammenarbeit während der ersten Probenahmekampagne in Cixi und unserer zahlreichen Treffen danken.

Mein ganz besonderer Dank gilt meinen Eltern und meinem Freund Micha für deren fortwährende Unterstützung. Sie haben auf ihre Art ganz wesentlich zum Gelingen dieser Arbeit beigetragen.

## Table of contents

<b>Summary</b>	<b>XVIII</b>
<b>Zusammenfassung</b>	<b>XXII</b>
<b>1. General introduction.....</b>	<b>1</b>
1.1 Rationale .....	1
1.2 Paddy soils .....	3
1.3 Redox potential and processes .....	5
1.4 Redox-induced iron mineral (trans)formations .....	7
1.5 Objectives and research questions .....	9
<b>2. Study area and characterization of soils.....</b>	<b>11</b>
2.1 Study area.....	11
2.2 Soil description.....	12
<b>3. Long-term transformations of soil minerals under alternating redox conditions ....</b>	<b>16</b>
3.1 Introduction .....	16
3.2 Material and Methods .....	18
3.2.1 Soil sampling and pre-treatment .....	18
3.2.2 Basic characteristics of the clay fractions .....	19
3.2.3 Selective chemical extractions .....	19
3.2.4 X-ray diffraction .....	19
3.2.5 Mössbauer spectroscopy .....	20
3.3 Results .....	20
3.3.1 Basic characteristics of the clay fractions .....	20
3.3.2 Selective wet chemical extractions .....	24
3.3.3 Clay mineral assemblage .....	24
3.3.4 Mössbauer spectroscopy: Assignment of the solid Fe phases .....	27
3.4 Discussion .....	36
3.4.1 Selective chemical extractions versus Mössbauer spectroscopy .....	40
3.5 Conclusion.....	41
<b>4. In-situ test of redox-induced mineral transformation .....</b>	<b>42</b>
4.1 Introduction .....	42
4.2 Material and methods .....	44
4.2.1 Test minerals .....	44
4.2.2 Set-up of field experiments .....	45
4.2.3 Sampling and pre-treatment of the test minerals .....	46
4.3 Characterization of the test minerals.....	46

4.4	Results .....	47
4.4.1	Redox and solution conditions during the field experiments .....	47
4.4.2	Goethite .....	47
4.4.3	Ferrihydrite .....	48
4.4.4	Nontronite .....	50
4.4.5	Organic matter adsorption .....	56
4.5	Discussion .....	56
4.6	Conclusion .....	60
<b>5.</b>	<b>Redox conditions and soil solution composition as related to the time of paddy cultivation .....</b>	<b>61</b>
5.1	Introduction .....	61
5.2	Material and methods .....	63
5.2.1	Set-up of field experiments .....	63
5.2.2	Analysis of soil solution .....	64
5.2.3	Alkalinity and sodium adsorption ratio (SAR) .....	64
5.2.4	Statistical Analysis .....	65
5.3	Results .....	65
5.3.1	Redox conditions .....	65
5.3.2	Soil reaction and alkalinity .....	70
5.3.3	Redox sensitive elements and compounds: nitrogen, manganese, iron, sulfate, and carbon .....	71
5.3.4	Electric conductivity and alkali/ earth alkali elements .....	77
5.3.5	Matrix elements: silicate and aluminium .....	78
5.3.6	Irrigation water .....	80
5.4	Discussion .....	80
5.5	Conclusion .....	93
<b>6.</b>	<b>Synopsis .....</b>	<b>94</b>
6.1	Final discussion .....	94
6.2	Final conclusion .....	101
	<b>References .....</b>	<b>103</b>
<b>A.</b>	<b>Appendix: Soil profiles .....</b>	<b>119</b>
<b>B.</b>	<b>Appendix: Soil properties .....</b>	<b>122</b>
<b>C.</b>	<b>Appendix: X-ray diffraction .....</b>	<b>126</b>
<b>D.</b>	<b>Appendix: Mössbauer spectroscopy .....</b>	<b>143</b>
<b>E.</b>	<b>Appendix: Soil redox potentials and soil solution composition .....</b>	<b>167</b>

## List of figures

- Figure 1-1: Schematic figure of an Anthraquic Anthrosol after Kögel-Knabner et al. (2010); horizon designation according to FAO (2006) and soil classification according to IUSS Working Group WRB (2014)..... 5
- Figure 2-1: Chronosequence of 100, 700 and 2000 year paddy (P100, P700, P2000) and 100 and 700 year non-paddy soils (NP100, NP700) located on the southern peninsula of Hangzhou Bay in the region of Cixi city (Zhejiang Province, PR China). A marshland soil (ML30) serves as reference point of initial soil formation..... 11
- Figure 3-1: Depth profile of the organic carbon (OC) concentrations in the clay fractions of paddy (P) and non-paddy sites (NP). The marshland site (ML30) is given as point zero of soil evolution. .... 21
- Figure 3-2: X-ray diffraction patterns (oriented texture specimens, Cu K $\alpha$  radiation) of the clay fractions in the Alp horizons of the 100, 700 and 2000 year paddy site (P100, P700, P2000) and the upper horizon (0–13 cm) of the marshland (ML30), corrected to the quartz peak at 3.34 Å or 26.7 °2 $\theta$ . Identification of clay minerals was done by means of following treatments: (A) Ca<sup>2+</sup> saturation, (B) ethylene glycol solvation, K<sup>+</sup> saturation (not shown) and (C) K<sup>+</sup> saturated specimens heated to 550 °C; chl = chlorite, ill = illite, kao = kaolinite, qtz = quartz, ver = vermiculite. .... 25
- Figure 3-3: X-ray diffraction patterns (oriented texture specimens, CuK $\alpha$ -radiation) of the clay fractions of the deepest subsoil horizon of the 100, 700 and 2000 year paddy sites (70–100 cm) (P100, P700, P2000) and the deepest horizon (13–30 cm) of the marshland (ML30), corrected to the qua298 Kz peak at 3.34 Å or 26.7 °2 $\theta$ ; lp = lepidocrocite. .... 27
- Figure 3-4: <sup>57</sup>Fe Mössbauer spectra at 298 and 4.2 K (modified according to Vogelsang et al., 2016a). The solid black line drawn through the data points is the calculated fit. The spectral components are assigned as follows: 298 K: S3-FeOx (central doublet) Fe(III) in aluminosilicates (e.g. illite, kaolinite and/or smectite) and paramagnetic hydrous oxides; S2 (wider doublet) Fe(II) in aluminosilicates; Hm (outer sextett) microcrystalline haematite; GtB (collapsed sextett) goethite near its magnetic blocking temperature; 4.2 K: S3 (central doublet) Fe(III) in aluminosilicates; S2 (wider doublet) Fe(II) in aluminosilicates; FeB (collapsed sextett) paramagnetic relaxation of Fe(III) in aluminosilicates; Hm (outer sextett) haematite; Gt (middle sextett) goethite; HFO (inner sextett) hydrous Fe oxide of low crystallinity, i.e. ferrihydrite..... 29
- Figure 3-5: Depth distribution of solid Fe phases along the chronosequence. Fe contents of each phase were calculated based on the corresponding <sup>57</sup>Fe Mössbauer spectral area. . 33
- Figure 3-6: Relative contents of microcrystalline (Hm<sub>m</sub>) and nanocrystalline haematite (Hm<sub>n</sub>) based on <sup>57</sup>Fe Mössbauer analysis. Results are expressed as % of total-haematite Fe, assuming equal Mössbauer assuming recoilless fractions. .... 34
- Figure 3-7: Relative contents of microcrystalline (Gt<sub>m</sub>) and nanocrystalline goethite (Gt<sub>n</sub>) based on <sup>57</sup>Fe Mössbauer analysis. Results are expressed as % of total-goethite Fe, assuming equal Mössbauer assuming recoilless fractions. .... 35

Figure 3-8: Ammonium-oxalate-extractable Fe contents versus Fe in poorly crystalline ferric oxides calculated from the  $^{57}\text{Fe}$  Mössbauer spectral area of the LHe-HFO phase (left) and DCB-extractable Fe contents versus Fe in ferric oxide contents calculated from  $^{57}\text{Fe}$  Mössbauer the spectral area of LHe-Hm, LHe-Gt and LHe-HFO phases (right) of all paddy (●), non-paddy (○) and marshland (x) samples. The solid (paddies) and dashed line (non-paddies) show the correlation between the two data sets. LHe-HFO vs.  $\text{Fe}_o$ :  $r^2 = 0.06$  (paddies) and  $0.62$  (non-paddies); LHe-Gt + Hm + HFO vs.  $\text{Fe}_d$ :  $r^2 = 0.87$  (paddies) and  $0.83$  (non-paddies). ..... 41

Figure 4-1: X-ray diffraction patterns of goethite before (org) and after 12 months exposure in the field at the 100, 700 and 2000 year paddy sites (P100, P700, P2000) (modified according to Vogelsang et al., 2016b). ..... 48

Figure 4-2: X-ray diffractions patterns of ferrihydrite before (org) and after 12 months exposure in the field at the 100, 700, and 2000 year paddy site (P100, P700, P2000) (modified according to Vogelsang et al., 2016b). ..... 49

Figure 4-3: Unaltered nontronite, bulk and grounded  $<200\ \mu\text{m}$  (a) and freeze-dried NAu-2 after one year exposure (b) to field conditions at the 2000 year paddy site (P2000). ..... 50

Figure 4-4: X-ray diffraction patterns of NAu-2 before (org) and after 12 months exposure in the field at the 100, 700 and 2000 year paddy sites (P100, P700, P2000) (modified according to Vogelsang et al., 2016b). ..... 51

Figure 4-5:  $^{57}\text{Fe}$  Mössbauer spectra at room temperature (298 K) of NAu-2 before (org) and after 12 months exposure in the 2000 year paddy subsoil (modified according to Vogelsang et al., 2016b). The solid black line drawn through the data points is the calculated fit. The spectral components are assigned as follows:  $\text{Oct}_{trans}$ : octahedral coordinated ferric Fe (trans);  $\text{Oct}_{cis}$ : octahedral coordinated ferric Fe (cis);  $\text{Tet}$ : tetrahedral coordinated ferric Fe. .... 53

Figure 4-6:  $^{57}\text{Fe}$  Mössbauer spectra at 4.2 K of NAu-2 before (org) and after 12 months exposure in the 2000 year paddy subsoil (modified according to Vogelsang et al., 2016b). The solid black line drawn through the data points is the calculated fit. .... 54

Figure 5-1: Redox conditions during the first 60 days after flooding at the 100 (A), 700 (B) and 2000 (C) year paddy sites. Data points are means of max. five replicates; error bars are one standard deviation. .... 66

Figure 5-2: Redox conditions during one entire paddy–winter crop cycle (March 2009 to March 2010) in the upper subsoil (35 cm) of the 100 year paddy and non-paddy site (A), the 700 year paddy and non-paddy site (B) and the 2000 year paddy site (C). Filled shapes represent the paddy sites, unfilled shapes the non-paddy sites. Data points are means of max. five replicates; error bars are one standard deviation. .... 68

Figure 5-3: Redox conditions during one entire paddy–winter crop cycle (March 2009 to March 2010) in the lower subsoil (55 cm) of the 100 year paddy and non-paddy site (A), the 700 year paddy and non-paddy site (B) and the 2000 year paddy site (C). Filled shapes represent the paddy sites, unfilled shapes the non-paddy sites. Data points are means of max. five replicates; error bars are one standard deviation. .... 69

Figure 5-4: Mean pH values in the soil solution of the upper (35 cm) and lower (55 cm) subsoil during the first two months after flooding (left); data points are means of max. four replicates, error bars are one standard deviation. Boxplots and corresponding data points illustrate distribution of pH values (right). .... 70

Figure 5-5: Mean alkalinity in the soil solution of the upper (35 cm) and lower (55 cm) subsoil during the first two months after flooding (left); data points are means of max. four replicates, error bars are one standard deviation. Boxplots and corresponding data points illustrate distribution of alkalinity (right). ..... 71

Figure 5-6: Mean  $\text{NO}_{2/3}^-$  concentrations (depicted as  $\text{NO}_{2/3}^- \text{-N}$ ) in the soil solution of the upper (35 cm) and lower (55 cm) subsoil during the first two months after flooding (left); data points are means of max. four replicates, error bars are one standard deviation. Boxplots and corresponding data points illustrate distribution of  $\text{NO}_{2/3}^-$  values (right).. 72

Figure 5-7: Mean  $\text{NH}_4^+$  concentrations in the soil solution of the upper (35 cm) and lower (55 cm) subsoil during the first two months after flooding (left); data points are means of max. four replicates, error bars are one standard deviation. Boxplots and corresponding data points illustrate distribution of  $\text{NH}_4^+$  concentrations (right). ..... 72

Figure 5-8: Mean Mn concentrations in the soil solution of the upper (35 cm) and lower (55 cm) subsoil during the first two months after flooding (left); data points are means of max. four replicates, error bars are one standard deviation. Boxplots and corresponding data points illustrate distribution of Mn concentrations (right). ..... 74

Figure 5-9: Mean Fe concentrations in the soil solution of the upper (35 cm) and lower (55 cm) subsoil during the first two months after flooding (left); data points are means of max. four replicates, error bars are one standard deviation. Boxplots and corresponding data points illustrate distribution of Fe concentrations (right). ..... 74

Figure 5-10: Mean  $\text{SO}_4^{2-}$  concentrations in the soil solution of the upper (35 cm) and lower (55 cm) subsoil during the first two months after flooding (left); data points are means of max. four replicates, error bars are one standard deviation. Boxplots and corresponding data points illustrate distribution of sulfate concentrations (right). ..... 75

Figure 5-11: Mean dissolved inorganic carbon (DIC) concentrations in the soil solution of the upper (35 cm) and lower (55 cm) subsoil during the first two months after flooding (left); data points are means of max. four replicates, error bars are one standard deviation. Boxplots and corresponding data points illustrate distribution of DIC concentrations (right). ..... 76

Figure 5-12: Mean dissolved organic carbon (DOC) concentrations in the soil solution of the upper (35 cm) and lower (55 cm) subsoil during the first two months after flooding (left); data points are means of max. four replicates, error bars are one standard deviation. Boxplots and corresponding data points illustrate distribution of DOC concentrations (right). ..... 76

Figure 5-13: Mean electric conductivity (EC) of the soil solution of the upper (35 cm) and lower (55 cm) subsoil during the first two months after flooding (left); data points are means of max. four replicates, error bars are one standard deviation. Boxplots and corresponding data points illustrate distribution of EC values (right). ..... 77

Figure 5-14: Mean Si concentrations in the soil solution of the upper (35 cm) and lower (55 cm) subsoil during the first two months after flooding (left); data points are means of max. four replicates, error bars are one standard deviation. Boxplots and corresponding data points illustrate distribution of Si concentrations (right). ..... 79

Figure 5-15: Changes in concentrations of the redox sensitive compounds upon flooding, exemplarily shown for the soil solution of the upper subsoil (35 cm) at the 700 year paddy site (P700). ..... 83

Figure 5-16: Relationship between redox potential in soil and $\text{NO}_{2/3}^-$ concentrations (depicted as $\text{NO}_{2/3}^-$ -N) in soil solutions at 35 and 55 cm depth of the paddy sites during the first two months after flooding.....	85
Figure 5-17: Relationship between redox potential in soil and Mn concentrations in soil solutions at 35 and 55 cm depth of the paddy sites during the first two months after flooding. ....	86
Figure 5-18: Relationship between redox potential in soil and Fe concentrations in soil solutions at 35 and 55cm depth of the paddy sites during the first two months after flooding. ....	87
Figure 5-19: Relationship between redox potential in soil and $\text{SO}_4^{2-}$ concentrations in soil solutions at 35 and 55cm depth of the paddy sites during the first two months after flooding. ....	88
Figure 5-20: Relationship between redox potential in soil and dissolved inorganic carbon (DIC) concentrations in soil solutions at 35 and 55 cm depth of the paddy sites during the first two months after flooding.....	89
Figure 5-21: Eh-pH-stability diagram of the different types of Fe oxides identified in the clay mineral assemblage of the studied paddy soils. $[\text{Fe}^{2+}] = 10^{-5} \text{ mol} \cdot \text{l}^{-1}$ .....	90
Figure 5-22: Mean dissolved organic carbon (DOC) concentrations in the soil solution plotted against mean redox values (Eh) of the three paddy sites during 60 days after flooding during the first two months after flooding.....	92
Figure A-1: Images of the soil chronosequence of the marshland site (30 years) as well as the paddy (100, 700 and 2000 years) and respective non-paddy sites (100, 700 years) (modified from Kalbitz et al., 2013, and Koelbl et al., 2013). Soils were classified according to IUSS Working Group WRB (2007). ....	119
Figure C-1: X-ray diffraction (XRD) patterns (oriented texture specimens, Cu $K\alpha$ radiation) of the clay fraction in the uppermost horizon (0–13 cm) of the 30 year marshland site (ML 30); patterns from bottom to top: $\text{Ca}^{2+}$ saturated, ethylene glycol solvated, $\text{K}^+$ saturated and $\text{K}^+$ saturated specimen heated to 550 °C.....	125
Figure C-2: XRD patterns (oriented texture specimens, Cu $K\alpha$ radiation) of the clay fraction in the second horizon (13–30 cm) of the 30 year marshland site (ML 30); patterns from bottom to top: $\text{Ca}^{2+}$ saturated, ethylene glycol solvated, $\text{K}^+$ saturated and $\text{K}^+$ saturated specimen heated to 550 °C.....	125
Figure C-3: XRD patterns (oriented texture specimens, Cu $K\alpha$ radiation) of the clay fraction in the Alp2 horizon (9–15 cm) of the 100 year paddy site (P100); patterns from bottom to top: $\text{Ca}^{2+}$ saturated, ethylene glycol solvated, $\text{K}^+$ saturated and $\text{K}^+$ saturated specimen heated to 550 °C. ....	127
Figure C-4: XRD patterns (oriented texture specimens, Cu $K\alpha$ radiation) of the clay fraction in the Ardp horizon (15–21 cm) of the 100 year paddy site (P100); patterns from bottom to top: $\text{Ca}^{2+}$ saturated, ethylene glycol solvated, $\text{K}^+$ saturated and $\text{K}^+$ saturated specimen heated to 550 °C. ....	127
Figure C-5: XRD patterns (oriented texture specimens, Cu $K\alpha$ radiation) of the clay fraction in the Bwg1 horizon (21–31 cm) of the 100 year paddy site (P100); patterns from bottom to top: $\text{Ca}^{2+}$ saturated, ethylene glycol solvated, $\text{K}^+$ saturated and $\text{K}^+$ saturated specimen heated to 550 °C.....	128

Figure C-6: XRD patterns (oriented texture specimens, Cu K $\alpha$  radiation) of the clay fraction in the Bwg2 horizon (30–50 cm) of the 100 year paddy site (P100); patterns from bottom to top: Ca<sup>2+</sup> saturated, ethylene glycol solvated, K<sup>+</sup> saturated and K<sup>+</sup> saturated specimen heated to 550 °C. .... 128

Figure C-7: XRD patterns (oriented texture specimens, Cu K $\alpha$  radiation) of the clay fraction in the Bwlg1 horizon (50–75 cm) of the 100 year paddy site (P100); patterns from bottom to top: Ca<sup>2+</sup> saturated, ethylene glycol solvated, K<sup>+</sup> saturated and K<sup>+</sup> saturated specimen heated to 550 °C. .... 129

Figure C-8: XRD patterns (oriented texture specimens, Cu K $\alpha$  radiation) of the clay fraction in the Bwlg2 horizon (70–100 cm) of the 100 year paddy site (P100); patterns from bottom to top: Ca<sup>2+</sup> saturated, ethylene glycol solvated, K<sup>+</sup> saturated and K<sup>+</sup> saturated specimen heated to 550 °C. .... 129

Figure C-9: XRD patterns (oriented texture specimens, Cu K $\alpha$  radiation) of the clay fraction in the Alp1 horizon (0–10 cm) of the 700 year paddy site (P700); patterns from bottom to top: Ca<sup>2+</sup> saturated, ethylene glycol solvated, K<sup>+</sup> saturated and K<sup>+</sup> saturated specimen heated to 550 °C. .... 130

Figure C-10: XRD patterns (oriented texture specimens, Cu K $\alpha$  radiation) of the clay fraction in the Alp2 horizon (10–16 cm) of the 700 year paddy site (P700); patterns from bottom to top: Ca<sup>2+</sup> saturated, ethylene glycol solvated, K<sup>+</sup> saturated and K<sup>+</sup> saturated specimen heated to 550 °C. .... 130

Figure C-11: XRD patterns (oriented texture specimens, Cu K $\alpha$  radiation) of the clay fraction in the Ardp horizon (16–22 cm) of the 700 year paddy site (P700); patterns from bottom to top: Ca<sup>2+</sup> saturated, ethylene glycol solvated, K<sup>+</sup> saturated and K<sup>+</sup> saturated specimen heated to 550 °C. .... 131

Figure C-12: XRD patterns (oriented texture specimens, Cu K $\alpha$  radiation) of the clay fraction in the Bg horizon (22–45 cm) of the 700 year paddy site (P700); patterns from bottom to top: Ca<sup>2+</sup> saturated, ethylene glycol solvated, K<sup>+</sup> saturated and K<sup>+</sup> saturated specimen heated to 550 °C. .... 131

Figure C-13: XRD patterns (oriented texture specimens, Cu K $\alpha$  radiation) of the clay fraction in the 2Ahg horizon (45–69 cm) of the 700 year paddy site (P700); patterns from bottom to top: Ca<sup>2+</sup> saturated, ethylene glycol solvated, K<sup>+</sup> saturated and K<sup>+</sup> saturated specimen heated to 550 °C. .... 132

Figure C-14: XRD patterns (oriented texture specimens, Cu K $\alpha$  radiation) of the clay fraction in the 2Blg1 horizon (69–106 cm) of the 700 year paddy site (P700); patterns from bottom to top: Ca<sup>2+</sup> saturated, ethylene glycol solvated, K<sup>+</sup> saturated and K<sup>+</sup> saturated specimen heated to 550 °C. .... 132

Figure C-15: XRD patterns (oriented texture specimens, Cu K $\alpha$  radiation) of the clay fraction in the Alp horizon (0–15 cm) of the 2000 year paddy site (P2000); patterns from bottom to top: Ca<sup>2+</sup> saturated, ethylene glycol solvated, K<sup>+</sup> saturated and K<sup>+</sup> saturated specimen heated to 550 °C. .... 133

Figure C-16: XRD patterns (oriented texture specimens, Cu K $\alpha$  radiation) of the clay fraction in the Ardp horizon (15–20 cm) of the 2000 year paddy site (P2000); patterns from bottom to top: Ca<sup>2+</sup> saturated, ethylene glycol solvated, K<sup>+</sup> saturated and K<sup>+</sup> saturated specimen heated to 550 °C. .... 133

Figure C-17: XRD patterns (oriented texture specimens, Cu K $\alpha$  radiation) of the clay fraction in the Bdg horizon (20–27 cm) of the 2000 year paddy site (P2000); patterns from bottom to top: Ca<sup>2+</sup> saturated, ethylene glycol solvated, K<sup>+</sup> saturated and K<sup>+</sup> saturated specimen heated to 550 °C..... 134

Figure C-18: XRD patterns (oriented texture specimens, Cu K $\alpha$  radiation) of the clay fraction in the 2AhgB horizon (27–35 cm) of the 2000 year paddy site (P2000); patterns from bottom to top: Ca<sup>2+</sup> saturated, ethylene glycol solvated, K<sup>+</sup> saturated and K<sup>+</sup> saturated specimen heated to 550 °C..... 134

Figure C-19: XRD patterns (oriented texture specimens, Cu K $\alpha$  radiation) of the clay fraction in the 2Bg1 horizon (35–50 cm) of the 2000 year paddy site (P2000); patterns from bottom to top: Ca<sup>2+</sup> saturated, ethylene glycol solvated, K<sup>+</sup> saturated and K<sup>+</sup> saturated specimen heated to 550 °C..... 135

Figure C-20: XRD patterns (oriented texture specimens, Cu K $\alpha$  radiation) of the clay fraction in the 2Bg2 horizon (50–70 cm) of the 2000 year paddy site (P2000); patterns from bottom to top: Ca<sup>2+</sup> saturated, ethylene glycol solvated, K<sup>+</sup> saturated and K<sup>+</sup> saturated specimen heated to 550 °C..... 135

Figure C-21: XRD patterns (oriented texture specimens, Cu K $\alpha$  radiation) of the clay fraction in the 2Blg horizon (70–100 cm) of the 2000 year paddy site (P2000); patterns from bottom to top: Ca<sup>2+</sup> saturated, ethylene glycol solvated, K<sup>+</sup> saturated and K<sup>+</sup> saturated specimen heated to 550 °C..... 136

Figure C-22: XRD patterns (oriented texture specimens, Cu K $\alpha$  radiation) of the clay fraction in the Ap1 horizon (0–14 cm) of the 100 year non-paddy site (NP100); patterns from bottom to top: Ca<sup>2+</sup> saturated, ethylene glycol solvated, K<sup>+</sup> saturated and K<sup>+</sup> saturated specimen heated to 550 °C..... 137

Figure C-23: XRD patterns (oriented texture specimens, Cu K $\alpha$  radiation) of the clay fraction in the Ap2 horizon (14–25 cm) of the 100 year non-paddy site (NP100); patterns from bottom to top: Ca<sup>2+</sup> saturated, ethylene glycol solvated, K<sup>+</sup> saturated and K<sup>+</sup> saturated specimen heated to 550 °C..... 137

Figure C-24: XRD patterns (oriented texture specimens, Cu K $\alpha$  radiation) of the clay fraction in the Bw horizon (25–30 cm) of the 100 year non-paddy site (NP100); patterns from bottom to top: Ca<sup>2+</sup> saturated, ethylene glycol solvated, K<sup>+</sup> saturated and K<sup>+</sup> saturated specimen heated to 550 °C..... 138

Figure C-25: XRD patterns (oriented texture specimens, Cu K $\alpha$  radiation) of the clay fraction in the BCwg1 horizon (30–38 cm) of the 100 year non-paddy site (NP100); patterns from bottom to top: Ca<sup>2+</sup> saturated, ethylene glycol solvated, K<sup>+</sup> saturated and K<sup>+</sup> saturated specimen heated to 550 °C..... 138

Figure C-26: XRD patterns (oriented texture specimens, Cu K $\alpha$  radiation) of the clay fraction in the BCwg2 horizon (38–70 cm) of the 100 year non-paddy site (NP100); patterns from bottom to top: Ca<sup>2+</sup> saturated, ethylene glycol solvated, K<sup>+</sup> saturated and K<sup>+</sup> saturated specimen heated to 550 °C..... 139

Figure C-27: XRD patterns (oriented texture specimens, Cu K $\alpha$  radiation) of the clay fraction in the BCwg3 horizon (70–100 cm) of the 100 year non-paddy site (NP100); patterns from bottom to top: Ca<sup>2+</sup> saturated, ethylene glycol solvated, K<sup>+</sup> saturated and K<sup>+</sup> saturated specimen heated to 550 °C..... 139

Figure C-28: XRD patterns (oriented texture specimens, Cu K $\alpha$  radiation) of the clay fraction in the Ap1 horizon (0–12 cm) of the 700 year non-paddy site (NP700); patterns from bottom to top: Ca<sup>2+</sup> saturated, ethylene glycol solvated, K<sup>+</sup> saturated and K<sup>+</sup> saturated specimen heated to 550 °C. .... 140

Figure C-29: XRD patterns (oriented texture specimens, Cu K $\alpha$  radiation) of the clay fraction in the Ap2 horizon (12–17 cm) of the 700 year non-paddy site (NP700); patterns from bottom to top: Ca<sup>2+</sup> saturated, ethylene glycol solvated, K<sup>+</sup> saturated and K<sup>+</sup> saturated specimen heated to 550 °C. .... 140

Figure C-30: XRD patterns (oriented texture specimens, Cu K $\alpha$  radiation) of the clay fraction in the Bw1 horizon (17–23 cm) of the 700 year non-paddy site (NP700); patterns from bottom to top: Ca<sup>2+</sup> saturated, ethylene glycol solvated, K<sup>+</sup> saturated and K<sup>+</sup> saturated specimen heated to 550 °C. .... 141

Figure C-31: XRD patterns (oriented texture specimens, Cu K $\alpha$  radiation) of the clay fraction in the –Bw2 horizon (23–45 cm) of the 700 year non-paddy site (NP700); patterns from bottom to top: Ca<sup>2+</sup> saturated, ethylene glycol solvated, K<sup>+</sup> saturated and K<sup>+</sup> saturated specimen heated to 550 °C. .... 141

Figure C-32: XRD patterns (oriented texture specimens, Cu K $\alpha$  radiation) of the clay fraction in the Bw11 horizon (45–70 cm) of the 700 year non-paddy site (NP700); patterns from bottom to top: Ca<sup>2+</sup> saturated, ethylene glycol solvated, K<sup>+</sup> saturated and K<sup>+</sup> saturated specimen heated to 550 °C. .... 142

Figure C-33: XRD patterns (oriented texture specimens, Cu K $\alpha$  radiation) of the clay fraction in the Bw12 horizon (70–100 cm) of the 700 year non-paddy site (NP700); patterns from bottom to top: Ca<sup>2+</sup> saturated, ethylene glycol solvated, K<sup>+</sup> saturated and K<sup>+</sup> saturated specimen heated to 550 °C. .... 142

Figure D-1: <sup>57</sup>Fe Mössbauer spectra at 298 K (top) and 4.2 K (bottom) of the clay fraction of the upper horizon (0–13 cm) of the marshland site (ML30). The solid black line drawn through the data points is the calculated fit. Corresponding Mössbauer parameters can be found in Table D-2 and Table D-4. .... 143

Figure D-2: <sup>57</sup>Fe Mössbauer spectra at 298 K (top) and 4.2 K (bottom) of the clay fraction of the lower horizon (13–30 cm) of the marshland site (ML30). The solid black line drawn through the data points is the calculated fit. Corresponding Mössbauer parameters can be found in Table D-2 and Table D-4. .... 144

Figure D-3: <sup>57</sup>Fe Mössbauer spectra at 298 K (top) and 4.2 K (bottom) of the clay fraction of the Alp1 horizon (0–9 cm) of the 100 year paddy site (P100). The solid black line drawn through the data points is the calculated fit. Corresponding Mössbauer parameters can be found in Table D-1 and Table D-3. .... 144

Figure D-4: <sup>57</sup>Fe Mössbauer spectra at 298 K (top) and 4.2 K (bottom) of the clay fraction of the Alp2 horizon (9–15 cm) of the 100 year paddy site (P100). The solid black line drawn through the data points is the calculated fit. Corresponding Mössbauer parameters can be found in Table D-1 and Table D-3. .... 145

Figure D-5: <sup>57</sup>Fe Mössbauer spectra at 298 K (top) and 4.2 K (bottom) of the clay fraction of the Ardp horizon (15–21 cm) of the 100 year paddy site (P100). The solid black line drawn through the data points is the calculated fit. Corresponding Mössbauer parameters can be found in Table D-1 and Table D-3. .... 145

Figure D-6:  $^{57}\text{Fe}$  Mössbauer spectra at 298 K (top) and 4.2 K (bottom) of the clay fraction of the Bwg1 horizon (21–30 cm) of the 100 year paddy site (P100). The solid black line drawn through the data points is the calculated fit. Corresponding Mössbauer parameters can be found in Table D-1 and Table D-3..... 146

Figure D-7:  $^{57}\text{Fe}$  Mössbauer spectra at 298 K (top) and 4.2 K (bottom) of the clay fraction of the Bwg2 horizon (30–50 cm) of the 100 year paddy site (P100). The solid black line drawn through the data points is the calculated fit. Corresponding Mössbauer parameters can be found in Table D-1 and Table D-3..... 146

Figure D-8:  $^{57}\text{Fe}$  Mössbauer spectra at 298 K (top) and 4.2 K (bottom) of the clay fraction of the Bwlg1 horizon (50–75 cm) of the 100 year paddy site (P100). The solid black line drawn through the data points is the calculated fit. Corresponding Mössbauer parameters can be found in Table D-1 and Table D-3..... 147

Figure D-9:  $^{57}\text{Fe}$  Mössbauer spectra at 298 K (top) and 4.2 K (bottom) of the clay fraction of the Bwlg2 horizon (75–100 cm) of the 100 year paddy site (P100). The solid black line drawn through the data points is the calculated fit. Corresponding Mössbauer parameters can be found in Table D-1 and Table D-3..... 147

Figure D-10:  $^{57}\text{Fe}$  Mössbauer spectra at 298 K (top) and 4.2 K (bottom) of the clay fraction of the Alp1 horizon (0–10 cm) of the 700 year paddy site (P700). The solid black line drawn through the data points is the calculated fit. Corresponding Mössbauer parameters can be found in Table D-1 and Table D-3..... 148

Figure D-11:  $^{57}\text{Fe}$  Mössbauer spectra at 298 K (top) and 4.2 K (bottom) of the clay fraction of the Alp2 horizon (10–16 cm) of the 700 year paddy site (P700). The solid black line drawn through the data points is the calculated fit. Corresponding Mössbauer parameters can be found in Table D-1 and Table D-3..... 148

Figure D-12:  $^{57}\text{Fe}$  Mössbauer spectra at 298 K (top) and 4.2 K (bottom) of the clay fraction of the Ardp horizon (16–22 cm) of the 700 year paddy site (P700). The solid black line drawn through the data points is the calculated fit. Corresponding Mössbauer parameters can be found in Table D-1 and Table D-3..... 149

Figure D-13:  $^{57}\text{Fe}$  Mössbauer spectra at 298 K (top) and 4.2 K (bottom) of the clay fraction of the Bg horizon (22–45 cm) of the 700 year paddy site (P700). The solid black line drawn through the data points is the calculated fit. Corresponding Mössbauer parameters can be found in Table D-1 and Table D-3..... 149

Figure D-14:  $^{57}\text{Fe}$  Mössbauer spectra at 298 K (top) and 4.2 K (bottom) of the clay fraction of the 2Ahgb horizon (45–69 cm) of the 700 year paddy site (P700). The solid black line drawn through the data points is the calculated fit. Corresponding Mössbauer parameters can be found in Table D-1 and Table D-3..... 150

Figure D-15:  $^{57}\text{Fe}$  Mössbauer spectra at 298 K (top) and 4.2 K (bottom) of the clay fraction of the 2Blg1 horizon (69–106 cm) of the 700 year paddy site (P700). The solid black line drawn through the data points is the calculated fit. Corresponding Mössbauer parameters can be found in Table D-1 and Table D-3..... 150

Figure D-16:  $^{57}\text{Fe}$  Mössbauer spectra at 298 K (top) and 4.2 K (bottom) of the clay fraction of the Alp horizon (0–15 cm) of the 2000 year paddy site (P2000). The solid black line drawn through the data points is the calculated fit. Corresponding Mössbauer parameters can be found in Table D-1 and Table D-3..... 151

Figure D-17:  $^{57}\text{Fe}$  Mössbauer spectra at 298 K (top) and 4.2 K (bottom) of the clay fraction of the Ardp horizon (15–20 cm) of the 2000 year paddy site (P2000). The solid black line drawn through the data points is the calculated fit. Corresponding Mössbauer parameters can be found in Table D-1 and Table D-3..... 151

Figure D-18:  $^{57}\text{Fe}$  Mössbauer spectra at 298 K (top) and 4.2 K (bottom) of the clay fraction of the Bdg horizon (20–27 cm) of the 2000 year paddy site (P2000). The solid black line drawn through the data points is the calculated fit. Corresponding Mössbauer parameters can be found in Table D-1 and Table D-3..... 152

Figure D-19:  $^{57}\text{Fe}$  Mössbauer spectra at 298 K (top) and 4.2 K (bottom) of the clay fraction of the 2AhgB horizon (27–35 cm) of the 2000 year paddy site (P2000). The solid black line drawn through the data points is the calculated fit. Corresponding Mössbauer parameters can be found in Table D-1 and Table D-3..... 152

Figure D-20:  $^{57}\text{Fe}$  Mössbauer spectra at 298 K (top) and 4.2 K (bottom) of the clay fraction of the 2Bg1 horizon (35–50 cm) of the 2000 year paddy site (P2000). The solid black line drawn through the data points is the calculated fit. Corresponding Mössbauer parameters can be found in Table D-1 and Table D-3..... 153

Figure D-21:  $^{57}\text{Fe}$  Mössbauer spectra at 298 K (top) and 4.2 K (bottom) of the clay fraction of the 2Bg2 horizon (50–70 cm) of the 2000 year paddy site (P2000). The solid black line drawn through the data points is the calculated fit. Corresponding Mössbauer parameters can be found in Table D-1 and Table D-3..... 153

Figure D-22:  $^{57}\text{Fe}$  Mössbauer spectra at 298 K (top) and 4.2 K (bottom) of the clay fraction of the 2Blg horizon (70–100 cm) of the 2000 year paddy site (P2000). The solid black line drawn through the data points is the calculated fit. Corresponding Mössbauer parameters can be found in Table D-1 and Table D-3..... 154

Figure D-23:  $^{57}\text{Fe}$  Mössbauer spectra at 298 K (top) and 4.2 K (bottom) of the clay fraction of the Ap1 horizon (0–14 cm) of the 100 year non-paddy site (NP100). The solid black line drawn through the data points is the calculated fit. Corresponding Mössbauer parameters can be found in Table D-2 and Table D-4..... 154

Figure D-24:  $^{57}\text{Fe}$  Mössbauer spectra at 298 K (top) and 4.2 K (bottom) of the clay fraction of the Ap2 horizon (14–25 cm) of the 100 year non-paddy site (NP100). The solid black line drawn through the data points is the calculated fit. Corresponding Mössbauer parameters can be found in Table D-2 and Table D-4. .... 155

Figure D-25:  $^{57}\text{Fe}$  Mössbauer spectra at 298 K (top) and 4.2 K (bottom) of the clay fraction of the Bw horizon (25–30 cm) of the 100 year non-paddy site (NP100). The solid black line drawn through the data points is the calculated fit. Corresponding Mössbauer parameters can be found in Table D-2 and Table D-4..... 155

Figure D-26:  $^{57}\text{Fe}$  Mössbauer spectra at 298 K (top) and 4.2 K (bottom) of the clay fraction of the BCwg1 horizon (30–38 cm) of the 100 year non-paddy site (NP100). The solid black line drawn through the data points is the calculated fit. Corresponding Mössbauer parameters can be found in Table D-2 and Table D-4. .... 156

Figure D-27:  $^{57}\text{Fe}$  Mössbauer spectra at 298 K (top) and 4.2 K (bottom) of the clay fraction of the BCwg2 horizon (38–70 cm) of the 100 year non-paddy site (NP100). The solid black line drawn through the data points is the calculated fit. Corresponding Mössbauer parameters can be found in Table D-2 and Table D-4. .... 156

Figure D-28:  $^{57}\text{Fe}$  Mössbauer spectra at 298 K (top) and 4.2 K (bottom) of the clay fraction of the BCwlg horizon (70–100 cm) of the 100 year non-paddy site (NP100). The solid black line drawn through the data points is the calculated fit. Corresponding Mössbauer parameters can be found in Table D-2 and Table D-4. .... 157

Figure D-29:  $^{57}\text{Fe}$  Mössbauer spectra at 298 K (top) and 4.2 K (bottom) of the clay fraction of the Ap1 horizon (0–11 cm) of the 700 year non-paddy site (NP700). The solid black line drawn through the data points is the calculated fit. Corresponding Mössbauer parameters can be found in Table D-2 and Table D-4. .... 157

Figure D-30:  $^{57}\text{Fe}$  Mössbauer spectra at 298 K (top) and 4.2 K (bottom) of the clay fraction of the Ap2 horizon (11–17 cm) of the 700 year non-paddy site (NP700). The solid black line drawn through the data points is the calculated fit. Corresponding Mössbauer parameters can be found in Table D-2 and Table D-4. .... 158

Figure D-31:  $^{57}\text{Fe}$  Mössbauer spectra at 298 K (top) and 4.2 K (bottom) of the clay fraction of the Bw1 horizon (17–23 cm) of the 700 year non-paddy site (NP700). The solid black line drawn through the data points is the calculated fit. Corresponding Mössbauer parameters can be found in Table D-2 and Table D-4. .... 158

Figure D-32:  $^{57}\text{Fe}$  Mössbauer spectra at 298 K (top) and 4.2 K (bottom) of the clay fraction of the Bw2 horizon (23–45 cm) of the 700 year non-paddy site (NP700). The solid black line drawn through the data points is the calculated fit. Corresponding Mössbauer parameters can be found in Table D-2 and Table D-4. .... 159

Figure D-33:  $^{57}\text{Fe}$  Mössbauer spectra at 298 K (top) and 4.2 K (bottom) of the clay fraction of the Bw11 horizon (45–70 cm) of the 700 year non-paddy site (NP700). The solid black line drawn through the data points is the calculated fit. Corresponding Mössbauer parameters can be found in Table D-2 and Table D-4. .... 159

Figure D-34:  $^{57}\text{Fe}$  Mössbauer spectra at 298 K (top) and 4.2 K (bottom) of the clay fraction of the Bw12 horizon (70–100 cm) of the 700 year non-paddy site (NP700). The solid black line drawn through the data points is the calculated fit. Corresponding Mössbauer parameters can be found in Table D-2 and Table D-4. .... 160

## List of tables

Table 2-1: Basic properties of the fine fraction (<2 mm) of selected paddy sites along the chronosequences in Cixi, Zhejiang (PR China) (data from Wissing et al, 2011 and Kölbl et al., 2014, respectively). .....	13
Table 2-2: Basic properties of the fine fraction (<2 mm) of the marshland site (point of zero soil formation) and selected non-paddy sites along the chronosequences in Cixi, Zhejiang (PR China) (data from Wissing et al., 2011 and Kölbl et al., 2014, respectively). .....	14
Table 3-1: Cation exchange capacity ( $CEC_{pH7}$ ), exchangeable base cations and base saturation (BS) of paddy (P) clay fractions. ....	22
Table 3-2: Total Fe ( $Fe_t$ ), dithionite–citrate–bicarbonate ( $Fe_d$ ) and ammonium–oxalate-extractable Fe ( $Fe_o$ ) in the clay fractions of paddy (P) and non-paddy (NP) soils. Fe contents of the marshland soil (ML30) are given as reference for point zero of soil formation. ....	23
Table 3-3: Identification of Fe oxides in the clay fractions of the paddy sites (P) based on their characteristic X-ray diffraction peaks. ....	26
Table 3-4: Range of $^{57}Fe$ Mössbauer parameters, isomer shift (IS), quadrupole splitting (QS) and hyperfine field ( $B_{hf}$ ), in the spectra taken at RT (298 K). ....	28
Table 3-5: Range of $^{57}Fe$ Mössbauer parameters isomer shift (IS), quadrupole splitting (QS) and hyperfine field ( $B_{hf}$ ) in the spectra taken at liquid helium temperature (4.2 K). ....	30
Table 3-6: $^{57}Fe$ Mössbauer parameters, isomer shift (IS), quadrupole splitting (QS) and hyperfine field ( $B_{hf}$ ), of the LHe-HFO phase at 4.2 K of the paddy (P) and non-paddy (NP) topsoil (modified according to Vogelsang et al., 2016a). ....	37
Table 4-1: $^{57}Fe$ Mössbauer parameters, isomer shift (IS) and quadrupole splitting (QS), of the N Au-2 (original) spectrum taken at room temperature (298 K). ....	55
Table 4-2: Cation exchange capacity at pH 7 ( $CEC_{pH7}$ ) and exchangeable cations of the original sample ( $Ca^{2+}$ -exchanged) and the N Au-2 samples after 12 months in the field at 100, 700, and 2000 year paddy sites (P100, P700 and P2000). ....	56
Table 5-1: Correlation of the electron conductivity (EC), earth alkali/alkali elements, chloride ( $Cl^-$ ) and the redox potential in the soil solution of the upper (35 cm) and lower (55 cm) subsoil of the three paddy sites P100, P700, and P2000. ....	78
Table 5-2: Correlation of DIC, Si and Fe concentrations in the soil solution of the upper (35 cm) and lower (55 cm) subsoil of the three paddy sites. ....	79
Table 5-3: Correlation of Eh with concentrations of the redox species in the soil solution of the upper (35 cm) and lower (55 cm) subsoil of the three paddy sites. ....	84
Table A-1: Field description of the study soils along the chronosequence of the marshland as well as paddy and non-paddy sites. Soil description was done according to FAO (2006) down to 1 m depth and classified according to IUSS Working Group WRB (2007) by R. Jahn and P. Schadt (DFG Research Group FOR 994 “Biogeochemistry of Paddy Soil Evolution”). ....	120

Table B-1: Total carbon ( $C_{\text{total}}$ ) and total nitrogen ( $N_{\text{total}}$ ) concentrations in the clay fractions of paddy (P) and non-paddy sites (NP). Organic carbon (OC) was calculated by subtracting total inorganic carbon (IC) from $C_{\text{total}}$ . The marshland site (ML30) is given as point zero of soil evolution.....	122
Table B-2: Total carbon ( $C_{\text{total}}$ ) and total nitrogen ( $N_{\text{total}}$ ) concentrations in the clay fractions of non-paddy sites (NP). The marshland site (ML30) is given as point zero of soil evolution. Organic carbon (OC) was calculated by subtracting total inorganic carbon (IC) from $C_{\text{total}}$ .....	123
Table B-3: Cation exchange capacity ( $\text{CEC}_{\text{pH7}}$ ), exchangeable cations and base saturation (BS) of non-paddy (NP) clay fractions. The marshland site (ML30) is given as point zero of soil evolution.....	123
Table B-4: Total element concentrations in the clay fractions of paddy (P) sites, determined with XRF.....	124
Table B-5: Total element concentrations in the clay fractions of non-paddy sites (NP), determined with XRF. The marshland site (ML30) is given as point zero of soil evolution.....	125
Table D-1: $^{57}\text{Fe}$ Mössbauer parameters, isomer shift (IS), quadrupole splitting (QS) and hyperfine field ( $B_{\text{hf}}$ ), of the spectra taken of paddy (P) clay fractions at room temperature (298 K).....	161
Table D-2: $^{57}\text{Fe}$ Mössbauer parameters, isomer shift (IS), quadrupole splitting (QS) and hyperfine field ( $B_{\text{hf}}$ ), of the spectra taken of marshland (ML) and non-paddy (NP) clay fractions at room temperature (298 K).....	162
Table D-3: $^{57}\text{Fe}$ Mössbauer parameters, isomer shift (IS), quadrupole splitting (QS) hyperfine field ( $B_{\text{hf}}$ ) and asymmetry (asym), of the spectra taken of paddy (P) clay fractions at liquid helium temperature (4.2 K).....	163
Table D-4: $^{57}\text{Fe}$ Mössbauer parameters, isomer shift (IS), quadrupole splitting (QS) hyperfine field ( $B_{\text{hf}}$ ) and asymmetry (asym), of the spectra taken of marshland (ML30) and non-paddy (NP) clay fractions at liquid helium temperature (4.2 K).....	165
Table E-1: Soil redox potential (Eh) determined at 10 cm (10), 35 cm (35) and 55 cm (55) below surface at the 100 year paddy site (P100).....	167
Table E-2: Soil redox potential (Eh) determined at 10 cm (10), 35 cm (35) and 55 cm (55) below surface at the 700 year paddy site (P700).....	170
Table E-3: Soil redox potential (Eh) determined at 10 cm (10), 35 cm (35) and 55 cm (55) below surface at the 2000 year paddy site (P2000).....	173
Table E-4: Soil redox potential (Eh) determined at 10 cm (10), 35 cm (35) and 55 cm (55) below surface at the 100 year non-paddy site (NP100).....	176
Table E-5: Soil redox potential determined at 10 cm (10), 35 cm (35) and 55 cm (55) below surface at the 700 year non-paddy site (NP700).....	179
Table E-6: pH values and alkalinity (alk) determined in the soil solution of the 100 year paddy soil (P100).....	182
Table E-7: pH values and alkalinity (alk) determined in the soil solution of the 700 year paddy soil (P700).....	183

Table E-8: pH values and alkalinity determined in the soil solution of the 2000 year paddy soil (P2000). .....	184
Table E-9: Electric conductivity (EC), sodium adsorption ratio (SAR) and chloride (Cl <sup>-</sup> ) contents determined in the soil solution of the 100 year paddy soil (P100). .....	185
Table E-10: Electric conductivity (EC), sodium adsorption ratio (SAR) and chloride (Cl <sup>-</sup> ) contents determined in the soil solution of the 700 year paddy soil (P700). .....	187
Table E-11: Electric conductivity (EC), sodium adsorption ratio (SAR) and chloride (Cl <sup>-</sup> ) contents determined in the soil solution of the 2000 year paddy soil (P2000). .....	189
Table E-12: Concentrations of earth alkali/alkali elements determined in the soil solution of the 100 year paddy soil (P100). .....	191
Table E-13: Concentrations of the earth alkali/alkali elements determined in the soil solution of the 700 year paddy soil (P700). .....	193
Table E-14: Concentrations of the earth alkali/alkali elements determined in the soil solution of the 2000 year paddy soil (P2000). .....	195
Table E-15: Concentrations of redox sensitive elements and compounds, respectively, determined in the soil solution of the 100 year paddy soil (P100). .....	197
Table E-16: Concentrations of redox sensitive elements and compounds, respectively, determined in the soil solution of the 700 year paddy soil (P700). .....	199
Table E-17: Concentrations of redox sensitive elements and compounds, respectively, determined in the soil solution of the 2000 year paddy soil (P2000). .....	201
Table E-18: Concentration of the redox sensitive elements and compounds, respectively, determined in the soil solution of the 100 year paddy soil (P100). .....	203
Table E-19: Concentration of the redox sensitive elements and compounds, respectively, determined in the soil solution of the 700 year paddy soil (P700). .....	205
Table E-20: Concentration of the redox sensitive elements and compounds, respectively, determined in the soil solution of the 2000 year paddy soil (P2000). .....	207
Table E-21: Concentrations of the matrix elements Si and Al determined in the soil solution of the 100 year paddy soil (P100). .....	209
Table E-22: Concentrations of the matrix elements Si and Al determined in the soil solution of the 700 year paddy soil (P700). .....	210
Table E-23: Concentrations of the matrix elements Si and Al determined in the soil solution of the 2000 year paddy soil (P2000). .....	211

## List of abbreviations

A <sup>-</sup>	conservative anions
Alk	alkalinity
BD	bulk density
B <sub>hf</sub>	hyperfine field
BS	base saturation
C <sup>+</sup>	conservative cations
CEC	cation exchange capacity
chl	chlorite
DCB	dithionite–citrate–bicarbonate
DIC	dissolved inorganic carbon
DOC	dissolved organic carbon
DOM	dissolved organic matter
EC	electric conductivity
EG	ethylen glycol
Eh	redox potential (defined as potential of a Pt electrode relative to a hydrogen electrode at zero potential)
ESP	exchangeable sodium percentage
EXAFS	extended X-ray absorption fine structure (spectroscopy)
FeB	paramagnetic relaxation of ferric iron in aluminosilicates
Fe <sub>d</sub>	dithionite–citrate–bicarbonate-extractable iron
Fe <sub>o</sub>	ammonium–oxalate-extractable iron
FeOx	paramagnetic iron hydrous oxides
Fe <sub>si</sub>	silicate bound iron (Fe <sub>t</sub> -Fe <sub>d</sub> )
Fe <sub>t</sub>	total iron
Fh	ferrihydrite
GRiSP	Global Rice Science Partnership
Gt	goethite
GtB	goethite near its magnetic blocking temperature
HFO	hydrous ferric oxides
Hm	haematite
IC	inorganic carbon
ill	illite
IS	isomer shift (δ )
IUSS	International Union of Soil Science
kao	kaolinite
LHe	liquid helium (temperature) (4.2 K)
Lp	lepidocrocite
n.a.	not analysed
n.d.	not detectable

*List of abbreviations*

---

NIRS	near-infrared spectroscopy
NP	non-paddy, e.g. NP100
OC	organic carbon
Oct <sub>cis</sub>	octahedral coordinated ferric Fe (trans)
Oct <sub>trans</sub>	octahedral coordinated ferric Fe (cis)
OM	organic matter
P	paddy, e.g. P100
PA	polyamid
pCO <sub>2</sub>	partial pressure of carbon dioxide (CO <sub>2</sub> )
PE	polyethylen
QS	quadrupole splitting ( $\Delta$ )
qtz	quartz
RT	room temperature (298 K)
S2	ferrous Fe bound in aluminosilicates
S3	ferric Fe bound in aluminosilicates
SAR	sodium adsorption ration
SOC	soil organic carbon
SSA	specific surface area
Tet	tetrahedral coordinated ferric Fe
T <sub>m</sub>	Morin temperature
UV/VIS	ultraviolet–visible (spectroscopy)
ver	vermiculite
WRB	World Reference Base of Soil Resources
XAS	X-ray absorption spectroscopy
XPS	X-ray photoelectron spectroscopy
XRD	X-ray diffraction
XRF	X-ray fluorescence

## Summary

More than 11% of the world's arable land is used for rice (*Oryza sativa* L.) production, mainly under temporarily submerged conditions (paddy fields). Alternating submergence and drainage of the fields during rice cultivation results in temporal as well as spatial variations in redox conditions in paddy soils. Iron (Fe) oxides, hydroxides and oxyhydroxides (collectively named Fe oxides) as well as Fe-bearing clay minerals are prone to transformations upon alternating redox conditions. Long-term effects of paddy cultivation and thus, spatial and temporal variations in redox conditions on the Fe-bearing minerals are still not fully understood. The main objective of this study was to elucidate Fe mineral transformations as evoked by long-term redox cycles. Additionally, related redox dynamics and the resulting effects on the composition of soil solution in paddy soils were studied.

Changes in the Fe mineral assemblage and properties of the clay fraction due to long-term reduction–oxidation cycles were studied along a soil chronosequence of irrigated paddy soils (100, 700, and 2000 years of cultivation) and non-irrigated arable soils (100 and 700 years) developed on comparable parent material (calcareous marine substrates) in the province of Zhejiang, China (*Chapter 2* and *Chapter 3*, respectively). To track short-term (trans)formations and identify possible paddy-specific Fe mineral phases and their precursors, an additional field experiment was conducted in which Fe(III) oxides differing in crystallinity (ferrihydrite, goethite) and a Fe(III)-bearing clay mineral (nontronite) were exposed *in-situ* to alternating redox conditions by placing them for one year in illuvial subsoil horizons along the soil chronosequence of the paddy soils (*Chapter 4*). Research questions addressed included: (1) does paddy cultivation intensify Fe mineral (trans)formations in comparison sites under permanent oxic conditions and does it relate to time of paddy cultivation, (2) does paddy cultivation result in the formation of paddy-specific mineral phases, (3) does the accumulation of organic matter (OM) in paddy topsoils influence abundance and crystallinity of Fe mineral phases and (4) does long-term paddy management result in changes of Fe-bearing clay minerals and of their properties. Identification of the Fe-bearing clay minerals was carried out by X-ray diffraction (XRD); in addition,  $^{57}\text{Fe}$  Mössbauer spectroscopy at variable temperatures (298 and 4.5 K) was applied for identification and characterisation as well as quantitative speciation of solid Fe mineral phases, complemented by selective chemical extractions (ammonium oxalate, dithionite–citrate–bicarbonate).

It could be demonstrated, that long-term cultivation of rice on calcareous marine substrates intensified Fe mineral weathering and redistribution of Fe in comparison to sites under permanent oxic conditions (non-paddy sites) and led to decoupling of top- and subsoil processes with respect to Fe contents and Fe mineral phases in the clay fraction. Different Fe mineral weathering and (trans)forming environments established in paddy top- and subsoils;

depth differentiation of these environments becomes increasingly distinct with time under paddy management, thus, with increasing numbers of redox cycles. Topsoils are characterised by reductive dissolution of the Fe minerals (silicates as well as crystalline and poorly crystalline oxide phases) during anoxic periods; upon oxic phases the coprecipitation of poorly crystalline Fe oxides with organic matter (OM) is prevalent, supported by the enrichment of OM in paddy topsoils. These organic–mineral interactions inhibit transformation and crystallisation of the Fe oxides present and lead to increasing proportions of poorly-crystalline, OM-rich hydrous ferric oxides and less well ordered goethite and haematite. The presence of OM controlled, at least partly, the composition and crystallinity of the Fe mineral assemblage in the topsoil. In subsoils, in contrast, organic–mineral interactions were of little importance for transformation processes of the hydrous Fe oxides, likely because little organic matter is transported into deeper soil layers. Transformation processes seem to be driven by dissolved Fe(II) leached from the topsoil or, under the environmental conditions less likely, by Fe(II) released *in-situ*. This resulted in increasing contents of Fe oxides and increasing crystallinity of the Fe oxides present, the latter likely due to secondary transformation catalysed by Fe(II). In consequence, microcrystalline goethite becomes the prevalent Fe mineral in paddy subsoils. In the deeper subsoils, likely because of little CO<sub>2</sub> concentrations, lepidocrocite forms in addition to goethite.

In contrast to Fe oxides, Fe-bearing clay minerals were less affected by repeated redox cycles. Little changes in the clay mineral assemblage were observed along the chronosequence; observed differences among the paddy sites could not directly be related to the time of cultivation. All clay fractions were characterised by a similar clay mineral assemblage: illite, kaolinite, (primary) chlorite, expandable and mixed-layered phases.

The *in-situ* experiments confirmed that less crystalline Fe oxides were prone to transformations to more crystalline minerals in paddy subsoils. The time under paddy management, i.e., the redox status of the soils, had strong influence of ferrihydrite transformation. With time of paddy cultivation, more crystalline Fe oxides, such as goethite and haematite, and partly lepidocrocite, were formed. At the site 100 years under paddy management, high pH and higher salinity hindered transformations of Fe oxides. Increasing magnetic interactions in the 4.2 K Mössbauer spectra upon *in-situ* exposure of the nontronite to paddy conditions indicated some structural modifications within little time. Such structural changes have been observed before only when exposing nontronite to harsh chemical reduction. Seemingly, biotic reduction under natural conditions can induce such transformations. To my best knowledge, this is the first study to show such changes under field conditions and within just one full redox cycle.

To elucidate changes in redox potential and subsequent changes in the composition of the soil solution as related to time of paddy cultivation and concomitant Fe mineral transformations, a one-year field experiment along selected soils of the chronosequence was conducted (Chapter

5). Research questions included (1) does the duration of paddy cultivation, along with progressing depth differentiation of redox sensitive elements and OM, result in significant changes in redox response to flooding and drying and (2) does the composition of the soil solution composition mirror the redox status and/or the mineral assemblage of the soil. Redox potentials measurements and soil solution sampling in subsoil horizons of 100, 700, and 2000 year old paddy and non-paddy soils were conducted for one entire paddy–winter crop cycle (12 month). Soil solutions were analysed for pH, electrical conductivity, nitrite/nitrate, ammonium, Mn, Fe, sulfate, dissolved inorganic and organic carbon, matrix elements and exchangeable cations. The experiments showed that rice cultivation led to distinct redox cycles at the three paddy sites with Eh ranges of +570 to –190 mV in the topsoils and +650 to –200 mV in the subsoils, respectively. After high spatial variability of the redox potential shortly after submergence redox conditions stabilised at approx. –200 mV throughout the profiles after two months. In the upper subsoil, (35 cm) redox changes were similar in all three paddy soils, despite higher abundances of electron donors (i.e., OM) and easily available electron acceptors (i.e., nitrate, poorly crystalline Fe oxides) in overlying topsoils and differences in concentration and crystallinity of Fe oxides in subsoils, respectively. In the lower subsoil (55 cm), the decrease of Eh became slower with the time of paddy cultivation, presumably due to higher groundwater tables at the younger sites. Thus, time span of paddy cultivation, along with progressing depth differentiation of redox sensitive elements and OM, did not result in significant changes in redox response to flooding and draining. Redox dynamics seemed to be a simple function of actual management, e.g., time and length of irrigation, and/or groundwater levels.

The soil solution composition of the paddy subsoils reflected the sequence of alternative terminal electron acceptors, i.e.,  $\text{NO}_3^-$ , Mn(III, IV), Fe(III) and  $\text{SO}_4^{2-}$ , after depletion in  $\text{O}_2$ , independent of the time of cultivation. The sequence of redox systems, however, was no strict chain, but showed overlaps, with co-occurrence of different reduction processes. The redistribution patterns of Fe (and OM) upon paddy cultivation were partly mirrored by the concentrations of the respective dissolved species/compound in the soil solutions. Despite low redox potentials, Fe concentrations in the soil solution were little ( $<40 \mu\text{mol l}^{-1}$ ), even at the oldest, most Fe oxide-rich site, likely due to small availability of microbial reducible Fe oxides at the given weakly alkaline and saline conditions and, most crucial, the lack of easily reducible, weakly crystalline Fe oxide phases. Also, Fe(II) leached from paddy topsoils might have been bound on the exchange complex and/or directly involved in solid state transformations, and thus, not contributed to dissolved Fe but to secondary transformations in the subsoil. Evidently paddy subsoils serve predominately as accumulation zones for Fe leached from reduced overlying topsoils, thus, being little to no sources of Fe leaching to the groundwater.

The chronosequence provided a unique opportunity to study biogeochemical processes fundamental to soils with alternating redox conditions, in particular to Fe cycling, Fe mineral weathering and (trans)formations as well as their interlinking with organic matter. The present study supported that Fe dynamics and Fe-bearing mineral transformations as well as the resulting depth profiles play a crucial role for the biogeochemistry and evolution of paddy soils, and are important for the differentiation of paddy from non-paddy soils under long-term cultivation.

## Zusammenfassung

Weltweit werden rund 11% der landwirtschaftlichen Fläche für den Anbau von Reis (*Oryza sativa* L.) genutzt. Hierbei überwiegt der Anbau mit periodischer Überflutung der Felder (Nassreisanbau), infolgedessen die Böden sowohl zeitlichen als auch räumlichen Redoxschwankungen unterworfen werden. Unter diesen Bedingungen kommt es zu redox-induzierten Neubildungen und Transformationen von Eisen(Fe)hydroxiden, -oxyhydroxiden und -oxiden (im folgenden Fe-Oxide) und Fe-haltigen Tonmineralen. Bis heute haben sich nur wenige Studien mit den Auswirkungen dauerhaft alternierender Redoxbedingungen auf die Mineralogie von Nassreisböden beschäftigt. Ziel der vorliegenden Arbeit war es daher, Langzeitauswirkungen von Nassreisanbau auf Mineralverwitterung und -transformationen sowie auf die Zusammensetzung der Bodenlösung in Relation zu den vorherrschenden Redoxbedingungen dieser Böden aufzuklären.

Die Untersuchungen wurden in der Zhejiang Provinz, China, entlang einer Chronosequenz rezenter Nassreisböden und nicht-bewässerter Ackerböden gleichen Ausgangsmaterials (kalkhaltige marine Sedimente) durchgeführt (*Kapitel 2*). Drei Nassreisböden (100, 700 und 2000 Jahre Nutzung) und nicht-bewässerte Vergleichsflächen (100, 700 Jahre Nutzung) wurden hinsichtlich der Unterschiede im Mineralbestand sowie der Eigenschaften ihrer Tonfraktion, als Spiegel der Langzeitbedingungen, untersucht (*Kapitel 3*). Um Kurzeitauswirkungen von Nassreisanbau auf Mineraltransformationen untersuchen zu können, wurde ergänzend ein *in-situ* Verwitterungsversuch mit drei eisenhaltigen Testmineralen (Goethit, Ferrihydrit und Nontronit) durchgeführt (*Kapitel 4*). Hierfür wurden die Testminerale für 12 Monate in den Illuvialhorizont der Nassreisböden (35 cm Tiefe) eingebracht. Es sollte überprüft werden, (1) ob Verwitterung, Transformation und Neubildung von Fe-Oxiden und eisenhaltige Tonmineralen unter andauernden Redoxschwankungen intensiviert werden und ob ein Zusammenhang mit der Nutzungsdauer zu erkennen ist, (2) ob es zur für Nassreisböden typischen Neubildung von Mineralphasen kommt, (3) inwieweit die häufig zu beobachtende Anreicherung organischer Substanz im Oberboden sowohl Vorkommen als auch Kristallinität Fe-haltiger Minerale beeinflusst sowie (4) ob Langzeitanbau von Reis zu Veränderungen Fe-haltiger Tonminerale und deren Eigenschaften führt. Die Charakterisierung des aktuellen Fe-Mineralbestandes der Tonfraktion erfolgte hierzu röntgendiffraktometrisch (XRD), durch  $^{57}\text{Fe}$  Mössbauer-Spektroskopie (298 und 4.2 K) sowie anhand selektiver Fe-Extraktion (Ammonium-Oxalat, Dithionit–Citrat–Bicarbonat).

Die Ergebnisse zeigten, dass Langzeitanbau von Reis und damit eine zunehmende Anzahl von Redoxzyklen die Mineralverwitterung sowie die redox-induzierte Umverteilung von Fe innerhalb des Profils im Vergleich zu Böden unter dauerhaft oxischen Verhältnissen (nicht-bewässerte Ackerböden) intensiviert. Nassreisanbau führte zur zunehmenden Entkopplung

von Transformationsprozessen und somit zur Ausbildung unterschiedlicher Milieus bezüglich der Transformation Fe-haltiger Minerale in Ober- und Unterboden. Mit andauernder Nutzung der Böden und somit einer steigenden Anzahl an Redoxzyklen ist eine zunehmende Ausprägung dieser unterschiedlichen Milieus zu beobachten (Tiefenprofilierung).

Oberböden waren in erster Linie durch die redox-induzierte Lösung von Eisenmineralen (Fe-haltige Tonminerale sowie schlecht-kristalline und kristalline Eisenoxide) während der reduzierenden Phase gekennzeichnet. Unter oxischen Bedingungen überwiegt hingegen die Ko-Präzipitation schwach kristalliner Fe-Oxide mit organischer Substanz, unterstützt durch die Anreicherung letzterer in den Tonfraktionen der Nassreisoberböden. Die organisch-mineralischen Interaktionen verhindern wiederum eine weitere Transformation und Kristallisation der vorhandenen Eisenoxide. Dies führt zur relativen Anreicherung von schlecht-kristallinen Fe-Oxiden, wie Ferrihydrit, reich an organischer Substanz, sowie von schwachkristallinem Goethit und Hämatit. Organische Substanz hat somit maßgeblich Einfluss auf Zusammensetzung und Kristallinität Fe-haltiger Mineralphasen in Nassreisböden. Im Gegensatz hierzu spielen im Unterboden der Nassreisstandorte organisch-mineralische Interaktionen nur eine untergeordnete Rolle bei der Transformation von Fe-Oxiden und Fe-haltigen Tonmineralen. Dies ist vermutlich in erster Linie auf einen reduzierten Transport von organischer Substanz aus dem Ober- in den Unterboden zurückzuführen. Die Transformationsprozesse im Unterboden werden hauptsächlich durch gelöstes Fe(II) aus dem Oberboden und/oder durch *in-situ* freigesetztes Fe(II) gesteuert. Durch Fe(II) katalysierte sekundäre Transformation resultiert in steigenden Gehalten an Fe-Oxiden und zunehmender Kristallinität der selbigen. Hier wurde insbesondere die Zunahme an makrokristallinem Goethit beobachtet. Eindeutige Veränderungen des Tonmineral-Bestands konnten entlang der Chronosequenz nicht beobachtet werden; die Standorte wiesen unabhängig vom Alter eine ähnliche Mineralzusammensetzung auf (u.a. Illit, Kaolinit, Chlorit, aufweitbare 2:1-Schichtsilikate).

Die *in-situ* Versuche bestätigten die in den Unterböden der Chronosequenz beobachtete Transformation schlecht-kristalliner Fe-Oxide in besser kristalline Fe-Oxide. Mit zunehmenden Nutzungsalter der Standorte konnte die Bildung kristalliner Fe-Oxide (Goethit, Hämatit) sowie Lepidokrokit bereits innerhalb eines Redoxzyklus beobachtet werden. Am jüngsten Standort, 100 Jahre Nassreisanbau, hingegen wurde die Transformation der Fe-Oxide vermutlich durch leicht alkaline und saline Bedingungen gehemmt. Die deutliche Zunahme magnetischer Wechselwirkungen im 4.2 K Mössbauer-Spektrum des Testminerals Nontronits nach nur 12-monatiger *in-situ* Exposition deutet auf redox-induzierte strukturelle Veränderungen hin. Solch strukturellen Veränderungen wurden bislang nur nach chemischer Reduktion von Nontronit im Labor beobachtet. Offensichtlich führt jedoch auch eine mikrobielle Reduktion unter natürlichen Bedingungen zu messbaren strukturellen

Veränderungen. Nach bestem Wissen ist dies eine der ersten Studien, die solche Veränderungen unter *in-situ* Bedingungen und nach nur einem Redoxzyklus aufzeigt.

Im zweiten Teil der vorliegenden Arbeit wurden die Redoxdynamik und damit einhergehenden Veränderungen der Zusammensetzung der Bodenlösung in Relation zur Nutzungsdauer und den damit einhergehenden Mineraltransformationen untersucht (*Kapitel 5*). Über einen Zeitraum von 12 Monaten wurden hierfür die Redoxwerte gemessen sowie Bodenlösungen gewonnen. An diesen erfolgte die Analyse der pH-Werte sowie des Stoffbestands (u.a. Nitrat/ Ammonium, Mn, Fe, Sulfat, DOC, DIC). Im Fokus standen die Fragen, (1) ob die Nutzungsdauer und die damit einhergehende Profildifferenzierung hinsichtlich Fe-Mineralogie und organischer Substanz zu signifikanten Änderungen der Intensität und Dauer von Redoxschwankungen führen, sowie (2) ob die Zusammensetzung der Bodenlösung die Redoxschwankungen als auch damit einhergehende Mineralverwitterungen über die Zeit widerspiegelt. Alle Nassreisstandorte zeigten über das Jahr ähnlich ausgeprägte Redoxzyklen (+570 bis -190 mV im Oberboden +650 bis -200 mV im Unterboden); in den nicht-bewässerten Vergleichsflächen verblieben die Redoxwerte hingegen stets im oxischen Bereich (>400 mV). Unmittelbar nach Flutung der Nassreisfelder zeigte sich zunächst eine hohe räumliche Variabilität der Redoxverhältnisse. Innerhalb weniger Wochen nach Flutung stabilisierten sich die Eh-Werte auf -200 mV unabhängig vom Nutzungsalter. Die Unterschiede zwischen den unterschiedlich alten Nassreisböden hinsichtlich der Redoxschwankungen im oberen Unterboden (35 cm) waren gering, trotz größerer Verfügbarkeit von Elektronendonatoren (z.B. organische Substanz) sowie leicht verfügbarer Elektronenakzeptoren (z.B. Nitrat, schlecht-kristallinen Eisenoxide) in den darüber liegenden Oberböden und Unterschieden in Konzentration und Kristallinität vorhandener Fe-Oxide. Lediglich im unteren Unterboden (55 bzw. 75 cm) kam es zu einem langsameren Abfall des Redoxpotentials mit zunehmender Nutzungsdauer der Nassreisböden. Dies ist vermutlich auf höhere Grundwasserstände an den jüngeren Standorten (P100 und P700) zurückzuführen. Die Dauer des Nassreisbaus und die damit einhergehenden Tiefendifferenzierung redox-sensitiver Elemente bzw. Verbindungen und der organischen Substanz führten somit nicht zu signifikanten Unterschieden der Redoxdynamik nach Flutung der Felder. Vielmehr scheint die Bewirtschaftung der Felder (z.B. Zeitpunkt und Dauer der Überflutung) und/oder die vorherrschenden Grundwasserhältnisse die Redoxdynamik zu steuern.

Die stoffliche Zusammensetzung der Bodenlösung folgte dem Redoxpotential und spiegelt unabhängig vom Alter der Standorte die sequentielle Abfolge von Redoxsystemen bis hin zur Sulfatreduktion wider. Die Abfolge der Redoxsysteme war jedoch nicht linear, sondern zeigte Überschneidungen, d.h. das gleichzeitige Auftreten verschiedener Reduktionsprozesse. Die Verteilungsmuster von Fe (und OM) im Tiefenprofil infolge des Nassreisbaus wurden zum Teil durch die Konzentrationen der entsprechenden gelösten Spezies bzw. Verbindung in der

Bodenlösung reflektiert. Selbst unter stark reduzierenden Bedingungen konnten im Unterboden jedoch nur geringe Gehalte an Fe ( $<40 \mu\text{mol l}^{-1}$ ) in der Bodenlösung nachgewiesen werden. Dies kann auf die geringe Verfügbarkeit von mikrobiell reduzierbaren Fe-Oxiden unter den gegebenen leicht alkalinen und salinen Bedingungen zurückgeführt werden. Von größerer Bedeutung ist jedoch vermutlich der geringe Gehalt an leicht reduzierbaren, schwach kristallinen Fe-Verbindungen, insbesondere in den älteren Nassreisböden. Auch die unmittelbare Bindung des aus dem Oberboden ausgewaschene Fe(II) an den Austauschkomplex des Bodens und/oder dessen direkte Beteiligung an der oben beschriebenen Fe(II)-katalysierten Mineraltransformation trägt möglicherweise zu den geringen Konzentrationen an gelöstem Fe im Unterboden bei. Offensichtlich sind die Unterböden der Nassreisstandorte vor allem Anreicherungszone für Fe aus den darüber liegenden reduzierten Oberböden und stellen somit keine Quellen von Fe zur Auswaschung in das Grundwasser dar.

Die Chronosequenz von Nassreisböden und nicht-bewässerten Vergleichsflächen bot die einmalige Gelegenheit, grundlegende biogeochemische Prozesse in Böden mit regelmäßig alternierenden Redoxbedingungen zu untersuchen. Es konnte gezeigt werden, dass die vorherrschende Eisendynamik sowie damit verbundene (Trans)formationsprozesse Fe-haltiger Minerale und die daraus resultierenden Tiefenprofile eine bedeutende Rolle für die Pedogenese von Nassreisböden und deren Biogeochemie spielen. Sie tragen somit wesentlich zur Abgrenzung der Nassreisböden von deren nicht-bewässerten Vergleichsböden bei.

# 1 General introduction

## 1.1 Rationale

Rice is the major staple food for half of the world's population (Greenland, 1997). Worldwide, more than 11% (159 million ha) of the 1381 million ha arable land is used for rice production (<http://faostat.fao.org>, 31.03.2015). Most of the rice fields are temporarily or permanently under waterlogged conditions (referred to as 'paddy fields' from *padi* = malay for rice, Kyuma, 2004). Paddy fields can be considered as the world's largest anthropogenic wetlands (Kögel-Knabner et al., 2010). The cycling of submergence and drainage of the fields during rice cultivation leads to temporal as well as spatial variations in redox conditions in paddy soils. Redox reactions regulate many of the biogeochemical processes in soils and influence mineral stability, metal release, and nutrient availability. They have profound influences on the development of soil properties throughout the soil column.

In anoxic soil environments, iron (Fe) minerals, e.g., (hydrated) Fe oxides, hydroxides and oxihydroxides (hereafter collectively named Fe oxides), and Fe-bearing clay minerals, are often the most important electron acceptors during microbial reduction and organic matter (OM) biodegradation (van Breemen, 1988; Favre et al., 2002; Stucki and Kostka, 2006; Komlos et al., 2007; Komlos et al., 2008; Stucki et al., 2007). Microbial Fe reduction during submergence of paddy soils has major effects on (trans)formation processes and distribution patterns of Fe minerals. Under anoxic soil conditions, even well-crystalline Fe(III) oxides are subjected to microbial induced reduction and subsequent dissolution (Bonneville et al., 2009). Vertical redistribution of Fe within the soil profile and distinct profile differentiation regarding Fe oxides and total Fe has frequently been observed under long-term paddy management and, thus, an increasing number of redox cycles (e.g., Zhang and Gong, 2003; Cheng et al., 2009; Chen et al., 2011; Kölbl et al., 2014). In paddy topsoils, oxalate-extractable Fe oxides dominate the Fe oxide assemblage (Wissing et al., 2013), whereas dithionite–citrate–bicarbonate (DCB)-extractable, and thus, more crystalline Fe oxides seem to accumulate in the subsoil (Gong, 1983; Zhang and Gong, 2003; Cheng et al., 2009).

Types and properties of Fe oxides occurring in soils with frequently changing redox conditions are still poorly understood. Upon rapid re-oxidation of Fe(II) released during anoxic periods, ferrihydrite is thought to be the common precipitate (Cornell and Schwertmann, 2003). In paddy soils, characterised by repeated redox cycles and increasing amounts of OM in paddy topsoils (Pan et al., 2003; Zhang and He, 2004; Kögel-Knabner et al., 2010; Wu, 2011; Wissing et al., 2011), Fe mineral transformation towards more crystalline phases such as goethite and haematite may be hampered (Schwertmann, 1966; Jones et al., 2009). Formation of dissolved organic Fe(III) complexes and disordered, organic-rich ferrihydrite upon re-oxidation of soluble Fe(II) is supported by dissolved organic matter

(DOM) in the soil solution (Ratering and Schnell, 2000; Rancourt et al., 2005). However, in short-term batch experiments, Thompson et al. (2006), however, observed increasing crystallinity of soil Fe oxides (haematite, goethite) with the number of redox oscillations. Wang et al. (1992) identified goethite as the dominant Fe oxide forming upon paddy cultivation in soils derived from haematite-red soil. Thus, information on (trans)formation processes of (Fe) minerals under frequently alternating redox conditions and on the nature of the involved phases is still partly contradictory.

Microbial reduction of Fe(III) in the crystal structures of clay minerals affects mineral surfaces and colloidal chemistry due to structural rearrangements (Kostka et al., 1999), and thus, has profound influence on the physicochemical properties of the clay minerals, i.e., cation exchange capacity, swelling properties, specific surface area, colour (Stucki, 2006). Favre et al. (2002) observed an increase in cation exchange capacity (CEC) and a loss of structural as well as free Fe upon reduction of the paddy soils. Laboratory studies demonstrated that the reversibility of the structural changes upon reoxidation depends on type (chemical vs. microbial) and extent of reduction as well as on the number of redox cycles the minerals are exposed to (summarized by Stucki, 2011). However, little is known on structural changes in Fe-bearing clay minerals under long-term alternating redox conditions.

In natural environments, Fe minerals are usually associated with OM, nutrients and/or contaminants, and thus, Fe mineral transformations and concomitant changing mineral properties may also affect the fate of associated compounds. Particularly organic carbon dynamics are closely linked to Fe soil mineralogy and *vice versa*. Hydrous Fe oxides and clay minerals are major sorbents of OM in soils (Kaiser and Guggenberger, 2000; Kalbitz et al., 2000; Mikutta et al., 2007). Co-precipitation upon ferrihydrite formation in the presence of DOM plays an important role in immobilizing DOM, especially in environments with changing pH or redox conditions (e.g., Riedel et al., 2013). These organic–mineral associations are important for OM stabilization in soils (Kaiser et al., 2002; Eusterhues et al., 2003; Eusterhues et al., 2005; Kalbitz et al., 2007; Kögel-Knabner et al., 2008) and contribute considerably to the long-term sequestration of organic carbon in paddy soils (Wissing et al., 2013). However, changes in contents and properties of Fe oxides upon paddy management appear to affect OM, presumably due to changing organic–mineral interactions (Wissing et al., 2013).

Fe(III)/Fe(II) is the most important redox couple in paddy soils (Ponnamperuma, 1972), Fe plays a critical role in buffering the soil redox potential (Yu, 2011). Organic matter acts as the main electron donor in microbial-induced reduction processes in soil, governing the overall intensity of redox reactions (Hutchinson and Hesterberg, 2004). The redox capacity (abundance and availability of electron donors and acceptors), among others, strongly governs the magnitude of reduction in a given soil (Achnich et al., 1995). Depth distribution of electron donors (i.e., organic substrates) and potential acceptors (e.g., Fe minerals) becomes

more pronounced with time of paddy cultivation (e.g., Gong, 1983; Cheng et al., 2009; Chen et al., 2011; Kölbl et al., 2014). This can directly affect the soils' redox status and, in consequence, the magnitude of redox changes and possibly mineral transformations. If and to what extent Fe mineral and OM distribution are mirrored by redox changes in paddy soils under long-term management is not fully understood.

Iron mineral phases and other redox-sensitive species, i.e., Mn, nitrate ( $\text{NO}_3^-$ ), and sulfate ( $\text{SO}_4^{2-}$ ), are stable under aerobic (oxidizing) conditions; upon the establishment of anoxic (reducing) conditions Fe and Mn minerals undergo reduction and become soluble (e.g., Ponnamperna, 1972; Reddy and Patrick, 1976; Kirk, 2004). Thus, reduction processes control the pH and the composition of the soil solution. In irrigated paddy fields, the composition of the soil solution may reflect the actual cropping season (Boivin et al., 2002). The rate of reductive dissolution of Fe phases depends on the solubility of the solid Fe phases (Bonneville et al., 2004) and availability and quality of OM (Ratering and Schnell, 2000; Tanji et al., 2003; van Asten et al., 2004; Gao et al., 2004). At the same time, release of OM into the soil solutions, contributes to reductive dissolution of Fe oxides (e.g., Fiedler et al., 2002; Sahrawat, 2003; Bishop et al., 2010). Dissolved Fe(II) and Mn(II) become often adsorbed in exchange for  $\text{Mg}^{2+}$  and  $\text{Ca}^{2+}$  (Brinkman, 1969/1970; Kyuma, 2004), possibly causing nutrient losses from the plough layer to deeper subsoil horizons and/or groundwater (Kato et al., 2004a). Thus, under anaerobic conditions, the (Fe) mineral assemblage of the soil partly controls the soil solution composition. Yet, the knowledge on the relationship between time of paddy cultivation, redox dynamics, concomitant (Fe) mineral transformations, and the composition of the soil solution is limited, especially for paddy subsoils.

## 1.2 Paddy soils

Cultivated rice is a semi-aquatic annual grass, which can be grown under a wide range of environmental (annual rainfall, solar radiation, temperature, altitude; Global Rice Science Partnership (GRiSP), 2013) and soil conditions (Kögel-Knabner et al., 2010). During cultivation, hydrological soil conditions might differ considerably, depending on the management system. Upland rice is grown under dryland conditions, whereas lowland rice (irrigated or rain-fed) is cultivated temporarily or permanently under waterlogged conditions. Today the majority of rice is cultivated under irrigation (93 million ha worldwide), providing 75% of the world's rice production (GRiSP, 2013). China is the world's largest rice producer (28% of the global rice production in 2013) (<http://faostat.fao.org>, 31.03.2015). The total paddy area in China amounted to 30.6 million ha in 2013 (19% of the global cultivation area) (<http://faostat.fao.org>, 31.03.2015) and essentially all rice fields are irrigated (GRiSP, 2013). Irrigated lowland rice may either be grown as a monoculture or in rotation with other non-irrigated crops, most commonly wheat. The rice is cultivated on banded fields with a standing

water table of approx. 5–10 cm above soil surface (GRiSP, 2013). Prior to seeding, fields are ploughed and puddled (mechanical homogenization of water-saturated soil; Sander and Gerke, 2007) to destroy the structure of the topsoil and develop a dense plough pan. Puddling may reduce the hydraulic conductivity in the plough pan; however, it does not prevent infiltration of irrigation water into the subsoil (Sander and Gerke, 2007). The topsoil is normally fully water-saturated; the subsoil may remain unsaturated with a certain proportion of air-filled pores (Gong, 1983; Favre et al., 2002). Depending on the extent of water saturation throughout the soil column one can differ between (1) endosaturation (entire soil column is saturated), (2) episaturation, where only the top soil layers are saturated and the underlying soil layers are unsaturated, and (3) anthric saturation (GRiSP, 2013). The latter is commonly found in irrigated paddy fields, where the saturation of the topsoil is controlled by flooding and puddling. Rice is planted either by direct seeding or transplanting of 1- to 6-week old seedlings, and is harvested after 115–120 days after crop establishment (GRiSP, 2013). Approximately 10–15 days before rice harvest paddy fields are drained. This periodic cycling of irrigation and drainage leads to spatial and temporal variations of redox conditions throughout the pedon, governing the development and biogeochemistry of the paddy soil. Anaerobic conditions establish during rice cultivation; aerobic conditions prevail after drainage and rice harvest (Kyuma, 2004). The most important aerobic/anaerobic interfaces are found at the soil surface layer in contact with the standing water still containing O<sub>2</sub>, and the plant rhizosphere, where O<sub>2</sub> is supplied by the rice plant's aerenchyma (Liesack et al., 2000). Also, the subsoil might be characterised by anaerobic or aerobic niches, depending on the overall water status. Up to date, knowledge on soil characteristics and redox conditions of paddy subsoils is far more limited.

As the result of specific paddy management practices and frequent redox changes soil horizons develop with characteristics often independent of the soils original character (Kirk, 2004). According to the IUSS Working Group WRB (2014), paddy soils can be classified as (Hydragric) Anthrosols, if anthraquic (or irrigic) and hydragric horizons have a combined thickness of >50 cm (Figure 1-1). The anthraquic horizon comprises the puddled layer and the underlying plough pan and shows evidence of reduction and oxidation (yellowish-brown to reddish-brown coatings or mottles along root holes and cracks). The puddled layer is characterised by loose packing of sorted small aggregates, whereas the plough pan has a platy structure, high bulk density (bulk density 20% higher than that of the puddled horizon) (IUSS Working Group WRB, 2014), and hence, low permeability, diminishing the amount of water percolating from the upper horizon into the subsoil (Chen and Liu, 2002). Characteristics of adjacent hydragric horizon (subsoil) are highly dependent on the water regime.

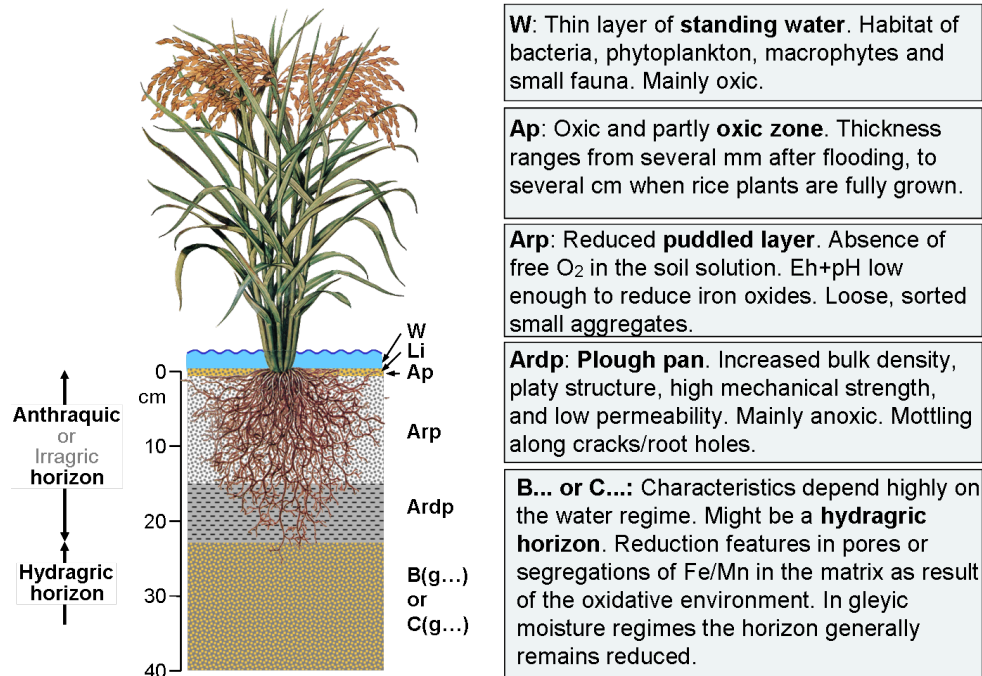


**Figure 1-1:** Schematic figure of an Anthraquic Anthrosol after Kögel-Knabner et al. (2010); horizon designation according to FAO (2006) and soil classification according to IUSS Working Group WRB (2014).

Paddy soils are not restricted to a specific soil type but can also be found among e.g., Gleysols, Planosols, Stagnosols, Fluvisols, or Cambisols. However, all together they are characterised by distinct redoximorphic features, such as zones of either depletion or accumulation of Fe and Mn (i.e., Mn/Fe concretions, reddish-brown to yellowish-brown Fe mottling on pore linings (ped faces, root channels) or parts of the soils matrix). Thus, important features of paddy profiles are Fe redistribution and subsequent Fe mineral (trans)formation.

### 1.3 Redox potential and processes

The key driver for development and biogeochemistry of paddy soils is the cycling of submergence and drainage of the fields during rice cultivation and concurrent frequent changes in soil redox conditions. A redox reaction can be considered as a pair of coupled half-reactions, which involve the transfer of electrons from one compound to another. Oxidation is defined as loss of electrons; reduction is the gaining of electrons. In soils, redox reactions are mainly microbial-driven processes, in which organic substrates or H<sub>2</sub> are oxidised (electron donator) to carbon dioxide (CO<sub>2</sub>) by microorganisms to obtain energy (microbial respiration). In well aerated terrestrial soils, oxygen serves as the prevalent electron acceptor. However,

waterlogging diminishes O<sub>2</sub> diffusion from the atmosphere into the soil, thus, limits O<sub>2</sub> availability. After submergence, oxygen is readily depleted by aerobic microbial respiration; microbes shift to facultative and obligate anaerobic respiration instead. The prevailing reduction processes proceed stepwise following a thermodynamic sequence, beginning with the reduction process generating most energy: NO<sub>3</sub><sup>-</sup>, Mn<sup>4+</sup>, Fe<sup>3+</sup>, SO<sub>4</sub><sup>2-</sup>, CO<sub>2</sub> and organic substrates (Ponnamperuma, 1972; Patrick and Reddy, 1978; Patrick and Jugsujinda, 1992). This is accompanied by a decrease in the redox potential. During the draining period, as typically found in paddy soils at the end of the cropping season, biochemical processes are usually reversed.

The intensity of soil reduction is characterised by the reduction–oxidation (redox) potential, thus, the electrochemical potential or electron availability within the soil system (Fiedler et al., 2007). The redox potential Eh is defined as the potential of a Pt electrode relative to a hydrogen electrode at zero potential. In soils and sediments, the measured redox potential is a composite of the electrochemical potentials of all redox couples present (Bohn, 1971; Stumm, 1984; Reddy and DeLaune, 2008). The redox capacity of a soil system, in contrast, is defined as the total amount of electrons accepted by the oxidants during microbial respiration (Patrick and DeLaune, 1972). Soil redox changes can be buffered by various redox-active compounds, of which Fe compounds seem especially important (Yu, 2011).

Most of the redox reactions that occur in natural environments involve hydrogen ions, H<sup>+</sup>, and are therefore pH dependant. The redox potential and the pH are inversely coupled: in accordance with the Nernst Equation an increase of the pH of one unit causes a decrease in redox potential by 59 mV. This is only true for redox reactions in pure solutions under standard state conditions; in natural systems the Eh-pH slope often deviates from the Nernst slope (Reddy and DeLaune, 2008). The shift in redox potential per unit pH depends on redox couples as well as on kinetics of the reaction, thus, may differ between different soil types (59–177 mV/pH; Bohn, 1971). Greater redox potential shifts per unit pH occur in soils dominated by the Fe(II)/Fe(III) redox couple (Reddy and DeLaune, 2008).

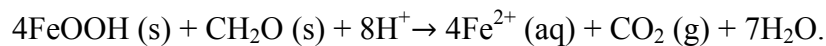
The redox potential in soils varies over time and spatially, which is mostly due to heterogeneity in temperature, water status, and availability of electron donors (reducible OM) and electron acceptors (e.g., reducible NO<sub>3</sub><sup>-</sup>, SO<sub>4</sub><sup>2-</sup>, Fe, Mn). In aerobic terrestrial soils, the redox potential ranges between 300 and 700 mV; in wetland soils redox potentials even vary between –300 and 700 mV (Reddy and DeLaune, 2008). Redox potentials above 300 mV (at pH 7) indicate oxic conditions, at Eh <300 mV reducing conditions prevail (Reddy and DeLaune, 2008).

In pure systems, the measured redox potential hints at the active redox couple and the ionic distribution of chemical species involved in the redox reaction. In soils, redox reactions are seldom at equilibrium, and various reduction processes may occur simultaneously at separate locations within a single horizon (Bohn, 1971), i.e., in so-called micro sites (Alewell et al.,

2006; Alewell et al., 2008). Changes in pH as well as in availability of electron acceptors and donors, including kinetic restrictions, may alter the thermodynamically predicted order of redox reactions. However, in anaerobic soils, the redox potential might be closely related to the dominating redox couple, such as Fe(II)/Fe(III) in paddy (Ponnamperuma, 1972) and most other soils and sediments (Reddy and DeLaune, 2008). Additional information on pH, ion composition of the soil solution, and soil mineralogy are needed for the identification of the active redox systems at given Eh values.

#### 1.4 Redox-induced iron mineral (trans)formations

Iron minerals are ubiquitous in soils and sediments and play fundamental roles in biogeochemical and physicochemical processes of soils and sediments. Under oxic conditions, Fe(III) oxides are essentially insoluble in the pH range for common soils (pH 4–9) and/or in the absence of complexing or reducing agents (Cornell and Schwertmann, 2003). Upon changing redox conditions, they are prone to (trans)formations. Iron (III) oxides might be subjected to microbial mediated reductive dissolution and release of Fe(II), as demonstrated by the following reaction (Bigham et al., 2002):



where CH<sub>2</sub>O represents organic substrate.

The reduction of Fe(III) oxides in non-sulfidogenic soils and sediments is largely catalysed by dissimilatory Fe reducing bacteria (Lovley, 1991), such as *Shewanella putrefaciens* (e.g., Kostka et al., 1996; O'Reilly et al., 2005) and *Geobacter metallireducens* (e.g., Lovley et al., 1993; Nevin and Lovley, 2000). Also, ferric iron in clay minerals serves as an electron acceptor for bacterial metabolism (e.g., Stucki, 1988; Wu et al., 1988; Kostka et al., 1999; Dong et al., 2003b; Li et al., 2004). Mechanisms of microbial reduction, including exocellular electron transfer, electron migration and electron redistribution within the mineral phase, are diverse and still not fully understood (for detailed information see, e.g., Nevin and Lovley, 2002 or Lovley et al., 2004).

Iron-reducing bacteria prefer using poorly crystalline Fe oxides as the primary terminal electron acceptor (Roden and Zachara, 1996; Roden et al., 2000; Zachara et al., 2002). This may lead to enrichment of more crystalline Fe oxides upon prolonged reducing conditions (Lovley and Phillips, 1986; Phillips et al., 1993). Even well-crystalline oxides can be prone to microbial-induced reductive dissolution (Roden and Zachara, 1996; Bonneville et al., 2004; Bonneville et al., 2009). The reactivity of Fe(III) oxides towards microbial-induced reductive dissolution increases with increasing surface area (Roden and Zachara, 1996), i.e., decreasing particle size and crystallinity. Bonneville et al. (2004; 2009) stated that Fe oxide solubility (ferrihydrite > lepidocrocite > goethite > haematite), rather than the specific surface area, might be a better predictor for the potential Fe reduction rate. Rate and extent of microbial

reduction of both Fe oxides and Fe-bearing clay minerals are strongly influenced by soil environmental conditions, such as Eh and pH, and the bacteria present (Stucki, 2006). Ferruginous smectites are redox-active over a wide Eh range; in the case of chemical reduction, the range is even much wider than theoretically predicted for the  $\text{Fe}^{3+}/\text{Fe}^{2+}$  redox couple (Gorski et al., 2012a; Gorski et al., 2012b; Gorski et al., 2013). Little is known about the Eh range of microbial reduction under field conditions.

Reductively released Fe(II) can induce a catalytic reaction, resulting in the recrystallisation of solid Fe(III) mineral phases and/or solid state transformations (Jeon et al., 2001; Jeon et al., 2003; Hansel et al., 2003; Williams and Scherer, 2004; Pedersen et al., 2005). It promotes structural transformation of poorly crystalline Fe oxides (e.g., ferrihydrite) to more crystalline and thermodynamically stable Fe oxide phases, such as haematite, goethite (Jones et al., 2009), and lepidocrocite (Pedersen et al., 2005). Under prolonged reducing conditions, ferrous Fe-induced mineral precipitation may hinder further microbial reduction, by limiting the accessibility of the Fe(III) mineral (Roden et al., 2000) or the bacterial surface (Urrutia et al., 1998). Also, the interactions with other soil compounds, i.e., OM, phosphorus and silicon, may considerably influence the reductive solubility (Cornell and Schwertmann, 2003) and transformation (Kukkadapu et al., 2004). Upon the reestablishment of oxic conditions, Fe(III) oxides will rapidly (re-)form upon oxidation of dissolved Fe(II) and subsequent hydrolysis of Fe(III). This spontaneous abiotic oxidation of Fe(II) is kinetically favoured at  $\text{pH} > 3$ , and will, thus, prevail over the slower process of microbial mediated oxidation and subsequent formation of extracellular Fe(III) precipitates (Cornell and Schwertmann, 2003). Microbial oxidation of Fe(II) by nitrate-dependent Fe oxidisers has been observed in anoxic soil environments and under sufficient nitrate supply (Weber et al., 2006), such as plough layers of paddy soil (Liesack et al., 2000). The nature of the Fe oxides formed upon oxidation depends on oxidation rate, pH, amounts of dissolved  $\text{O}_2$ , soluble counter ions (e.g., carbonate, sulfate, chloride, silicate), and OM present, as well as the biological activity (Bigham et al., 2002). Thermodynamic predictions, on the contrary, are only partly applicable to soils, as the chemical equilibrium is seldom reached and often hindered by slow kinetics (Cornell and Schwertmann, 2003). Poorly crystalline ferrihydrite is thought to be the primary oxidation product if oxidation is rapid, and in the presence of crystallization inhibitors (Childs, 1992; Cornell and Schwertmann, 2003), i.e., dissolved Si (Cornell and Schwertmann, 2003) or OM (Schwertmann, 1966). The presence of OM, for example, hampers ferrihydrite growth during precipitation, resulting in smaller crystal sizes and greater structural disorder (Schwertmann et al. 2005; Mikutta et al. 2008; Eusterhues et al. 2008; Mikutta 2011; Cismasu et al. 2011) of the coprecipitated ferrihydrite, thus, changing its surface properties (Chen et al., 2014) and reactivity (Mikutta et al., 2014; Shimizu et al., 2013; Eusterhues et al. 2014). Mineral bound OM influences reduction rates of ferrihydrite coprecipitated with OM as well of ferrihydrite with adsorbed OM and alters its secondary transformation pathways (Shimizu et al., 2013; Eusterhues et al. 2014; Chen et al., 2015).

Under stable oxic conditions, ferrihydrite slowly transforms to thermodynamically more stable Fe oxide forms, such as haematite and/or goethite, by Ostwald ripening (Cornell and Schwertmann, 2003). Slow oxidation and pH values <5, in contrary, favour direct goethite formation by polymerization of  $\text{Fe}(\text{OH})_x^{3-x}$  (Bigham et al., 2002). Partial oxidation and hydrolysis of Fe(II) may lead to formation of highly reactive, mixed-valent green-rust (Trolard and Bourrié, 2008), which can serve as a precursor for lepidocrocite, goethite, and maghemite upon further oxidation, depending on soil reaction and present ions.

In the case of clay minerals, i.e., smectite, microbial reduction of structural Fe(III) may result in dissolution and neof ormation of biogenic smectite (Dong et al., 2003a) and illite (Kim et al., 2004). Most often, reduction of octahedral Fe(III) in clay minerals results in structural changes, such as dehydroxilation (Lear and Stucki, 1985) and *cis* to *trans* migration of Fe within the octahedral sheet. The latter may result in defects in the crystal structure (Drits and Manceau, 2000) and, possibly, loss of structural Fe (Favre et al., 2002; Yang et al., 2012).

Thus, (trans)formation processes and interconversions of Fe mineral phases are diverse in soil environments with changing redox conditions. It can be assumed that most intensive redox-induced transformations occur in soils with frequently alternating water regime, and thus, periodically changing redox conditions, such as paddy soils.

## 1.5 Objectives and research questions

Knowledge on Fe mineral dynamics in soils is essential for understanding reduction reactions and biogeochemical processes. Paddy soils are prone to periodically changing redox conditions and, thus, can serve as a model system for studying Fe transformation processes upon reduction–oxidation alternations. The main objective of this study was to elucidate mineral transformations as evoked by long-term redox cycles. Also, I was interested in related redox dynamics and the resulting effects on the composition of soil solution in paddy soils.

In China, paddy rice cultivation has a 5000 year old tradition (Zong et al., 2007). In the Cixi region, Zhejiang province, dykes were built consecutively for reclamation of arable land during the last 2000 years. After land embankment and initial desalination, the land is used for either paddy rice cultivation or the cultivation of non-irrigated crops (i.e, wheat, maize, water melon, rape). Both, the construction of the dykes as well as the time of cultivation are well-documented (for further information see Cheng et al., 2009), thus, providing a soil chronosequence up to 2000 years of paddy and non-irrigated soils on comparable parent material (calcareous marine deposits). The chronosequence offers a unique opportunity to study processes of mineral (trans)formations under long-term paddy versus non-paddy cultivation.

Following **research questions** were addressed and are dealt with in detail in the named chapters:

- *Does long-term cultivation of rice intensify Fe mineral (trans)formation processes in comparison to sites under permanent oxic conditions (non-paddy sites)?* (Chapter 3 and 4)
- *Are there paddy-specific Fe mineral phases forming?* (Chapter 3 and 4)
- *How does the accumulation of OM in the paddy topsoils influence abundance and crystallinity of the Fe mineral phases present?* (Chapter 3 and 4)
- *Does long-term paddy management result in changes of the assemblage of the Fe-bearing clay minerals and of its properties?* (Chapter 3 and 4)
- *Does the time span of paddy cultivation, along with progressing depth differentiation of redox sensitive elements and OM, result in significant changes in redox response to flooding and drying?* (Chapter 5)
- *To what extent is the soil solution composition a mirror of the redox status and/or the mineral assemblage of the soil?* (Chapter 5)

Soil characteristics and mineral assemblage along the chronosequence mirror (trans)formations of Fe minerals caused by long-term paddy cultivation. Spatial variability of soil properties and the composition of the mineral assemblage in the clay fractions of selected paddy and non-paddy soils were studied (Chapter 3). In order to track short-term (trans)formation Fe(III) oxides differing in crystallinity (ferrihydrite, goethite) and a Fe(III)-bearing clay mineral (nontronite) were exposed *in-situ* to alternating redox conditions by placing them for one year in subsoil horizons along the soil chronosequence of the paddy soils (Chapter 4). To elucidate changes in redox potential and subsequent changes in the composition of the soil solution as related to time of paddy cultivation and concomitant mineral transformations a one-year field experiment (Chapter 5) at paddy and non-paddy soils under cultivation for 100, 700, and 2000 years was conducted.

With the synopsis of the results I hope to gain insight to biogeochemical processes fundamental to soils with alternating redox conditions, in particular to the Fe cycling and mineral transformations as well as their interlinking with organic matter.

## 2. Study area and characterization of soils

### 2.1 Study area

The study area is located on the southern coastal plain of the Bay of Hangzhou in the region of Cixi city (N30 11.328 E121 08.034) in the north-east of Zhejiang Province, China (Figure 2-1). The total area of the peninsula is 433 km<sup>2</sup> (in 1988), with the altitude ranging from 2.6 to 5.7 m above sea level (Zhang et al., 2004). The local climate is influenced by the subtropical monsoon; the mean annual temperature is 16.3 °C (min: -9.3 °C; max: 38.5 °C) and the mean annual precipitation amounts to 1325 mm (min: 676 mm; max: 1822 mm), with maximum rainfall occurring from April to October. The average ground water table was between 30 and 60 cm, depending on the season (Cheng et al., 2009).



**Figure 2-1:** Chronosequence of 100, 700 and 2000 year paddy (P100, P700, P2000) and 100 and 700 year non-paddy soils (NP100, NP700) located on the southern peninsula of Hangzhou Bay in the region of Cixi city (Zhejiang Province, PR China). A marshland soil (ML30) serves as reference point of initial soil formation.

Qiantang and Cao-e River are the main sources for water and sediments discharging into Hangzhou Bay (Xie, Wang and de Gao, 2009). However, the Yangtze (Changjiang) estuary is situated immediately north of the Hangzhou Bay. The Yangtze River, having an 1.92 million km<sup>2</sup> drainage area reaching from the Qinghai–Tibetan Plateau down to coast of Eastern China, is the main source of terrestrial material to the East China Sea. It has a mean

annual water volume of 925 km<sup>3</sup> and a mean annual sediment load of 4.8 10<sup>8</sup> tons discharging into the Eastern China Sea (Liu et al., 2012); most sediments derive from the upper Yangtze reaches (Wang et al., 2008). Under the influence of the Taiwan Strait warm current, these sediments are transported southwards into Hangzhou Bay. Several studies have shown that mainly coastal marine sediments, originally deriving from the Yangtze River hinterland, substantially supported the accretion of the southern tidal flat area of Hangzhou Bay (Su and Wang, 1989; Wright and Nittrouer, 1995).

In the Cixi area nine dykes were constructed for the reclamation of arable land during the past 2000 years, resulting in a chronosequence of soil formation under paddy as well as non-irrigated crop cultivation on coastal marine substrates. The age of the sites was reconstructed from historical records of the time of dyke construction and land usage (Cixi County Annals, compendious information available in Chinese at [www.cixi.gov.cn](http://www.cixi.gov.cn)), summarized by Cheng et al. (2009).

The coastal plain of Cixi is densely populated and characterised by rural and urban areas. Rice is traditionally cropped once a year during wet season (May–October) followed by wheat (or other non-irrigated crops (cotton, rape, vegetables, fruits) during dry season (own observations, 2008–2011). Irrigation of the paddy fields is carried out through a dense network of channels. In subtropical Asia a total seasonal water input of approx. 1300–1500 mm is needed to maintain standing water in the paddy fields (GRiSP, 2013).

## 2.2 Soil description

Three soils under paddy cultivation for 100, 700, and 2000 years (P100, P700, P2000), and two soils under non-paddy cultivation for 100 and 700 years (NP100, NP700) were used in the present study. It was not possible to locate soils, which had been used as non-paddy soils for more than 700 years. As point zero of soil formation, a non-cultivated soil of a marshland (ML30) behind the most recent dyke (built in 1977) was chosen. Soils were described according to FAO (2006) down to 1 m depth and classified according to IUSS Working Group WRB (2007) as Gleyic Fluvisol (ML30), Endogleyic Anthraquic Cambisol (P100), Endogleyic Anthraquic Anthrosol (P700, P2000), Endogleyic Cambisol (NP100) and Haplic Cambisol (NP700) (Kölbl et al., 2014). Basic soil characteristics can be found in Table 2-1 (paddy soils) and Table 2-2 (non-paddy soils).

**Table 2-1:** Basic properties of the fine fraction (<2 mm) of selected paddy sites along the chronosequences in Cixi, Zhejiang (PR China) (data from Wissing et al, 2011 and Kölbl et al., 2014, respectively).

Type	Years of cultivation	Site	Depth cm	Horizon	Texture class	Clay content %	pH (KCl)	EC <sub>1:2.5</sub> μS cm <sup>-1</sup>	BD g cm <sup>-3</sup>
Paddy	100	P100	0–9	Alp1	SiCL	27.9	5.1	379	1.0
			9–15	Alp2	SiCL	28.1	5.9	365	1.2
			15–21	Ardp	SiCL	28.1	6.9	320	1.5
			21–30	Bwg1	SiCL	32.9	7.5	341	1.6
			30–50	Bwg2	SiCL	33.3	7.1	327	1.5
			50–75	Bwlg1	SiCL	29.3	7.4	232	1.5
			75–100	Bwlg2	SiCL	28.6	7.5	218	1.3
Paddy	700	P700	0–10	Alp1	SiCL	28.6	6.8	557	1.0
			10–16	Alp2	SiCL	27.7	6.7	629	1.2
			16–22	Ardp	SiCL	28.4	6.6	479	1.5
			22–45	Bg	SiCL	27.5	6.7	342	1.5
			45–69	2Ahgb	SiCL	49.0	6.5	300	1.5
			69–106	2Blg1	SiCL	49.1	6.4	309	1.5
Paddy	2000	P2000	0–15	Alp	SiL	27.7	5.1	382	1.0
			15–20	Ar(d)p	SiL	23.8	5.5	222	1.2
			20–27	Bdg	SiCL	27.8	6.5	128	1.6
			27–35	2AhgB	SiCL	35.9	6.3	115	1.6
			35–50	2Bg1	SiCL	47.4	6.3	121	1.4
			50–70	2Bg2	SiCL	37.5	6.1	95	1.4
			70–100	2Blg	SiCL	32.4	6.1	77	1.5

EC<sub>1:2.5</sub> = electric conductivity (soil/water ratio 1:2.5), BD = bulk density

**Table 2-2:** Basic properties of the fine fraction (<2 mm) of the marshland site (point of zero soil formation) and selected non-paddy sites along the chronosequences in Cixi, Zhejiang (PR China) (data from Wissing et al., 2011 and Kölbl et al., 2014, respectively).

Type	Years of cultivation	Site	Depth cm	Horizon	Texture class	Clay content %	pH (KCl)	EC <sub>1:2.5</sub> μS cm <sup>-1</sup>	BD g cm <sup>-3</sup>
Marshland	30	M30	0–13	n.d.	SiL	13.7	7.8	214	n.a.
			13–30	n.d.	SiL	12.3	8.0	319	n.a.
Non-Paddy	100	NP100	0–14	Ap1	SiCL	27.2	7.5	304	1.3
			14–25	Ap2	SiL	26.1	7.4	272	1.4
			25–30	Bw	SiCL	29.1	7.3	287	1.5
			30–38	BCwg1	SiCL	31.9	7.5	365	1.6
			38–70	BCwg2	SiCL	32.8	7.4	409	1.5
			70–100	BCwlg	SiCL	31.1	7.5	424	1.5
Non-Paddy	700	NP700	0–12	Ap1	SiL	19.0	6.0	139	1.3
			12–17	Ap2	SiL	22.2	6.5	221	1.3
			17–23	Bw1	SiL	24.9	6.5	93	1.4
			23–45	Bw2	SiL	19.2	7.2	160	1.4
			45–70	Bw11	SiL	14.6	7.4	185	1.4
			70–100	Bw12	SiL	22.8	7.5	230	1.4

EC<sub>1:2.5</sub> = electric conductivity (soil/water ratio 1:2.5), BD = bulk density

n.a. not determined

Top soils of the paddy profiles were characterised by a puddled horizon, low in bulk density (BD) ( $\sim 1 \text{ g cm}^3$ ), and an underlying dense plough pan ( $1.4\text{--}1.6 \text{ g cm}^{-3}$ ). Both top- and subsoil horizons showed Fe/Mn concretions and redoximorphic colour patterns (i.e., reduced matrix colours and red Fe oxide coatings in root channels in the topsoil; bleached aggregate surfaces and Fe oxide concentrations in the interior of aggregates in the subsoil), both increasing with time of cultivation. Dark coloured horizons in the subsoil of P700 and P2000 (Munsell-Colour: 2.5 Y 3/1 and 2.5 Y 4/1, respectively) were classified as buried A horizons (Kölbl et al., 2014). Non-paddy soils were homogenous in structure and colour, however, due to ascending groundwater the younger site (NP100) was characterised by gleyic properties below 50 cm. Non-irrigated cultivation had led to the formation of two ploughed A horizons, with similar bulk density ( $1.3\text{--}1.4 \text{ g cm}^{-3}$ ). The similarity of the parent material was confirmed by comparable soil textures (silty to clayey loam) and total element contents, as well as similar mineral assemblages in the bulk soils (Kölbl et al., 2014). A radiocarbon analysis of the studied soils revealed a similar age composition (Bräuer et al., 2013). The allochthonous terrigenous origin of the parent material from the Yangtze hinterland was well reflected by the lipid composition of the study sites (Kölbl et al., 2014).

### 3. Long-term transformations of soil minerals under alternating redox conditions

#### 3.1 Introduction

Hydrous Fe oxides and Fe-bearing clay minerals play fundamental roles in biogeochemical and physicochemical processes of soils. The mobility and bioavailability of contaminants as well as of nutrients is closely linked to the biogeochemical cycle of Fe. The reactivity of Fe mineral phases depends on their crystallinity (i.e., crystal size and bonding environment), surface area and coverage (Roden and Zachara, 1996), solubility (Bonneville, et al., 2004), thus, on the type of Fe mineral present. Iron mineral phases are prone to transformations under changing redox conditions. Most intensive redox-induced transformations of Fe mineral phases occur in soils with frequently alternating water regime, such as those cropped with submerged rice, i.e., paddy soils. Long-term paddy management, i.e., increasing numbers of redox cycles, cause vertical redistribution of Fe and distinct depth differentiation regarding Fe oxides and total Fe (e.g., Zhang and Gong, 2003; Cheng et al., 2009; Chen et al., 2011; Kölbl et al., 2014). Poorly crystalline Fe oxides (determined as oxalate-extractable Fe) dominate the Fe oxide assemblage of paddy topsoils (Wissing et al., 2013), whereas crystalline Fe oxides (DCB-extractable Fe) tend to accumulate in the subsoil (Gong, 1983; Zhang et al., 2003; Cheng et al., 2009). Oxalate and DCB extractions are not selective for specific Fe oxide phases, hence, the information on the identity of the Fe mineral phases participating in redistribution and (trans)formation processes under frequently alternating redox conditions is limited.

Even well-crystalline Fe(III) oxides are subjected to microbial induced reduction and subsequent dissolution under anoxic soil conditions (Bonneville et al., 2009); abiotic reduction of Fe oxides may occur via surface processes (Stumm and Sulzberger, 1992; Tanwar et al., 2009; Catalano et al., 2010). The Fe(II) released oxidizes upon reestablishment of oxic conditions, with the formed Fe(III) precipitating into hydrous oxides. This may happen *in-situ* or after lateral and vertical translocation of the mobile Fe(II), which is typical for paddy soils (Gong, 1983). Depending on geochemical factors, such as Eh, pH, O<sub>2</sub>, and Fe<sup>2+</sup> concentration and supply rate, the presence of other ions (e.g., Al and Si) and OM, the water and temperature regime, different Fe mineral phases are formed during redox reactions (Cornell and Schwertmann, 2003). Poorly crystalline ferrihydrite is assumed to be the primary oxidation product upon rapid reoxidation, then slowly transforming to thermodynamically more stable Fe oxides, such as haematite and/or goethite, by Ostwald ripening under stable oxic conditions (Cornell and Schwertmann, 2003). In soil environments with repeated cycling of redox conditions the crystallisation process might be interrupted, resulting in the accumulation of poorly crystalline Fe oxide phases. However, van der Zee et al. (2003)

showed that nanocrystalline goethite instead of ferrihydrite was the predominant Fe oxide phase formed at oxic–anoxic interfaces in lacustrine and marine sediments. Thompson et al. (2006) observed in short-term batch experiments that the crystallinity of soil Fe oxides (haematite, goethite) increases with the number of redox oscillations. It is not clear how these partly contradictory results can be transferred to soils under long-term paddy management.

A typical feature of paddy soils is the accumulation of OM in the topsoils (Pan et al., 2003; Zhang and He, 2004; Kögel-Knabner et al., 2010; Wu, 2011; Wissing et al., 2011). Organic matter acts as the main electron donor in microbial induced reduction processes in soil. The abundance of electron donors, i.e., easily degradable OM, may enhance structural changes in clay minerals and transformations of hydrous Fe oxides. The presence of dissolved OM (DOM) supports the formation of aqueous organic Fe(III) complexes and of disordered, organic-rich ferrihydrite (Ratering and Schnell, 2000; Rancourt et al., 2005). Dissolved OM, as other solutes (i.e., Si, Al), retards Fe mineral transformation into more crystalline phases (Schwertmann, 1966; Jones et al., 2009). Zhang and Lin (2008) suspected that increasing contents of OM might be responsible for the lower crystallinity of Fe oxides in paddy topsoils upon long-term cultivation.

Also Fe-bearing clay minerals play an important role in the Fe cycle of waterlogged soils. Microbes are capable of reducing Fe(III) in the crystal structures of clay minerals (Wu et al., 1988; Kostka et al., 1996; Dong et al., 2003b; Li et al., 2004), which affects mineral surfaces and colloidal chemistry (Kostka et al., 1999b). Laboratory studies showed that reduction of structural Fe(III) promotes dissolution of clay minerals in presence of organic ligands (Kostka et al., 1999a; Dong et al., 2003a) and neof ormation of minerals, such as smectite and vivianite, as well as of fine-grained silica (Dong et al., 2003a) and illite (Kim et al., 2004). In one of the few field studies, Favre et al. (2002) investigated changes in CEC and structural Fe in a paddy soils (Vertisol) cropped with rice twice a year. They observed an increase of CEC and a loss of structural as well as free Fe upon reduction in the paddy fields as compared to adjacent fields which were not flooded. The results were explained by intensified weathering upon irrigation and subsequent leaching of mineral constituents. To date, no study on changes in the Fe-bearing clay minerals and structural Fe levels upon long-term rice cultivation (>100 years) has been carried out.

The objective of the study was to elucidate (trans)formation processes of Fe-bearing minerals, as related to alternating redox conditions and, hence, to time of rice cultivation and to identify the Fe mineral phases participating.

Following research questions were addressed:

- Does long-term cultivation of rice, i.e., the number of redox cycles, intensify Fe mineral weathering in comparison to sites under permanent oxic conditions (non-paddy sites)?
- How does the accumulation of OM in the paddy topsoils influence abundance and crystallinity of the Fe mineral phases present?
- Are there paddy-specific Fe mineral phases forming in the illuvial subsoil horizons?
- Do structural Fe contents decrease with increasing time of rice cultivation and can changes in the Fe-bearing clay mineral assemblage be observed?

Clay fractions of selected soils along a chronosequence of soils developed from marine sediments and either under paddy or non-paddy management were analysed for physicochemical properties (i.e., exchangeable cations, cation exchange capacity, carbon and total element contents) and mineral assemblage. Identification of the Fe-bearing clay minerals was carried out by X-ray diffraction (XRD);  $^{57}\text{Fe}$  Mössbauer spectroscopy at 298 K and 4.2 K was applied for identification of Fe oxides and quantitative speciation of solid Fe mineral phases, complemented by selective chemical extractions (oxalate, dithionite–citrate–bicarbonate). Mössbauer spectroscopy also provided information on the oxidation state of mineral Fe as well as on the crystallinity (i.e., crystal size and order, substitution by other elements, organic–mineral interactions) of identified Fe mineral phases.

## 3.2 Material and Methods

### 3.2.1 Soil sampling and pre-treatment

Selected soils from the chronosequence, P100, P700, and P2000, and two non-irrigated counterparts, NP100 and NP700, were sampled in June 2008 shortly before the beginning of the rice cropping season. Additionally, a non-cultivated soil of a marshland behind the most recent dike (built in 1977) was sampled as point zero of soil formation.

Paddy and non-paddy soils were sampled by horizon down to depth of approx. 100 cm, except for the marshland site, which was sampled down to 30 cm. Bulk soil samples were air-dried and passed through a 2-mm sieve. The clay fraction ( $<2\ \mu\text{m}$ ) was obtained by sedimentation according to Stoke's law, without prior destruction of the carbonates and OM, in order to prevent alteration of minerals by chemical pre-treatments (Mikutta et al., 2005). Before sedimentation, the samples were dispersed by sonication (60 and 240 J ml<sup>-1</sup>, respectively), followed by wet-sieving to separate the fraction  $<63\ \mu\text{m}$  from the coarser fractions. All fractions were freeze-dried, weighed, and stored cool and dry prior to analyses.

### 3.2.2 Basic characteristics of the clay fractions

Total carbon of the clay fraction was determined by dry combustion at 900°C with a CNS analyser (VarioMax, Elementar GmbH, Hanau, Germany). Total inorganic carbon (IC) was measured by dissolution of carbonates with 42% phosphoric acid and subsequent infrared detection of the evolving CO<sub>2</sub> (C-MAT 550, Ströhlein GmbH, Viersen, Germany); organic carbon (OC) was calculated by subtracting inorganic carbon from the total carbon content. Both analyses were performed in duplicate.

The cation exchange capacity at pH 7 (CEC<sub>pH7</sub>) and exchangeable cations (Ca<sup>2+</sup>, Na<sup>+</sup>, K<sup>+</sup>, Mg<sup>2+</sup>) were determined according to Lavkulich (1981). Exchangeable cations were measured with ICP-OES (Inductively Coupled Plasma-Optical Emission Spectroscopy, Ultima 2, Horiba Jobin-Yvon S.A.S., Longjumeau, France) in the supernatant after saturation with 1 M NH<sub>4</sub> acetate buffered at pH 7; the CEC<sub>pH7</sub> was measured as NH<sub>4</sub><sup>+</sup> (San++ CFA, Skalar, Netherlands) in the supernatant after reexchange with 1 M KCl. Analyses were carried out in duplicate.

Total element contents of Al, Ca, Cl, Fe, K, Mg, Mn, Na, P, S, Si, Ti in the clay fractions were determined by X-ray fluorescence analysis (SRS 3000, Siemens AG, Karlsruhe, Germany), using 5-g powder pellets.

### 3.2.3 Selective chemical extractions

Iron from poorly crystalline oxides and bound to OM was extracted using ammonium–oxalate (Fe<sub>o</sub>; Schwertmann, 1964). Iron in poorly crystalline and well-crystalline oxides was analysed using dithionite–citrate–bicarbonate (Fe<sub>d</sub>; Mehra and Jackson, 1960; Blakemore et al., 1987). Iron in the extracts was determined by ICP-OES (Ultima 2). Silicate-bound iron (Fe<sub>si</sub>) was calculated by subtracting Fe<sub>d</sub> from the total Fe content determined by XRF (Fe<sub>t</sub>). Analyses were done in duplicate.

### 3.2.4 X-ray diffraction

For characterisation of the clay mineral assemblage, samples were analysed as oriented texture specimens (D5005, Siemens AG, Karlsruhe, Germany, with Bragg-Brentano-Geometry) after following treatments: (a) Ca<sup>2+</sup> saturation, (b) ethylene glycol (EG) solvation, (c) K<sup>+</sup> saturation and (d) heating K<sup>+</sup>-saturated specimens to 550 °C for 1 h. Analyses were carried out using Ni-filtered CuK $\alpha$  radiation ( $\lambda = 0.154$  nm), generated at 40 kV and 30 mA. Samples were scanned from 4 to 30 °2 $\theta$  (EG-, K<sup>+</sup>-treated samples) and 4 to 80 °2 $\theta$  (Ca<sup>2+</sup>-treated samples), respectively, with a step size of 0.02 °2 $\theta$  and dwell time per step of 6 s. The slit was fixed at 0.2 °2 $\theta$ . Identification of clay minerals was done using X'Pert HighScore Plus (PANalytical, Almelo, The Netherlands). For correcting the °2 $\theta$  position of each peak fitted, quartz, naturally present in all samples, was used as internal standard.

### 3.2.5 Mössbauer spectroscopy

Transmission  $^{57}\text{Fe}$  Mössbauer spectra of the clay fractions were recorded at room temperature (RT: 298 K) and at liquid helium temperature (LHe: 4.2 K) with a standard electromechanical spectrometer (Wissenschaftliche Elektronik GmbH, Seehausen, Germany), using a sinusoidal velocity waveform and a  $^{57}\text{Co}$  source in Rh matrix. For measurements at 4.2 K, a liquid He bath cryostat was used to cool both source and absorber. This practically eliminates contributions from the second order Doppler shift on the isomer shift. Thus, isomer shifts,  $\delta$ , are given with respect to the  $^{57}\text{Co}$ –Rh source. To refer to  $\alpha$ -Fe foil at ambient temperature,  $0.11 \text{ mm s}^{-1}$  must be added to  $\delta$  for the measurements at RT, and  $0.24 \text{ mm s}^{-1}$  for the measurements at LHe. All measurements were performed in a velocity range of  $\pm 10.6 \text{ mm s}^{-1}$ . Samples were mounted with approx.  $150 \text{ mg cm}^{-2}$ . The detection limit ranges between 1 to 3%  $\text{Fe}_t$ .

#### *Fitting procedure*

After folding of the raw data, which also eliminates the geometry effect, the spectra were least-square fitted. Electric quadrupole interactions were fitted with doublet patterns with single Lorentzian line shapes. The magnetically split spectral components (sextets) were fitted with single Lorentzian lines or with static Gaussian distributions of hyperfine fields, respectively. Lorentzian line widths at half maximum were assumed to be  $0.25 \text{ mm s}^{-1}$  for single Lorentzian lines as well as Gaussian distributions. The line intensity was constrained to be equal for doublets; in the case of sextets it was fixed in the ratio of 3:2:1:1:2:3. Spectra were not corrected for thickness effects (Rancourt et al., 1993). Detailed information on the fitting procedure for each spectral component is given in Chapter 3.3.4.

## 3.3 Results

### 3.3.1 Basic characteristics of the clay fractions

No inorganic carbon was detected in the clay fractions. Organic carbon concentrations in the clay fractions of the topsoil (puddled horizon and plough pan) of the paddy sites varied between 16.6 (P100, Ardp) and  $55.2 \text{ g kg}_{\text{clay}}^{-1}$  (P2000, Alp). Concentrations of OC in topsoils and underlying B horizons (P100, Bwg1: 9.3; P700, Bg: 12.0; P2000, Bdg:  $15.1 \text{ g kg}_{\text{clay}}^{-1}$ ) increased with duration of paddy cultivation. Trends for the non-paddy sites were similar, though less distinct; OC concentrations ( $29.7 \text{ g kg}_{\text{clay}}^{-1}$ ) were largest in the Ap1 horizon of NP700. Contents of OC gradually decreased with depth in all soils, with differences between top and subsoil being more pronounced for paddy than for non-paddy profiles (Figure 3-1).

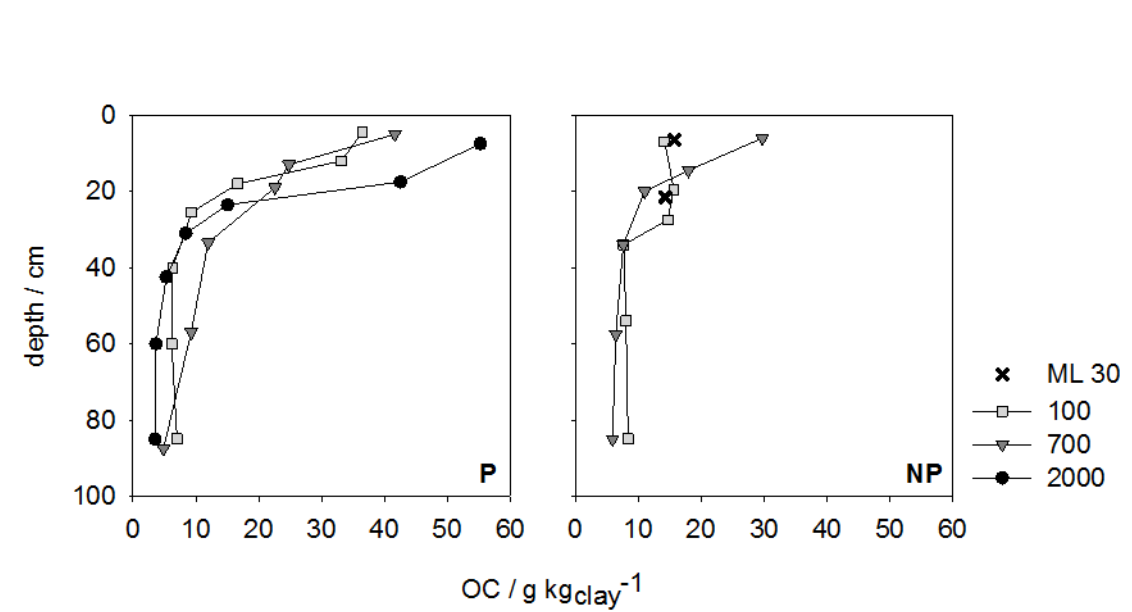


**Figure 3-1:** Depth profile of the organic carbon (OC) concentrations in the clay fractions of paddy (P) and non-paddy sites (NP). The marshland site (ML30) is given as point zero of soil evolution.

The  $CEC_{pH7}$  ranged between 396 and 608  $mmol_c kg_{clay}^{-1}$  for paddy sites (Table 3-1). Similar values were observed for the non-paddy sites (453 to 654  $mmol_c kg_{clay}^{-1}$ ); the clay fractions of the NP700 topsoil had the highest  $CEC_{pH7}$  (see Appendix). The  $CEC_{pH7}$  was generally higher in topsoils, due to higher OM contents:  $CEC_{pH7}$  and OC contents were significantly correlated for each paddy profile ( $r^2 = 0.857, 0.781, \text{ and } 0.645$  for P100, P700, and P2000, respectively) and non-paddy profile ( $r^2 = 0.780$  and  $0.934$  for NP100 and NP7000, respectively).

The dominant exchangeable cation in all soils was  $Ca^{2+}$  (95 to 373  $mmol_c kg_{clay}^{-1}$ ), followed by  $Mg^{2+}$  (21 to 165  $mmol_c kg_{clay}^{-1}$ ). Exchangeable  $Na^+$  and  $K^+$  were only present in small amounts ( $<11 mmol_c kg_{clay}^{-1}$ ); exchangeable K contents decreased with time of cultivation. The base saturation (BS, defined as the fraction of all exchangeable cations of the CEC at pH 7) was generally high (64 to 100%) at the paddy sites, only the uppermost horizon of P2000, Alp, had a significantly lower BS (24%). The BS decreased with prolonged paddy cultivation. The BS of the non-paddy soils tended to be slightly higher (72 to 100%) than of the paddy soils.

**Table 3-1:** Cation exchange capacity ( $CEC_{pH7}$ ), exchangeable base cations and base saturation (BS) of paddy (P) clay fractions.

Site	Depth cm	Horizon	$CEC_{pH7}$	$Ca^{2+}$	$Mg^{2+}$	$Na^+$	$K^+$	BS %
P100	0–9	Alp1	516.9	242.7	103.1	6.2	7.0	69
	9–15	Alp2	508.5	228.9	94.1	1.8	5.8	65
	15–21	Ardp	480.4	275.0	106.0	4.4	8.4	82
	21–30	Bwgl	402.5	268.1	70.9	1.1	8.0	86
	30–50	Bwgl2	396.3	293.5	91.9	2.7	8.2	100
	50–75	Bwgl1	399.5	290.5	97.9	1.6	9.5	100
	75–100	Bwgl2	401.3	288.4	99.6	2.6	10.7	100
P700	0–10	Alp1	608.3	373.2	113.9	8.1	7.3	83
	10–16	Alp2	487.1	352.7	103.8	3.7	8.5	96
	16–22	Ardp	534.4	277.0	123.8	5.0	7.8	77
	22–45	Bg	522.1	251.8	164.6	9.0	9.6	83
	45–69	2Ahgb	445.4	176.7	163.8	10.7	7.6	81
	69–106	2Blg1	408.0	132.6	163.2	4.3	9.0	76
P2000	0–15	Alp	501.0	95.2	21.3	0.8	1.9	24
	15–20	Ar(d)p	501.4	248.0	64.9	2.0	3.5	64
	20–27	Bdg	487.2	256.4	85.2	3.7	4.4	72
	27–35	2AhgB	444.9	238.7	101.0	2.1	5.7	78
	35–50	2Bg1	402.6	187.4	99.6	0.4	5.9	73
	50–70	2Bg2	449.4	211.8	124.3	2.0	7.1	77
	70–100	2Blg	442.0	205.7	115.6	1.1	7.2	75

Little changes in total contents of Al, Si, Ti as well as of Mg, K, and Na (see Appendix) were observed for paddy and non-paddy soils, neither with depth nor age. Highest concentrations of  $Ca_t$  were found in the subsoil of P100 and in NP100 and NP700 in those horizons still containing  $CaCO_3$  in the bulk soil, though no carbonate was detected in the clay fractions. Total S and P contents were generally higher in top- than subsoils (see Appendix) and correlated to the OM content. Differences in the vertical distribution were only found for total Mn and Fe in the paddy soils.

**Table 3-2:** Total Fe ( $Fe_t$ ), dithionite–citrate–bicarbonate ( $Fe_d$ ) and ammonium–oxalate–extractable Fe ( $Fe_o$ ) in the clay fractions of paddy (P) and non-paddy (NP) soils. Fe contents of the marshland soil (ML30) are given as reference for point zero of soil formation.

Site	Depth cm	$Fe_t$ -----	$Fe_d$ g kg <sub>clay</sub> <sup>-1</sup>	$Fe_o$ -----	$Fe_d/Fe_t$	$Fe_o/Fe_d$
M30	0–13	63.2	17.1	1.5	0.3	0.1
	13–30	67.2	17.9	1.6	0.3	0.1
P100	0–9	68.7	13.2	10.1	0.2	0.8
	9–15	76.9	20.4	6.3	0.3	0.3
	15–21	75.7	13.2	2.9	0.2	0.2
	21–30	84.3	12.1	2.0	0.1	0.2
	30–50	77.4	28.8	2.9	0.4	0.1
	50–75	89.4	29.9	4.2	0.3	0.1
	75–100	76.2	31.0	4.8	0.4	0.2
P700	0–10	70.4	14.1	11.6	0.2	0.8
	10–16	77.4	14.8	6.9	0.2	0.5
	16–22	73.2	16.4	7.4	0.2	0.5
	22–45	74.4	25.6	3.8	0.3	0.1
	45–69	70.2	26.9	1.3	0.4	<0.1
	69–106	107.9	48.9	1.4	0.5	<0.1
P2000	0–15	51.1	7.6	8.6	0.1	1.1
	15–20	59.3	10.5	10.1	0.2	1.0
	20–27	89.0	43.1	3.7	0.5	0.1
	27–35	68.5	27.1	0.8	0.4	<0.1
	35–50	101.3	59.3	0.8	0.6	<0.1
	50–70	87.9	37.0	1.5	0.4	<0.1
	70–100	86.3	42.8	3.5	0.5	0.1
NP100	0–14	74.3	15.3	4.6	0.2	0.3
	14–25	72.0	15.4	7.4	0.2	0.5
	25–30	77.3	16.4	5.4	0.2	0.3
	30–38	79.9	28.9	4.1	0.4	0.1
	38–70	75.3	29.0	6.3	0.4	0.2
	70–100	76.7	28.9	6.5	0.4	0.2
NP700	0–12	73.4	13.6	6.0	0.2	0.4
	12–17	74.8	13.0	6.7	0.2	0.5
	17–23	81.9	12.3	5.3	0.2	0.4
	23–45	80.7	27.2	3.5	0.3	0.1
	45–70	82.2	30.3	3.5	0.4	0.1
	70–100	81.6	27.8	5.9	0.3	0.2

### 3.3.2 Selective wet chemical extractions

Total Fe oxide contents ( $Fe_d$ ) were generally little, ranging from 7.6 (P2000, Alp) to 59.3 g  $kg_{clay}^{-1}$  (P2000, 2Bg1) (Table 3-2). Most Fe is bound within silicates:  $Fe_d/Fe_t$  ratios varied between 0.1 and 0.6. Surface horizons of the paddy soils showed loss of total Fe under prolonged paddy cultivation. The loss can mainly be explained by depletion in well-crystalline Fe oxides ( $Fe_c = Fe_d - Fe_o$ ) in favour of poorly crystalline Fe oxides ( $Fe_o$ ), which is emphasized by increasing  $Fe_o/Fe_d$  ratios. In the topsoil of the P2000,  $Fe_o$  amounts to  $Fe_d$  (Alp: 7.6 vs. 8.6, Ardp: 10.5 vs. 10.1 g  $kg_{clay}^{-1}$ ), indicating that absence of crystalline hydrous Fe oxides. The opposite was observed for the subsoils of the paddy sites: with increasing number of redox cycles, the well-crystalline Fe oxide fraction ( $Fe_c$ ) increased, from 10.1 (P100, Bwg1) to 58.3 g  $kg_{clay}^{-1}$  (P2000, 2Bg1). Decreases of silicate Fe ( $Fe_{si} = Fe_t - Fe_d$ ) were slightly higher in the top- than the subsoil. No such trends were found under the permanently oxic conditions of non-paddy soils.

### 3.3.3 Clay mineral assemblage

Clay fractions of paddy and non-paddy soils were characterised by largely similar clay mineral assemblages. Figure 3-2 exemplarily depicts the sequences of X-ray diffraction patterns after saturation with either  $Ca^{2+}$  or  $K^+$ , ethylene glycol solvation, and heat treatment (550 °C) for paddy topsoils (for all spectra please see the Appendix).

Quartz is the dominant mineral in all clay fractions, as indicated by well-defined peaks at 4.25 and 3.34 Å. Illite was identified based on its characteristic (001) peaks at 10.0, 5.0 and 3.3 Å (the latter overlapping with quartz) before and after all chemical and heat treatments. All diffractograms had reflections at 7.1 Å and 5.57 Å, becoming weaker after heating the samples to 550 °C. This is indicative for kaolinite. A small 7.0 Å peak remained even after heating, which was attributed to (primary) chlorite (Moore and Reynolds, 1997). This was supported by peaks at 14.3 Å and 5.53 Å after all treatments. X-ray diffraction patterns of glycolated  $Ca^{2+}$  samples indicated the presence of expandable 2:1 silicates (i.e., smectite; broad peaks at 16.0–18.0 Å). The 14.1–14.3 Å peaks persisted even after glycolation, which points at chlorite and/or vermiculite. In the  $K^+$ -saturated sample heated to 550 °C, a 12.2 Å peak occurred in most samples, suggesting the presence of mixed-interlayer clay minerals. A species-level distinction of smectite and mixed-interlayer clay minerals was not aimed at.

Comparing the primary basal (001) peak reflections of the different clay minerals in the upper solum of the paddy sites, it can be assumed that illite, followed by kaolinite, was the dominant clay mineral. Only the P2000 site was characterised by larger proportions of kaolinite than of illite.

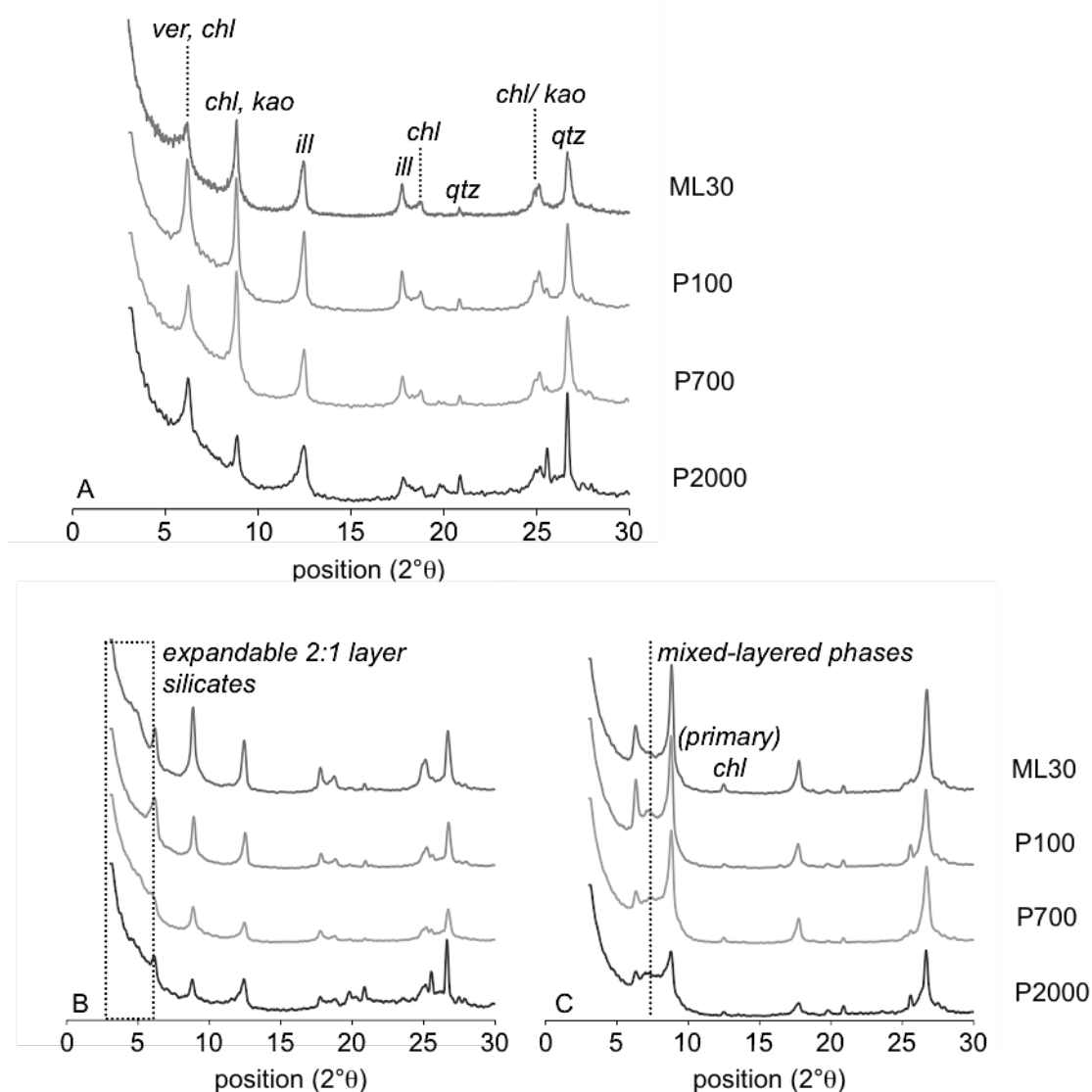


**Figure 3-2:** X-ray diffraction patterns (oriented texture specimens, Cu K $\alpha$  radiation) of the clay fractions in the Alp horizons of the 100, 700 and 2000 year paddy site (P100, P700, P2000) and the upper horizon (0–13 cm) of the marshland (ML30), corrected to the quartz peak at 3.34 Å or 26.7 °2 $\theta$ . Identification of clay minerals was done by means of following treatments: (A) Ca<sup>2+</sup> saturation, (B) ethylene glycol solvation, K<sup>+</sup> saturation (not shown) and (C) K<sup>+</sup> saturated specimens heated to 550 °C; chl = chlorite, ill = illite, kao = kaolinite, qtz = quartz, ver = vermiculite.

Iron oxides could only be identified in few spectra (Figure 3-3). Diffraction lines at 2.69, 2.51, and 1.69 Å were allocated to well-crystalline haematite. Goethite was identified based on diffraction lines at 4.21, 2.69, and 2.44 Å. Lepidocrocite was only identified in the 2Blg1 horizon of P700 (at 69–106 cm depth) and the 2Bg2 and 2Blg horizons of P2000 (at 50–70 and 70–100 cm depth, respectively) based on its characteristic 020 diffraction line at 14.15 °2θ or 0.63 nm (Cornell and Schwertmann, 2003).

**Table 3-3:** Identification of Fe oxides in the clay fractions of the paddy sites (P) based on their characteristic X-ray diffraction peaks.

Site	Depth cm	Horizon	Gt	Hm ----- present -----	Lp
M30	0–13	–	✓	✓	
	13–30	–	✓	✓	
P100	0–9	Alp1		✓	
	9–15	Alp2		✓	
	15–21	Ardp			
	21–30	Bwg1	(✓)		
	30–50	Bwg2	✓	✓	
	50–75	Bwlg1	✓	✓	
	75–100	Bwlg2	✓	✓	
P700	0–10	Alp1	✓	✓	
	10–16	Alp2	✓	✓	
	16–22	Ardp	✓		
	22–45	Bg	✓		
	45–69	2Ahgb	✓	(✓)	(✓)
	69–106	2Blg1	✓	✓	✓
P2000	0–15	Alp	(✓)	(✓)	
	15–20	Ar(d)p		(✓)	
	20–27	Bdg	✓	(✓)	
	27–35	2AhgB	✓	(✓)	
	35–50	2Bg1	✓	(✓)	
	50–70	2Bg2	(✓)	✓	✓
	70–100	2Blg	(✓)	✓	✓

Hm = haematite, Gt = goethite, Lp = lepidocrocite

✓ = present, (✓) = present in traces

– = not determined

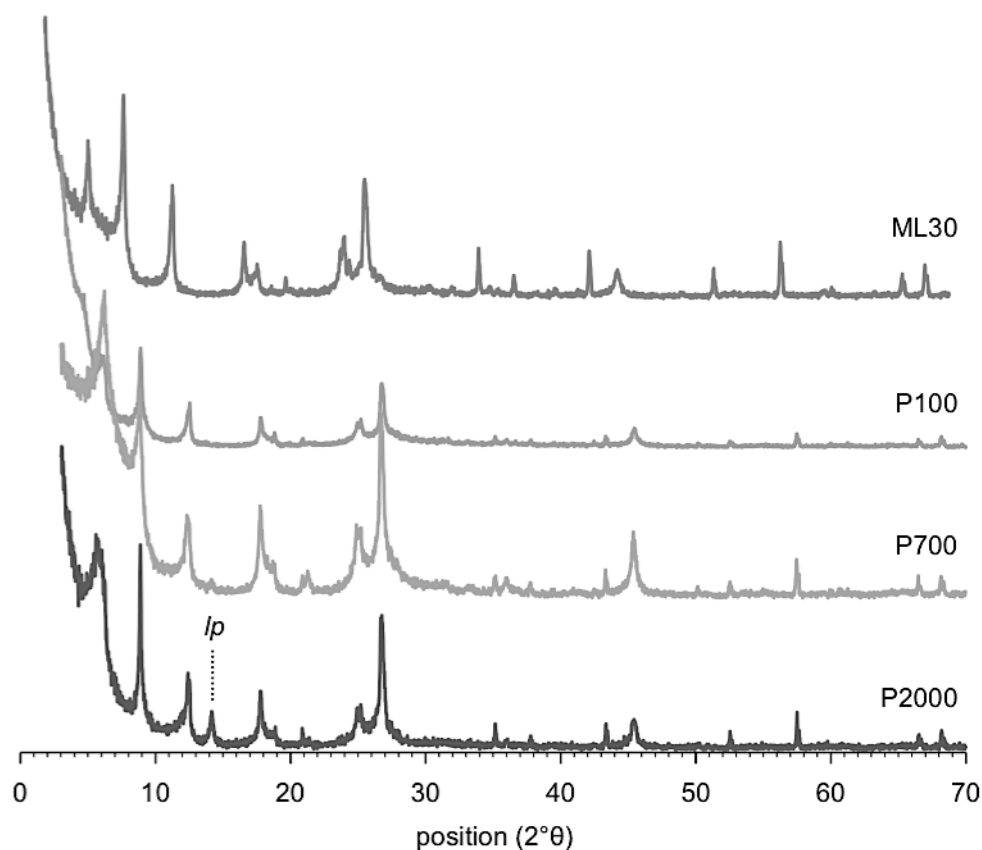


**Figure 3-3:** X-ray diffraction patterns (oriented texture specimens,  $\text{CuK}\alpha$ -radiation) of the clay fractions of the deepest subsoil horizon of the 100, 700 and 2000 year paddy sites (70–100 cm) (P100, P700, P2000) and the deepest horizon (13–30 cm) of the marshland (ML30), corrected to the quartz peak at 3.34 Å or 26.7 °2 $\theta$ ; lp = lepidocrocite.

It was not possible to identify any poorly crystalline Fe oxides (e.g., nanocrystalline goethite and ferrihydrite). Due to smaller crystals and higher structural disorder, diffraction lines of such short range-order hydrous Fe oxides are broadened, hampering their identification in complex spectra, especially if only present in small amounts.

### 3.3.4 Mössbauer spectroscopy: Assignment of the solid Fe phases

In each Mössbauer spectra, the same set of Fe-bearing phases was found, however, with somewhat varying Mössbauer spectral parameters and abundances. Mössbauer spectral parameters for each spectral component at 298 K and 4.2 K are listed in Table 3-4 and Table 3-5, respectively. Figure 3-4 illustrates the phase assignment for the Mössbauer spectra.

**Spectra at room temperature (298 K)**

Spectra at room temperature (RT) consisted of four spectral components. The low-energy Fe quadrupole doublet (RT-S3-FeOx) was fitted with a single Lorentzian line with an isomer shift (IS) between  $\delta = 0.253$  and  $0.263 \text{ mm s}^{-1}$  and a quadrupole splitting (QS) of  $\Delta = 0.576$  to  $0.630 \text{ mm s}^{-1}$ . These values are consistent with octahedrally coordinated ferric Fe (e.g., Dyar et al., 2006), occurring in various phases (e.g., aluminosilicates, Fe in organic complexes, Fe oxides). Iron atoms in silicates and organic complexes are paramagnetic due to greater distances between each other and do not order magnetically at RT. The RT spectra of superparamagnetic Fe in nanocrystalline goethite and haematite as well as in oxides having not passed their Curie or Neel temperature, respectively, at RT (i.e., ferrihydrite, lepidocrocite) may also exhibit a low-energy doublet. Thus, it is assumed that the quadrupole doublet RT-S3-FeOx is a superposition of the subspectra of different ferric phases. Consequently, the doublet was assigned to paramagnetic Fe(III) in aluminosilicates, organic-complexed Fe, and superparamagnetic Fe oxides. Differentiation between those phases is only possible at lower temperatures.

The high-energy Fe quadrupole doublet was attributed to paramagnetic Fe(II) in aluminosilicates (RT-S2). An IS between  $\delta = 0.998$  and  $1.023 \text{ mm s}^{-1}$  and a QS of  $\Delta = 2.610$  to  $2.719 \text{ mm s}^{-1}$  are consistent with those reported for Fe(II) in aluminosilicates, such as chlorite (Smyth, 1997) and kaolinite (Murad and Cashion, 2004). These two Fe-bearing sheet silicates were found in all clay fractions.

The third spectral component was a sextet, which was fitted with a single Lorentzian line. Its hyperfine field ( $B_{\text{hf}}$ ) was ranging between 50.9 and 51.7 T, the IS between  $\delta = 0.260$  and  $0.298 \text{ mm s}^{-1}$  and the QS between  $\varepsilon = -0.205$  and  $-0.275 \text{ mm s}^{-1}$ ; the sextet was assigned to magnetically ordered, well-crystalline haematite (RT-Hm) (Murad and Cashion, 2004).

**Table 3-4:** Range of  $^{57}\text{Fe}$  Mössbauer parameters isomer shift (IS), quadrupole splitting (QS) and hyperfine field ( $B_{\text{hf}}$ ) in the spectra taken at RT (298 K).

RT (298 K)	Assigned Phase	Mössbauer parameters		
		IS ( $\text{mm s}^{-1}$ ) <sup>a</sup>	QS ( $\text{mm s}^{-1}$ )	$B_{\text{hf}}$ (T)
S3-FeOx	ferric Fe in silicates/Fe oxides	0.25 to 0.26	0.58 to 0.63	–
S2	ferrous Fe in silicates	1.00 to 1.02	2.61 to 2.71	–
GtB	goethite	0.25 <sup>b</sup>	–0.68 to –0.01	14.7 to 31.1
Hm	haematite	0.26 to 0.30	–0.21 to –0.28	50.9 to 51.7

a given with respect to the  $^{57}\text{Co}$ –Rh source; to refer to  $\alpha$ -Fe add  $0.11 \text{ mm s}^{-1}$

b fixed value

– not applicable

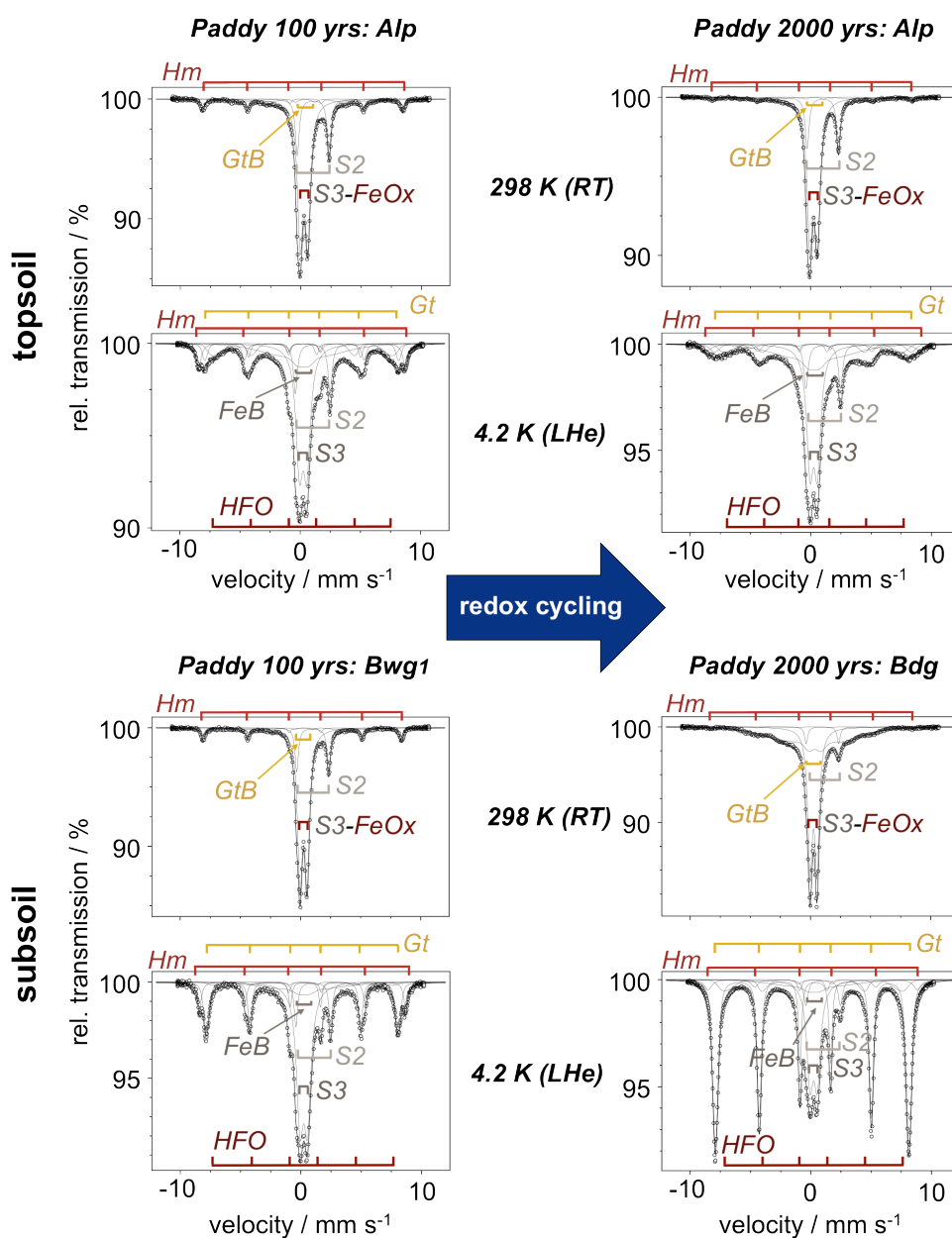


**Figure 3-4:**  $^{57}\text{Fe}$  Mössbauer spectra at 298 and 4.2 K (modified according to Vogelsang et al., 2016a). The solid black line drawn through the data points is the calculated fit. The spectral components are assigned as follows: **298 K:** S3-FeOx (central doublet) Fe(III) in aluminosilicates (e.g. illite, kaolinite and/or smectite) and paramagnetic hydrous oxides; S2 (wider doublet) Fe(II) in aluminosilicates; Hm (outer sextet) microcrystalline haematite; GtB (collapsed sextet) goethite near its magnetic blocking temperature; **4.2 K:** S3 (central doublet) Fe(III) in aluminosilicates; S2 (wider doublet) Fe(II) in aluminosilicates; FeB (collapsed sextet) paramagnetic relaxation of Fe(III) in aluminosilicates; Hm (outer sextet) haematite; Gt (middle sextet) goethite; HFO (inner sextet) hydrous Fe oxide of low crystallinity, i.e. ferrihydrite.

A sextet with an exceptionally large line width (collapsed sextet) was fitted with a Gaussian distribution of hyperfine fields and was assigned to goethite near its blocking (= magnetic ordering) temperature (RT-GtB). The isomer shift was constrained to  $\delta = 0.250 \text{ mm s}^{-1}$ , the QS was ranging between  $\varepsilon = -0.004$  and  $-0.753 \text{ mm s}^{-1}$  and the mean  $B_{\text{hf}}$  varied between 14.7 T and 31 T. Well-crystallized goethite is expected to exhibit a magnetically split component at RT, with a  $B_{\text{hf}}$  of about 38 T and a splitting of  $-0.26$  (Murad and Cashion, 2004). Lower crystallinity of goethite can lead to superparamagnetism, causing breakdown of the magnetic order at RT. Superparamagnetic relaxation at RT, as indicated by the collapsed sextet, is typical for goethite of particle sizes  $<15$  to  $20 \text{ nm}$ , as found in natural environments (Murad and Cashion, 2004). Goethite particles  $<12 \text{ nm}$  may even exhibit a ferric doublet at RT (van der Zee et al., 2003). Thus, it is assumed that goethite in the study clay fractions was of lower crystallinity than bulk goethite and is most likely characterised by a continuum of crystallinities.

#### ***Spectra at liquid helium temperature (4.2 K)***

Six spectral components could be identified in each spectrum (Table 3-5). Two components exhibited a quadrupole splitting and were fitted as quadrupole doublets with single Lorentzian line shapes. The low-energy Fe(III) quadrupole doublets represent paramagnetic Fe(III) in aluminosilicates (LHe-S3; IS =  $0.236$  to  $0.246 \text{ mm s}^{-1}$ , QS =  $0.588$  to  $0.655 \text{ mm s}^{-1}$ ); the high-energy Fe(II) quadrupole doublets were assigned to paramagnetic Fe(II) in aluminosilicates (LHe-S2; IS =  $1.021$  to  $1.038 \text{ mm s}^{-1}$ , QS =  $2.856$  to  $2.933 \text{ mm s}^{-1}$ ).

**Table 3-5:** Range of  $^{57}\text{Fe}$  Mössbauer parameters isomer shift (IS), quadrupole splitting (QS) and hyperfine field ( $B_{\text{hf}}$ ) in the spectra taken at liquid helium temperature (4.2 K).

LHe (4.2 K)	Assigned Phase	Mössbauer parameters		
		IS ( $\text{mm s}^{-1}$ ) <sup>a</sup>	QS ( $\text{mm s}^{-1}$ )	$B_{\text{hf}}$ (T)
S3	ferric Fe in silicates	0.24 to 0.25	0.59 to 0.66	–
S2	ferrous Fe in silicates	1.02 to 1.04	2.86 to 2.93	–
FeB	ferric/ferrous Fe in silicates	0.25b	0.00b	14.8 to 24.2
Hm	haematite	0.22 to 0.26	$-0.21$ to $-0.05$	52.9 to 53.8
Gt	goethite	0.24 to 0.26	$-0.29$ to $-0.22$	49.2 to 49.9
HFO	hydrous ferric oxide, poorly crystalline	0.20 to 0.21	$-0.00$ b	44.6 to 47.9

<sup>a</sup> given with respect to the  $^{57}\text{Co}$ –Rh source; to refer to  $\alpha$ -Fe at ambient temperature add  $0.24 \text{ mm s}^{-1}$  to IS

<sup>b</sup> pre-set value

– not applicable

There were four magnetically split components visible in the 4.2 K spectra. One was attributable to magnetically ordered haematite (LHe-Hm) and fitted with a Lorentzian line

sextet ( $B_{\text{hf}} = 52.9$  to  $54.5$  T,  $IS = 0.215$  to  $0.260$  mm s<sup>-1</sup>,  $QS = 0.210$  to  $0.049$  mm s<sup>-1</sup>). Well-crystallized haematite is expected to change from the weakly ferromagnetic to the antiferromagnetic state at a Morin temperature of  $T_M \approx 265$  K due to loss of spin canting (Evans and Heller, 2003). Haematite found was weakly ferromagnetic (wf phase) even at 4.2 K. That means haematite underwent Morin transition in none of the samples, which is typical for soil haematite of smaller particle size and substitution by other elements (e.g., Al) (Murad, 1989). Comparing spectral area at RT and 4.2 K indicates that at least some haematite was superparamagnetic at RT, likely due to particle sizes <8 nm (Murad and Cashion, 2004).

The second magnetically split component was fitted with a symmetric Gaussian distribution of hyperfine fields and assigned to magnetically ordered goethite (LHe-Gt) with a mean hyperfine field  $B_{\text{hf-mean}}$  between 49.2 and 50.5 T,  $QS_{\text{mean}} = 0.289$  to  $1.66$  mm s<sup>-1</sup> and  $IS_{\text{mean}} = 0.240$  to  $0.258$  mm s<sup>-1</sup>. It was easily distinguished from the haematite sextets by its mean quadrupole shifts and lower mean hyperfine fields ( $B_{\text{hf}}$  of haematite >52.9 T).

A third, broad magnetically split pattern was fitted with a Gaussian distribution of hyperfine fields with asymmetry, i.e., an inward broadening of the hyperfine field distribution. This fitting approach was successfully applied in ferrihydrite studies (Eusterhues et al., 2008; Mikutta et al., 2008; Mansfeldt et al., 2012). Consequently, the component was assigned to a poorly crystalline ferric hydrous oxide (i.e., ferrihydrite) (LHe-HFO). In spectra of goethite-rich samples, the spectral components assigned to LHe-HFO were largely covered by strong LHe-Gt lines and, therefore, could scarcely be fitted without constraints. To overcome the problem, the same fitting parameters of spectra from (1) the same sample site and (2) with a good resolution of the LHe-HFO component (in all cases topsoil spectra) were used to fit the partly “hidden” LHe-HFO components. Including the LHe-HFO spectral component improved the quality of fits (strong increase of chi-square) compared to spectra fitted without the additional component. Without the LHe-HFO phase, by contrary, not all of the spectral area could be explained by the model fit.

Mean  $B_{\text{hf}}$  of the LHe-HFO phase ranged between 44.6 and 47.9 T. This is in agreement with values for natural ferrihydrite ( $B_{\text{hf}} = 50$ – $45$  T for 6 and 2-line ferrihydrite, respectively) (Murad, 1988; Murad, 1989) and ferrihydrite associated with OM ( $B_{\text{hf}} = 46$  T for Ferrihydrite with a C/Fe ratio of 0.54; Eusterhues et al., 2008). The mean IS of LHe-HFO subspectra was between 0.197 to 0.210 mm s<sup>-1</sup>; mean QS was constrained to 0.000 mm s<sup>-1</sup> for all LHe-HFO phases. Near-zero QS indicates lower structural disorder and lower degree of asymmetry (Marchand and Rancourt, 2009; 2008). According to Murad and Schwertmann (1980), individual characteristics of different Fe oxides gradually disappear with decreasing particle sizes. The spectral component assigned to poorly crystalline hydrous Fe oxide, thus, may include ferrihydrite and nanocrystalline goethite or lepidocrocite. More general speaking, LHe-HFO represents Fe oxides of small particle size (nm range), high OM or cation substitution, or other structural defects.

X-ray diffractions indicated the presence of lepidocrocite in several clay fractions (see above) Mössbauer spectra of magnetically split lepidocrocite (Lp) are characterised by a very low  $B_{hf}$  (45–46 T; Johnson, 1969; Murad and Schwertmann, 1984). Ferrihydrite can normally easily be distinguished from lepidocrocite due to higher mean  $B_{hf}$  (50 T for pure ferrihydrite and 48–49 T, if some Fe is substituted by Al or Si) (Childs et al., 1984). As discussed above, ferrihydrite associated with OM has lower  $B_{hf}$  and, thus, the mean  $B_{hf}$  of lepidocrocite and OM-rich ferrihydrite are similar. Likely, the spectral component in deeper subsoil horizons assigned to LHe-HFO is a superposition of the spectral area of lepidocrocite and ferrihydrite. This highlights the importance of combining methods, i.e., Mössbauer spectroscopy and XRD, for identification of solid Fe mineral phases, and also, shows the limitations of the fitting approach.

Additionally, a collapsed sextet occurred in all 4.2 K spectra. To my best knowledge, all Fe oxides are hyperfine split at 4.2 K it was assigned to slowly relaxing, paramagnetic Fe(III) and Fe(II) in aluminosilicates, such as Fe-poor illite (Murad and Wagner, 1994).

No Fe(II)-bearing mineral phases other than aluminosilicates could be identified. However, samples were taken before the paddy fields were flooded, thus, oxic conditions prevailed (data not shown). It is assumed that ferrous Fe contents possible present were little at the time of sampling. As a consequence, no measurements were taken to prevent Fe(II) oxidation during sampling, transportation, and treatment of the samples.

### ***Changes in abundance and characteristics of the Fe solid phases upon paddy cultivation***

Assuming that all phases have similar recoilless fractions, the spectral area of a specific Fe mineral phase is equivalent to the abundance of the respective phase in the sample. This assumption is expected to be valid at liquid helium temperatures (Murad and Cashion, 2004) and allows quantitative speciation for each Fe mineral phase based on the 4.2 K spectra. In the present study calculation of phase abundances was done as follows: Abundances of the ferric silicate phases was calculated subtracting the abundances of the nanocrystalline haematite and goethite, and the LHe-HFO phase from the spectral abundance of the RT-S3-FeOx component. Abundances of ferrous Fe in aluminosilicates were calculated based on the spectral area of RT-S2; the abundance of goethite and haematite was calculated based on the spectral area of LHe-Gt and LHe-Hm, respectively. The amount of microcrystalline goethite was assumed to be equal to the area of RT-GtB; the abundance of microcrystalline haematite was derived from the spectral area of RT-Hm. Nanocrystalline haematite and goethite, respectively, were calculated by subtracting the microcrystalline abundances from total abundances of the respective phase. Abundances of the poorly crystalline hydrous ferric oxides (HFO) were calculated using the LHe-HFO spectral area. Iron contents of each Fe mineral phase can be calculated by multiplying the fraction of the respective Mössbauer spectral area by the total Fe content of the sample (Table 3-2).

According to Mössbauer results, the dominant solid Fe phases in paddy and non-paddy clay fractions were Fe-bearing silicates ( $\text{Fe}_{\text{Si}}$ ). As shown in Figure 3-5, with few exceptions more than half of the Fe present was bound as structural Fe(II) and Fe(III) in aluminosilicates.

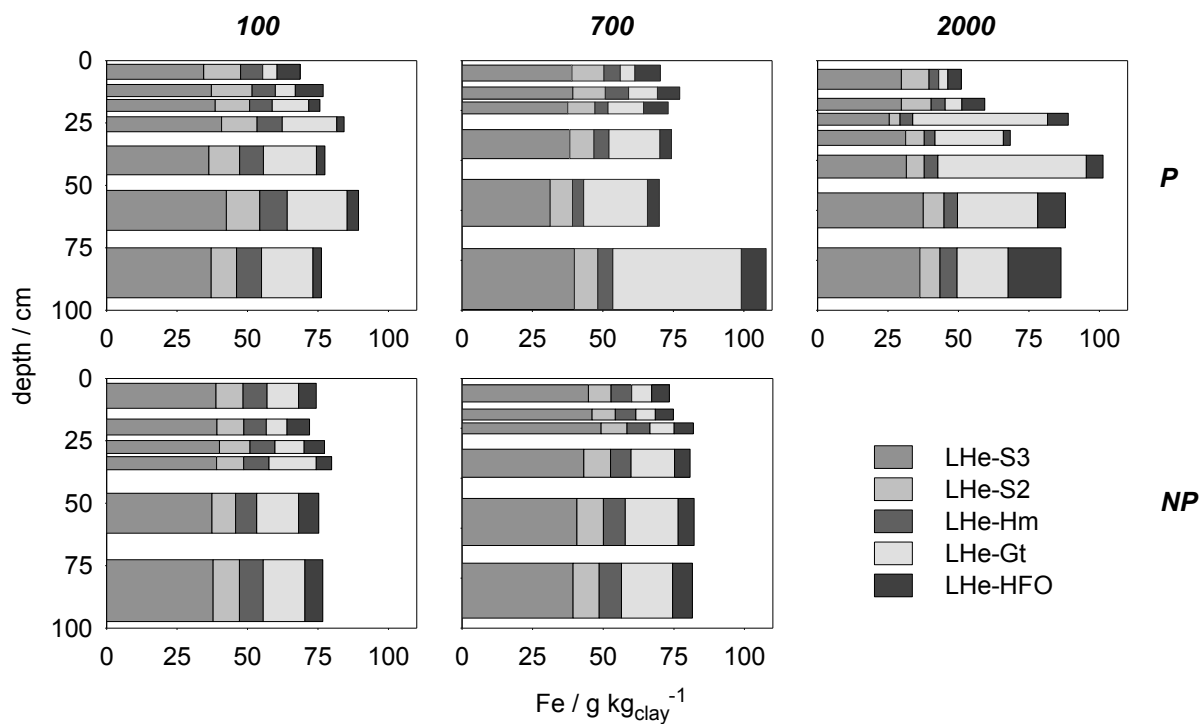


**Figure 3-5:** Depth distribution of solid Fe phases along the chronosequence. Fe contents of each phase were calculated based on the corresponding  $^{57}\text{Fe}$  Mössbauer spectral area.

There was a slight loss of the structural Fe in aluminosilicates with time of paddy management; lowest contents of silicate Fe were found in the topsoil of P2000. Fe(II)/Fe(III) ratios in aluminosilicates differed between top and subsoil, especially in the older paddy soil, with higher ratios and, hence, relatively more Fe(II) in the topsoil than in the deeper horizons (P2000 0–15 cm: 0.33, 20–27 cm: 0.15).

Paddy soil Fe oxide fractions were characterised by increasing profile differentiation with time of paddy cultivation and a continuum of crystallinities. Fe bound in haematite ranged between 3.4 (P2000 Alp) and 8.3  $\text{g kg}_{\text{clay}}^{-1}$  (P700 Alp2). With increasing time of paddy cultivation, haematite Fe contents decreased throughout the soil profile, most likely due to reductive dissolution of the haematite inherited from the parent material.

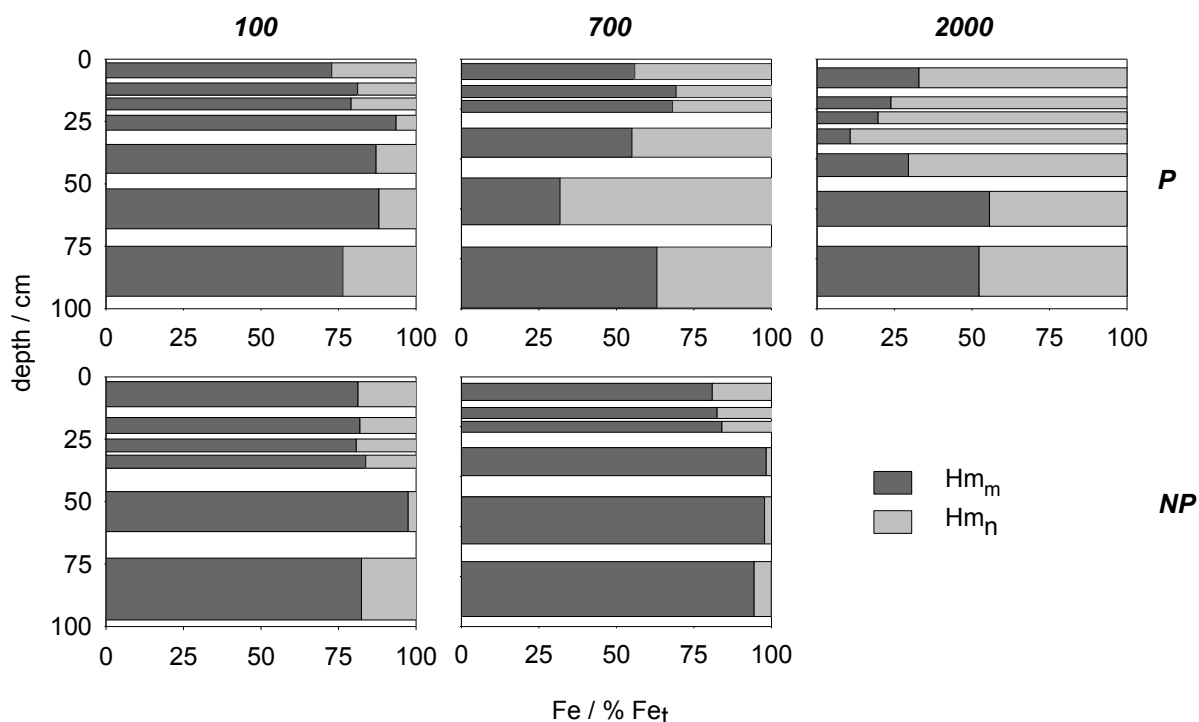


**Figure 3-6:** Relative contents of microcrystalline ( $Hm_m$ ) and nanocrystalline haematite ( $Hm_n$ ) based on  $^{57}\text{Fe}$  Mössbauer analysis. Results are expressed as % of total-haematite Fe, assuming equal Mössbauer assuming recoilless fractions.

Figure 3-6 illustrates the proportion of Fe bound in nanocrystalline (<20 nm) and microcrystalline haematite in relation to total haematite Fe contents. As shown by decreasing contents, haematite seems prone to reductive dissolution during paddy soil evolution. Surprisingly though, a relative increase in nanocrystalline haematite (<20 nm) was observed with prolonged paddy cultivation. This can only be explained by neo-formation of haematite less crystalline than the inherited haematite. This is in accordance with findings of Murad (1989), who showed that haematite formed in soils usually of poor crystallinity.

Goethite was identified as the major Fe oxide phase in most clay fractions, ranging between 3.2 (P2000 Alp) and 52.7 (P2000 2Bg1)  $\text{Fe g kg}_{\text{clay}}^{-1}$  (Figure 3-5). Increasing number of redox cycles resulted in depletion of goethite in favour of the poorly crystalline hydrous Fe oxide phase (LHe-HFO) in the topsoil. In the subsoil, conversely, contents of goethite Fe increased with prolonged paddy cultivation, even exceeding Fe contents of the aluminosilicate fraction in some subsoil horizons of P2000 (Bdg = 47.8  $\text{g kg}_{\text{clay}}^{-1}$ ; 2Bg = 52.7  $\text{g kg}_{\text{clay}}^{-1}$ ). The deepest subsoil horizons (2Bg2 and 2Blg) of P2000, however, had lower goethite Fe contents (28.5 and 18.1  $\text{g kg}_{\text{clay}}^{-1}$ , respectively). An increase in microcrystalline proportions for goethite was observed, especially in the subsoil of P700 and P2000, whereas in the topsoil the abundance of nanocrystalline goethite increased (Figure 3-7). Highest proportions of

microcrystalline goethite were found below the plough pan in the top B horizon (Bdg) of P2000.

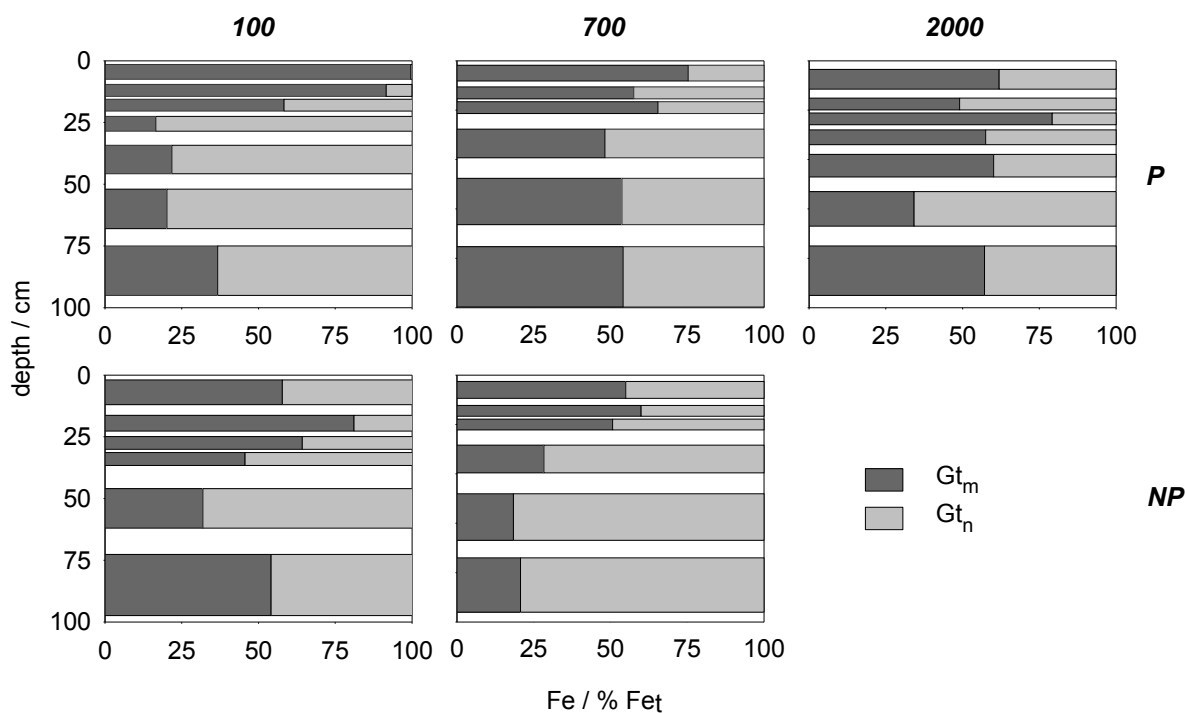


**Figure 3-7:** Relative contents of microcrystalline ( $Gt_m$ ) and nanocrystalline goethite ( $Gt_n$ ) based on  $^{57}\text{Fe}$  Mössbauer analysis. Results are expressed as % of total-goethite Fe, assuming equal Mössbauer assuming recoilless fractions.

Topsoil contents of Fe bound in HFO were slightly larger in the paddy soils than in non-paddy soils. With increasing time of paddy cultivation, contents were slightly decreasing. Contents of HFO Fe were lowest in the Alp horizon of P2000 ( $2.5 \text{ g kg}_{\text{clay}}^{-1}$ ). Smaller mean and maximum hyperfine fields ( $B_{\text{hf-mean}}$  or  $B_{\text{hf-max}}$  of LHe-HFO; Table 3-5) indicate smaller particle sizes and higher structural disorder of the HFO phases in the topsoil of P700 and P2000 than in non-paddy topsoils, presumably due to higher C/Fe ratios, as shown by Eusterhues et al. (2008).

Increasing spectral areas of the LHe-HFO component occurred in the subsoil upon paddy cultivation. Highest HFO Fe contents were found below 50 cm in the subsoil horizons of P2000, 2Bg2 and 2Blg ( $9.8$  and  $18.7 \text{ g kg}_{\text{clay}}^{-1}$ , respectively). This can be explained by the presence of lepidocrocite ( $L_p$ ), as identified by XRD (Chapter 3.3.3) in the clay fractions of at 45–69 and 69–100 cm depth of P700 and at 50–70 and 70–100 cm depth of P2000. As discussed above, it was not possible to resolve the lepidocrocite phase and the LHe-HFO phase with the fitting approach used. Thus, the spectral area attributed to the LHe-HFO phase

in these specific horizons not only originates from poorly crystalline hydrous ferric oxides in *sensu strictus* but also from lepidocrocite.

Iron contents bound in oxides were notably lower at 27–35 cm depth of P2000 in comparison to those of the adjoining subsoil horizons, and independent of the Fe oxide phase. Kölbl et al. (2014) classified this horizon as a buried A horizon (2AhgB), which might explain why Fe oxide contents are comparable to those observed for topsoils rather than subsoils.

For non-paddy soils, no such profile differentiation was observed for any of Fe phases: Abundances and, hence, contents of the different Fe mineral phases hardly differed between NP100 and NP700 (Figure 3-5) and were comparable to those of P100. As for the paddy sites, lowest total Fe contents were observed in the topsoils.

### 3.4 Discussion

#### ***Long-term cultivation of paddy rice leads to proportional increase in organic matter-rich, poorly crystalline hydrous ferrous oxides in the topsoils***

Results from wet chemical extractions ( $Fe_o$  and  $Fe_d$ ) and Mössbauer spectroscopy demonstrate that an increasing duration of paddy cultivation results in decreasing hydrous Fe(III) oxide contents in the clay fractions of topsoils, with higher losses of crystalline Fe oxides, such as goethite and haematite, hence, an relative enrichment of the poorly crystalline phases ( $Fe_o$  and LHe-HFO, respectively). Concurrently, a proportional increase of the silicate Fe fraction was observed.

Ferrihydrite is generally the first precipitate upon rapid reoxidation of dissolved Fe(II). It slowly transforms into thermodynamically more stable Fe oxides, i.e., goethite and haematite, under stable oxic conditions (Cornell and Schwertmann, 2003). Organic matter can retard or even inhibit transformation into more crystalline oxides (Schwertmann, 1966; Jones et al., 2009). Enrichment of OM in the uppermost horizons is a prominent feature of most paddy soils (Kögel-Knabner et al., 2010). Increasing OC concentrations in the clay fractions of the selected paddy sites were observed, especially in the topsoils. The topsoil accumulation of OM was more pronounced for the paddy than for the non-paddy sites. Increasing OC stocks in the paddy topsoil are mainly due to accumulation of OC in the silt and coarse clay fraction because of retarded decomposition of OM under waterlogged conditions and the formation of microaggregates upon interaction of Fe phases with OM (Wissing et al., 2013).

**Table 3-6:**  $^{57}\text{Fe}$  Mössbauer parameters, isomer shift (IS), quadrupole splitting (QS) and hyperfine field ( $B_{\text{hf}}$ ), of the LHe-HFO phase at 4.2 K of the paddy (P) and non-paddy (NP) topsoil (modified according to Vogelsang et al, 2016b).

site	Mössbauer parameters of LHe-HFO				
	mean IS ( $\text{mm s}^{-1}$ ) <sup>a</sup>	mean QS ( $\text{mm s}^{-1}$ ) <sup>b</sup>	mean $B_{\text{hf}}$ (T)	max $B_{\text{hf}}$ (T)	sdev $B_{\text{hf}}$ (T)
ML30	0.202	0.000	47.9	49.8	3.199
P100	0.209	0.000	45.1	47.0	3.047
P700	0.210	0.000	45.8	47.9	3.485
P2000	0.206	0.000	44.6	46.5	3.199
NP100	0.206	0.000	46.7	48.8	3.535
NP700	0.197	0.000	46.8	48.9	3.361

<sup>a</sup> given with respect to the  $^{57}\text{Co}$ -Rh source; to refer to  $\alpha$ -Fe at ambient temperature add  $0.24 \text{ mm s}^{-1}$  to IS

<sup>b</sup> pre-set value

Even small amounts of OM can influence particle size and structural order of ferrihydrite, resulting in smaller crystals, increased lattice spacing, and distorted  $\text{Fe}(\text{O},\text{OH})_6$  octahedra (Eusterhues et al., 2008). According to Mikutta et al. (2008), coprecipitation with OM might decrease the magnetic super-exchange between ferrihydrite particles, which they explained with the diluting effect of OM on the magnetic properties of the Fe mineral phase. The smaller mean and maximum hyperfine field attributed to the poorly crystalline hydrous Fe oxide phase (LHe-HFO) in the studied samples was characterised by decreasing  $B_{\text{hf}}$  with time of paddy cultivation. That indicates increasing OM–mineral interactions, as shown by Eusterhues et al. (2008), who observed decreasing mean magnetic hyperfine fields ( $B_{\text{hf}}$ ) of ferrihydrite associated with OM (46.5 T). Apparently, the weakly crystalline Fe oxides in paddy topsoils were more loaded with OM than those in the non-paddy topsoils. Hyperfine fields of the LHe-HFO spectral component fitted for NP100 and NP700 topsoils remain constant. The presence of increasing contents of OM in older paddy topsoils favours the formation of OM-rich, poorly crystalline Fe oxide phase. Such phases form likely by coprecipitation rather than by adsorption of OM (Eusterhues et al., 2011). Repeated anoxic conditions not only promote the microbial-induced reductive dissolution of poorly crystalline but also of well-crystalline oxides, such as goethite and haematite (Roden and Zachara, 1996; Bonneville et al., 2009). Thompson et al. (2011) observed increasing fractions of highly disordered ferric oxide phase along a redox gradient in a basaltic soil with increasing rainfall and suggested that the accumulation of poorly crystalline Fe oxides is supported by anoxic cycles, paired with a high water throughput and subsequent leaching of Fe(II), and the presence of high concentrations of OM during Fe(II) oxidation. Hydrous oxides in the soils of the test chronosequence may undergo similar transformations. Fe(II) released from crystalline and poorly crystalline Fe oxides is leached into the subsoil with the percolating irrigation

water (Gong, 1983); upon drainage, the Fe(II) remaining in topsoils is oxidised, and poorly crystalline hydrous Fe(III) oxide phases precipitate in the presence of increasing contents of OM. In result, topsoil Fe oxide fractions (LHe-HFO+Gt+Hm) decrease in favour of the silicate Fe fraction (LHe-S2+S3) and the remaining Fe oxides become increasingly less ordered and more OM-loaded. Also the crystallinity of haematite and goethite decreased with on-going paddy cultivation, as evident from increasing proportions of nanocrystalline forms.

***Microcrystalline goethite accumulates in the subsoil horizon adjacent to the plough pan, whereas lepidocrocite is the dominant Fe oxide in the groundwater influenced zone***

In contrary to the topsoils, total Fe contents increase and crystalline Fe oxides became prevalent in paddy subsoils. In comparison to the P100 as well as to the sites under non-irrigated cultivation microcrystalline goethite increased in the upper part of the solum of both P700 and P2000. Under oxic conditions goethite is forming via dissolution/reprecipitation from ferrihydrite (Manceau and Drits, 1993; Cornell and Schwertmann, 2003) and/or lepidocrocite (Schwertmann and Taylor, 1972). Paddy subsoils were also subject to changing redox conditions, with Eh values decreasing below  $-200$  mV at all paddy sites (35 and 55 cm) upon flooding. Under redox fluctuations two pathways of microcrystalline goethite formation and enrichment are possible:

(1) Residual enrichment, as the more soluble Fe oxides are dissolved preferentially (Munch and Ottow, 1980; Thamdrup, 2000; Zachara et al., 2002; Mansfeldt et al., 2012). The reduction of Fe(III) oxides correlates with the solubility of the Fe oxides (ferrihydrite > lepidocrocite > goethite > haematite) (Bonneville et al., 2004; Bonneville et al., 2009). Thus, under weakly reducing conditions poorly crystalline Fe oxides phases (i.e., ferrihydrite) tend to become dissolved first. However, that would only lead to a relative enrichment, but an absolute increase of Fe-bound goethite at no losses of total Fe was observed.

(2) Under anoxic conditions reductively released Fe(II) can induce a catalytic reaction, resulting in the recrystallisation and/or solid state transformation of solid Fe(III) mineral phases (Pedersen et al., 2005). This secondary transformation is induced by electron transfer between the aqueous Fe(II) and the solid Fe(III) mineral after adsorption of Fe(II) on the mineral surface (Williams and Scherer, 2004). It results in the dissolution of the mineral and the subsequent recrystallisation of the Fe(III) into more stable Fe oxides species (Jeon et al., 2001; Jeon, Dempsey and Burgos, 2003; Hansel et al., 2003; Williams and Scherer, 2004; Pedersen et al., 2005; Yee et al., 2006). In the absence of OM, it promotes structural transformation of poorly crystalline Fe oxides (e.g., ferrihydrite) to more crystalline and thermodynamically stable Fe oxide phases, such as haematite and goethite (Jones et al., 2009) and lepidocrocite (Pedersen et al., 2005). In a batch experiment Thompson et al. (2006) demonstrated that redox oscillation, indeed, can lead to increasing crystallinity of goethite and haematite due to the formation of aqueous Fe(II) and subsequent Fe(II)-catalysed solid state

transformation of remaining Fe(III) oxides. In paddy soils, aqueous Fe(II) might originate from reduction of Fe(III) minerals *in-situ* or is leached from horizons above with the irrigation water (Gong, 1983). The secondary mineral species formed upon Fe(II)-catalysed transformation depends on the supply rate and the concentration of Fe(II) in the soil solution (Fredrickson et al., 1998; Benner et al., 2002; Hansel et al., 2003; Zachara et al., 2002; Yee et al., 2006). Low contents of Fe(II) promote the conversion of 2-line ferrihydrite to goethite, whereas magnetite is expected to preferentially form at elevated dissolved Fe(II) concentrations (Benner et al., 2002; Hansel et al., 2003; Hansel et al., 2005) and/or prolonged anoxic periods (Hansel et al., 2003). In a study of Hansel et al. (2003), addition of only 40  $\mu\text{M}$  of ferrous Fe led to an almost complete conversion of the 2-line ferrihydrite to goethite and lepidocrocite. Aqueous Fe contents in soil solutions sampled at both 35 and 55 cm were little and did not exceed 40  $\mu\text{mol l}^{-1}$ , despite Eh values within the Fe reduction range under the given environmental conditions (see Chapter 5). Since microcrystalline goethite is less prone to reductive dissolution than ferrihydrite (Hansel et al., 2003), it may, once formed, accumulate in soil.

Increasing abundance of lepidocrocite was observed in the lower part of the solum of P700 (>70 cm depth) and P2000 (>50 cm depth), which is typical for hydromorphic soils, i.e., stagnosols (Fitzpatrick et al., 1985). Smeck and Bingham (2002) suggested that lepidocrocite concentrates in horizons only part-time groundwater saturated (<50% of the time with >5 °C). Groundwater levels were highest at the P100 site and decreased at the older sites (P700, P2000). However, Eh measurements did not reveal significant differences in the length of reducing conditions between the paddy sites. All paddy subsoils showed reduced conditions (Eh <400 mV) for most of the year, even during the fallow period (Chapter 5). Lepidocrocite is a polymorph of goethite and in natural environments often closely associated to the latter (Cornell and Schwertmann, 2003). Goethite and lepidocrocite are thought to have competing formation pathways. Lepidocrocite is formed via the mixed valence phase green rust (Schwertmann and Fechter, 1994) and at low  $\text{pCO}_2$  (Carlson and Schwertmann, 1990). Respiration in the upper part of the pedon and hence elevated  $\text{pCO}_2$  (Chapter 5) may favour the formation of goethite in topsoils, largely restricting the occurrence of lepidocrocite to the deeper solum.

#### ***Long-term paddy cultivation has little effect on Fe-bearing aluminosilicates***

Both XRD and Mössbauer measurements revealed little distinct change in the soil clay assemblage upon 2000 years of paddy cultivation. Illite, kaolinite, chlorite, vermiculite, expandable 2:1 silicate and mixed-interlayer clay minerals were present in varying proportions.

However, total Fe silicate contents were slightly decreasing in the paddy topsoil but not in non-paddy topsoils, indicating that intermittent drainage and waterlogged conditions cause

loss of silicate Fe. This is concurrent with results from Favre et al. (2002), who observed lower silicate Fe contents in paddy topsoils than in uncropped fields after only 22 cycles of rice cropping.

No distinct chronological changes were observed in the silicate mineral assemblage in the subsoil of P100 and P700: differences between the different paddy soils as well as between paddy and non-paddy soils were likely due to differences in the parent material rather than to time of cultivation. At the 2000 year site, however, relatively lower contents of illite in comparison to kaolinite were observed in the X-ray diffractograms of the upper solum (<30 cm). Both Barré et al. (2007) and Cornu et al. (2012) showed that spatial and temporal changes of illite-like minerals are closely related to the K cycle. The loss of illite after 2000 years of paddy cultivation parallels the decreasing total and exchangeable K contents with the time of paddy cultivation. Intensive agriculture causes decreases in illite contents of the surface horizons of temperate soils if no K fertilizer is applied (Barré et al., 2007). Li et al. (2003) observed the loss of K-bearing clay minerals within 80 years of paddy cultivation despite of regular K fertilization. It cannot be fully excluded that observed changes in the kaolinite–illite ratio are also due to variations of deposited material.

### 3.4.1 Selective chemical extractions versus Mössbauer spectroscopy

Figure 3-8 illustrates that DCB-extractable Fe was strongly correlated with the amount Fe bound in well-crystalline Fe oxides calculated by Mössbauer spectroscopy (LHe-Hm+Gt+HFO) for both paddy and non-paddy soils ( $r^2 = 0.87$  and  $0.83$ , respectively). Oxalate-extractable Fe and Fe contents in poorly crystalline Fe oxides from Mössbauer spectroscopy (LHe-HFO phase) have no apparent correlation ( $r^2 = 0.06$ ) for the paddy soils. This may partly be explained by higher contents of LHe-HFO than of  $Fe_0$  in the deepest subsoil horizons of P700 and P2000 due to the contribution of lepidocrocite to the spectral area of the LHe-HFO phase. Removing these outliers from the correlation improves the correlation coefficient ( $r^2 = 0.49$ ). However, Mössbauer spectroscopy generally resulted in higher values. Parfitt and Childs (1988) noted that ferrihydrite dissolution can be incomplete in a single oxalate extraction.

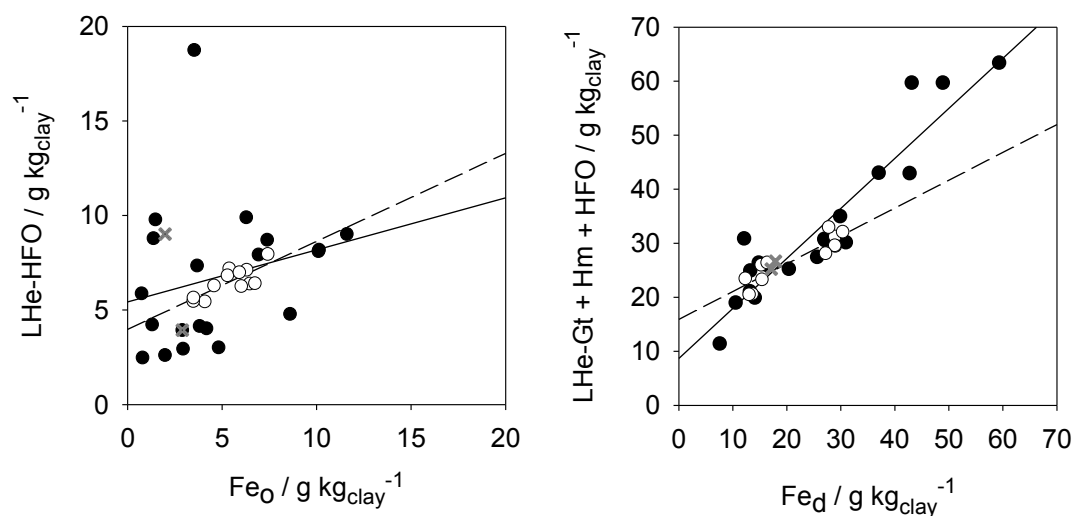


**Figure 3-8:** Ammonium-oxalate-extractable Fe contents versus Fe in poorly crystalline ferric oxides calculated from the  $^{57}\text{Fe}$  Mössbauer spectral area of the LHe-HFO phase (left) and DCB-extractable Fe contents versus Fe in ferric oxide contents calculated from  $^{57}\text{Fe}$  Mössbauer the spectral area of LHe-Hm, LHe-Gt and LHe-HFO phases (right) of all paddy (●), non-paddy (○) and marshland (×) samples. The solid (paddies) and dashed line (non-paddies) show the correlation between the two data sets. LHe-HFO vs.  $\text{Fe}_0$ :  $r^2 = 0.06$  (paddies) and  $0.62$  (non-paddies); LHe-Gt + Hm + HFO vs.  $\text{Fe}_d$ :  $r^2 = 0.87$  (paddies) and  $0.83$  (non-paddies).

### 3.5 Conclusion

Paddy soils are characterised by repeated redox cycles. Two thousand years of paddy cultivation led to depletion of hydrous Fe, resulting in an increasing profile differentiation and decoupling of top- and subsoil processes with respect to Fe contents and the participating solid Fe mineral phases in the clay fraction. Transformation of Fe mineral phases in the topsoils is characterised by the reductive dissolution of the Fe minerals (silicates as well as crystalline and poorly crystalline oxide phases) during anoxic periods and the coprecipitation of poorly crystalline hydrous Fe oxides with OM during oxic phases. The organic–mineral interactions inhibit transformation and crystallisation of the Fe oxides present and lead to an accumulation of poorly crystalline, OM-rich hydrous ferric oxides and less well ordered goethite and haematite. In the upper subsoil, transformation processes seem to be driven by dissolved Fe(II) leached from the topsoil, resulting in increasing contents of Fe oxides and increasing crystallinity of the goethite present. Under the influence of fluctuating groundwater levels and/or lower  $\text{pCO}_2$  levels, however, lepidocrocite can form in the deeper subsoil. Thus, long-term paddy cultivation on marine substrates creates different Fe mineral forming environments within the paddy profile.

## 4. In-situ test of redox-induced mineral transformation

### 4.1 Introduction

In many paddy soils, Fe(II)–Fe(III) is the most important redox couple (Ponnamperuma, 1972); Fe-bearing minerals are prone to microbially mediated transformations induced by frequent redox changes. Numerous interconversions between the solid Fe oxide phases can take place in soil, some of which are still only partly understood. Hydrated Fe(III) oxides are subjected to microbial induced reduction and subsequent dissolution under anoxic conditions (Bonneville et al., 2004). The reactivity of Fe(III) oxides towards reductive dissolution decreases with decreasing surface area (Roden and Zachara, 1996) and thus, increasing particle size and crystallinity. The Fe oxide solubility (ferrihydrite > lepidocrocite > goethite > haematite) can serve as good predictor for the potential Fe reduction rate (Bonneville et al., 2004; Bonneville et al., 2009). Less stable hydrated Fe(III), such as ferrihydrite, are reduced preferentially (Munch and Ottow, 1980; Thamdrup, 2000; Zachara et al., 2002). More crystalline Fe oxides might also be prone to reductive dissolution, depending on the environmental conditions (pH, Eh) (Bonneville et al., 2004; Bonneville et al., 2009). Upon the reestablishment of oxic conditions, soluble Fe(II) is oxidised and poorly crystalline hydrated Fe(III) oxides precipitate. Over time, these less well ordered minerals can transform into thermodynamically more stable phases, i.e., goethite and/or haematite, either by topotactic reactions or dissolution–reprecipitation mechanisms, i.e., Ostwald ripening (Cornell and Schwertmann, 2003). Frequent redox cycles, however, may prevent transformation process to more crystalline phases, and thus, favour the formation of poorly crystalline hydrated Fe oxides.

A typical feature of paddy soils is the accumulation of OM over time of paddy cultivation, especially in the topsoils (Zhang and He, 2004; Pan et al., 2003; Kögel-Knabner et al., 2010; Wu, 2011; Wissing et al., 2011). The presence of DOM supports the formation of aqueous organic Fe(III) complexes and of disordered, organic-rich ferrihydrite (Ratering and Schnell, 2000; Rancourt et al., 2005). Organic complexation may hamper the transformation of poorly crystalline Fe oxides to better crystalline phases (Schwertmann, 1966; Jones et al., 2009; Eusterhues et al., 2008; Thompson et al., 2011).

However, upon frequent redox cycles recrystallisation of solid ferric Fe phases as induced by the catalytic action of aqueous ferrous Fe may lead to an increase in crystallinity of the Fe oxide mineral assemblage (Thompson et al., 2006; Thompson et al., 2011; see also Chapter 3). The product of that transformation process, involving goethite, haematite, lepidocrocite, and/or magnetite, is highly dependent on the Fe(II) supply rate and concentration in the soil solution (Fredrickson et al., 1998; Benner et al., 2002; Zachara et al., 2002; Hansel et al., 2003; Yee et al., 2006). Thus, the biogeochemical cycling of Fe in soils prone to frequent

redox cycles is governed by Fe oxide mineral transformations as induced by microbial reduction and reoxidation. It is unknown to what extent these transformations take place upon the sharply contrasting redox oscillations as found in paddy subsoils.

Another important redox-active species is structural Fe of clay minerals (Stucki, 1988). Ferruginous smectites are redox-active over a wide Eh range; in the case of chemical reduction the range is even much wider than theoretically predicted for the  $\text{Fe}^{3+}/\text{Fe}^{2+}$  redox couple (Gorski et al., 2012a; Gorski et al., 2012b; Gorski et al., 2013). Structural Fe(III) in clay minerals can either be reduced chemically or biologically by Fe-reducing bacteria; in soils microbial reduction is the predominant reduction pathway (Achnich et al., 1995). Reduction of octahedral Fe(III) within the clay structure can induce cis- to trans- migration of Fe within the octahedral sheet, resulting in the formation of trioctahedral domains and subsequent dehydroxilation (Lear and Stucki, 1985; Manceau et al., 2000b), structural distortion, and finally loss of structural Fe (Favre et al., 2002; Yang et al., 2012). Neof ormation of smectite, vivianite and poorly crystalline silica ( $\text{SiO}_2$ ) (Dong et al., 2003) as well as illite (Kim et al., 2004) has been reported upon microbial reduction of structural Fe(III) and subsequent dissolution of the clay minerals. The oxidation state of structural Fe has impact on the physicochemical properties of the clay itself, i.e., cation exchange capacity, swelling properties, specific surface area, colour (Stucki, 2006). Most intensive reduction has been observed for chemical reduction (e.g., Lee et al., 2006; Stucki, 2011). However, some studies also reported extensive biotic reduction (Kostka et al., 1999b; Kim et al., 2004; Jaisi et al., 2005; Jaisi et al., 2007a, Jaisi et al., 2008a). Wu et al. (1988) reported extensive Fe bacterial reduction (41%) of an iron-rich smectite using a rice paddy inoculum. The reversibility of structural changes is dependent on the extent of reduction and on the number of redox cycles the minerals are exposed to (Stucki, 2011). Due to the more intensive reduction, reversibility is generally less for chemical than for microbial induced reduction (Lee, et al. 2006, 2006; Ribeiro et al., 2009). Gorski et al. (2012b) demonstrated that after repeated redox cycling structural changes may partly be irreversible. Most studies on structural changes of Fe-bearing smectites were performed in the laboratory. Thus, little is known if the structural changes induced by microbial reduction do occur also under field conditions.

The redox capacity (abundance and availability of electron donors and acceptors), among others, strongly governs the magnitude of reduction of a given soil (Achnich et al., 1995). Depth distribution of electron donors (i.e., organic substrates) and potential acceptors (e.g., Fe minerals) becomes more pronounced with time of paddy cultivation the (e.g., Gong, 1983; Cheng et al., 2009; Chen et al., 2011; Kölbl et al., 2014). This can direct influence on the soils redox status and, in consequence, the magnitude of redox changes and possibly mineral transformations.

Identification of transformation processes of Fe-bearing minerals is challenging in a heterogeneous system, such as soil. Thus, to study *in-situ* mineral transformations and identify possible paddy-specific iron mineral phases and their precursors in the illuvial subsoil mineral bags each filled with a single Fe-bearing mineral were exposed to paddy conditions. This mineral bag technique has been first applied by Ranger et al. (1991) and Nugent et al. (1998) in temperate forest soils. Augusto et al. (2001) successfully used the technique to study the influence on tree species on weathering of vermiculite.

Following research questions were formulated:

- Does the ferrihydrite turn into disordered organic–mineral composites or is an increase in crystallinity due to solid state transformation processes observed?
- Are well-crystalline hydrous Fe(III) oxides, i.e., goethite, involved in transformation processes?
- Does the Fe(III)-bearing clay minerals exhibit higher Fe(II)/Fe(III) ratios and does reduction-reoxidation in the field result in structural changes or even phase transformations?
- Are these changes linked to the time of paddy cultivation, i.e., by increasingly contrasting redox status of soils?

Field experiments were conducted in which common hydrous Fe(III) oxides of differing crystallinity (ferrihydrite, goethite) and a ferruginous smectite (nontronite) were exposed to alternating redox conditions in subsoil layers along a 2000-year chronosequence of paddy soils for 12 months. Test minerals were analysed for surface properties and possible structural transformation using XRD and  $^{57}\text{Fe}$  transmission Mössbauer spectroscopy at variable temperatures (RT and 4.5 K). To our best knowledge, this is one of the few studies focusing on redox-induced transformations of Fe-bearing minerals under field conditions.

## 4.2 Material and methods

### 4.2.1 Test minerals

Three Fe-bearing minerals were chosen as test minerals: Ferrihydrite and goethite, two hydrous Fe oxides, as well as nontronite, a Fe-rich dioctahedral smectite.

Nontronite was chosen as a representative for Fe-bearing clay minerals. It is a ferruginous smectite (2:1 swelling sheet silicate), occurring in soils mainly as a weathering product of Fe-rich silicates (Eggleton, 1977; Koch et al., 1995). Bulk nontronite N Au-2 from the Uley Graphite Mine (SA, Australia) was purchased from the Source Clays Repository (Purdue, IN, USA). N Au-2 has been shown to be easily reducible by both bacteria (e.g., Jaisi et al., 2005; Jaisi et al., 2007a; Jaisi et al., 2007b; Jaisi et al., 2008a; Jaisi et al., 2005; Schaefer et al., 2011; Yang et al., 2012) and chemical reductants (e.g., Jaisi et al., 2008a). The mineral was

characterised by Keeling et al. (2000). Its composition was calculated as  $M^{+}_{0.72}[Si_{7.55}Al_{0.45}][Fe_{3.83}Mg_{0.05}]O_{20}(OH)_4$ , with M representing the interlayer cations  $Ca^{2+}$ ,  $Na^{+}$ , and  $K^{+}$ , respectively. Infrared spectra indicated that at least some Fe is in tetrahedral coordination (Gates et al., 2002). NAu-2 is generally of high purity; however, it may contain trace amounts of submicron carbonate and Fe oxides. The clay fraction of the bulk samples is >85%. X-ray fluorescence (XRF) revealed that NAu-2 is constituted by 18% of Fe (own observation). The bulk nontronite was gently grounded using an agate mortar (<200  $\mu m$ ). To ensure a homogenous cation exchange complex, the test mineral was subsequently saturated with  $Ca^{2+}$ , using a 1 M  $CaCl_2$  solution. After freeze-drying, the NAu-2 was again grounded and sieved to <200  $\mu m$ .

Ferrihydrite was synthesized (for analysis EMSURE® ACS, Reag. Ph Eur, Merck) by rapid hydrolysis of a 1 M  $FeCl_3 \cdot 6 H_2O$  solution at room temperature and circumneutral pH (synthesis modified according to Schwertmann and Cornell, 2000; successfully applied by Kaiser and Guggenberger, 2007; Hanke et al., 2014). Under constant stirring the pH was raised to 7 with 10 M and 1 M NaOH, respectively. For synthesis of goethite, the same method was used as described for ferrihydrite, however, the pH was raised to 12, followed by aging of the precipitates at 55°C for 24–48 h until their colour had completely changed to ochre. After synthesis ferrihydrite and goethite suspensions were rapidly centrifuged and dialyzed in cellulose tubing (Nalo® Cellulose, porosity of 0.25 to 0.30 nm) against deionised  $H_2O$  until the electric conductivity of the suspension was <40  $\mu S/cm$ . Then, the suspensions were freeze-fried and, if necessary, aggregates were gently grounded, and finally sieved <200 $\mu m$ .

#### 4.2.2 Set-up of field experiments

Six g of nontronite and 8 g of ferrihydrite and goethite, respectively, were filled into bags of polyamide (PA) gauze with a mean mesh size of 20  $\mu m$ . Bags were closed by sewing with threads of different colour, for easier recognition. The mineral bags were then placed horizontally in trenches at 35 cm depth. The bottoms of the trenches were just beneath the plough layers. Two trenches were prepared at each site, in order to have duplicate sets. To prevent soil material entering the mineral bags, they were placed between fine layers (approx. 0.5 cm) of acid-washed, calcinated coarse grained (<1 mm) quartz below and above. Distance between individual mineral bags was at least 20 cm. Trenches were back-filled with respect to the original succession of the soil horizons, including recompaction of the plough layer.

The submerged periods at the paddy fields lasted from June to late October; the rest of the year the fields remained fallow.

### 4.2.3 Sampling and pre-treatment of the test minerals

Test minerals were retrieved 12 months after exposure in the field, after drainage of the paddy fields and rice harvest. Retrieved test minerals were immediately placed in two component Al/PE bags, which were evacuated, flushed with N<sub>2</sub>, and then stored at -20 °C to minimize alterations during transport to the laboratory. Test samples were freeze-dried, weighed, and gently grounded (<200 µm). Samples were stored cool, in the dark and under ambient atmosphere, thus under oxic conditions as under conditions while retrieving, before further analyses.

## 4.3 Characterization of the test minerals

### *X-ray diffraction and Mössbauer spectroscopy*

All test minerals were characterised by X-ray powder diffraction. X-ray diffraction was carried out with a XRD 3000 TT with a graphite secondary beam monochromator and scintillation detector (Seifert, Ahrensburg, Germany), using CuK $\alpha$  radiation ( $\lambda = 0.154178$  nm, 40 kV, 30 mA) in Bragg–Brentano configuration (automatic divergence slit, irradiated sample width: 10 mm; specified measuring range: 10–75 °2 $\theta$ ; step size: 0.03 °2 $\theta$ , dwell time per step: 2 s).

Additionally, structural Fe(II)/Fe(III) ratio and Fe site occupancy of selected nontronite sample (P2000) were analysed using <sup>57</sup>Fe Mössbauer spectroscopy at room-temperature (298 K) and liquid helium temperature (4.2 K). The instrumental set-up was as described in Chapter 3.

### *Specific surface area*

For initial characterisation the specific surface area (SSA) of the minerals before exposure in paddy subsoils was measured by N<sub>2</sub> gas adsorption at 77 K (NOVA 4000, Quantachrome Instruments, Boynton Beach, USA) and calculated according to the Brunauer–Emmet–Teller equation (Brunauer et al., 1938) on the basis of 11 data points in the relative pressure range of 0.05–3.0 p/p<sub>0</sub>. Prior to analysis, samples were degassed at 10<sup>-3</sup> mbar at 40 °C for 48 h.

### *Carbon content*

Total carbon of the test minerals before and after exposure in paddy subsoils was determined by dry combustion at 900 °C with a CNS analyzer (VarioMax, Elementar GmbH, Hanau, Germany). As inorganic carbon (IC) was not detectable, organic carbon (OC) was considered equivalent to TC.

### ***Cation exchange capacity and exchangeable cations***

The nontronite NAu-2 was additionally analysed for its cation exchange capacity ( $CEC_{pH7}$ ) and exchangeable cations at pH 7 before and after exposure in paddy subsoils (Lavkulich, 1981).

## **4.4 Results**

### **4.4.1 Redox and solution conditions during the field experiments**

All paddy soils were characterised by temporal and spatial changes in redox conditions over the course of flooding and drainage. Redox measurements paralleling the exposure of test minerals (Chapter 3) for great part of the experiments indicated that the test minerals were exposed to at least one redox cycle. Mean redox values ranged between +602 and -216 mV at P100, +577 and -249 mV at P700, and +653 and -224 mV P2000, with persisting reducing conditions ( $Eh < 300$  mV) during most time of the study period (see Chapter 5).

Soil solution reaction at the paddy sites prior to flooding was neutral (P2000: pH 6.9) to slightly (P100: pH 8.1) and strongly alkaline (P700: pH 8.9). During submergence pH values remained high; at P700 soil solutions were alkaline, with pH values exceeding pH 8.4. Soil solution pH at the P2000 site increased by about one unit during the first two months of submergence.

Detailed information on redox conditions and soil reaction during the paddy season 2009 are given in Chapter 5.

### **4.4.2 Goethite**

X-ray diffraction indicated the goethite was pure and of moderate crystallinity. It had a SSA of  $44 \text{ m}^2 \text{ g}^{-1}$ . Irrespective of the age of the paddy sites, X-ray diffraction patterns of goethite were identical before and after 12 months of *in-situ* exposure to paddy subsoil conditions (Figure 4-1).

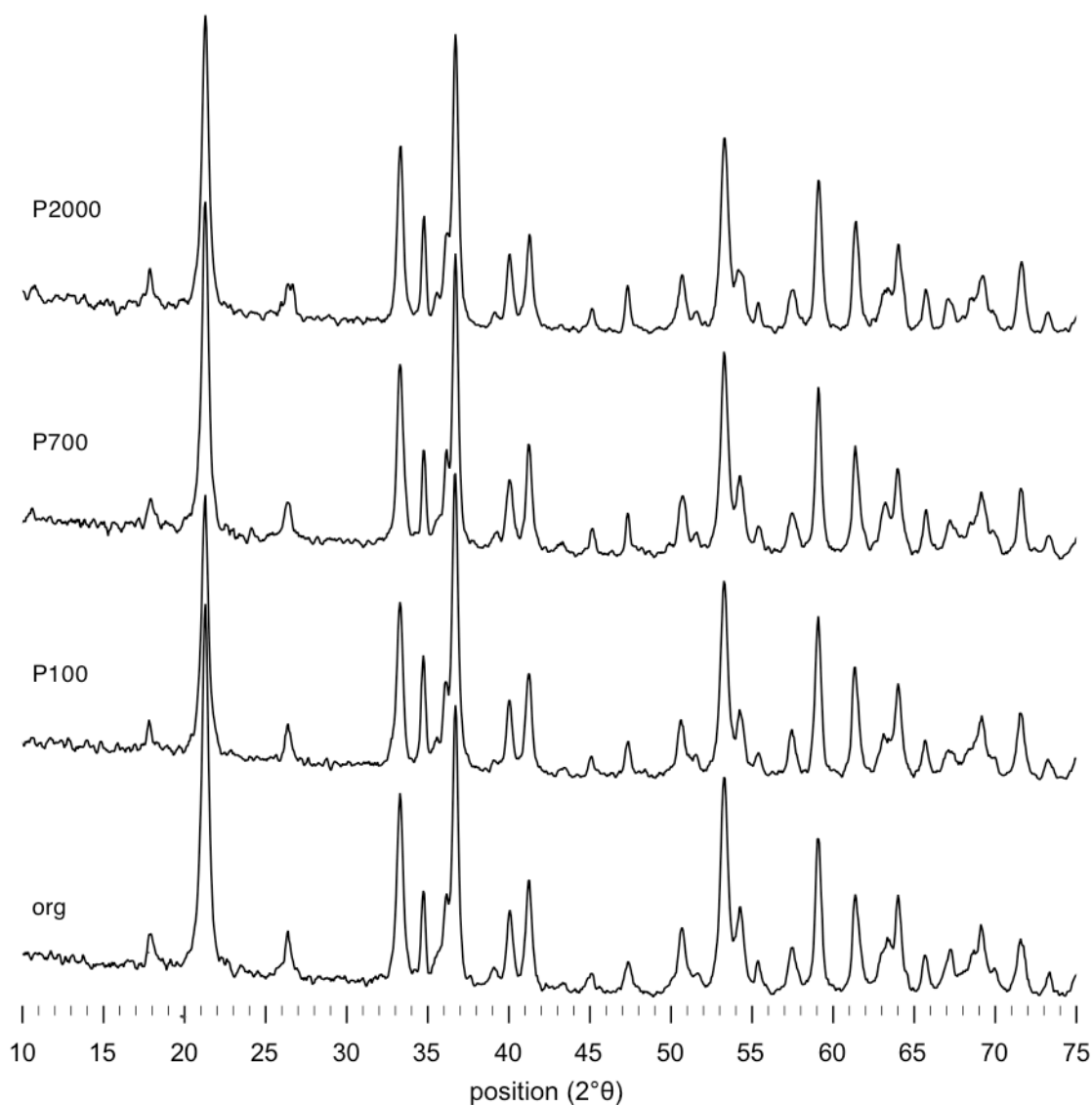


**Figure 4-1:** X-ray diffraction patterns of goethite before (org) and after 12 months exposure in the field at the 100, 700 and 2000 year paddy sites (P100, P700, P2000) (modified according to Vogelsang et al., 2016b).

Mass balance analyses of goethite samples before and after exposure did neither indicate significant gain nor loss of goethite during exposure in the field either. Losses averaged 3.8% weight but included material that could not be retrieved from the netting.

#### 4.4.3 Ferrihydrite

The SSA was  $270 \text{ m}^2 \text{ g}^{-1}$ , which is in accordance with literature data on ferrihydrite ( $200\text{--}400 \text{ m}^2 \text{ g}^{-1}$ ; Cornell and Schwertmann, 2003). X-ray diffraction patterns of the original ferrihydrite (Fh org) showed broad diffraction peaks (Figure 4-2), largely resembling those of 2-line-ferrihydrite. However, some few more pronounced peaks may indicate also the

presence of some 6-line ferrihydrite (e.g., Towe and Bradley, 1967; Chukrov et al., 1973; Schwertmann et al., 1999; Yu et al., 2002; Majzlan et al., 2004; Manceau, 2009). Six-line ferrihydrite normally forms at *elevated* synthesis temperatures (70–80 °C) (Schwertmann and Cornell, 2000). Temperatures during synthesis never exceeded 40 °C, but it cannot be excluded that small areas within the viscous slurry had higher temperatures due to the exothermic reaction of FeCl<sub>3</sub> with NaOH, supporting formation of some 6-line ferrihydrite. Also, the sample may contain trace amounts of poorly crystalline goethite and akaganeite.

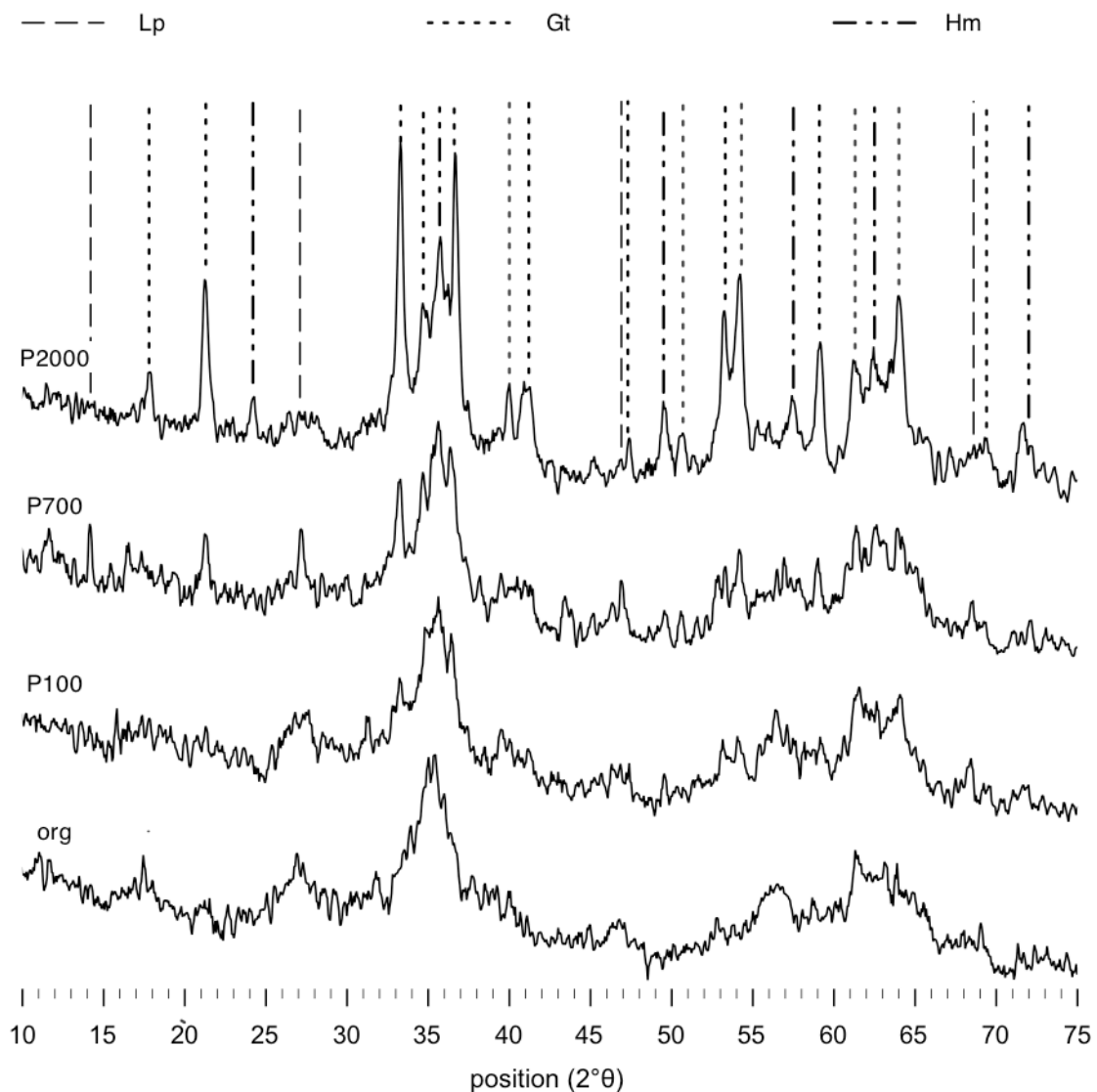


**Figure 4-2:** X-ray diffractions patterns of ferrihydrite before (org) and after 12 months exposure in the field at the 100, 700, and 2000 year paddy site (P100, P700, P2000 ) (modified according to Vogelsang et al., 2016b).

Changes in XRD patterns of the ferrihydrite samples after 12 months field exposure were most pronounced at the oldest paddy site, P2000. They showed numerous signals ascribed to goethite and haematite. At the P100 changes in the XRD pattern were almost negligibly. At the P700 site, XRD patterns indicated the presence of some lepidocrocite as well as of traces of goethite and haematite.

No signal due to clay minerals occurred in the XRD spectra of any of Fe oxide samples, indicating no transport of clay particles into the mineral bags. This supports that iron oxides transformation were result of *in-situ* transformations.

#### 4.4.4 Nontronite

The XRD patterns of the original nontronite were comparable to those by Keeling et al. (2000). The SSA of N Au-2 (<200  $\mu\text{m}$ ) was  $48.5 \text{ m}^2 \text{ g}^{-1}$ . The most obvious alteration of N Au-2 after exposure to paddy subsoil conditions was a distinct change in colour at the mineral surface. All samples of the original brownish coloured N Au-2 were characterised by a green-blue mineral coating (Figure 4-3b) after 12 months in the field.

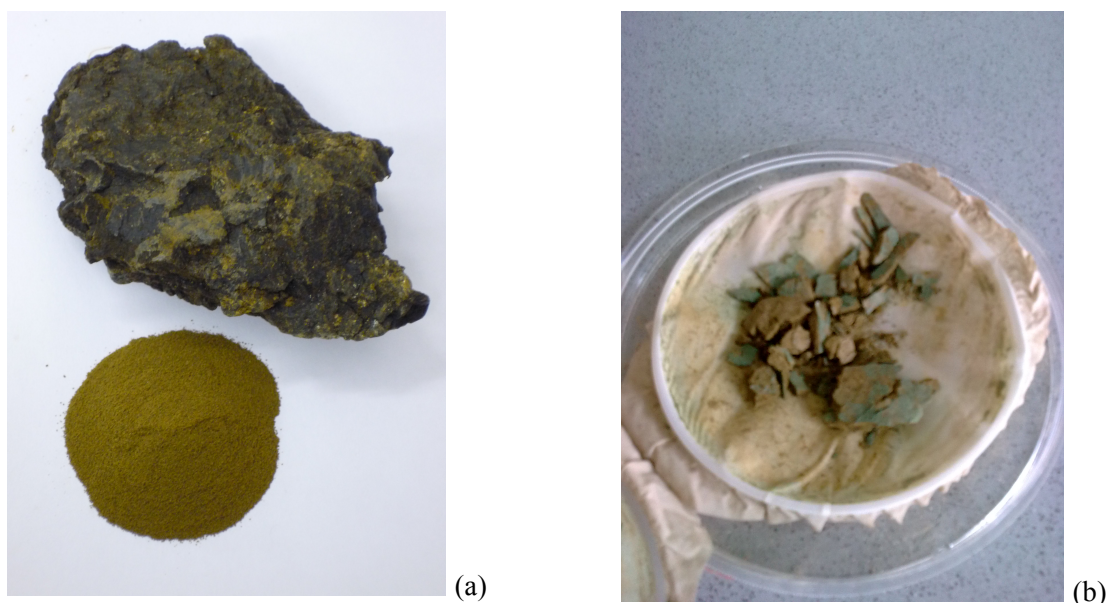


**Figure 4-3:** Unaltered nontronite, bulk and grounded <200  $\mu\text{m}$  (a) and freeze-dried N Au-2 after one year exposure (b) to field conditions at the 2000 year paddy site (P2000).

The colour change was restricted to the surface; the bulk material was not affected. The XRD patterns showed an overall decrease in intensity a slight broadening of signals at  $6.55^\circ 2\theta$  ( $\sim 1.35$  nm) of all NAu-2 samples at the three paddy sites (Figure 4-4). At P700, signal at  $6.55^\circ 2\theta$  showed a slight shift towards higher angles ( $11.87^\circ 2\theta$ ); otherwise XRD patterns remained unchanged. No other mineral phases were detected.

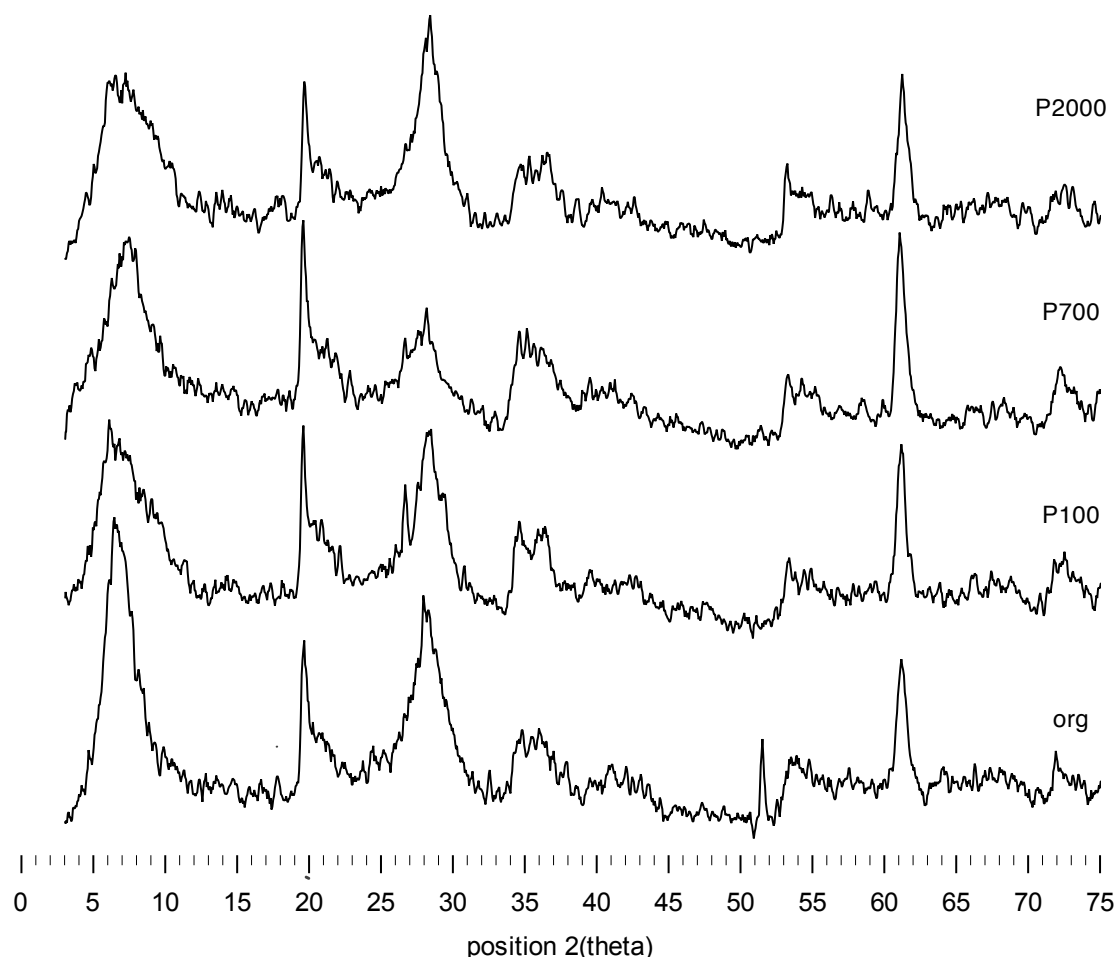


**Figure 4-4:** X-ray diffraction patterns of NAu-2 before (org) and after 12 months exposure in the field at the 100, 700 and 2000 year paddy sites (P100, P700, P2000) (modified according to Vogelsang et al., 2016b).

Additional analyses using Mössbauer spectroscopy at 298 K (RT) of the P2000 nontronite sample before and after exposure revealed spectra consisting of three spectral components (Figure 4-5). These were fitted with Gaussian distributions of quadrupole doublets, each corresponding to a different Fe(III) site occupancy (Table 4-1). The quadrupole doublet with the lowest quadrupole splitting (QS;  $0.21 \text{ mm s}^{-1}$ ) was attributed to octahedral coordinated

ferric Fe in cis-position ( $\text{Oct}_{\text{cis}}$ ). The outer Fe quadrupole doublet with the largest QS ( $1.24 \text{ mm s}^{-1}$ ) was also attributed to ferric Fe in octahedra, but trans-coordinated ( $\text{Oct}_{\text{trans}}$ ). IS of  $\delta = 0.24 \text{ mm s}^{-1}$  and QS of  $\Delta = 0.64 \text{ mm s}^{-1}$  are consistent with tetrahedral ferric Fe (Tet; Cornell and Schwertmann, 2003; Dyar et al., 2006). The abundance of octahedral coordinated Fe as derived spectra at RT was 82%; that of tetrahedral coordinated Fe 18%. Mössbauer measurements at RT did not reveal the presence of ferrous Fe, neither before nor after exposure to paddy cultivation.

The portion of tetrahedral Fe in N Au-2 is slightly higher than reported by Gates et al. (2002), who calculated a maximum content of 12% based on results of NIRS, EXAFS and XRD. Others (Schaefer et al., 2011; Yang et al., 2012) have assigned both octahedral Fe(III) doublets in the N Au-2 spectra to cis-coordinated Fe(III) in different environments (with respect to the tetrahedral chemical composition), as unreduced nontronite is supposed to be trans-vacant (Manceau et al., 2000b; Gates et al., 2002). Also tetrahedral Fe(III) has not always been considered during spectra fitting.

Six subspectra were identified in the Mössbauer spectra of N Au-2 retrieved from the P2000 site at 4.2 K. The spectrum can be fitted with a Gaussian distribution of three quadrupole doublets and three magnetically split sextets. The three quadrupole doublets were assigned to octahedral coordinated ferric Fe in cis- and trans-position as well as tetrahedral coordinated ferric Fe, still paramagnetic at 4.2 K. Magnetically ordered sorbed  $\text{Fe}^{2+}$  and  $\text{Fe}^{3+}$  was not accounted for. Magnetic ordering at low temperatures is typical for Fe-rich nontronites (Ribeiro et al., 2009). Assignment of the sextets was difficult. Magnetic ordering of N Au-2 was also observed by Yang et al. (2012) at 12 K, but no information was given on the assignment of the magnetic hyperfine fields to specific Fe environments. Jaisi et al. (2005), in contrast, did not observe any magnetic ordering at the same temperature. However, differences in magnetic ordering might be due to small variations in the chemical composition and/or the slightly different temperatures at which Mössbauer spectra were recorded (Johnston et al., 1986). Cardile et al. (1986) studied the magnetic ordering in nontronites with different Fe contents at 4.2 and 1.3 K. Some of the nontronites exhibited complex spectra and magnetic ordering at 4.2 K; the spectra were fitted with three overlapping sextets: the sextets with larger magnetic fields (ranging between 50.7 and 41.6 T) were attributed to magnetically ordered Fe(III) in different environments in the octahedral sheet, the sextets with smaller hyperfine field (41.0 to 34.7 T) to Fe(III) to magnetically ordered ferric Fe in tetrahedral sites. A small hyperfine field was assigned to interlayer  $\text{Fe}^{3+}$  (35.9 T). Fitting in line with the ideas of Cardile et al. (1986) resulted in relative peak areas of the sextets and matching doublets at 4.2 K not congruent with the areas of the corresponding  $\text{Fe}^{3+}$  doublets at RT. Thus, assignment of the fitted sextets is still unresolved.

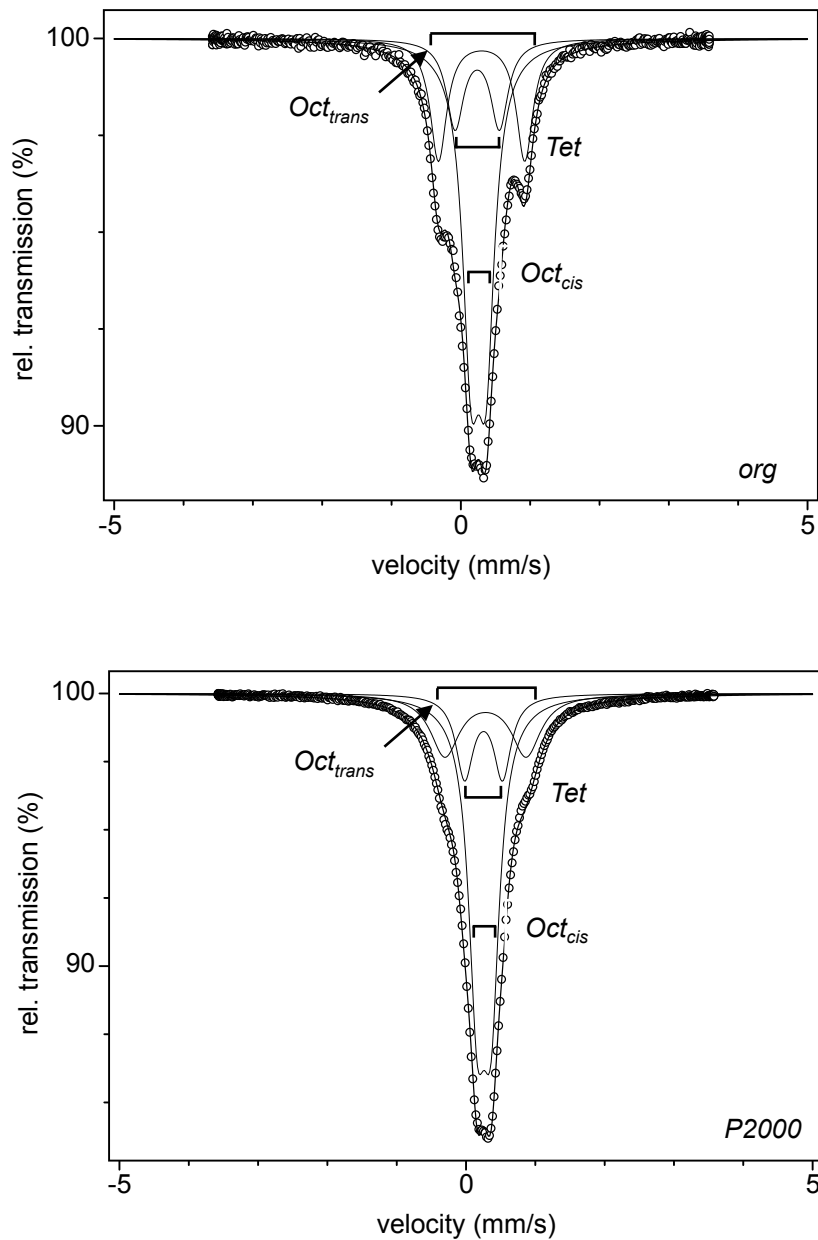


**Figure 4-5:**  $^{57}\text{Fe}$  Mössbauer spectra at room temperature (298 K) of NAu-2 before (org) and after 12 months exposure in the 2000 year paddy subsoil (modified according to Vogelsang et al., 2016b). The solid black line drawn through the data points is the calculated fit. The spectral components are assigned as follows:  $Oct_{trans}$ : octahedral coordinated ferric Fe (trans);  $Oct_{cis}$ : octahedral coordinated ferric Fe (cis);  $Tet$ : tetrahedral coordinated ferric Fe.

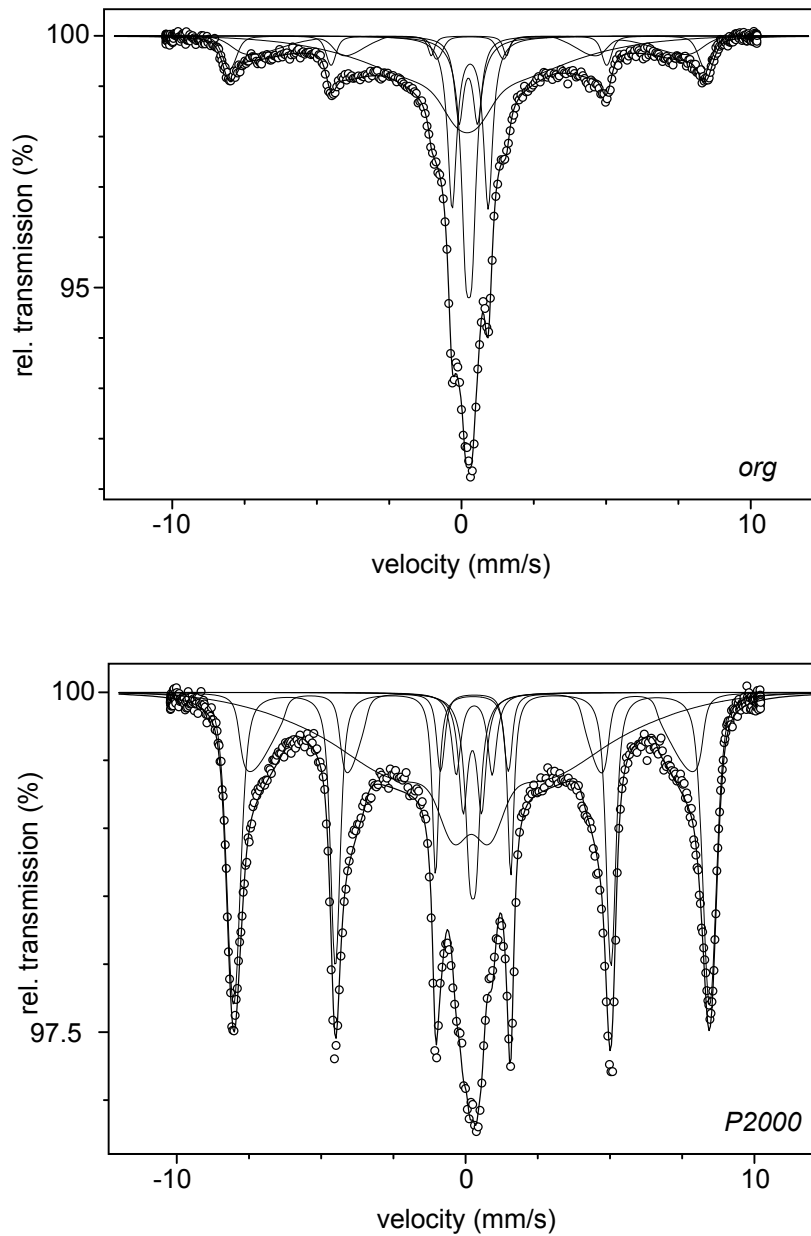


**Figure 4-6:**  $^{57}\text{Fe}$  Mössbauer spectra at 4.2 K of NAu-2 before (org) and after 12 months exposure in the 2000 year paddy subsoil (modified according to Vogelsang et al., 2016b). The solid black line drawn through the data points is the calculated fit.

After exposure to paddy subsoil conditions for one year, a slight change in relative intensities as well as an increase in line width of  $\text{Fe}_{\text{trans}}$  (1.2 to 2.0  $\text{mm s}^{-1}$ ) in the RT spectra of the nontronite sample was observed. No additional spectral components were observed. Mössbauer spectra at 4.2 K revealed a clearly enhanced magnetic ordering in comparison to the original sample, as revealed by the increase in spectral area (approx. 66% before vs. 84% after exposure) and in intensity of the multiple sextets (Figure 4-6). This indicates structural changes and/or phase transformations of NAu-2 upon exposure to paddy conditions. The multiple sextets could not be attributed to any specific mineral phase. Thus, the observed changes in magnetic order rather indicate structural rearrangements within the tetrahedral and octahedral domains (Ribeiro et al., 2009).

**Table 4-1:**  $^{57}\text{Fe}$  Mössbauer parameters, isomer shift (IS) and quadrupole splitting (QS), of the NAu-2 (original) spectrum taken at room temperature (298 K).

Subspectra	Assigned Phase	Mössbauer parameters		
		Area (%)	IS ( $\text{mm s}^{-1}$ ) <sup>a</sup>	QS ( $\text{mm s}^{-1}$ )
Oct <sub>cis</sub>	octahedral coordinated ferric Fe (cis)	58	0.25	0.21
Oct <sub>trans</sub>	octahedral coordinated ferric Fe (trans)	24	0.30	1.24
Tet	tetrahedral coordinated ferric Fe	18	0.24	0.64

<sup>a</sup> given with respect to the  $^{57}\text{Co}$ -Rh source; to refer to  $\alpha$ -Fe add 0.11 mm/s

Reduction of structural Fe(III) in the octahedral sheet of the clay mineral might lead to an imbalance of the overall electric charge, and thus, an increase in the layer charge and increasing CEC (Stucki et al., 2002; Stucki, 2011; Favre et al., 2002; Favre et al., 2004). However, no distinct changes in  $\text{CEC}_{\text{pH}7}$  of NAu-2 samples exposed to field conditions at the three paddy sites (Table 4-2) could be observed. Differences were only observed with respect to the exchangeable cations. Obviously one year of paddy cultivation and the concurrent changes in redox conditions had no sustainable or measurable effects on the exchange capacity of NAu-2.

**Table 4-2:** Cation exchange capacity at pH 7 ( $\text{CEC}_{\text{pH7}}$ ) and exchangeable cations of the original sample ( $\text{Ca}^{2+}$ -exchanged) and the N Au-2 samples after 12 months in the field at 100, 700, and 2000 year paddy sites (P100, P700 and P2000).

NAu-2 sample	$\text{CEC}_{\text{pH7}}$	$\text{Ca}^{2+}$	$\text{K}^+$	$\text{Mg}^{2+}$	$\text{Na}^+$
original	572.4	564.4	1.9	3.6	2.5
P100	585.9	256.9	2.3	306.5	20.2
P700	609.8	352.5	1.3	238.6	17.4
P2000	560.1	385.1	1.4	166.6	6.9

The composition of the exchangeable cations clearly reflected the soil solution composition at the different paddy sites (Chapter 5). The share of  $\text{Na}^+$  and  $\text{Mg}^{2+}$  decreased with age and distance from the coast.

#### 4.4.5 Organic matter adsorption

Little accumulation of OC to the test minerals exposed to paddy subsoil conditions was observed; differences between the different sites were small. Largest OC contents were determined for ferrihydrite, ranging between 0.5 and 0.7% OC. Organic carbon contents of goethite and nontronite were generally below 0.2%.

### 4.5 Discussion

#### *Goethite is not affected by environmental conditions in the studied paddy subsoils*

Goethite revealed no structural changes upon exposure to paddy subsoil conditions at the three test sites. One reason could be OM sorbed to Fe oxide surfaces, preventing microbial reduction of structural ferric Fe and/or reaction with  $\text{Fe}^{2+}$ . However, no strong OM accumulation was found. More likely, the given environmental conditions disfavoured redox-induced structural changes (see also Chapter 3). The Eh and pH values in the soil solution at the three paddy sites were mostly in the range of the stability of goethite.

#### *Ferrihydrite is transformed to goethite, haematite, and lepidocrocite, with more pronounced changes at older paddy sites*

During 12-months of exposure to paddy subsoil conditions, ferrihydrite was partly converted to goethite and haematite, with the most distinct changes occurring at the oldest paddy site, P2000. At P700 site, also lepidocrocite was found.

Assuming that ferrihydrite serves as a precursor for both haematite and goethite, there are two possible transformation processes conceivable, depending on the redox conditions

predominating. At oxic conditions, haematite is formed from ferrihydrite through aggregation–dehydration rearrangement in the presence of water at circumneutral pH (Cornell and Schwertmann, 2003). In contrast, dissolution of ferrihydrite is prerequisite for goethite formation, and thus, dependent on the solubility of ferrihydrite, which is lowest at pH 7 to 8 (Cornell and Schwertmann, 2003). Outside that pH region, a mixture of haematite and goethite may form (Cornell and Giovanoli, 1985; Cornell et al., 1989). Soil solution pH at the test paddy sites at 35 cm depth prior to flooding ranged from neutral 6.9 (P2000) to 8.9 (P700). At such high pH values, haematite is thought to be the dominant transformation product under oxic conditions. However, throughout the experiment period, the three paddy sites were mostly characterised by reducing conditions. Under such conditions, Fe(II) released may serve as catalyst for recrystallisation of solid hydrous Fe(III) oxide phases, i.e., by Fe<sup>2+</sup>-stimulated dissolution of the Fe(III) oxides and subsequent recrystallisation, and/or solid state transformations (Jeon et al., 2001; Jeon et al., 2003; Hansel et al., 2003; Williams and Scherer, 2004; Pedersen et al., 2005). In result, transformation of ferrihydrite to thermodynamically more stable phases, such as goethite, haematite, and magnetite (Liu et al., 2007; Hansel et al., 2003; Jeon et al., 2003; Jones et al., 2009) as well as lepidocrocite (Pedersen et al., 2005; Liu et al., 2007) may prevail over dissolution.

Organic–mineral interactions were of little importance for transformation processes. Only little OM was accumulated (max. 0.7% OC for ferrihydrite), despite of concentrations of dissolved organic carbon (DOC) up to 30 mg l<sup>-1</sup> in soil solution of the upper paddy subsoil, directly beneath the plough pan. Obviously the high solution pH (6.9 to 8.9) hampered strong sorptive interaction between DOM and Fe oxides and thus, transformation of ferrihydrite into disordered organic–mineral composites was negligible.

Comparing the three study sites, changes in the mineral composition were most pronounced for the oldest paddy sites. Concentrations aqueous of Fe<sup>2+</sup> in the soil solution were low (<0.1 mmol l<sup>-1</sup> aqueous Fe) at all three paddy sites, with largest concentrations of soluble Fe occurring at the older paddy sites (see Chapter 5). Solution conditions (Eh/pH) at P2000 favoured dissolution of poorly crystalline Fe oxides, concomitant ferrous Fe production and hence, mineral transformations catalysed by Fe(II). The younger paddy sites, P100 and P700, were characterised by alkaline soil reactions (Chapter 5), due to irrigation with sodium-rich water, thus, reducing the availability of most Fe oxides to microbial reduction.

At constant pH and alkalinity, Fe(II) concentrations largely govern the formation of secondary solids. According to Liu et al. (2007), higher pH values support the adsorption of Fe<sup>2+</sup> and thus, solid state transformation of ferrihydrite to haematite; at lower pH values lepidocrocite and goethite formation are favoured via dissolution–reprecipitation mechanisms. At Fe(II) small concentrations, ferrihydrite tends to transform to lepidocrocite and goethite (Hansel et al., 2003). The presence of chloride supports the conversion of ferrihydrite to lepidocrocite at circum neutral pH following the abiotic reaction of Fe(II) with ferrihydrite;

sulfate supports both goethite and lepidocrocite formation (Hansel et al., 2005). Concentrations of sulfate in the soil solutions (see Chapter 5) were similar at the three paddy sites. However, for chloride, concentrations at P700 (2.25 to 5.10 mmol l<sup>-1</sup> at 35 cm) were almost double in comparison to those at P2000. The higher chloride concentrations at P700 may have supported the formation of some lepidocrocite at P700.

Independent of the ligand, increasing Fe(II) concentrations (aqueous Fe<sup>2+</sup> >0.3 mmol l<sup>-1</sup>; Hansel et al., 2003) favour magnetite formation (Benner et al., 2002; Zachara et al., 2002). However, concentrations of aqueous Fe were small in the study soil solutions, which can explain why no magnetite was detected in any of the ferrihydrite samples.

### ***Nontronite is characterised by structural modifications particularly in the surface region***

Favre et al. (2006) compared the redox properties of structural Fe in Fe oxides and ferruginous smectites and showed that structural Fe in clay minerals might be reduced prior to Fe in oxides. Gorski et al. (2013) demonstrated that the onset of chemical reduction of structural Fe(III) in N Au-2 is at about Eh = 0 mV and pH 7.5, with sharply increasing Fe<sup>2+</sup>/Fe<sub>total</sub> ratios at Eh values <-200 mV; the total Eh range where N Au-2 was “redox-sensitive” was about 600 mV. Re-oxidised samples of N Au-2 were even more easily reducible, i.e., at higher Eh values than the original material. It can be assumed that at the given pH/Eh values the nontronite samples were at least partly reduced during submergence and reoxidised after drainage and/or excavation.

The most obvious difference between the original test mineral and those samples exposed to paddy subsoil conditions was the change in surface colour. Changes of bulk colour are sensitive indicators for structural modifications of ferruginous smectites. Upon chemical and bacterial reduction the colour of ferruginous smectite suspensions alter (e.g., Komadel et al., 1990; Stucki, 2006). Changes in colour upon reduction–reoxidation of structural Fe were ascribed to structural rearrangements, and thus, changes in Fe<sup>3+</sup> ligand field transitions (Sherman and Vergo, 1988). The colour of ferruginous smectite changes with increasing level of reduction from 0 to 92% from yellow-brown to green, blue-green, blue and grey (Komadel et al., 1990). Even though these changes are normally reversed upon reoxidation, UV/VIS spectra of unaltered and reoxidised sample may still differ considerably (Komadel et al., 1990; Stucki, 2011): Structural rearrangements upon reduction, as opposed to the visible colour changes, are not fully reversible. The surface colour after exposure to paddy cultivation was blue-green. A change from brown to blue-green was also observed for moderately reduced smectite in suspension (Komadel et al., 1990; Merola and McGuire, 2009; Schaefer et al., 2011; Benzine et al., 2013) and attributed to Fe(II)–Fe(III) pairing (Cornell and Schwertmann, 2003) and Fe(II)-O-Fe(II) groups (Komadel et al., 1990), respectively. Mössbauer analyses at RT of the P2000 sample though did not reveal structural Fe(II), however, at these temperatures Fe(II) contents of (partly) reduced Fe-rich smectites

may be underestimated (Schaefer et al., 2011). In the 4.2 K spectrum, no Fe(II) doublet was detectable either, and so it is assumed that no Fe(II) was present or below the detection limit of Mössbauer spectroscopy (1–3% Fe). The observed colour change was restricted to the surface area; the unaltered bulk material might have diluted ferrous Fe contents of the whole sample, thus, hampering detection by Mössbauer spectroscopy. Based on the methods applied the observed surface colour changes cannot conclusively be explained. Nevertheless, they are strong indicators for structural modifications in the surface region. Additional measurements with more surface sensitive methods, such as X-ray photoelectron spectroscopy (XPS) and/or X-ray adsorption spectroscopy (XAS), could give additional information on the surface composition (i.e., oxidation and structural state of Fe), and thus, reveal nature and origin of the observed colour change.

Selective Mössbauer analyses of the sample retrieved from the P2000 subsoil indicated structural changes after exposure paddy conditions, i.e., changing redox conditions. Increased magnetic hyperfine interactions as deduced from multiple sextets in the 4.2 K Mössbauer spectra indicate increased magnetic ordering in comparison to the original test mineral. Ferrous Fe released upon microbial reduction of N<sub>Au</sub>-2 is adsorbed on highly reactive surface sites (Yang, 2010), especially at pH >6.8 (Schultz and Grundl, 2004); sorbed Fe(II) might be rapidly oxidised within hours upon exposure to oxygen, whereas the oxidation rate of structural Fe(II) is much slower (~300h) (Yang et al., 2012). Under reducing conditions, Schaefer et al. (2011) found formation of lepidocrocite upon oxidation of sorbed ferrous Fe via interfacial electron transfer from structural Fe(III). As the samples were analysed under oxic conditions, any ferrous Fe sorbed to the exchange complex was most likely oxidised, possibly leading neof ormation of Fe oxide phases, and thus, to enhanced magnetic ordering. However, the Mössbauer parameter (shape and magnetic field) of the sextets could neither be assigned to any mineral phase documented in literature. X-ray diffraction measurements neither provided evidence of any Fe mineral phase. Exposure of nontronite to field conditions obviously did not favour *in-situ* formation of new mineral phases. If sorbed Fe itself orders magnetically remains unclear (Johnston et al., 1986). According to Gangas et al. (1985), also intercalated Fe might increase magnetic ordering of ferruginous smectites due to magnetic coupling between the intercalated Fe atoms and the Fe atoms bound in tetra- and octahedral coordination within the clay lattice. However, intercalation by Fe increases basal spacing (Gangas et al., 1985), thus, causing changing peak position in XRD. No such changes, however, occurred. The XRD pattern of N<sub>Au</sub>-2 after exposure to paddy cultivation showed a general decrease in intensity and a slight broadening of the 7 °2θ peak (001 reflection). Jaisi et al. (2008a) reported release of structural Fe(II) and subsequent dissolution of nontronite (N<sub>Au</sub>-2) with increasing level of chemical reduction, going along with decreasing crystallinity of the residual (reduced) nontronite, discernible by the broadening of the 001 peak. It is assumed that the increase of the magnetic interactions in the sample retrieved from the P2000 subsoils is not due to a distinct mineral phase but an intrinsic feature of the reduced

and reoxidised nontronite. According to Stucki (2011), increase in magnetic ordering indicates irreversible changes of the bonding relationships between the structural ferric Fe ions. Increasing magnetic ordering in the Mössbauer spectra has been observed upon microbial reduction for Garfield nontronite and NAu-2 (Yang et al., 2012; Ribeiro et al., 2009, respectively). The increase in magnetic hyperfine interactions was attributed to the increase of magnetically ordered domains (structural Fe present in clusters) within the crystal structure; so far no structural models were found to fit such Mössbauer spectra (Ribeiro et al., 2009). Upon reoxidation, the structural changes were completely reversed. In the same study, irreversible magnetic ordering upon redox cycling (reduction and reoxidation) was only observed for the extensive abiotic reducing of nontronite and was ascribed to Fe migrating from cis- to trans-octahedral sites during structural Fe(III) reduction (Manceau et al., 2000a). To our best knowledge, this is the first time an irreversible increase in magnetic ordering after one full redox cycle has been observed upon biotic reduction. However, that observation remains to be verified by additional analyses. Also, it remains unclear if the increased magnetic ordering is directly related to the surface colour change.

#### **4.6 Conclusion**

Well-crystalline hydrous Fe oxide, i.e., goethite, did not show any changes within one year of exposure in the paddy soils. Likely, the neutral to weakly alkaline pH conditions in the study soils prevented microbial reduction and subsequent dissolution and/or transformation. Clear changes were found, however, for ferrihydrite. The time under paddy management, i.e., the redox status of the study soils, had strong influence of ferrihydrite transformation. With increasing time of paddy cultivation, more crystalline Fe oxides, such as goethite and haematite, and partly lepidocrocite, were formed, most likely due to solid state transformation induced by Fe(II). At the youngest paddy site, just 100 years under paddy management, high pH and relatively high salinity, impede transformations of Fe oxides. Thus, time under paddy management, i.e., the redox status of the study soils, had strong influence of ferrihydrite transformation. Organic–mineral interactions were only of little importance for transformation processes of the hydrous Fe oxides in paddy subsoils; this is consistent with relatively small concentrations of OC in the soil solution. In contrast to Fe oxides, for nontronite no neoformation of other mineral phases occurred. X-ray diffraction patterns (broadening of the 001-peak), surface colour change, as well as the increased magnetic ordering in the Mössbauer spectra at 4.2 K indicate structural modifications, especially in the surface region, upon exposure to paddy conditions. Such structural changes have been observed before only when exposing nontronite to harsh chemical reduction. However, seemingly also biotic reduction under natural conditions can induce similar transformations within little time.

## 5. Redox conditions and soil solution composition as related to the time of paddy cultivation

### 5.1 Introduction

Flooding and subsequent changes in the redox status results in major biogeochemical changes in the soil (Ponnamperuma, 1972; Kirk, 2004) and colloid chemistry (Thompson et al., 2006). Redox processes can trigger mineral transformations, thus, can control the mobility and cycling of various elements, of nutrients, and DOM. The soil solution composition relates closely to the prevailing redox conditions (Bücher, 2001; Tanji et al., 2003; Zhou et al., 2005). Both redox status and the related composition of the soil solution of paddy fields are important for vertical distribution of nutrients (Katoh et al., 2004a; Katoh et al., 2004b) as well as losses to the groundwater (Chae et al., 2004; Chae et al., 2009; Choi et al., 2013). In the topsoil of paddy soils, redox processes relate directly to management, which involves irrigation, puddling, and the formation of the plough pan (Kyuma, 2004). As flooding generally occurs from above, the paddy topsoil is fully saturated during most of the cropping season and reducing conditions prevail (Kyuma, 2004). Knowledge on redox conditions and the soil solution of paddy soils, especially in the subsoil, is limited.

Water saturation and reduction in the subsoil depends on numerous factors, such as water and soil management, soil structure and texture, bulk density and, thus, its permeability (Janssen and Lennartz, 2007) and percolation rate as well as groundwater levels (Wickham and Singh, 1978). The magnitude of reduction in the subsoil does not only depend on the water status, but also on the redox capacity (oxidizing vs. reducing capacity), i.e., the abundance and availability of electron donors (i.e., degradable organic compounds) and acceptors (i.e., reducible nitrate, manganese and iron oxides, sulfate and organic substrates) of the specific soil (Achnich et al., 1995). In most paddy soils, Fe(II)/Fe(III) is the most important redox couple (Ponnamperuma, 1972). Batch and field experiments with paddy soils showed that iron reduction highly influences carbon metabolism, i.e., CO<sub>2</sub> production (Yao et al., 1999) and CH<sub>4</sub> emission (Jäckel and Schnell, 2000; Jäckel et al., 2005). Thus, both availability and distribution of the Fe minerals should have direct influence on the soils redox capacity and, in consequence, the magnitude of redox changes in paddy soils. It has been shown that with increasing time of paddy cultivation the depth distribution of electron donors and potential acceptors becomes more distinct (e.g., Gong, 1983; Cheng et al., 2009; Chen et al., 2011; Kölbl et al., 2014): Reduced Fe and Mn species (dissolved Fe<sup>2+</sup>, Mn<sup>2+</sup>) may be leached from the top into the subsoil with water moving downwards (Gong, 1983). In soil zones with higher redox potentials, they can be reoxidized and precipitated as hydrous Fe/Mn oxides. This leads to a redistribution of redox-sensitive elements such as Fe and Mn within the soil column, causing depletion of topsoils and enrichment of Fe/Mn in underlying horizons. The

study on changes in Fe minerals (Chapter 3) upon long-term paddy cultivation showed that there is a clear profile differentiation with regard to the crystallinity of Fe oxide phases, i.e., poorly crystalline, and hence, easily reducible Fe oxides are the dominant phase in the topsoil, whereas more crystalline Fe oxides become enriched in the subsoil. Horizons low in easily reducible Fe minerals (or other alternative electron acceptors) may have a reduced Eh buffering capacity, in those with larger contents the Eh buffering capacity should be greater (Reddy and DeLaune, 2008). Quality and degradability of OM control redox processes in soils (Johnston et al, 2009). The accumulation of OM in paddy topsoils, and hence, the abundance of electron donors can accelerate the establishment of reducing conditions after flooding (Xu et al., 2000) and controls the overall intensity of redox reactions (Hutchinson and Hesterberg, 2004). To what extent the distribution patterns are not only a result but also drivers of redox reactions in paddy soils under long-term management is not fully known.

In a field study on irrigated rice fields in the Senegal, Boivin et al. (2002) observed periodic changes in the soil solution chemistry of the topsoils. The soil solution composition followed the redox status of the soil and hence, reflected the actual cropping season. Many redox-sensitive species, i.e., Mn, Fe, nitrate and sulfate, are stable under aerobic (oxidizing) conditions; upon the establishment of anoxic (reducing) conditions, however, they undergo reduction and become released into solution (e.g., Ponnampereuma, 1972; Reddy and Patrick, 1976; Kirk, 2004). The rate of reductive dissolution of Fe phases depends on the solubility of the solid Fe phases (Bonneville et al., 2004) and on OM availability and quality (Ratering and Schnell, 2000; Tanji et al., 2003; van Asten et al., 2004; Gao et al, 2004). Poorly crystalline Fe oxides, i.e., ferrihydrite, release  $\text{Fe}^{2+}$  more easily and rapid than the more crystalline oxides, mainly due to their less ordered nature and higher specific surface area (Roden and Zachara, 1996). Soluble Fe(II) and Mn(II) are often adsorbed in exchange for  $\text{Mg}^{2+}$  and  $\text{Ca}^{2+}$  (Brinkman, 1969/1970; Kyuma, 2004), thus, causing increases in electric conductivity (EC) of the soil solution and nutrient losses to the groundwater. Consequently, the soil solution composition under anaerobic conditions is, at least partly, controlled by the mineral assemblage of the soil.

The objective of the study was to elucidate changes in redox potential and subsequent changes in the composition of the soil solution as related to time of rice cultivation. The focus was on redox-sensitive elements (Fe, Mn, sulfate etc.) and dissolved carbon in the subsoil. Following research questions were addressed:

- Does the time span of paddy cultivation, along with progressing depth differentiation of redox sensitive elements and OM, result in significant changes in redox response to flooding and drying?
- Is the soil solution composition a mirror of the redox status of the soil?
- Are (re)distribution patterns of Fe(III) oxides and OM upon paddy cultivation reflected by the composition of the soil solution?

To monitor changes in soil redox conditions and composition of the soil solution redox electrodes and suction cups were installed in subsoil horizons of paddy and non-paddy under cultivation for 100, 700 and 2000 years. In addition, redox conditions were monitored in the topsoil during the first two weeks after flooding. Sampling of soil solutions was done parallel to readings of the redox potentials during one entire paddy–winter crop cycle (March 2009 to March 2010). Soil solutions were analysed for pH, electrical conductivity and Na, Ca, K, Mg, Li, Fe, Mn, Al, Si, Cl, sulfate, phosphate, nitrite/nitrate, ammonium, dissolved inorganic carbon, and dissolved organic carbon.

## 5.2 Material and methods

### 5.2.1 Set-up of field experiments

Redox electrodes (Pt electrodes) and suction cups (porous cup: 0.45- $\mu$ m PA membrane filter/porous PE substructure and cover shield; ecoTech GmbH, Bonn, Germany) were installed horizontally from soil pits at 35 and 55 cm depth at 100, 700 and 2000 year paddy (P100, P700, P2000) and non-paddy sites (NP100, NP700). Suction cups and redox electrodes were placed at about 50 cm distances from the pit wall to avoid disturbance. Pits were back-filled after installation of instruments. All sites were equipped with 5 electrodes and 4 suction cups per depth, respectively. Equipment was installed half a year before measurements started to allow for equilibration. Additional Pt electrodes (4 per site) were installed vertically at 10 cm depth during the first three weeks after submergence.

Redox potentials were monitored during one entire paddy–winter crop cycle (March 2009 to March 2010) in subsoils. Redox values in the puddled horizon were only studied during the first three weeks after submergence; afterwards the redox electrodes had to be removed to allow for regular management of the paddy topsoils. Redox measurements were done manually daily during the first three weeks after flooding and during drainage, and biweekly during the rest of the measurement period, using a portable pH/Eh meter. Redox data was corrected for the potential of a standard hydrogen electrode by adding 213 mV (20 °C, Fiedler et al., 2007) to the experimental values.

Soil solutions were obtained for 60 days after flooding of the paddy fields at the end of May/beginning of June 2009, daily during the first two weeks and afterwards at weekly and biweekly intervals. The suction cups were connected by PTFE tubes (diameter 1 mm) to 1000 ml PE sampling bottles placed at soil surface. 0.5 hPa of suction was applied to the suction cups using a hand-operated vacuum pump. Sampling was done one day after vacuum application. Soil solutions were stored at –18 °C until analysis.

### 5.2.2 Analysis of soil solution

The pH of the soil solutions was measured using a pH electrode (pH/Cond 340i, WTW); electric conductivity was determined using an EC meter (pH/Cond 340i, WTW).

Total element contents (Ca, Mg, K, Na, Al, S, Si as well as Fe and Mn) were measured with ICP-OES (Ultima 2, Horiba Jobin-Yvon S.A.S., Longjumeau, France) after acidification with concentrated HNO<sub>3</sub> (pH ≈ 1). It was not possible to directly measure Fe<sup>2+</sup> as reoxidation during sampling could not entirely be excluded. Thus, it is assumed that dissolved Fe<sub>t</sub> and Mn<sub>t</sub> were in reduced state (Fe<sup>2+</sup>/Mn<sup>2+</sup>), however, it cannot be excluded that dissolved Fe<sub>t</sub> also comprises colloidal Fe, such as Fe(III) oxides and/or Fe(III)–OM complexes. These complexes may be formed upon rapid oxidation of aq. Fe<sup>2+</sup> in the presence of oxygen and dissolved organic complexing agents (Liang et al., 1993a; Liang et al., 1993b; Ratering and Schnell, 2000; Rancourt et al., 2005). Total dissolved organic (DOC) and inorganic carbon (DIC, i.e., CO<sub>2aq</sub>, H<sub>2</sub>CO<sub>3</sub>, HCO<sub>3</sub><sup>-</sup>, CO<sub>3</sub><sup>2-</sup>) were analysed with a carbon analyser (DIMA-TOC 100, Dimatec, Germany).

Prior to analysis of nitrate, ammonia and sulfate, the soil solutions were filtered through a 0.1 µm polysulfonate membrane filters (SUPOR-100, Pall Science, Ann Arbor, MI, USA). Nitrite/nitrate (NO<sub>2/3</sub><sup>-</sup>) and ammonium (NH<sub>4</sub><sup>+</sup>) were analysed photometrically using a continuous flow analyser (San++ CFA, Skalar, Netherlands). Sulfate (SO<sub>4</sub><sup>2-</sup>), phosphate (PO<sub>4</sub><sup>2-</sup>) and chloride (Cl<sup>-</sup>) contents were determined by ion chromatography (DIONEX DX-120, Dionex Cooperation, Sunnyvale, CA, USA).

Most soil solutions had precipitates after defrosting. The composition of these precipitates was tested by analysing an aliquot of the filtered soil solution for total element and carbon contents. Comparison of elemental concentrations in unfiltered and filtered soil solutions revealed that precipitation primarily affected DIC, as well as Fe, Mn, and Ca. Likely, DIC and Ca precipitated into CaCO<sub>3</sub> due to decreasing pCO<sub>2</sub> upon sampling and sample treatment (Suarez, 1987). Precipitation of Fe and Mn could be either due to oxidation during sampling or coprecipitation with CaCO<sub>3</sub> (Schwartz and Miehlich, 1993), respectively. The relatively large DIC content of precipitates hints at the latter.

No or only very little (<50 ml) soil solution could be acquired during the whole sampling campaign (June–August 2008) at the non-paddy sites. Therefore, only the soil solution composition of the paddy sites will be presented and discussed in the following chapters.

### 5.2.3 Alkalinity and sodium adsorption ratio (SAR)

According to Stumm and Morgan (1996) for a carbonate system alkalinity is defined as

$$[Alk] = [HCO_3^-] + 2[CO_3^{2-}] + [OH^-] - [H^+]$$

with respect to the reference species H<sub>2</sub>CO<sub>3</sub>\* (defined as the sum of H<sub>2</sub>CO<sub>3</sub> and CO<sub>2aq</sub>) and H<sub>2</sub>O.

An alternative definition of alkalinity can be derived when considering that alkalinity and charge balance of natural water are closely related (Stumm and Morgan, 1996; Zeebe and Wolf-Gladrow, 2001). Alkalinity can then be defined as the sum of the conservative cations ( $C^+$ ) minus the sum of the conservative anions ( $A^-$ ).

$$[Alk] = [C^+] - [A^-]$$

Accordingly, alkalinity was calculated using following formula:

$$[Alk] = [Na^+] + [K^+] + 2[Ca^{2+}] + 2[Mg^{2+}] + [NH_4^+] - [Cl^-] - 2[SO_4^{2-}] - [NO_3^-]$$

The calculation does not comprise phosphate species and organic acids. Phosphate species were generally below detection limit and, thus, were not included in the alkalinity calculation. According to Kirk (2004) organic acids do not contribute much to the charge balance of solutions of submerged soils. In accordance, organic acid concentrations in the analysed samples did not exceed 0.7 mmol and were therefore neglected.

The sodium adsorption ratio (SAR) was calculated, based on the concentrations in  $mg\ l^{-1}$ , as

$$SAR = \left[ \frac{Na}{23} \right] / \left[ \frac{Ca}{40} + \frac{Mg}{24} \right]^{1/2}$$

where 23, 40 and 24 are the atomic weights of  $Na^+$ ,  $Ca^{2+}$  and  $Mg^{2+}$ , respectively (Evangelou, 1998). The magnitude of SAR reflects the relative amount of sodium with respect to Ca and Mg in soil water.

## 5.2.4 Statistical Analysis

Boxplots were prepared with R 2015 (R Core Team, Vienna, Austria) with the end of the whiskers reaching to the lowest and highest datum still within 1.5 IQR of the lower and upper quartile, respectively (*Tukey* boxplot); data not included between the whiskers is defined as outliers and depicted as unfilled circles.

Pearson correlations (two-sided) were carried out with IBM SPSS Statistics vers. 20 (IBM, Armonk, NY, USA).

## 5.3 Results

### 5.3.1 Redox conditions

Redox changes over one entire paddy-winter crop cycle of paddy and non-paddy sites are shown in Figure 5-2 (35 cm, upper subsoil) and Figure 5-3 (55 cm, lower subsoil). All paddy soils were characterised by temporal and spatial (vertical and horizontal) changes in redox conditions over the course of flooding and drainage. Throughout the year, mean redox values ranged between +602 and -216 mV at P100, +577 and -249 mV at P700 and +653 and -224 mV at P2000, respectively. Changes in redox conditions were most pronounced during the first 60 days after flooding (Figure 5-1). All paddy topsoils were already moderately reduced

(according to Zhi-Guang, 1985) with Eh values  $\leq 150$  mV before submergence. Mean redox values at 10 cm depth ranged between  $-96$  (P100) and  $13$  mV (P700) the day before flooding; no data was available until day 5 after flooding for P2000. In contrary, subsoils were mainly characterised by oxic conditions. Only the lower subsoil (55 cm) of P100 was weakly reduced (Eh  $< 250$  mV) before flooding, indicating an already largely water-saturated soil column. It is assumed that was due to the higher groundwater level, which was at about 55 cm depth before rice cropping started (June 2008).

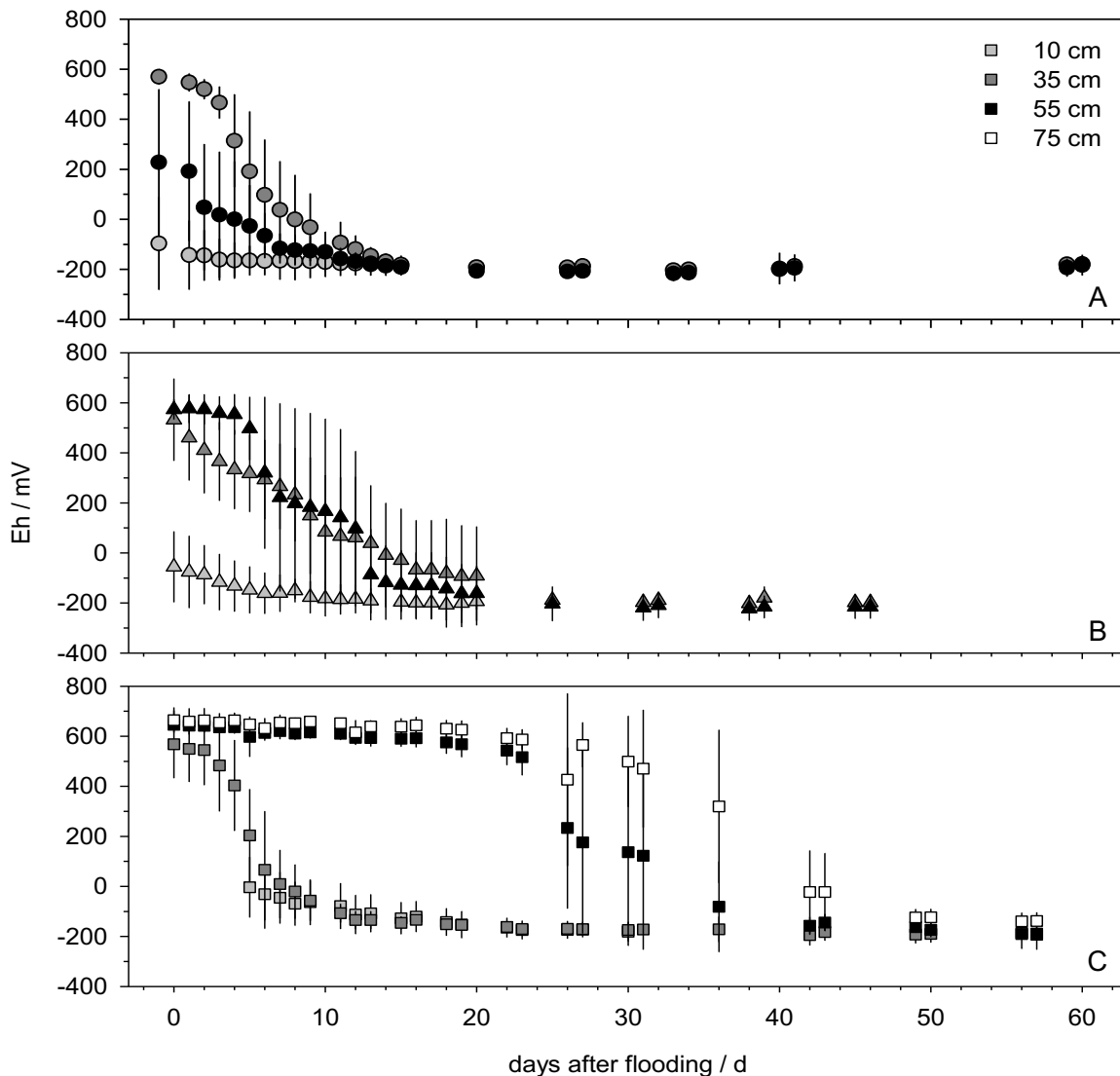


**Figure 5-1:** Redox conditions during the first 60 days after flooding at the 100 (A), 700 (B) and 2000 (C) year paddy sites. Data points are means of max. five replicates; error bars are one standard deviation.

During the initial period of submergence, redox potentials showed high spatial variability. Changes in Eh upon submergence in the upper subsoil were similar between paddy sites: Redox potentials were in the oxic range at the beginning of flooding and progressively decreased to  $\leq -200$  mV (highly reduced soil, according to Zhi-Guang, 1985) within three weeks. At P100 and P700 strongly reducing conditions in both top- and subsoil established within two and three weeks after flooding, respectively. The lower subsoil of P2000 (55 cm and 75 cm) remained oxic (Eh  $>600$  mV) for three weeks after flooding. The redox potential dropped thereafter, reaching constant values of about  $-200$  mV 42 and 50 days after flooding, respectively, thus, resulting in an entirely reduced soil profile.

Highly reducing conditions persisted until the end of the rice cropping season at all three paddy sites. Drainage shortly before rice harvest, caused increasing Eh values (Figure 5-2 and Figure 5-3); however, never exceeding 400 mV. Spatial variability in redox potential increased for P100 and P2000, while redox values remained stable at low values at P700 presumably due to high precipitation shortly after harvest ( $45 \text{ l m}^{-2}$  within 24 h) and during winter months. Mean redox values one week after harvest ranged between  $-134$  mV (P700) and  $+541$  mV (P100) at 10 cm,  $-205$  mV (P700) and  $+517$  (P100) at 35 cm and between  $-249$  (P700) to  $+620$  mV (P2000) at 55 cm. Prolonged anoxic conditions during the fallow period presumably result from high precipitation and low evapotranspiration rates during the winter season, leading to a largely water-saturated soil.

Oxic conditions prevailed throughout the measurement period at the non-paddy sites (Figure 5-2 and Figure 5-3). No significant differences were found neither between sites (NP100, NP700) nor depths. Mean Eh values ranged from  $+402$  to  $+633$  mV at NP100 and between  $+404$  mV to  $+658$  mV at NP700 throughout the year.

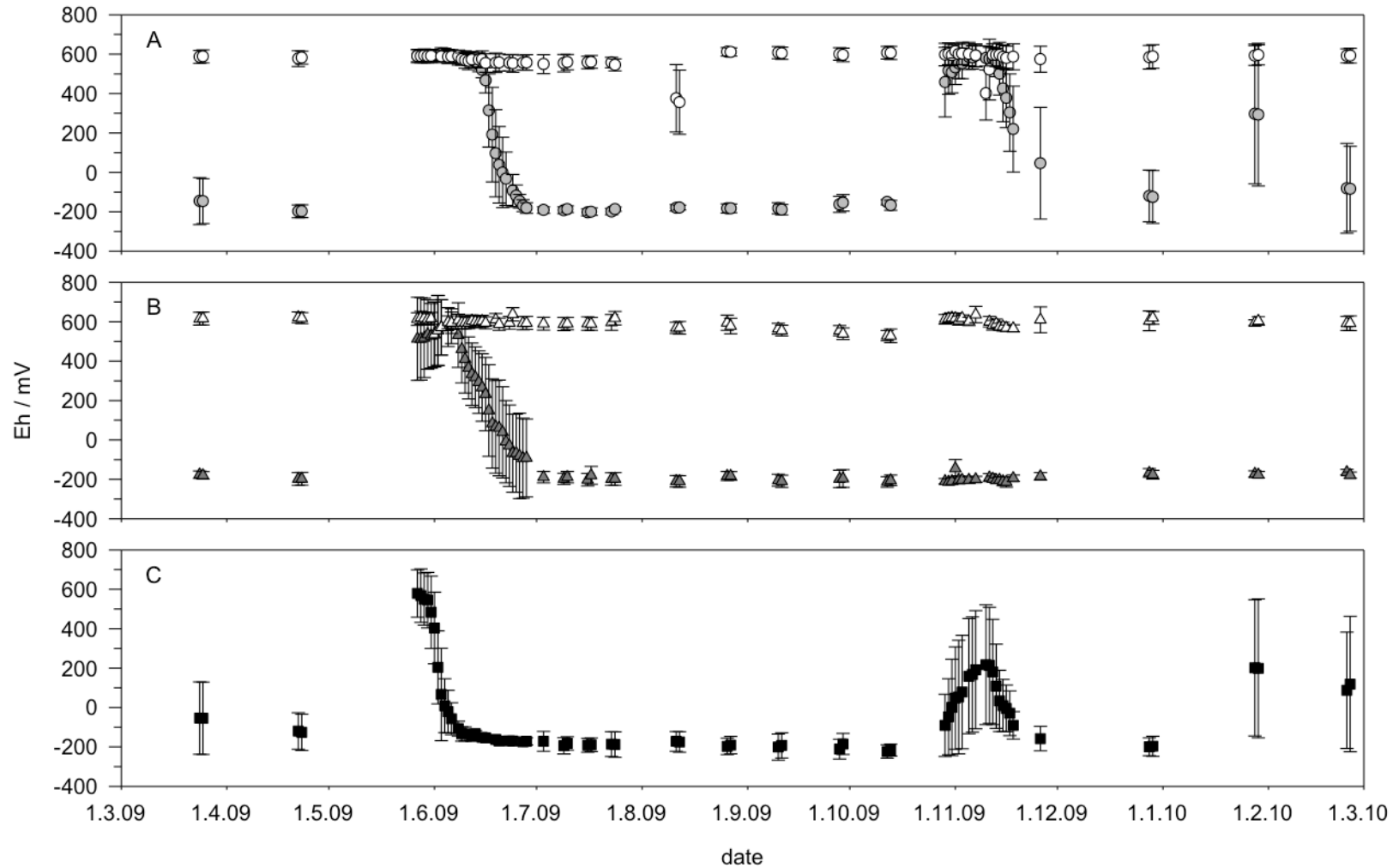


**Figure 5-2:** Redox conditions during one entire paddy-winter crop cycle (March 2009 to March 2010) in the upper subsoil (35 cm) of the 100 year paddy and non-paddy site (A), the 700 year paddy and non-paddy site (B) and the 2000 year paddy site (C). Filled shapes represent the paddy sites, unfilled shapes the non-paddy sites. Data points are means of max. five replicates; error bars are one standard deviation.

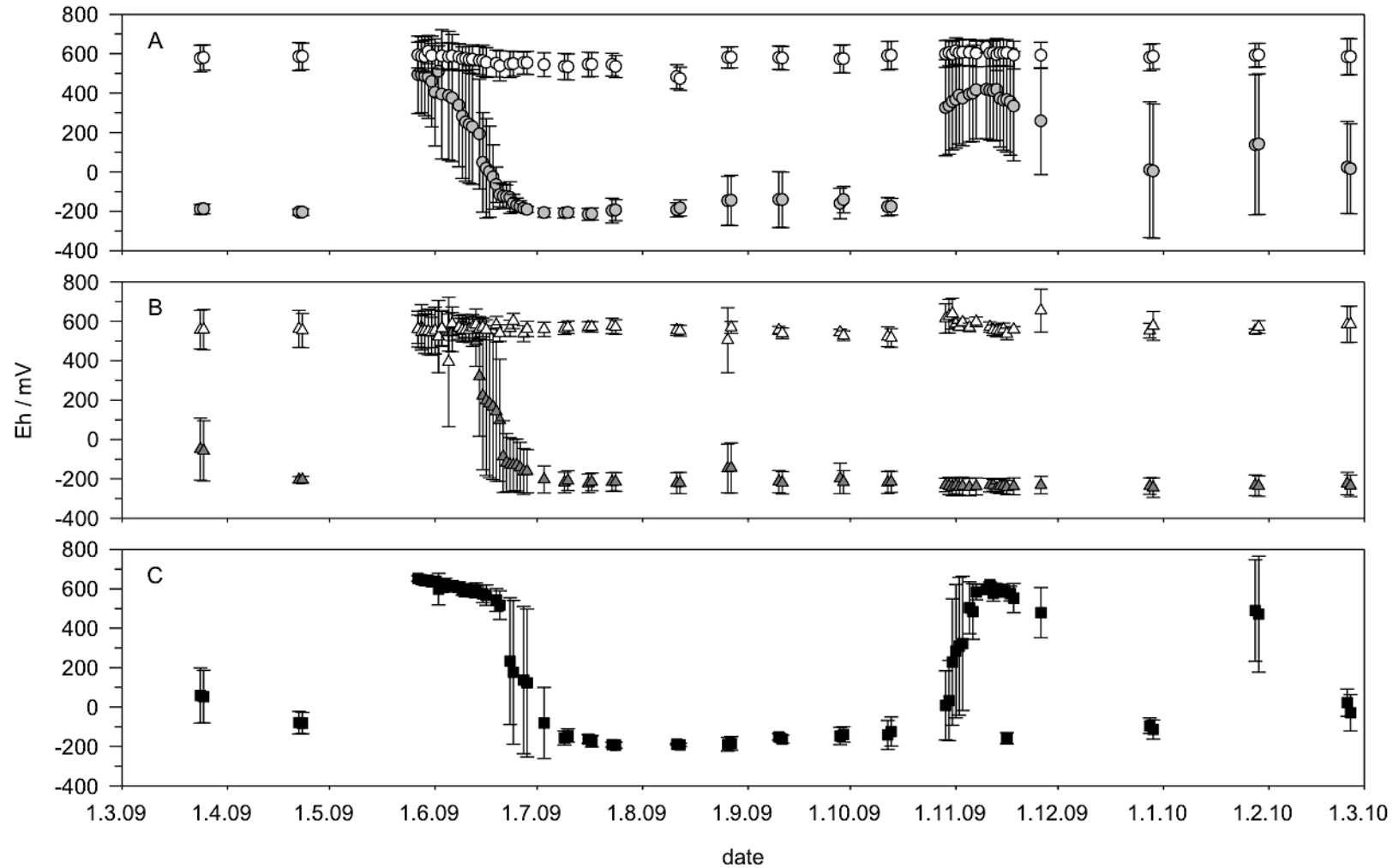


**Figure 5-3:** Redox conditions during one entire paddy-winter crop cycle (March 2009 to March 2010) in the lower subsoil (55 cm) of the 100 year paddy and non-paddy site (A), the 700 year paddy and non-paddy site (B) and the 2000 year paddy site (C). Filled shapes represent the paddy sites, unfilled shapes the non-paddy sites. Data points are means of max. five replicates; error bars are one standard deviation.

### 5.3.2 Soil reaction and alkalinity

Initial soil solution reaction at the paddy sites was neutral (P2000, 35 and 55 cm: pH 6.9) to slightly (P100, 35 and 55 cm: pH 8.1) and strongly alkaline (P700, 35 and 55 cm: pH 8.9 and 9.1, respectively). This was about one pH unit above the pH values of the corresponding horizons (Chapter 3). Highest pH values over the entire measurement period after submergence occurred at P700, closely followed by P100; pH values at the P2000 were one pH unit lower than at the two younger paddy sites (Figure 5-4). Soil solution pH increased by about one unit during the first two months of submergence at the P2000 site. In contrast, pH values remained rather constant during the first 4 weeks of flooding at P100 and P700; largest pH values were determined at the end of the measurement period. No significant difference in pH could be observed between the different depths.

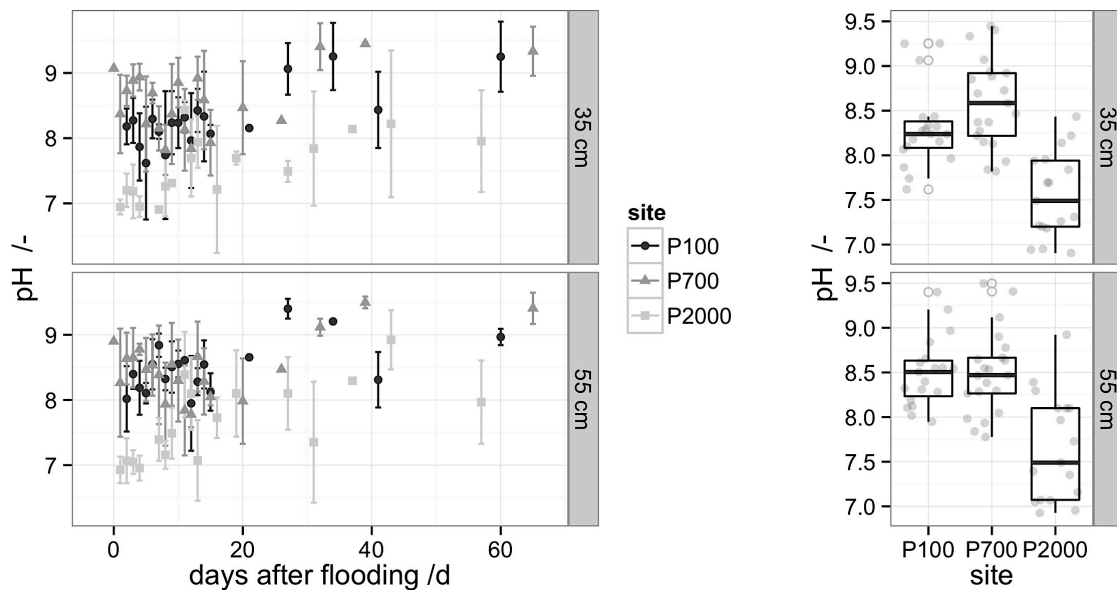


**Figure 5-4:** Mean pH values in the soil solution of the upper (35 cm) and lower (55 cm) subsoil during the first two months after flooding (left); data points are means of max. four replicates, error bars are one standard deviation. Boxplots and corresponding data points illustrate distribution of pH values (right).

With respect to the level of alkalinity, a strong age dependency was observed (Figure 5-5). Highest levels of alkalinity were found at P100, followed by P700 and P2000, which is in line with the soils' carbonate contents. Alkalinity increased at all paddy sites after flooding except for soil solutions at 55 cm depth of P100, which showed no distinct trend over the measurement period.

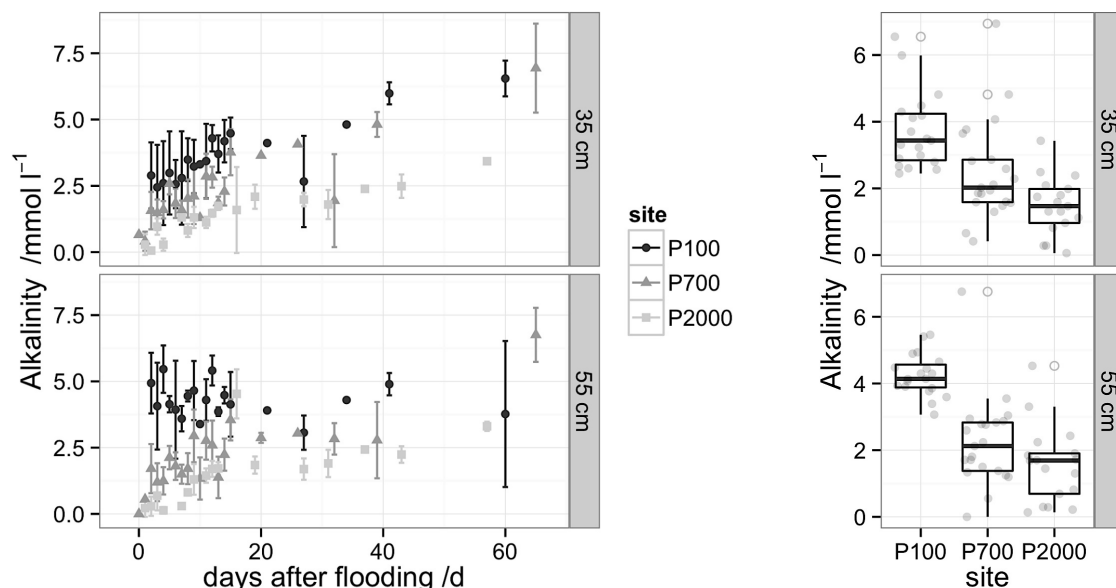


**Figure 5-5:** Mean alkalinity in the soil solution of the upper (35 cm) and lower (55 cm) subsoil during the first two months after flooding (left); data points are means of max. four replicates, error bars are one standard deviation. Boxplots and corresponding data points illustrate distribution of alkalinity (right).

### 5.3.3 Redox sensitive elements and compounds: nitrogen, manganese, iron, sulfate, and carbon

$N_{\min}$  (sum of  $\text{NO}_{2/3}^-$ -N and  $\text{NH}_4^+$ -N) of the bulk soil was low at all study sites and only contributed little to total N of the bulk soil (0.5% according to Roth et al., 2011). This was reflected by very low  $\text{NO}_{2/3}^-$  and  $\text{NH}_4^+$  concentrations in the soil solution (Figure 5-6 and Figure 5-7). The observed slight increase in  $\text{NH}_4^+$  concentrations during the first three weeks of submergence most likely results from microbial release of  $\text{NH}_4^+$  during decomposing OM (ammonification), as the lack of oxygen inhibits nitrification, i.e., transformation of  $\text{NH}_4^+$  to nitrate (via nitrite) (Ponnamperuma, 1972).  $\text{NH}_4^+$  concentrations in the soil solutions were generally lower than typically found in submerged soils (0.1 to 5 mM; Kirk, 2004). However,  $\text{NH}_4^+$  can be fixed on the soil's cation exchange complex (Schneiders and Scherer, 1998; Sahrawat and Ponnamperuma, 1978), and thus, might not be detectable in the soil solution. Also, the high solutions pH values may promote formation of ammonia, thus, partial release to the atmosphere despite the limited gas exchange under submerged conditions.

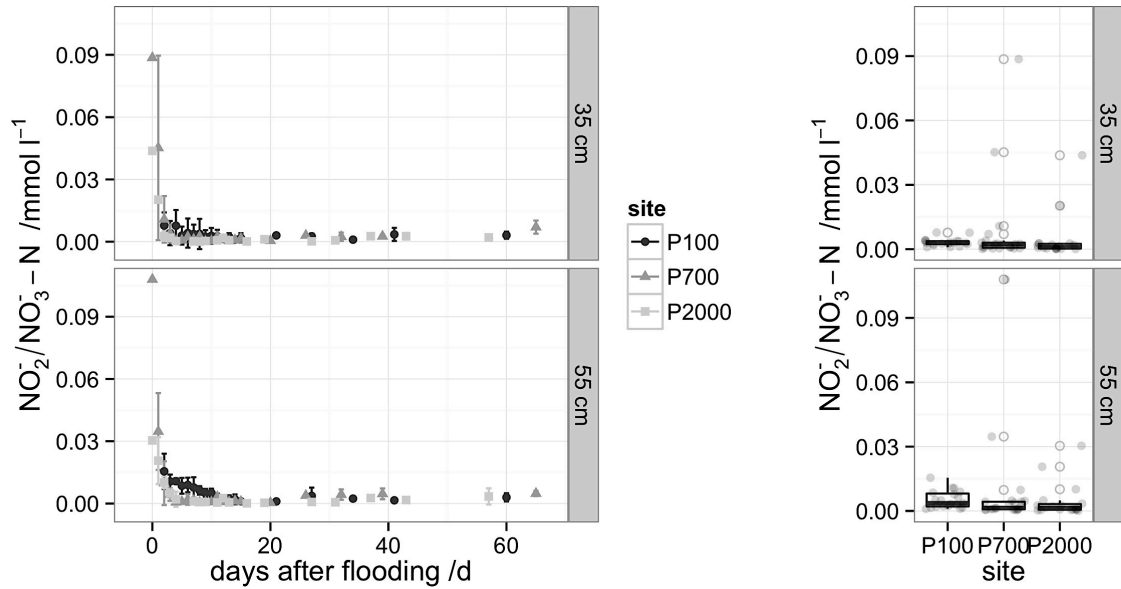


**Figure 5-6:** Mean  $\text{NO}_{2/3}^-$  concentrations (depicted as  $\text{NO}_{2/3}^- \text{N}$ ) in the soil solution of the upper (35 cm) and lower (55 cm) subsoil during the first two months after flooding (left); data points are means of max. four replicates, error bars are one standard deviation. Boxplots and corresponding data points illustrate distribution of  $\text{NO}_{2/3}^-$  values (right).

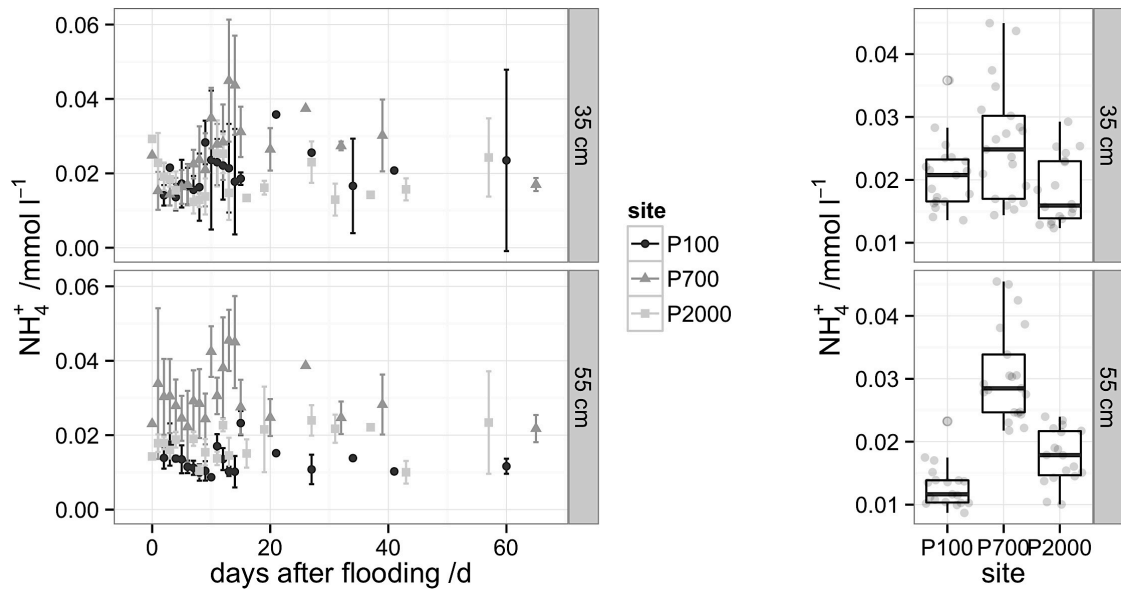


**Figure 5-7:** Mean  $\text{NH}_4^+$  concentrations in the soil solution of the upper (35 cm) and lower (55 cm) subsoil during the first two months after flooding (left); data points are means of max. four replicates, error bars are one standard deviation. Boxplots and corresponding data points illustrate distribution of  $\text{NH}_4^+$  concentrations (right).

No  $\text{NO}_{2/3}^-$  was detectable throughout the entire measurement period at 35 cm depth at P100. Highest  $\text{NO}_{2/3}^-$  concentrations ( $0.1 \text{ mmol l}^{-1}$ ) were detected at 55 cm depth at P700 at the day of flooding. Concentrations of  $\text{NO}_{2/3}^-$  decreased rapidly at all paddy sites and depths immediately after submergence; within two to five days nitrate concentrations fell below the detection limit ( $0.01 \text{ mmol l}^{-1}$ ). Obviously,  $\text{NO}_{2/3}^-$  was the major alternative electron acceptor right after flooding.

$\text{NH}_4^+$  concentrations in the soil solution (Figure 5-7) ranged between 9 and  $50 \text{ } \mu\text{mol l}^{-1}$ . Generally,  $\text{NH}_4^+$  concentrations were highest at P700. There was a slight, though not distinct increase in  $\text{NH}_4^+$  concentrations during the first three weeks of submergence at most paddy sites.

Increases in dissolved Fe and Mn indicate reduction of the respective mineral phases. Solution concentrations of Mn increased immediately after flooding in all three paddy soils (Figure 5-8), indicating an early on-set of Mn reduction. The increase in dissolved Mn was slightly retarded in the lower subsoil of P100 and P700. However, concentrations remained low throughout the entire measurement period irrespective the age of the paddy site ( $<0.05 \text{ mmol l}^{-1}$ ). At the oldest paddy site, P2000, the concentrations of Mn levelled off after about 18 days after flooding. In contrast, there was a sharp increase in Mn concentrations at the end of the measurement period at the youngest site. Dissolved Mn concentrations were lower in the lower than in the upper subsoil at all three paddy sites, reflecting Mn contents in the bulk soil. All soils had maximum contents of Mn oxides in the horizons beneath the plough pan (Kölbl et al., 2014).

No Fe was detected in the soil solutions during the first days of submergence (Figure 5-9, left). Dissolved Fe concentrations exceeded the detection limit ( $0.7 \text{ } \mu\text{mol l}^{-1}$ ) after three to five days and progressively increased thereafter. In the upper subsoil of P2000, Fe concentrations increased sharply ( $\geq 0.014 \text{ mmol l}^{-1}$ ) after one week, indicating enhanced Fe reduction. However, even under the most reductive conditions ( $\leq -200 \text{ mV}$ ) little Fe was detected in the soil solutions. Highest concentrations ( $0.04 \text{ mmol l}^{-1}$ ) were found in the lower subsoil of P700 at the end of the measurement period.

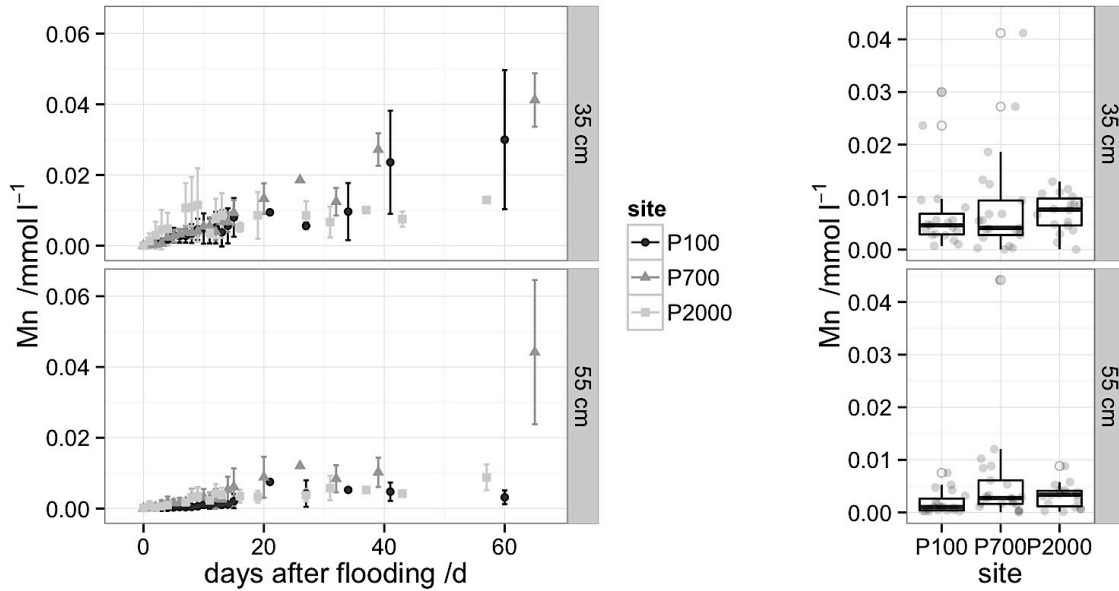


**Figure 5-8:** Mean Mn concentrations in the soil solution of the upper (35 cm) and lower (55 cm) subsoil during the first two months after flooding (left); data points are means of max. four replicates, error bars are one standard deviation. Boxplots and corresponding data points illustrate distribution of Mn concentrations (right).

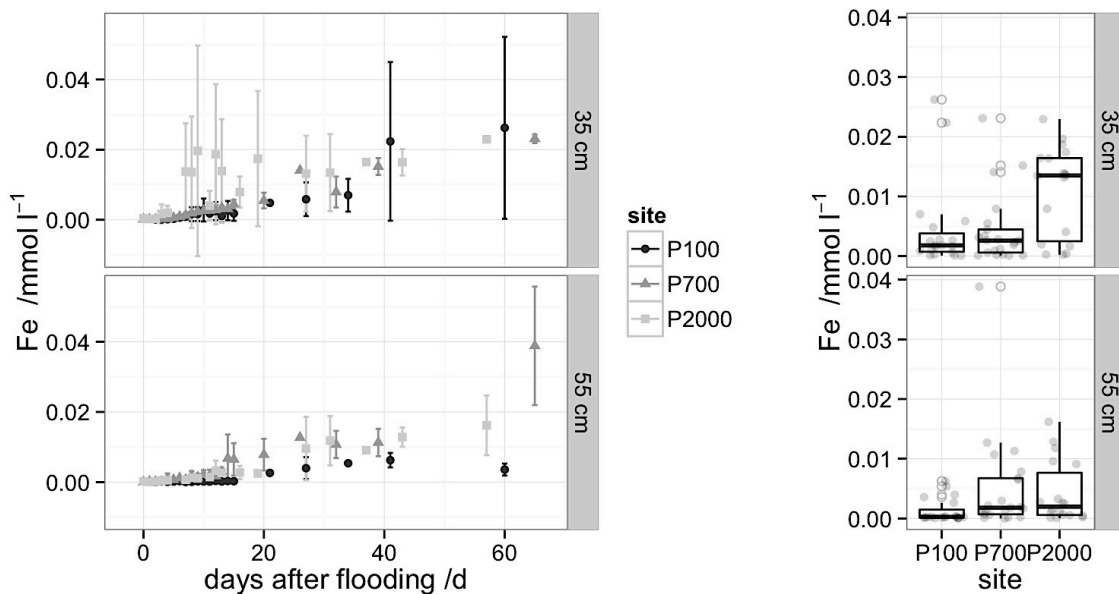


**Figure 5-9:** Mean Fe concentrations in the soil solution of the upper (35 cm) and lower (55 cm) subsoil during the first two months after flooding (left); data points are means of max. four replicates, error bars are one standard deviation. Boxplots and corresponding data points illustrate distribution of Fe concentrations (right).

Concentrations of  $\text{SO}_4^{2-}$  were similar at the three paddy sites (Figure 5-10, right). With prolonged submergence, mean  $\text{SO}_4^{2-}$  concentrations constantly decreased from 2.4 to 0.2  $\text{mmol l}^{-1}$ . Sulfate seemed to serve as a major electron acceptor throughout the growing season.

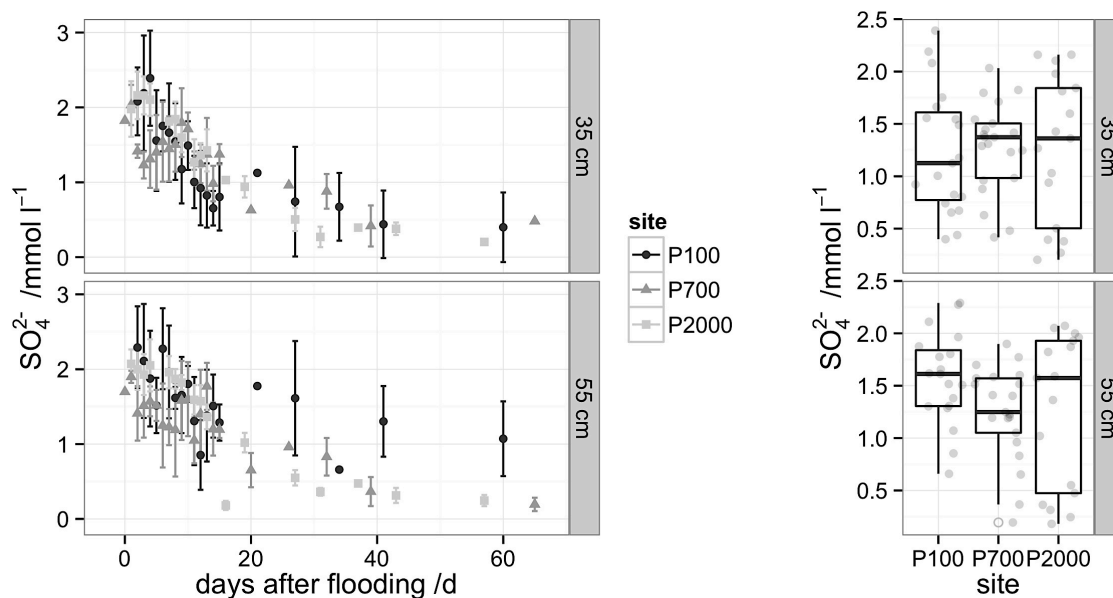


**Figure 5-10:** Mean  $\text{SO}_4^{2-}$  concentrations in the soil solution of the upper (35 cm) and lower (55 cm) subsoil during the first two months after flooding (left); data points are means of max. four replicates, error bars are one standard deviation. Boxplots and corresponding data points illustrate distribution of sulfate concentrations (right).

Dissolved organic carbon concentrations in soil solutions showed a clear trend with increasing age of the paddy sites (Figure 5-11, left). Highest DIC levels occurred at P100, followed by P700 and P2000 (Figure 5-11, right). Upon flooding, DIC concentrations increased at all paddy sites and sampling depths. With time of paddy cultivation, overall DIC levels in the soil solution of the paddy sites decreased ( $\text{P100} > \text{P700} > \text{P2000}$ ). This reflects the extent of decalcification of the bulk soil, as described by Kölbl et al. (2014). Inorganic carbon concentrations of the bulk soil ranged between 0.2 and 2.9  $\text{mg g}^{-1}$  in the subsoil of P100; the soil profiles at P700 and P2000 had no more inorganic carbon. Thus, at P100 not only microbial respiration but also the dissolution of carbonates contributed to the higher DIC concentrations.

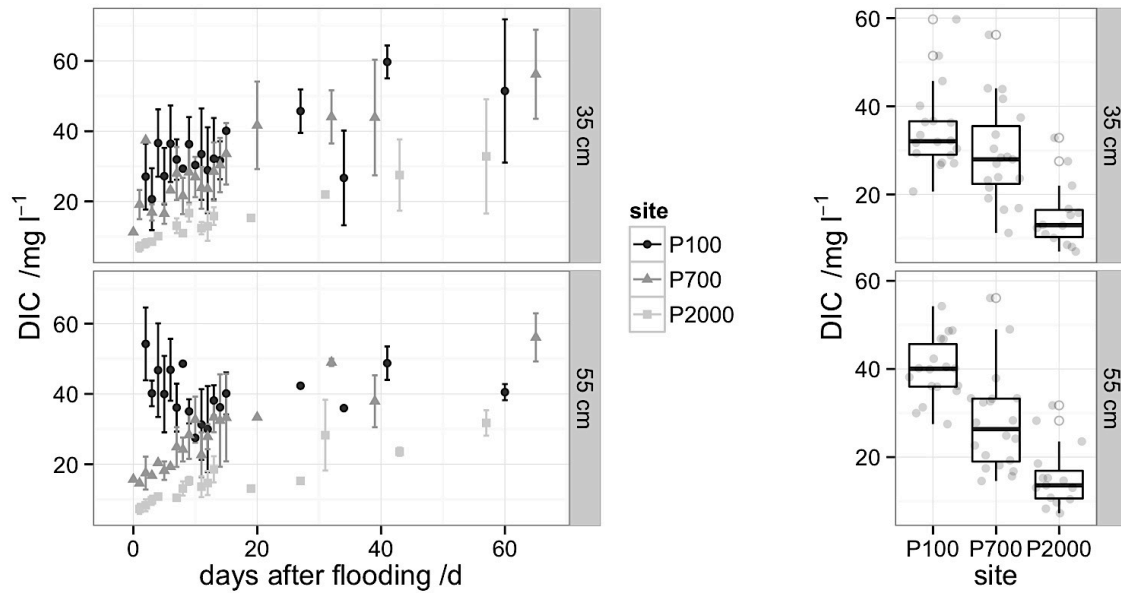


**Figure 5-11:** Mean dissolved inorganic carbon (DIC) concentrations in the soil solution of the upper (35 cm) and lower (55 cm) subsoil during the first two months after flooding (left); data points are means of max. four replicates, error bars are one standard deviation. Boxplots and corresponding data points illustrate distribution of DIC concentrations (right).

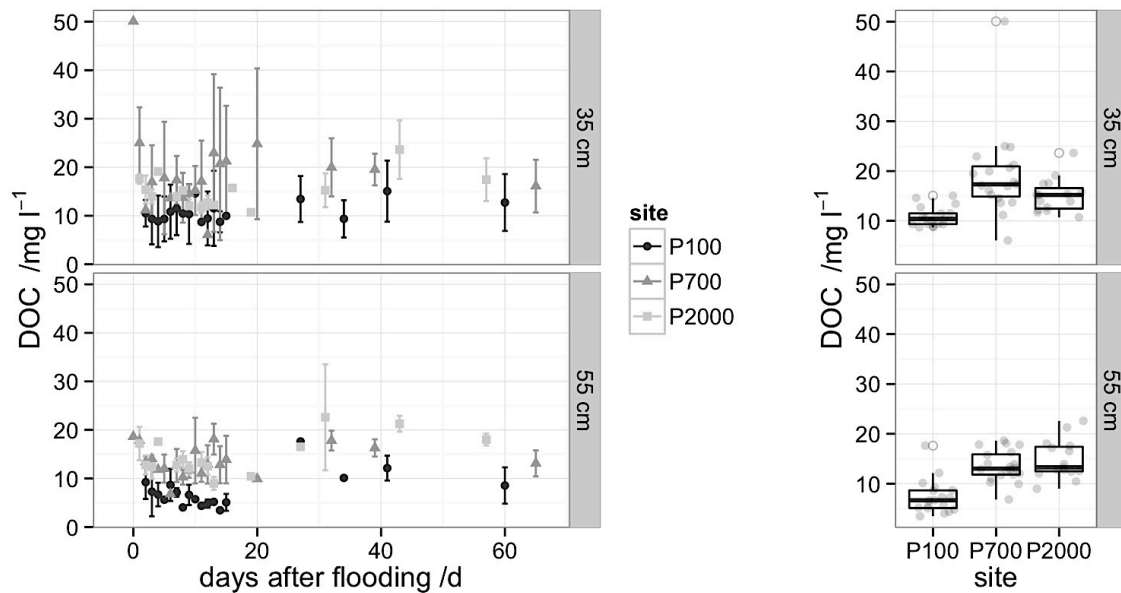


**Figure 5-12:** Mean dissolved organic carbon (DOC) concentrations in the soil solution of the upper (35 cm) and lower (55 cm) subsoil during the first two months after flooding (left); data points are means of max. four replicates, error bars are one standard deviation. Boxplots and corresponding data points illustrate distribution of DOC concentrations (right).

Dissolved organic carbon concentrations in the soil solution showed high spatial and temporal variations (Figure 5-12, left). Overall, DOC concentrations were relatively low. Highest DOC concentrations occurred in soil solutions of P2000 and at P700; soil solutions of P100 had less DOC (Figure 5-12, right).

### 5.3.4 Electric conductivity and alkali/ earth alkali elements

Highest electric conductivities were measured at P100 and values decreased with time of paddy cultivation (Figure 5-13). A slight decrease of EC at both depths at P100 and P2000 was observed after submergence, which might be due to dilution by the irrigation water. At P700 no clear trend was found.

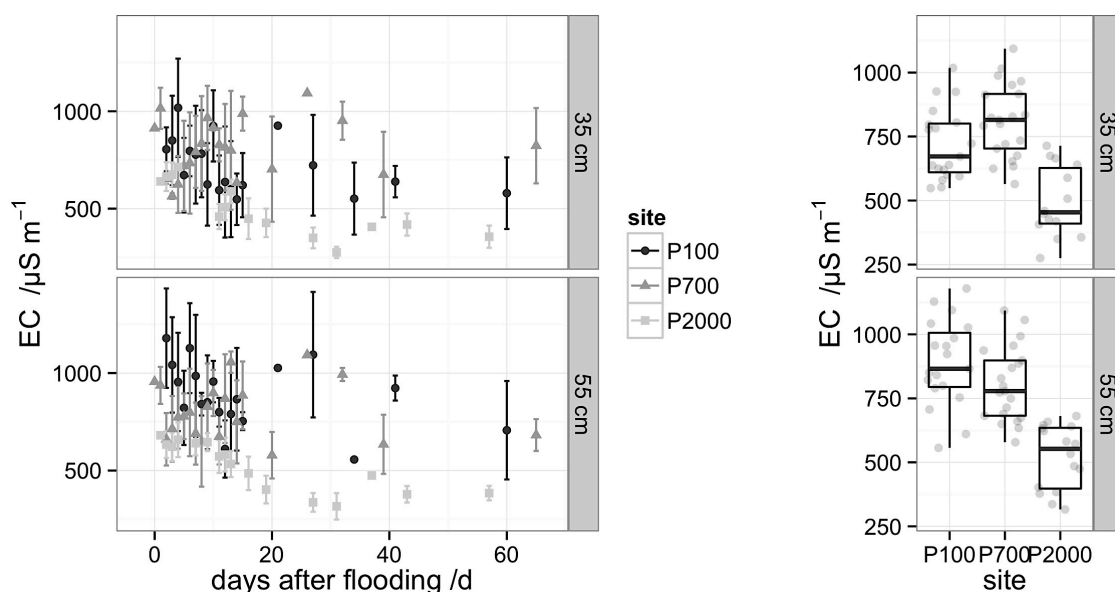


**Figure 5-13:** Mean electric conductivity (EC) of the soil solution of the upper (35 cm) and lower (55 cm) subsoil during the first two months after flooding (left); data points are means of max. four replicates, error bars are one standard deviation. Boxplots and corresponding data points illustrate distribution of EC values (right).

Concentrations of Na and Mg in the soil solutions correlate well with EC; weaker but still significant correlations can be found for K and Ca, for the latter only at the oldest paddy site (Table 5-1): Highest concentrations of both alkali and earth alkali elements occurred at the younger paddy sites (P100 and P700). Sodium was the dominant cation in almost all soil solutions, ranging between 0.63 and 5.16 mmol l<sup>-1</sup>), followed by Ca (0.78 to 2.92 mmol l<sup>-1</sup>) and Mg (0.35 to 1.65 mmol l<sup>-1</sup>).

**Table 5-1:** Correlation of the electron conductivity (EC), earth alkali/alkali elements, chloride ( $\text{Cl}^-$ ) and the redox potential in the soil solution of the upper (35 cm) and lower (55 cm) subsoil of the three paddy sites P100, P700, and P2000.

	Site	Depth cm	Eh	$\text{Cl}^-$	Ca	K	Mg	Na	$r^2$
EC	P100	35	.765**	.956**	.101**	.227	.750**	.905**	
		55	.577*	.983**	.006	.464*	.900**	.978**	
	P700	35	-.082	.919**	.062	.356	.687**	.882**	
		55	.024	.961**	.047	.553**	.693**	.901**	
	P2000	35	.831**	.917**	.652**	.451	.811**	.861**	
		55	.792**	.793**	.684**	.144	.822**	.785**	

\*\* p < 0.01 and

\* p < 0.05 (Pearson correlation, two-sided significance level)

Especially at the younger sites, the Na dominance is most pronounced. This was clearly reflected by the sodium adsorption ratio. Highest SARs were calculated for P700 (ranging between 2.2 to 4.6), followed by P100 (1.5 to 4.0). SAR levels at P2000 were lower (0.5 to 1.7). Potassium concentrations in the soil solution were little, ranging between 0.01 and 0.1  $\text{mmol l}^{-1}$ , with the lowest concentrations occurring at the oldest paddy site, P2000 ( $\leq 0.04 \text{ mmol l}^{-1}$ ).

Chloride concentrations were closely correlated with EC (Table 5-1), with slightly decreasing concentrations after flooding. Highest  $\text{Cl}^-$  concentrations were found at P100 and P700 (1.82 to 5.10  $\text{mmol l}^{-1}$  and 2.25 to 5.10  $\text{mmol l}^{-1}$ , respectively); chloride concentrations were almost half at P2000 and ranged between 0.53 to 2.11  $\text{mmol l}^{-1}$ . Concentrations of  $\text{Cl}^-$  concentrations showed a high variability between the replicates at all sites.

### 5.3.5 Matrix elements: silicate and aluminium

Silicate concentrations in the soil solution slightly increased with prolonged submergence at all paddy sites (Figure 5-14); the most pronounced increase occurred at P2000.

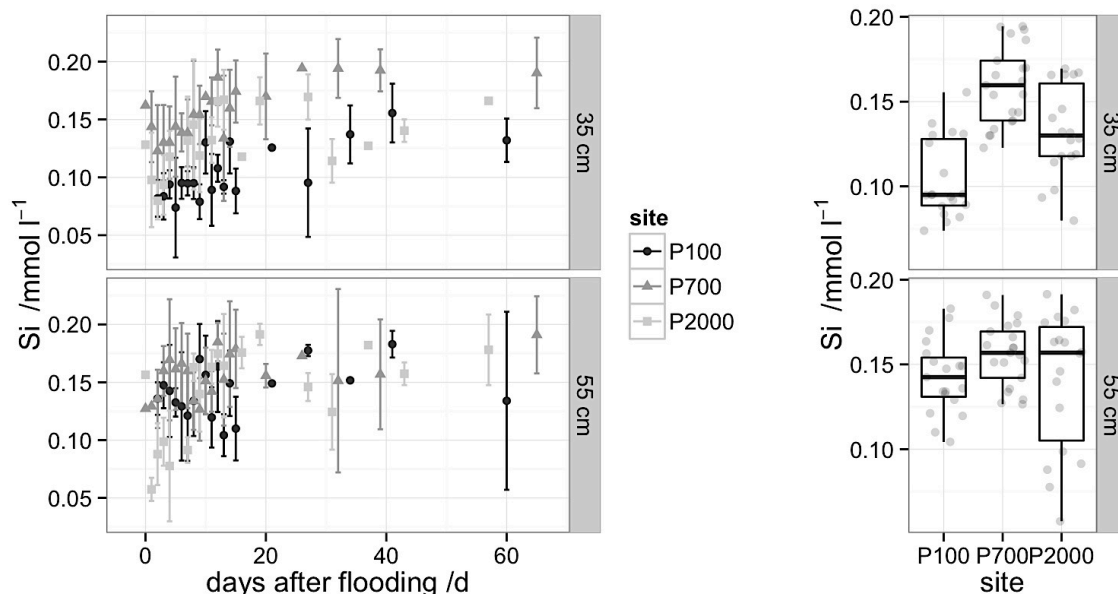


**Figure 5-14:** Mean Si concentrations in the soil solution of the upper (35 cm) and lower (55 cm) subsoil during the first two months after flooding (left); data points are means of max. four replicates, error bars are one standard deviation. Boxplots and corresponding data points illustrate distribution of Si concentrations (right).

Solution concentrations of Fe, DIC, and Si were significantly positively correlated after submergence at all three sites (Table 5-2). Thus, the increase in Si concentrations after flooding might be due to (1) release of sorbed silica during the reductive dissolution of hydrous Fe oxides and/or (2) a release of Si from aluminosilicates due to increasing pH and DIC levels (Bricker et al., 1968).

**Table 5-2:** Correlation of DIC, Si and Fe concentrations in the soil solution of the upper (35 cm) and lower (55 cm) subsoil of the three paddy sites.

	Site	Depth cm	Fe $r^2$	DIC $r^2$
<b>Si<sub>t</sub></b>	P100	35	.699**	.478*
		55	.532*	.482*
	P700	35	.730**	.616*
		55	.527*	.531*
	P2000	35	.682**	.535*
		55	.396	.460*

\*\* p < 0.01 and

\* p < 0.05 (Pearson correlation, two-sided significance level)

Concentrations of Al were generally very little ( $<5.0 \cdot 10^{-3} \text{ mmol l}^{-1}$ ). In most soil solutions, Al concentrations were below the detection limit of  $2.9 \cdot 10^{-3} \text{ mmol l}^{-1}$ .

### 5.3.6 Irrigation water

No data on the elemental composition of the original irrigation water is available for our sampling period. Samples of the standing water in the paddy fields taken at the beginning of the irrigation period show a similar elemental composition for all paddy sites and concentrations matched those of the soil solutions at the beginning of flooding (data not shown).

## 5.4 Discussion

### *Time of cultivation has little influence on the redox dynamics of the different paddy fields*

All paddy soils were characterised by temporal changes in redox conditions in the course of flooding and drainage. The observed range of Eh values (+570 to -190 mV in the topsoils, +650 to -200 mV in the subsoils) is in line with those usually observed in paddy (Ponnamperuma, 1972) and other submerged soils (Vorenhout et al., 2004). Particularly during the initial period of submergence spatial heterogeneity of the soil profile was well reflected by the redox potential: Eh showed high spatial variability at all three paddy sites, likely due to microsites within horizons, i.e., sites with higher  $\text{O}_2$  and/or OM concentrations, both influencing the redox status of the soil (Vepraskas and Faulkner, 2001; Fiedler et al., 2007).

Upon flooding reducing conditions established more quickly in topsoil than in subsoil layers. Rice roots predominately grow in the topsoil, resulting in higher root and microbial activity (Ratering and Schnell, 2000). Paddy topsoils had higher abundances of electron donors (organic compounds) and easily available electron acceptors (i.e., nitrate, poorly crystalline Fe oxides) than the subsoils (Chapter 3), thus, supporting a more rapid drop in Eh (Ratering and Schnell, 2000; Gao et al., 2004). In the upper subsoil (35 cm), redox dynamics were also largely comparable in all three soils. Differences in the concentration of Fe oxide contents and, hence, in redox capacity between the paddy sites at 35 cm were not reflected by the redox potential. Thus, time of paddy cultivation seemed to have little effect on the response of the soils' redox regime to flooding in the topsoil and upper subsoil of the paddy sites; redox dynamics seemed to be a simple function of management, e.g., time and length of irrigation. In the lower subsoil (55 cm), in contrast, the decrease of Eh became slower with the time of paddy cultivation, i.e., age of the paddy sites. The lower subsoil at P100 was already moderately reduced before submergence, likely due to a higher groundwater level. Temporal changes in redox conditions in the lower as well as in the upper subsoil of P700 were similar; Eh values below -200 mV established within three weeks. In the lower subsoil at P2000, oxic

conditions prevailed much longer (~3 weeks) than at younger sites. The establishment of anoxic conditions proceeded from top- to subsoil, indicating successive water saturation due to percolating irrigation water. Water infiltration in paddy fields is influenced by many factors, e.g., soil texture and structure, standing water depth and depth of the groundwater table (Wickham and Singh, 1978). Soil texture and thickness as well as water management were similar at the three paddy sites. According to Cheng et al. (2009) and our own observations in June 2008, groundwater tables are between 30 to 60 cm beneath surface in the Cixi area, with higher groundwater tables at sites closer to the new dykes. Thus, we assume that at the P700 site, as at the P100 site, rising groundwater fastens the saturation of the lower subsoils. Rising groundwater levels are common effects after paddy flooding (Greppi, 2004). Also, capillary rise of water can increasingly contribute to the saturation of deeper soil horizons the higher the groundwater table is. Thus, at the younger paddy sites, P100 and P700, two superimposing processes control soil saturation and redox potentials: (1) submergence, mainly affecting topsoils and upper subsoils and (2) rising groundwater levels, affecting the lower subsoils. At the oldest paddy site, P2000, groundwater levels are much lower ( $\geq 100$  cm beneath surface), thus, water saturation most likely was driven by infiltration of irrigation water.

***Younger paddy sites are characterised by alkaline soil reactions, presumably due to irrigation with sodium-rich water***

Initial pH values of the soil solution are in accordance with the different levels of decalcification of the three paddy sites, with highest pH values measured in bulk soils (Kölbl et al., 2014) and soil solutions of the younger paddy sites. pH values were high throughout the measurement period; at P700 soil solutions were alkaline, with pH values exceeding pH 8.4. That hints at Na carbonate controlling pH (Gupta and Abrol, 1990). All paddy fields were at least 10 km from the sea; thus, direct flooding with sea water cannot occur. However, the soils derived from marine substrates and show a strong decrease in EC and Na saturation level (ESP) within 30 years after land reclamation (Kölbl et al., 2014). Nonetheless, P100 and P700 were still hyposodic (according to FAO, 2006), having a Na saturation of  $\geq 6\%$  in almost all horizons. The irrigation water originates from the small channels draining the area and is not completely salt free, especially at the younger sites closer to the coastline, e.g., P100 and P700 (Zhi-Hong Cao, Chinese Academy of Sciences, Nanjing, personal communication). Consequently, Kölbl et al. (2014) assumed that the younger paddy soils, i.e., P100 and P700, still receive salt inputs from brackish irrigation and groundwater. This is supported by the composition of the soil solution. The EC was relatively high and closely linked to the Na and  $\text{Cl}^-$  concentrations (Table 5-1). Sodium was dominating the cation composition in all soil solutions and  $\text{Cl}^-$  was often the predominant anion.

Calcium carbonate precipitations in some soil solutions indicate a shift in the calcium carbonate solubility equilibrium. Sampling of soil solutions can lead to degassing, and thus, decreasing  $p\text{CO}_2$  levels in the soil solution and increasing pH values (Suarez, 1986; Suarez, 1987). However, most soil solutions were in a pH range where changes in carbonate concentrations have little effect. Thus, the maximum impact on the overall pH level and its temporal changes was small. Another explanation for the observed calcite precipitation could be that these solutions were already highly oversaturated with respect to  $\text{CaCO}_3$ , as it is often found in groundwaters and subsoils (e.g., Kindler et al., 2011). Calcite does not instantly precipitate from even highly oversaturated solutions since nucleation is slow (Amrhein et al., 1993).

Soil solution pH values remained constant at P100 and P700 under prolonged submergence until the last two weeks, where we observed slightly increasing pH values. The pH values at P2000 were initially lower than at the younger sites but steadily increasing with time of submergence, but never exceeded pH 8.4. Likely, the site is less impacted by brackish water inputs. Cary and Trolard (2008) observed an increase in pH from 7.5 to 8.6 in soil solutions of paddy sites upon alternation of the non-irrigated to the irrigated period, stabilizing at pH 8.2. A pH increase is typical for the initial period of reduction (Kyuma, 2004) and may be explained by proton consumption during all major reduction processes (i.e., denitrification, reduction of Mn, Fe, and  $\text{SO}_4^{2-}$ ). The extent of pH increase depends on the  $\text{H}^+$  consumption during electron transfer, which is largest for the reduction of hydrous Fe oxides (Kyuma, 2004). Thus, the pH is already influenced by little Fe reduction. Under prolonged submergence, however, the pH of an originally alkaline to neutral soil is expected to decrease and stabilize at around pH 7 (Ponnamperuma et al. 1966). This decrease in pH is mainly explained by increasing  $p\text{CO}_2$  due to microbial respiration and limited gas transfer due to submergence and, hence, an increase of DIC in the soil solution (Kirk, 2004). Organic acids from decomposing of OM, outbalancing the proton consumption by reduction processes taking place, can also contribute to the decrease in pH (Ponnamperuma, 1972; Kirk, 2004). Indeed, increasing DIC concentrations during submergence were observed at all three paddy sites. The increase in pH by one unit at P2000 (Figure 5-4) during the first two months of submergence indicates that the consumption of  $\text{H}^+$  by reductive processes (complete reduction of nitrate, on-going reduction of Fe, Mn, and  $\text{SO}_4^{2-}$ ) had a stronger influence on pH than the accumulation of  $\text{CO}_2$  in pore-water due to microbial respiration.

Alkalinity is closely related to the charge balance of a soil solution. All biogeochemical processes that either consume or generate  $\text{H}^+$  or  $\text{OH}^-$  affect alkalinity. Processes characteristic for submerged soils, such as denitrification,  $\text{Mn}^{4/3+}$  and  $\text{Fe}^{3+}$  reduction, and  $\text{SO}_4^{2-}$  reduction, will increase alkalinity in soil solutions (Stumm and Morgan, 1996). No correlations of alkalinity with dissolved Mn and Fe ( $r^2 \leq 0.4$ ) were found, but probably not all Mn(IV, III) and Fe(III) reduced is actually detectable (see section below). Close correlations ( $p < 0.01$ ) with

alkalinity were observed for  $\text{SO}_4^{2-}$  and DIC ( $r^2 \geq 0.9$ ) at all paddy sites, except for 55 cm depth at P100 ( $r^2 = 0.491$ ). The accumulation of  $\text{CO}_2$ , i.e., increasing DIC concentrations, as well as the reduction of  $\text{SO}_4^{2-}$  contributed most significantly to increasing levels of alkalinity during submergence of the study paddy sites.

***The soil solution composition generally follows redox dynamics and reflects the thermodynamic sequence of the redox processes (sequential reduction).***

Strictly, only redox measurements in the soil solution are thermodynamically meaningful (Kirk, 2004). Redox potentials measured in the soil solution and bulk soil can differ considerably (Mansfeldt, 2004; Kirk, 2004). Considering the experimental set-up chosen, both Pt electrodes (measuring the Eh in the bulk soil) and suction cups (sampling the soil solution) are spatially separated, they might not necessarily be representative of the same environmental conditions at the time of sampling (Mansfeldt, 2004). However, Mansfeldt (2004) demonstrated that the overall relationship between the measured redox potential and solute concentrations of nitrate,  $\text{Mn}^{2+}$ , and  $\text{Fe}^{2+}$  indicate the prevalent redox processes in soils. The redox potential at the three paddy sites dropped from 600 mV to  $-200$  mV during the first two months of submergence, thus, theoretically crossing the thermodynamic equilibria of  $\text{NO}_3^-/\text{NH}_4^+$ ,  $\text{MnO}^2/\text{Mn}^{2+}$ ,  $\text{FeOOH}/\text{Fe}^{2+}$  and  $\text{SO}_4^{2-}/\text{HS}$  (Bartlett and James, 2000), suggesting substantial changes in the biogeochemistry of the bulk soil and soil solutions (Ponnamperuma, 1972; Patrick and Reddy, 1978; Gao et al., 2002).

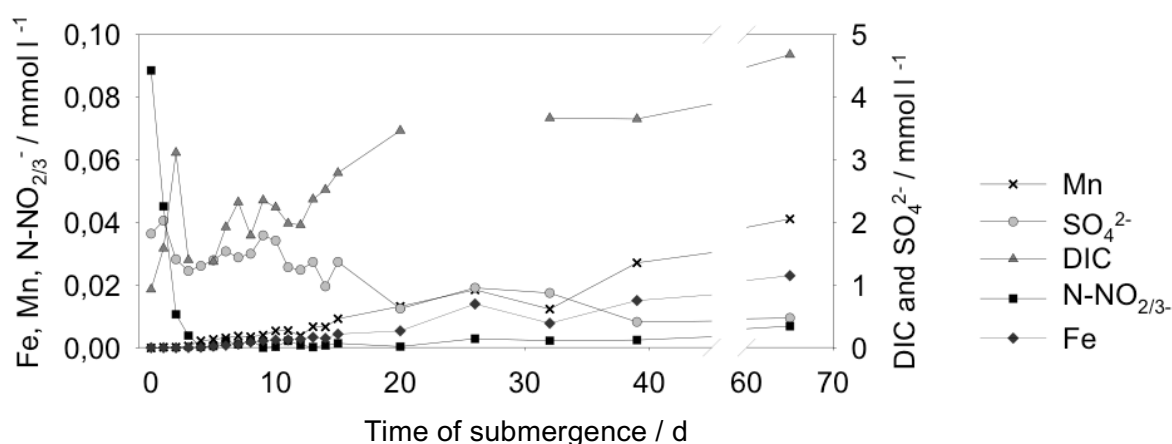


**Figure 5-15:** Changes in concentrations of the redox sensitive compounds upon flooding, exemplarily shown for the soil solution of the upper subsoil (35 cm) at the 700 year paddy site (P700).

Redox species showed a clear relationship to Eh (Figure 5-16 to Figure 5-19; Table 5-3) and followed the sequence of reduction as thermodynamically predicted (Figure 5-15). Nevertheless, we observed overlapping of the different redox processes, i.e., the reduction of Mn and Fe with  $\text{SO}_4^{2-}$  reduction. This simultaneous occurrence of reduction processes was already described for paddy (Peters and Conrad, 1996; Gao et al., 2002) as well as for forested fens and floodplain soils (Alewell et al., 2006; Alewell et al., 2008).

**Table 5-3:** Correlation of Eh with concentrations of the redox species in the soil solution of the upper (35 cm) and lower (55 cm) subsoil of the three paddy sites.

Site	Depth cm	$\text{NO}_{2/3}^-$	Mn	Fe $r^2$	$\text{SO}_4^{2-}$	DIC	
<b>Eh</b>	<b>P100</b>	35	.799**	-.517*	-0,452	.920**	-.513*
		55	.953**	-.694**	-.514*	.751**	.438
	<b>P700</b>	35	.531*	-.763**	-.758**	.771**	-.795**
		55	.405	-.548*	-.611**	.704**	-.878**
	<b>P2000</b>	35	.587*	-.726**	-.839**	.789**	-.520*
		55	.237	-.762**	-.984**	.781**	-.861**

\*\* p < 0.01 and

\* p < 0.05 (Pearson correlation, two-sided significance level)

The rapid decrease and depletion in  $\text{NO}_{2/3}^-$  occurred at all sites and depths within three days after flooding (Figure 5-16), similar to what Ponnampereuma (1972) observed for paddy topsoils. Chemistry of N in soil is controlled by nitrification under oxic conditions, whereas upon the establishment of moderately and strongly reducing conditions denitrification, i.e., the microbial reduction of  $\text{NO}_3^-$  via  $\text{NO}_2^-$  to gaseous N compounds becomes dominant, coupled to the oxidation of organic carbon (Vepraskas and Faulkner, 2001). Nitrate reduction starts at redox potentials between 450 and 550 mV (at pH 7; Patrick and Reddy, 1978), and becomes increasingly instable between +200 and +300 mV (pH 7) (Patrick, 1960). In this Eh range denitrification is the major reduction process in most soils (Reddy and Patrick, 1986). In a batch experiment with paddy soil suspensions, Kralova et al. (1992) observed highest losses of  $\text{NO}_3^-$  at Eh  $\approx$  +200 mV. Concentrations of  $\text{NO}_{2/3}^-$  in the studied soil solutions fell below detection limit at mean redox potentials of 366 mV (P700) and 545 mV (P2000) at 35 cm. In the lower subsoil (55 cm), critical redox values ranged between 559 mV (P700) and 636 mV (P2000).

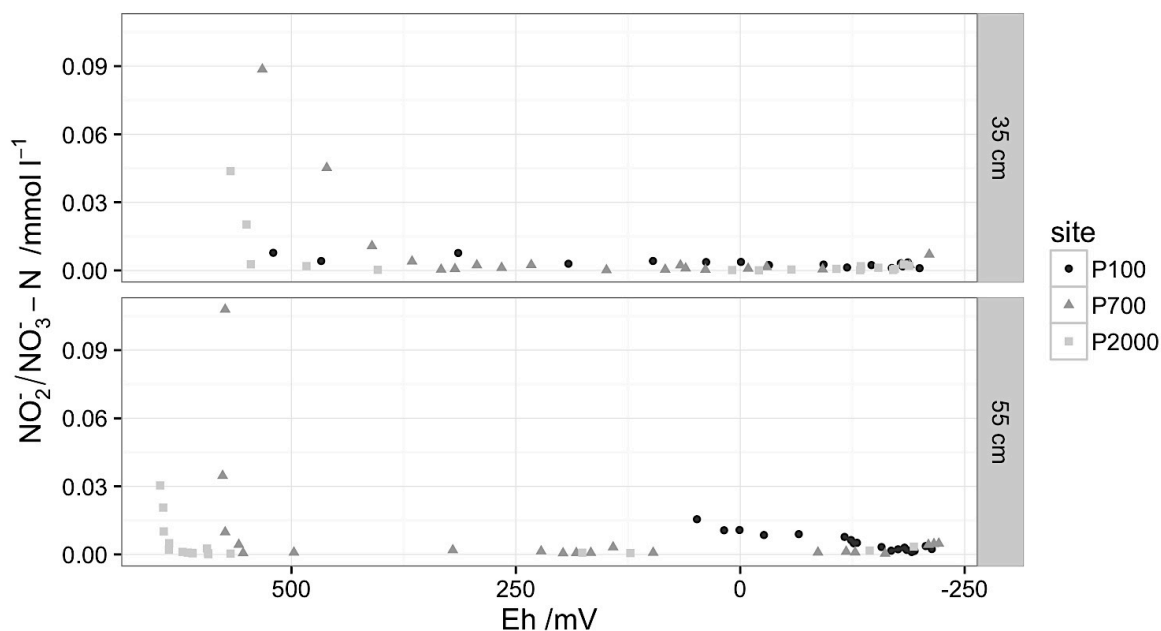


**Figure 5-16:** Relationship between redox potential in soil and  $\text{NO}_{2/3}^-$  concentrations (depicted as  $\text{NO}_{2/3}^-$ -N) in soil solutions at 35 and 55 cm depth of the paddy sites during the first two months after flooding.

Denitrification takes place in anaerobic zones (Ponnamperuma 1972), such as small microsites, characterised by elevated contents of labile OM (Vepraskas and Faulkner, 2001). Sextstone et al. (1985) observed denitrification within soil aggregates in an overall oxic soil system. Nitrite can even be denitrified in the presence of oxygen (Ponnamperuma, 1972). This may explain the fast decline of  $\text{NO}_{2/3}^-$  concentrations at Eh potentials still indicating an aerated soil (Eh >500 mV at pH 7). However, decreasing  $\text{NO}_{3/2}^-$  concentrations in the subsoil solutions might also result from dilution upon infiltration of nitrate-depleted water from upper soil layers (Alewell et al., 2008). Redox values measured at 10 cm indicate that the topsoils become reduced first and redox values drop rapidly into the range of nitrate reduction (topsoil Eh 3 days after flooding: -160 mV at P100 and -120 mV at P700). The puddled layer and possibly also the plough pan serve as a reduction barrier for  $\text{NO}_3^-$ , i.e., originating from the irrigation water and overlying horizons. Decreasing  $\text{NO}_3^-$  concentrations may not be exclusively an indicator for reduction *in-situ*, but also a mirror of the redox status and soil solution composition in the above lying horizons (Choi et al., 2013).

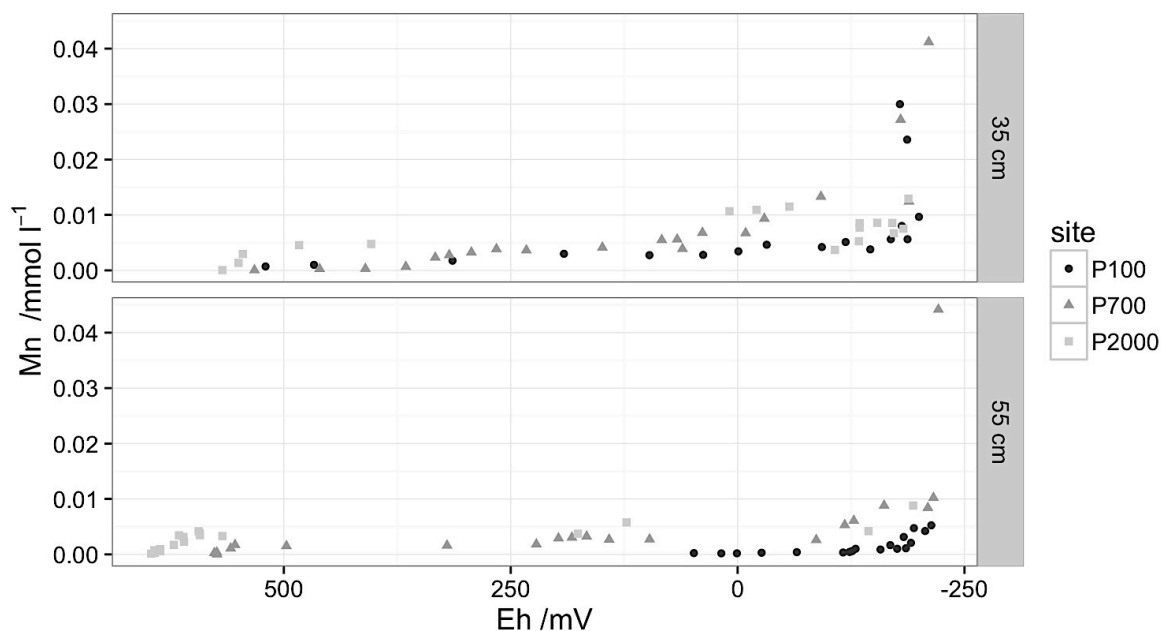


**Figure 5-17:** Relationship between redox potential in soil and Mn concentrations in soil solutions at 35 and 55 cm depth of the paddy sites during the first two months after flooding.

Denitrification was closely followed by the reduction of Mn(III, IV) and Fe(III). Increases in dissolved Mn (Figure 5-17), and, with slight delay, Fe (Figure 5-18) indicate microbial induced reductive dissolution of corresponding mineral phases, e.g., oxides. At circum neutral conditions Mn reduction usually starts at redox potentials between 200 and 250 mV (e.g., Patrick and Jugsujinda, 1992). Solution concentrations of Mn increased immediately after flooding in all three paddy soils and at higher redox values than thermodynamically expected. Concentrations remained low throughout the entire measurement period ( $<0.05 \text{ mmol l}^{-1}$ ). At the oldest paddy site, P2000, the concentrations of Mn levelled off after about 18 days, presumably due to depletion in reducible Mn oxides or precipitation of  $\text{MnS}$  (Gao et al., 2002) under the given Eh/pH conditions. In contrast, there was a sharp increase in  $\text{Mn}_t$  concentrations at the end of the measurement period at the youngest site; likely the given pH-Eh values ( $\text{pH} \geq 8.2$ ;  $\text{Eh} \leq -100 \text{ mV}$ ) were finally in the range where reductive dissolution of Mn oxide phases was possible.

The critical redox potential for iron reduction ranges between 150 to 180 mV at pH 7 (Patrick and Reddy, 1978; Patrick and Jugsujinda, 1992). A distinct increase in Fe occurred between 10 to  $-190 \text{ mV}$  in the upper subsoil and at 180 to  $-200 \text{ mV}$  in the lower subsoil. Critical redox potentials were highest at the oldest paddy sites, and were negatively correlated to pH. According to Gotoh and Patrick (1974), critical redox potentials for the on-set of Fe reduction decrease with increasing pH (pH 8 at  $\sim \text{Eh} -100 \text{ mV}$ ). Soil solutions at P100 and P700 were alkaline, which could explain the delayed on-set of Fe reduction (see section below).

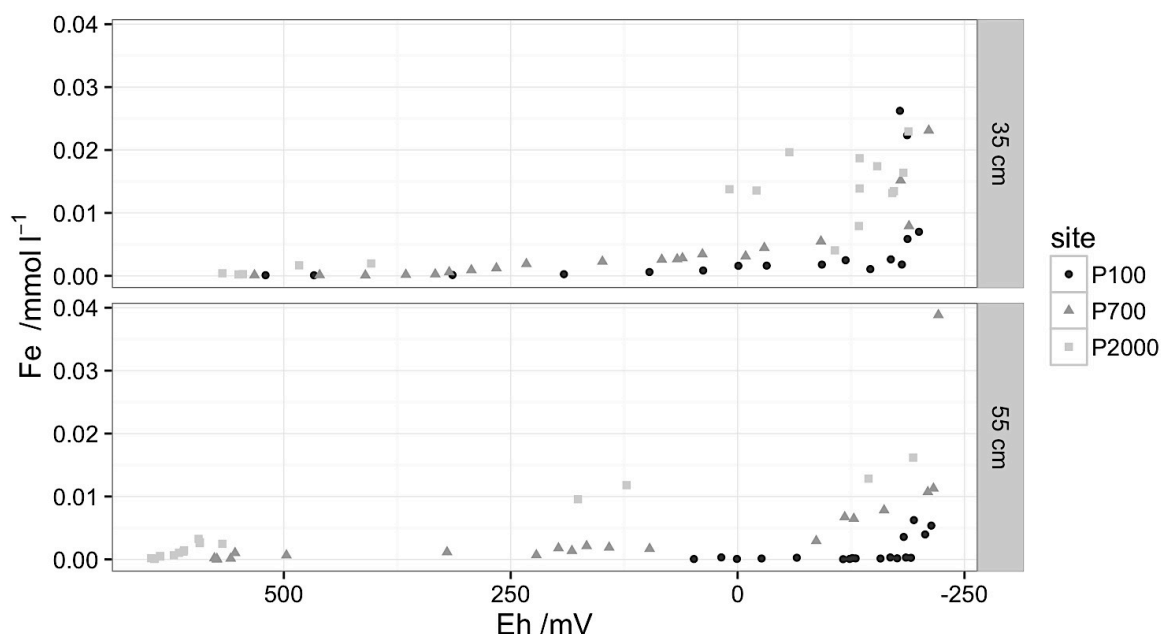


**Figure 5-18:** Relationship between redox potential in soil and Fe concentrations in soil solutions at 35 and 55cm depth of the paddy sites during the first two months after flooding.

Sulfate concentrations become instable at  $Eh \leq 120$  mV to 180 mV (e.g., Patrick and Reddy, 1978). Sulfate concentration in the soil solutions of all three paddy sites progressively decreased after submergence, with the most pronounced decrease at redox potentials below  $Eh = 0$  mV (Figure 5-19). The decrease in  $SO_4^{2-}$  concentrations in the lower subsoil at P2000 occurred already shortly after flooding and at Eh values of  $\geq 600$  mV. This could indicate  $SO_4^{2-}$  reduction at much higher redox potentials than thermodynamically predicted ( $Eh -50$  mV at pH 7). However, sulfate-reducing bacteria have been found in oxidized and even oxic sediment layers (Canfield and Des Marais, 1991). As for  $NO_3^-$ , sulfate reduction might not necessarily take place *in-situ* (i.e., at 55 cm), but in the reduced topsoil of P2000. Sulfate-depleted water percolating from above may dilute subsoil  $SO_4^{2-}$ . In neutral to alkaline soils, concentrations of  $SO_4^{2-}$  may be depleted within 6 weeks of submergence (Ponnamperuma, 1972), however, within the measurement period no depletion of  $SO_4^{2-}$  was observed at any of the test paddy sites. A continuous replenishment of  $SO_4^{2-}$  with the irrigation water seems likely.

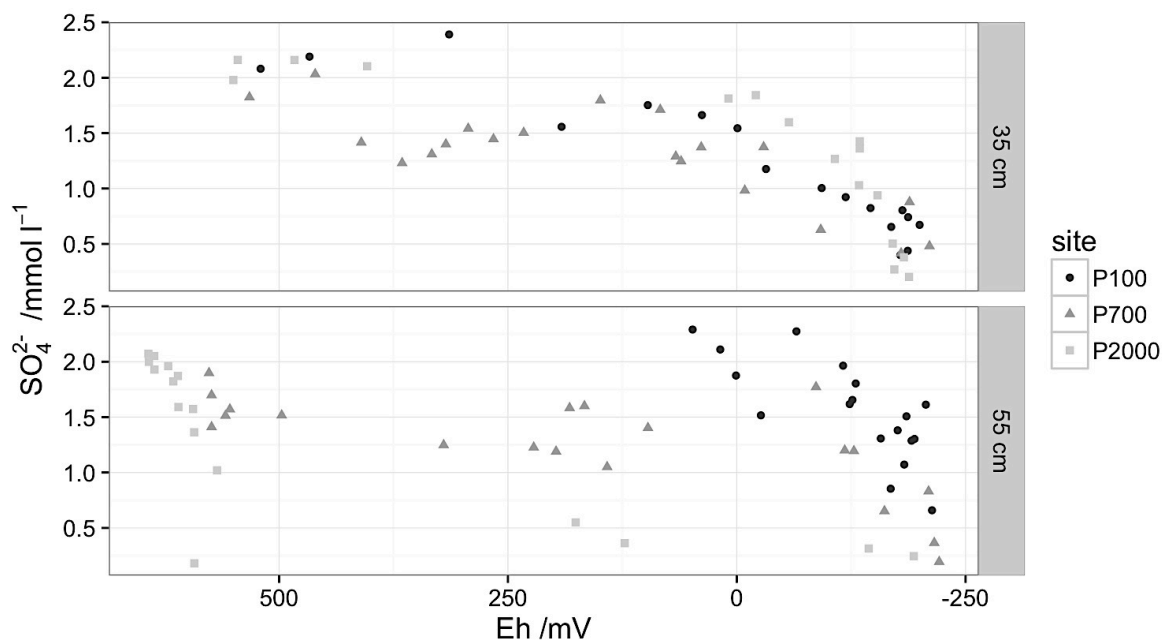


**Figure 5-19:** Relationship between redox potential in soil and  $\text{SO}_4^{2-}$  concentrations in soil solutions at 35 and 55cm depth of the paddy sites during the first two months after flooding.

Increasing DIC concentrations were observed at all paddy sites upon submergence, with the most pronounced increase at Eh values  $>0$  mV (Figure 5-20). This can be explained by  $\text{CO}_2$  accumulations in the paddy soils resulting from (anaerobic) microbial respiration and limited gas transfer due to water saturation (Kirk, 2004). Levelling of DIC contents can hint at the onset of methanogenesis (Ratering and Schnell, 2000), in which  $\text{CO}_2$  may serve as electron acceptor. Methane is an evidence of strongly reducing conditions (Ponnamperuma, 1972) and redox conditions ( $\leq -200$  mV) were theoretically low enough. However, DIC concentrations increased over the whole measurement period at all paddy sites. Thus, there were no indications of methanogenesis. According to Oremland and Polcin (1982) and Achtnich et al. (1995), methanogenesis is hampered until easily reducible  $\text{Fe(III)}$  and  $\text{SO}_4^{2-}$  are fully depleted, as methanogenic bacteria are usually outcompeted for common substrates, as  $\text{H}_2$  and acetate, by bacteria reducing  $\text{Fe}^{3+}$  or  $\text{SO}_4^{2-}$ . Estop-Aragones et al. (2013) showed for saturated peat soils that methanogenesis is strongly dampened by  $\text{SO}_4^{2-}$  at concentrations  $>100 \mu\text{mol l}^{-1}$ . In paddy soils methane production can be inhibited by ferric iron reduction processes (Jugsujinda and Patrick, 1996) and might increase again when iron reduction stops (Frenzel et al., 1999). Ferric Fe reduction by methanogens itself may also contribute to  $\text{Fe(III)}$  inhibition of methanogenesis (van Bodegom et al., 2004). In carbon-poor horizons, such as in subsoils, methane production is expected to be lower than in those with higher carbon contents (Ratering and Schnell, 2000). It is assumed that within the first 60 days of submergence methanogenesis was no important redox process in the subsoil of the study paddy sites.

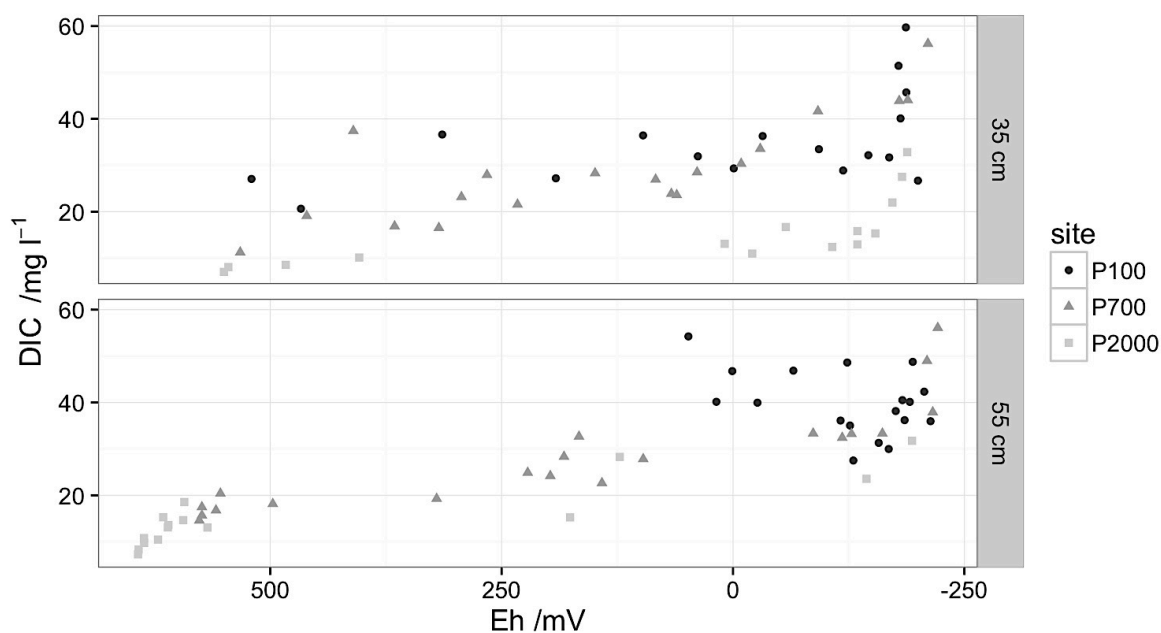


**Figure 5-20:** Relationship between redox potential in soil and dissolved inorganic carbon (DIC) concentrations in soil solutions at 35 and 55 cm depth of the paddy sites during the first two months after flooding.

***Low soluble Fe concentrations despite higher Fe oxide contents in the subsoil are result of low availability of the Fe oxides to microbial reduction***

Even under the most reductive conditions ( $\leq -200$  mV) little dissolved Fe occurred in soil water ( $\leq 0.01$  mmol  $\text{l}^{-1}$ ), despite clear morphological evidence of redox-induced Fe transformation and translocation in the test profiles. The  $\text{Fe}^{2+}$  activity in flooded soils may be largely governed by solubility of Fe(III) oxides (Bonneville et al., 2004). Their solubility increases with increasing surface area (Roden and Zachara, 1996), which again is closely related to their particle size and crystallinity.

Formation of microcrystalline goethite, as observed in the subsoil of the older paddy sites (Chapter 3), can dramatically decrease the reactivity of the solid matrix towards reductive dissolution (Hansel et al., 2003). The Eh–pH stability diagram (Figure 5-21) demonstrates that the measured Eh–pH values were mostly in the range of the stability of the different ferric oxide phases, especially at the younger paddy sites. Only at P2000, Eh–pH values indicate possible release of  $\text{Fe}^{2+}$  with respect to ferrihydrite, i.e., Eh–pH values were in the range where reductive dissolution of ferrihydrite-type mineral phases seems possible. Such minerals were abundant in all the test soils (Chapter 3).

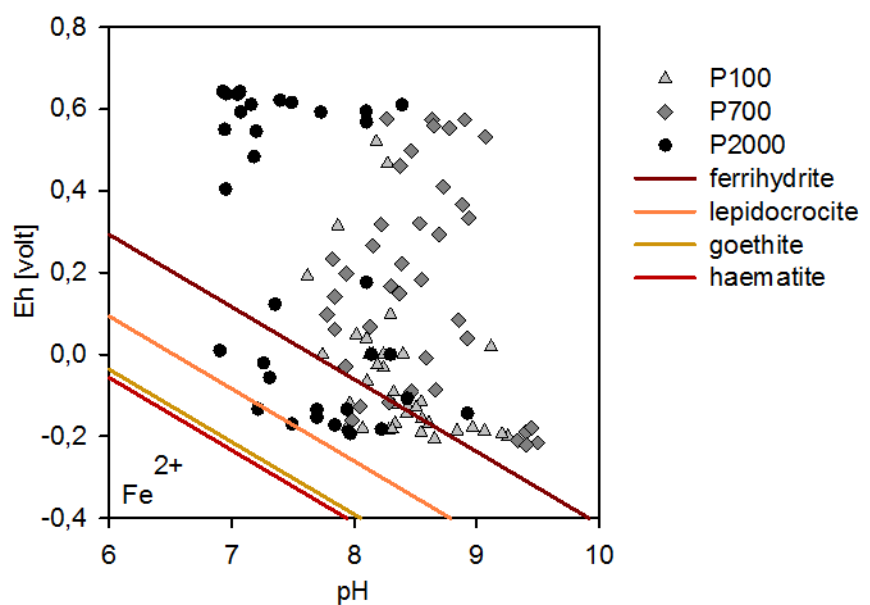


**Figure 5-21:** Eh-pH-stability diagram of the different types of Fe oxides identified in the clay mineral assemblage of the studied paddy soils.  $[\text{Fe}^{2+}] = 10^{-5} \text{ mol} \cdot \text{l}^{-1}$ .

Low availability of the Fe oxides to microbial reduction can explain the little dissolved Fe despite the higher Fe oxide contents at 35 and 55 cm at P700 and P2000. Solution concentrations of Fe of P700 and P2000 were larger than of P100. The youngest paddy sites were characterised by (1) high solution pH values throughout the measurement period and (2) mostly lower Fe oxide contents (Chapter 3). This could explain the smaller Fe concentrations at P100 than at the older paddy sites. The results indicate that the soil solution composition with respect to Fe was highly dependent on the Fe mineral assemblage. However, low Fe concentrations in the soil solution might not only be attributed to low contents of easily reducible Fe mineral phases at given environmental conditions but also be due to re-adsorption of  $\text{Fe}^{2+}$  to mineral and solid organic surfaces, with clay minerals, such as nontronite, becoming more important with increasing pH values (Jaisi et al., 2008b; Zhu and Elzinga, 2014). Ratering and Schnell (2000) reported that most Fe(II) was adsorbed to the solid-phase or immobilized as siderite and vivianite in a reduced paddy topsoil. In a batch experiment with paddy soil suspensions, only 4% of the water-soluble plus exchangeable Fe(II) was dissolved in the soil solution at a pH 8 and Eh of  $-250 \text{ mV}$  (Gotoh and Patrick, 1974). Thus, a considerable fraction of the Fe(II) is bound on the exchange complex at the measured Eh/pH values, and not in the soil solution. Due to decreasing pH levels with increasing paddy age the exchangeable fraction becomes most likely less important at the oldest paddy site, P2000, which contributes to increasing Fe concentrations with time under submergence. Precipitation of secondary Fe(II) minerals such as siderite (Fe carbonate), green rust (hydroxyl-interlayered

Fe oxide; Trolard and Bourri , 2008), troilite (FeS) and pyrite (FeS<sub>2</sub>) (Br mmer, 1974) is another possible explanation for small Fe concentrations. Formation of vivianite is unlikely as phosphate levels in the study soils were low (Zou et al., 2011). Siderite was reported to be the dominant precipitate in soils with a carbonate alkalinity  $\geq 1$  mmol l<sup>-1</sup>. Neither <sup>57</sup>Fe M ssbauer spectra nor XRD measurements of the clay fraction provided evidence of any ferrous minerals (see Chapter 3). However, these analyses have been carried out with oxidised samples, thus, hampering the identification of ferrous mineral phases, even if they were present during reduced periods. Sorption of Fe<sup>2+</sup> to mineral and solid organic surfaces has been shown to be kinetically favoured over precipitation of ferrous minerals at circumneutral to high pH (Charlet et al., 1998). Under prolonged reducing conditions ferrous Fe induced mineral precipitation may also hinder further microbial reduction by limiting the accessibility of the Fe(III) mineral or the bacterial surface (Roden and Zachara, 1996; Urrutia et al., 1998; Roden and Urrutia, 2002). Nevertheless, with the experimental set-up chosen we cannot fully elucidate, which of the mechanism controls/contribute to the small Fe concentrations.

A low availability of Fe to microbial reduction, however, could explain the rapid decrease of the redox potentials down to -200 mV and the overlapping of different redox processes, as observed at the test paddy sites (see section above). Fe(III) is the most important alternative electron acceptor in the absence of oxygen (Ponnamperuma, 1972; van Breemen, 1988). In wetland soils, changes in Eh and pH are mainly governed by the reduction of Fe(III) (Kirk, 2004). If at given environmental conditions only little Fe is available to microbial Fe reduction other electron acceptors are used instead, e.g., SO<sub>4</sub><sup>2-</sup>, and Eh values decrease rapidly.

***Higher organic carbon concentrations in the soil solution of the older paddy sites are partly attributed to downward transport of dissolved organic carbon from the organic matter-rich topsoils***

Dissolved organic matter plays a key role in the stabilization and mobilization of soil OM and thus, C dynamics in soils (Neff and Asner, 2001). Under anoxic conditions decomposition of OM results in increasing levels of water-soluble intermediate metabolites (Sahrawat, 2003) and high DOM concentrations (Quantin et al., 2008). Organic matter bound to Fe oxides may be released upon reductive dissolution of the sorbents and is thought to be an important factor governing DOC release into soil solution (Fiedler and Kalbitz, 2003; Sahrawat, 2003; Bishop et al., 2010). At the paddy sites studied no clear trend in DOC concentrations was observed upon decreasing redox values (Figure 5-22) only in the lower subsoils we observed a slight increase of DOC contents with time of submergence.

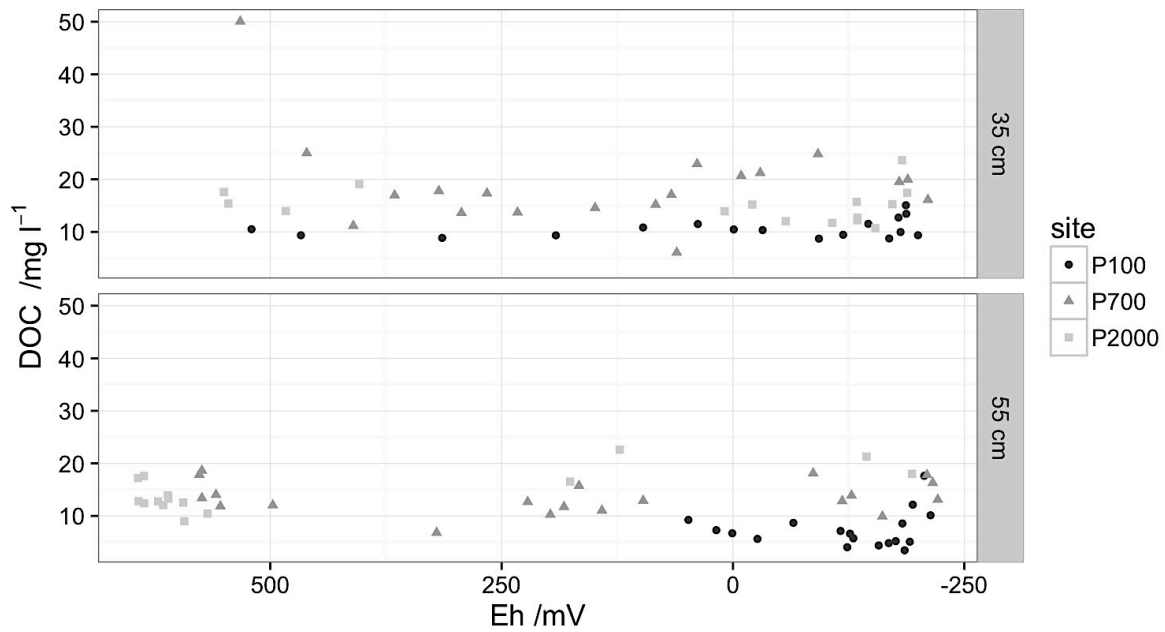


**Figure 5-22:** Mean dissolved organic carbon (DOC) concentrations in the soil solution plotted against mean redox values (Eh) of the three paddy sites during 60 days after flooding during the first two months after flooding.

Largest DOC concentrations were found in the subsoil solutions of the older paddy sites (P2000 > P700 > P100), even though OC concentrations in the respective subsoil horizon were smallest (Kölbl et al., 2014). It is assumed that DOC leaching from the top- into the subsoil horizons contributes to higher DOC concentrations in subsoils with time of paddy cultivation. Organic carbon concentrations in the topsoil increased with increasing time of paddy cultivation and were highest at the paddy 2000 site (Wissing et al., 2011, Kölbl et al., 2014). Sorption to Fe oxides was identified as an important mechanism of OM sequestration in the topsoils of older paddy sites (Wissing et al., 2013). As demonstrated in Chapter 3, paddy topsoil where characterised by the accumulation of poorly-crystalline, OM-rich hydrous ferric oxides and the decrease in crystallinity of goethite and haematite phases. These Fe minerals become reduced under anoxic conditions as found in paddy topsoils (Eh ranged between about +15 and -200 mV upon submergence); OM sorbed to the oxides might then be released. Also, compositional changes of DOM produced and processed in paddy topsoils under anoxic in comparison to oxic conditions may lead to a reduced adsorption on the surface of Fe oxide phases in paddy subsoils (Hanke et al., 2014) and thus, promote the mobility of DOM within paddy profiles during anoxic phases.

In batch experiments, Hanke et al. (2013) exposed paddy topsoils of the test chronosequence to alternating redox conditions. During anoxic periods ( $Eh \leq +150$  mV) they observed increasing DOC levels with increasing soil organic carbon (SOC) contents, and therefore, with time of cultivation, despite little Fe mineral reduction. This was explained by increasing

pH values during anoxic periods and, hence, an increasing solubility of OM and therefore enhanced desorption of sorbed OM from clay minerals and Fe oxides. According to Grybos et al. (2009), pH variations upon changing redox conditions can have an even stronger control on DOM release than the reductive dissolution of Fe oxides. Unlike P100 and P700, pH values in the subsoil of P2000 increased upon establishment of reducing conditions and, thus, might have additionally favoured the higher DOM concentrations in the soil solutions of the oldest paddy site.

## 5.5 Conclusion

Field measurements revealed similar redox patterns throughout the year for all paddy sites. In the lower subsoil of P100 and P700 temporal changes in redox potential were linked to raising groundwater tables in the course of paddy submergence, whereas at the oldest paddy site saturation of the soil column was solely due to irrigation. Thus, time of paddy cultivation and the resulting profile differentiation with respect to availability of electron donors (i.e., OM) and electron acceptors, e.g., Fe and Mn oxides, had little control on redox dynamics and the temporal sequence of redox processes. The soil solution composition of the paddy subsoils effectively reflected the sequence of alternative terminal electron acceptors, i.e.,  $\text{NO}_3^-$ , Mn(III, IV), Fe(III), and  $\text{SO}_4^{2-}$ , after depletion in  $\text{O}_2$ . In result, dissolved Fe, Mn, and DOC increased, and nitrate/nitrite and sulfate markedly decreased. The sequence of redox systems, however, was no strict chain, but showed overlaps, with co-occurrence of different reduction processes. Despite low redox potentials, Fe concentrations in the soil solution were little ( $<40 \mu\text{mol l}^{-1}$ ), even at the oldest, most Fe oxide-rich paddy site. It is assumed that to be due to the small overall low solubility of Fe oxides at the given weakly alkaline and saline conditions. Seemingly, high pH and high salinity hamper the redox cycling of Fe oxides and Mn oxides; the redox cycling of sulfate and nitrate is less affected. The most crucial factor for the little reductive release of  $\text{Fe}^{2+}$  in the subsoil could be the lack of rapidly reducible, weakly crystalline Fe oxide phases. The dominating Fe oxides are well-crystalline, thus, dissolve much slower, which might have contributed to the observed rapid decrease of the redox potentials down to  $-200 \text{ mV}$  and the co-occurrence of different redox processes. Thus, the redistribution patterns of Fe (and OM) upon paddy cultivation were partly mirrored by the concentrations of the respective dissolved species/compound in the soil solutions. The result supports the general idea of paddy subsoils being predominately accumulation zones for Fe leached from reduced overlying topsoils, thus, being little to no sources of Fe leaching to the groundwater. The subsoil solution compositions also indicated that the study paddy sites functioned as sinks for sulfate and nitrate.

## 6. Synopsis

### 6.1 Final discussion

#### *Iron mineral (trans)formations under long-term paddy cultivation*

Iron mineral phases are prone to transformations under changing redox conditions. The studied chronosequence provided a unique opportunity to study processes of mineral (trans)formations under long-term paddy usage. The paddy soils were characterised by an increasing profile differentiation of the Fe oxide fractions with the time of paddy cultivation and a continuum of crystallinities. In contrast, the non-paddy soils did not differ much in their depth distribution of Fe fractions, except for slight increases of goethite Fe in subsoils with time. In paddy topsoils, prolonged paddy cultivation and, hence, increasing numbers of redox cycles caused loss of Fe oxides and relative enrichment of poorly crystalline Fe oxides (Chapter 3). Despite generally high pH values throughout the chronosequence, as shown in the field experiments (Chapter 5), repeated anoxic conditions promoted the microbial-induced reductive dissolution of poorly crystalline as well as of well-crystalline oxides, such as goethite and haematite. With on-going paddy cultivation, the crystallinity of haematite and goethite decreased, in turn, proportions of nanocrystalline forms increased. Ferric iron released from crystalline and poorly crystalline Fe oxides was either leached into the subsoil with the percolating irrigation water, removed laterally with drainage water, or, upon drainage, oxidised *in-situ*. On the other hand some ferrous Fe was obviously introduced by irrigation and/or groundwater as indicated by mass balances along the study chronosequence (Kölbl et al., 2014). Rapid reoxidation of dissolved Fe(II) generally results in the precipitation of poorly crystalline Fe oxides such as ferrihydrite. The crystallisation process towards thermodynamically more stable Fe oxides, i.e., goethite and haematite (Cornell and Schwertmann, 2003), might be interrupted in soil environments with repeated redox cycling; poorly crystalline Fe oxide phases, such as ferrihydrite, accumulate instead. <sup>57</sup>Fe Mössbauer spectroscopy of the clay mineral fractions, however, indicated increasing organic–mineral interactions with time of paddy cultivation. Organic C in the clay fraction of the test soils related to Fe in poorly crystalline Fe oxides in the topsoil. It is assumed that in **paddy topsoils** the **present poorly-crystalline hydrous Fe oxide phases turn into** even more **disordered organic–mineral composites** with time of paddy cultivation. Paddy topsoils along the chronosequence were characterised by the accumulation of OM in the clay fraction as well as in the bulk soil (Kölbl et al., 2014), a common feature for paddy soils (Pan et al., 2003; Zhang and He, 2004; Kögel-Knabner et al., 2010; Wu, 2011). Increasing contents of OM are suspected to be responsible for the lower crystallinity of Fe oxides in paddy topsoils upon long-term cultivation (Zhang and Lin, 2002). According to Thompson et al. (2011), anoxic cycles in combination with high water throughput, subsequent Fe(II) leaching, and the

presence of high concentrations of OM during Fe oxidation results in increasing proportional abundance of poorly crystalline Fe oxides in soil environments prone to redox cycling. Comparable conditions can be expected for paddy soils. Upon reoxidation of soluble Fe(II), formation of dissolved organic Fe(III) complexes and disordered, organic-rich ferrihydrite is supported by DOM in the soil solution (Ratering and Schnell, 2000; Rancourt et al., 2005). The presence of OM during precipitation hampers ferrihydrite growth, resulting in smaller crystal sizes and greater structural disorder of the coprecipitated ferrihydrite (Schwertmann et al. 2005; Mikutta et al. 2008; Eusterhues et al. 2008; Mikutta 2011; Cismasu et al. 2011). During oxic periods mineral-associated OM may retard or even inhibit ferrihydrite transformation towards more crystalline Fe oxides (Schwertmann, 1966; Jones et al., 2009; Thompson et al., 2011). During anoxic periods, reductively released Fe(II) can induce catalytic reactions, resulting in the recrystallisation and/or solid state transformation of solid Fe(III) mineral phases (Pedersen et al., 2005). However, coprecipitated OM might decrease the extent of Fe(II) catalysed transformation of ferrihydrite or even inhibit transformation process towards more crystalline phases if C/Fe molar ratios are high enough (>1.6, Chen et al., 2015; Eusterhues et al., 2014). Obviously, in paddy topsoils increasing abundance of OM and coprecipitation of ferrihydrite-like phases with OM hindered mineral transformation towards more crystalline Fe oxides, leading to relative enrichment of poorly crystalline Fe oxide phases. Thus, the **accumulation of OM in paddy topsoils influences abundance and crystallinity of the Fe mineral phases present**. Wissing et al. (2013) proposed that these paddy-specific soil environments of Fe oxide (trans)formation are already established within 50 years of paddy cultivation along the study chronosequence. Thus, the presence of OM during Fe mineral transformation processes might be as important as the interruption of the crystallisation process by anoxic periods for lowering the crystallinity of topsoil Fe oxides during paddy soil evolution.

At the same time Fe oxides seem to control, at least partly, OM available to microbial consumption, presumably due to changing organic–mineral interactions and the formation of microaggregates upon interaction of Fe phases with OM (Wissing et al., 2014). Sorption to Fe oxides was identified as an important mechanism of OM sequestration in the topsoils of older paddy sites (Wissing et al., 2013). However, as Fe minerals are reduced under anoxic conditions (Eh ranged between about +15 and –200 mV upon submergence of paddy topsoils; Chapter 5) OM sorbed to the oxides might be released (e.g., Fiedler and Kalbitz, 2003; Sahrawat, 2003; Bishop et al., 2010) contributing to higher DOC concentrations in the soil solution at the older paddy sites (Chapter 5). The observed pH variations upon changing redox conditions might also contribute to DOM release (Grybos et al., 2009; Hanke et al., 2014).

In the OM poorer subsoil, different Fe oxide (trans)formation pathways were observed in comparison to paddy topsoils: instead of relative enrichment of poorly crystalline Fe oxide

phases, microcrystalline goethite became the prevalent Fe mineral. More crystalline phases may become enriched when Fe-reducing bacteria preferentially dissolve poorly crystalline Fe oxides (Munch and Ottow, 1980; Thamdrup, 2000; Zachara et al., 2002; Mansfeldt et al., 2012). However, results indicated that not residual enrichment caused the accumulation of the better crystalline Fe oxides in paddy subsoils, but secondary (trans)formation processes. The characterisation of the clay mineral assemblage as well as the *in-situ* experiments (Chapter 4) showed that at the older paddy sites less crystalline Fe oxides, i.e., ferrihydrite phases transform to more crystalline Fe oxides phases, such as goethite, haematite, and lepidocrocite. Ferrous Fe is known to promote structural transformation of poorly crystalline Fe oxides (e.g., ferrihydrite) to more crystalline and thermodynamically stable Fe oxide phases, such as haematite and goethite (Jones et al., 2009) and lepidocrocite (Pedersen et al., 2005). An **increase in crystallinity of Fe oxides in paddy subsoils** is thought to be largely **due to recrystallisation and/or solid state transformation** processes upon **repeated redox oscillations catalysed by aqueous Fe(II)**. Thompson et al. (2006) made similar observations in a batch experiment. Both supply rates and concentrations of Fe(II) in soil solution are important factors governing the secondary mineral species formed (Fredrickson et al., 1998; Benner et al., 2002; Hansel et al., 2003; Zachara et al., 2002; Yee et al., 2006). The observed low dissolved Fe concentrations ( $<0.04 \text{ mmol l}^{-1}$ ; Chapter 5) are thought to favour mainly goethite and lepidocrocite formation (Benner et al., 2002; Hansel et al., 2003). Largest concentrations of soluble Fe occurred at the older paddy sites, P700 and P2000. At these sites, goethite, haematite, and lepidocrocite formation was observed in the clay fractions of the subsoil as well as in the *in-situ* experiments with ferrihydrite.

Whereas goethite and haematite was detected in all subsoil horizons, results revealed that lepidocrocite formation was mainly restricted to the deeper subsoil, presumably due to lower  $p\text{CO}_2$  (Carlson and Schwertmann, 1990) and/or horizons characterised by higher chloride concentrations (Hansel et al., 2005) in soil solution due to the irrigation with brackish water. The *in-situ* weathering experiments (Chapter 4) supported that organic–mineral interactions were only of little importance for transformation processes of the hydrous Fe oxides in paddy subsoils; this is consistent with relatively small concentrations of OC in the soil solution (Chapter 5). Downward movement of OM is diminished by the paddy specific dense plough pan (Kalbitz et al., 2013; Bräuer et al. 2013). Thus, in **paddy subsoils, ferrous Fe instead of OM largely influences secondary Fe mineral transformations**, resulting in a decoupling of transformation processes between top- and subsoils. At the same time, the given environmental conditions along the paddy chronosequence obviously disfavoured redox-induced (structural) changes of the better-crystalline Fe oxide phases, such as goethite. Presumably, also formation of microcrystalline goethite, as observed in the subsoil of the older paddy sites and in the *in-situ* experiments, decreased the reactivity of the solid matrix towards reductive dissolution with time of paddy cultivation. The *in-situ* weathering experiments with synthetic microcrystalline goethite (Chapter 4) indicated that once formed,

microcrystalline goethite remains stable against microbial reduction, supporting its accumulation in the (upper) subsoil. To further elucidate the influence of both OM and ferrous Fe on mineral changes during paddy soil development batch experiments with paddy topsoils and subsoils under controlled Eh and pH conditions but with varying contents of (dissolved) OM and/or ferrous Fe concentrations seem plausible.

Besides Fe oxides, Fe-bearing clay minerals may play an important role in the Fe cycle of waterlogged soils. In the study soils, structural Fe of clay minerals amounted to half of the total Fe present (Chapter 3). Under long-term cultivation, **total Fe contents in aluminosilicates were slightly decreasing in paddy topsoils** but not in non-paddy topsoils, indicating that intermittent drainage and waterlogged conditions cause loss of silicate Fe, presumably due to intensified weathering upon irrigation and subsequent leaching of mineral constituents (Favre et al., 2002). Especially in the presence of organic ligands, reduction of structural Fe(III) can lead to clay mineral dissolution (Kostka et al., 1999; Dong et al. 2003a). The increasing abundance of OM in the older paddy topsoils may have additionally supported mineral weathering. In contrast to the Fe oxides assemblage, **little changes in the clay mineral assemblage along the chronosequence** were found. X-ray diffraction measurements of the clay mineral assemblage along the chronosequence as well as of the *in-situ* exposed nontronite (NAu-2) did not show neoformation of Fe-bearing aluminosilicates, such as smectite or illite as observed by Dong et al., (2003a) and Kim et al. (2004), respectively, in batch experiments. The **overall Fe(II)/Fe(III) ratios remained rather constant**, indicating constant weathering. However, the *in-situ* exposed nontronite showed distinct changes in surface colour from brown to blue-green (Chapter 4). The colour changes are strong indicators of **structural modifications in the surface region**. They are commonly observed for ferruginous smectite suspensions upon chemical and bacterial reduction of structural Fe(III) (e.g., Komadel et al., 1990, Lee et al., 2006) and can be ascribed to structural rearrangements in the crystal lattice (Stucki, 2011). Upon reoxidation of structural Fe(II), visible colour changes of the smectite are normally reversed, even though concurrent structural rearrangements are not fully reversible (Komadel et al., 1990; Stucki, 2011). It is assumed that the tested nontronite samples were least partly reduced at the pH and Eh values established during most time of submergence (Chapter 5) (Gorski et al., 2013) and reoxidised upon drainage and/or excavation, as no ferrous Fe could be detected using Mössbauer spectroscopy. Mössbauer analyses of the P2000 sample suggested structural modifications of nontronite at the oldest paddy site. Multiple sextets in the 4 K Mössbauer spectra revealed increased magnetic ordering in comparison to the original mineral. Likely, the increase in magnetic interactions in the sample retrieved from the P2000 subsoils is an intrinsic feature of reduced and reoxidised nontronites. No mineral phase documented literature could be matched to the Mössbauer parameters of the observed sextets. An increase in magnetic ordering can indicate irreversible changes of bonding relationships between the structural ferric Fe ions upon microbial reduction (Stucki, 2011) and was observed before for

nontronites, such as Garfield nontronite and NAu-2 (Yang et al., 2012 and Ribeiro et al., 2009, respectively). Irreversible magnetic ordering upon reduction and reoxidation was only observed for the extensive abiotic reducing of nontronite (Ribeiro et al., 2009) and ascribed to Fe migrating from cis- to trans-octahedral sites during structural Fe(III) reduction (Manceau et al., 2000a). To my best knowledge, this is the first time an obviously irreversible increase in magnetic ordering has been observed upon biotic reduction. It remains unclear if the increased magnetic ordering is directly related to the surface colour change. To clarify, additional measurements under controlled conditions in the laboratory or greenhouse seem necessary. Also, additional measurements with surface sensitive methods, such as X-ray photoelectron spectroscopy (XPS) and/or X-ray absorption spectroscopy (XAS), could give additional information on the surface composition (i.e., oxidation and structural state of Fe), and thus, reveal nature and origin of the colour change and its relation to the observed Mössbauer spectra.

### ***Redox dynamics upon long-term paddy management and subsequent changes in the soil solution composition***

Rice cultivation led to distinct redox cycles at the three paddy sites of the chronosequence with Eh ranges (+570 to –190 mV in the topsoils, +650 to –200 mV in the subsoils) (Chapter 5), comparable with those observed for other paddy (Ponnamperuma, 1972) and other submerged soils (Vorenhout et al., 2004).

As discussed above, depth distribution of electron donors (organic compounds) and potential acceptors (i.e., Fe minerals), and thus, the redox capacity, became more pronounced with time of paddy cultivation (Chapter 3). This redox capacity, among others, strongly governs the magnitude of reduction of a given soil (Achtlich et al., 1995). The three paddy sites were characterised by high spatial variability of the redox potential shortly after submergence, reflecting the spatial heterogeneity of the paddy soil profiles, and the stabilization of redox conditions at approx. –200 mV throughout the profiles after two months. Reducing conditions established more quickly in topsoil than in subsoil layers. Paddy topsoils are characterised by higher root and microbial activity (Ratering and Schnell, 2000) as well as higher abundance of OM than the subsoils, which supports a more rapid drop in Eh (Ratering and Schnell, 2000; Gao et al., 2004). Comparing the three paddy sites, differences in redox capacity were not reflected by redox dynamics in paddy subsoils: In the upper subsoil (35 cm), redox changes were similar in all three paddy soils, despite higher abundances of electron donors and easily available electron acceptors (i.e., nitrate, poorly-crystalline Fe oxides) in overlying topsoils and differences in concentration and crystallinity of Fe oxides in subsoils, respectively (Chapter 3). In the lower subsoil (55 cm), the decrease of Eh became slower with the time of paddy cultivation. However, this can be explained by generally higher groundwater tables at the younger sites. Rising groundwater obviously fastens the saturation of the deeper subsoils (e.g., Greppi, 2004); water saturation was achieved in subsoils at the same time or even before

topsoils. At P2000, groundwater levels were much lower ( $\geq 100$  cm beneath surface), thus, water saturation most likely was driven by infiltration of irrigation water. **Time span of paddy cultivation**, along with progressing depth differentiation of redox sensitive elements and OM, **did not result in significant changes in redox response to flooding and drying**. Redox dynamics seemed to be a simple function of actual management, e.g., time and length of irrigation, and/or groundwater levels. However, differences in the subsoils' water status between the three paddy sites might have partly masked potential differences in redox dynamics due to varying soil characteristics.

The increasing poor microbial reducibility of the Fe mineral assemblage in paddy subsoils (Chapter 3 and 4) might somewhat supported the similarity of redox changes between the three paddy sites. In wetland soils, changes in Eh and pH are mainly governed by the reduction of Fe(III) (Kirk, 2004). If at given environmental conditions only little Fe is available to microbial Fe reduction, other electron acceptors are used instead, e.g.,  $\text{SO}_4^{2-}$ , and Eh values decrease rapidly. The low availability of Fe to microbial reduction might contribute to the rapid decrease of the redox potentials to  $-200$  mV at all paddy sites, irrespective of time of paddy cultivation, and the overlapping of different redox processes, as observed at the test paddy sites (see above).

The redox potential at the three paddy sites theoretically crossed the thermodynamic equilibria of  $\text{NO}_3^-/\text{NH}_4^+$ ,  $\text{MnO}_2/\text{Mn}^{2+}$ ,  $\text{FeOOH}/\text{Fe}^{2+}$  and  $\text{SO}_4^{2-}/\text{HS}$  (Bartlett and James, 2000), suggesting substantial changes in the biogeochemistry of the bulk soil and soil solutions (Ponnamperuma, 1972; Patrick and Reddy, 1978; Gao et al., 2002). This was confirmed by the composition of the soil solutions at the three paddy sites during the first two months of submergence. The **soil solution composition clearly reflected the redox dynamics** in paddy subsoils, as already observed by, e.g., Boivin et al. (2002). All redox species showed a clear relationship to Eh and followed the sequence of reduction as thermodynamically predicted (Ponnamperuma, 1972), i.e.,  $\text{NO}_3^-$ , Mn(III, IV), Fe(III) and  $\text{SO}_4^{2-}$ . There were no clear indications of methanogenesis, i.e., decreasing  $\text{CO}_2$  levels. Methanogenesis can be hampered until reducible Fe(III) and  $\text{SO}_4^{2-}$  are fully depleted (Oremland and Polcin, 1982; Achtnich et al., 1995; Frenzel et al., 1999). The overlapping of the different redox processes, i.e., the reduction of Mn and Fe with sulfate reduction, indicated the simultaneous occurrence of reduction processes, which was already described for paddy (Peters and Conrad, 1996; Gao et al., 2002) as well as for riparian soils (Paul et al., 2006; Alewell et al., 2006; Alewell et al., 2008): Due to high small-scale heterogeneity of the soil different redox processes occur simultaneously but spatially separated in distinct micro- and mesosites (Alewell et al., 2006) not detectable by bulk redox measurements with Pt electrodes.

Both, composition of the mineral assemblage as well as the morphology of the paddy profiles, suggested Fe redistribution (Chapter 3). Surprisingly, only little dissolved Fe occurred in soil water ( $\leq 0.04 \text{ mmol} \cdot \text{l}^{-1}$ ) even under the most reductive conditions ( $\leq -200$  mV) (Chapter 5).

Complete desalination and decalcification/decarbonatisation are prerequisites for significant reductive Fe mobilisation (Kölbl et al., 2014). Paddy soils along the study chronosequence were desalinated within 50 years of embankment; decarbonatisation throughout the pedon was complete after 700 years of paddy cultivation (Kölbl et al., 2014). However, the field experiments indicated that both P100 and P700 still receive salt inputs with brackish irrigation and groundwater.  $\text{Na}^+$  and  $\text{Cl}^-$  were the dominant cation and anion, respectively, in most soil solutions of the two younger paddy sites. Soil solution reactions partly exceeded pH values of 8.4, indicating Na carbonate controlling pH (Gupta and Abrol, 1990). Under these conditions microbial Fe reduction capabilities may be reduced (Rietz and Haynes, 2003).

The  $\text{Fe}^{2+}$  activity in flooded soils is largely governed by microbial controlled dissolution of Fe(III) oxides. The reduction of Fe(III) oxides correlates with the solubility of the Fe oxides (ferrihydrite > lepidocrocite > goethite > haematite) (Fischer, 1987; Bonneville et al., 2004; Bonneville et al., 2009). The measured Eh–pH values were mostly in the range of the stability of ferric oxide phases present (i.e., goethite, haematite, ferrihydrite; Chapter 3), and thus, little Fe(II) can be released. Only at P2000 Eh–pH conditions favoured dissolution of less crystalline, ferrihydrite-type mineral phases, and thus, supported concomitant ferrous Fe production and mineral transformations catalysed by Fe(II). However, also at P700 increasing contents of soluble Fe were observed upon submergence, but slightly delayed in comparison to the P2000 site. The **composition of the soil solution somewhat reflects the (re)distribution patterns of Fe(III) oxides**. Ferrous Fe directly involved in secondary transformation processes, and thus, contributing to the accumulation of more crystalline Fe oxide phase, will not be present in the soil solution. Re-adsorption of  $\text{Fe}^{2+}$ , either released *in-situ* or leached from reduced topsoil, to mineral and solid organic surfaces (Gotoh and Patrick, 1974; Ratering and Schnell, 2000) might contributed to small Fe concentrations in the soil solution. At the measured Eh–pH values, a considerable fraction of the Fe(II) may be readsorbed and bound to the exchange complex. Some of the dissolved Fe in the soil solutions of the older paddy sites, P700 and P2000, presumably originated from paddy topsoil. Redox measurements at the three paddy sites (Chapter 5) support that redox ranges in paddy topsoils (+570 to –190 mV) were wide enough to produce  $\text{Fe}^{2+}_{\text{aq}}$  fluctuations. Increasing proportions of organic-rich, low crystalline Fe oxide phases with time of paddy cultivation and thus, better availability to microbial reduction might have contributed to Fe(II) release at the older paddy sites. No data on dissolved Fe in soil water exists for paddy topsoils to verify these assumptions. However, overall decreasing Fe oxide concentrations in paddy topsoils indicate that a considerable part of the Fe(II) is removed, i.e. by being leached downwards (Gong, 1983).

## 6.2 Final Conclusion

The present study supported that Fe dynamics and Fe-bearing mineral transformations play a crucial role for the biogeochemistry and evolution of paddy soils, and are important for the differentiation of paddy from non-paddy soils under long-term cultivation. With respect to the formulated research questions (see Chapter 1.5) following final conclusions can be drawn:

*Does long-term cultivation of rice intensify Fe mineral (trans)formation processes in comparison to sites under permanent oxic conditions (non-paddy sites)?*

Long-term cultivation of rice on calcareous marine substrates intensified Fe mineral weathering and redistribution of Fe in comparison to sites under permanent oxic conditions (non-paddy sites) and led to decoupling of top- and subsoil processes with respect to Fe contents and Fe mineral phases in the clay fraction. No such changes were observed in the non-paddy counterparts with permanent oxic conditions.

*Are there paddy-specific Fe mineral phases forming?*

Different Fe mineral-forming environments established in paddy top- and subsoils. Topsoils are characterised by reductive dissolution of the Fe minerals (silicates as well as crystalline and poorly crystalline oxide phases) during anoxic periods; upon oxic phases the coprecipitation of poorly crystalline Fe oxides with OM is prevalent. In paddy subsoils, in contrast, transformation processes seem to be mainly driven by dissolved Fe(II) leached from the topsoil or, under the environmental conditions less likely, by Fe(II) released *in-situ*. This resulted in increasing contents of Fe oxides and increasing crystallinity of the Fe oxides present, likely due to secondary transformation catalysed by Fe(II). *In-situ* experiments with test minerals confirmed that less crystalline Fe oxides were prone to transformations to more crystalline minerals in paddy subsoils. The time under paddy management, i.e., the redox status of the soils, had strong influence of ferrihydrite transformation. With time of paddy cultivation, more crystalline Fe oxides, such as goethite and haematite, and partly lepidocrocite, were formed. At the youngest paddy site, 100 years under paddy management, high pH and higher salinity, however, hindered transformations of Fe oxides.

*How does the accumulation of OM in the paddy topsoils influence abundance and crystallinity of the Fe mineral phases present?*

Obviously, in paddy topsoils organic–mineral interactions inhibit transformation and crystallisation of the Fe oxides present and lead to increasing proportions of poorly-crystalline, OM-rich hydrous ferric oxides and less well ordered goethite and haematite. Thus, the presence of OM controlled, at least partly, the composition and crystallinity of the Fe mineral assemblage in paddy topsoils. In paddy subsoils, in contrast, organic–mineral interactions were of little importance for transformation processes of the hydrous Fe oxides, likely because little organic carbon is transported into deeper soil layers.

*Does long-term paddy management result in changes of the assemblage of the Fe-bearing clay minerals and of its properties?*

In contrast to Fe oxides, Fe-bearing clay minerals were less affected by repeated redox cycles. Little changes in the clay mineral assemblage were observed along the chronosequence; observed differences among the paddy sites could not directly be related to the time of cultivation. However, the *in-situ* experiments with nontronite indicated some structural modifications, especially in the surface region, upon exposure to paddy conditions within little time. Such structural changes have been observed before only when exposing nontronite to harsh chemical reduction. Seemingly, also biotic reduction under natural conditions can induce such transformations. To my best knowledge this is the first study to show such changes under field conditions and within just one full redox cycle.

*Does the time span of paddy cultivation, along with progressing depth differentiation of redox sensitive elements and OM, result in significant changes in redox response to flooding and drying?*

Time of paddy cultivation and the resulting profile differentiation with respect to availability of electron donors (i.e., OM) and electron acceptors, e.g., Fe and Mn oxides, had little segregating control on redox dynamics and the temporal sequence of redox processes of the three paddy soils. At the study sites redox dynamics seemed to be a simple function of actual management, e.g., time and length of irrigation, and/or groundwater levels.

*To what extent is the soil solution composition a mirror of the redox status and/or the mineral assemblage of the soil?*

The soil solution composition of the paddy subsoils reflected the sequence of alternative terminal electron acceptors, i.e.,  $\text{NO}_3^-$ , Mn(III, IV), Fe(III) and  $\text{SO}_4^{2-}$ , after depletion in  $\text{O}_2$ , independent of the time of cultivation. The sequence of redox systems, however, was no strict chain, but showed overlaps, with co-occurrence of different reduction processes. The redistribution patterns of Fe (and OM) upon paddy cultivation were partly mirrored by the concentrations of the respective dissolved species/compound in the soil solutions. Despite low redox potentials, Fe concentrations in the soil solution were little ( $<40 \mu\text{mol l}^{-1}$ ), even at the oldest, most Fe oxide-rich site, presumably due to the small availability of microbial reducible Fe oxides at the given weakly alkaline and saline conditions. The most crucial factor for the little reductive release of  $\text{Fe}^{2+}$  in the subsoil could be the lack of rapidly reducible, weakly crystalline Fe oxide phases. Also, Fe(II) leaching from paddy topsoils might have been bound on the exchange complex and/or directly involved in solid state transformations, and thus, not contributed to soluble Fe contents but to secondary transformations in the subsoil. Evidently paddy subsoils serve predominately as accumulation zones for Fe leached from reduced overlying topsoils, thus, being little to no sources of Fe leaching to the groundwater.

## References

- Achtnich C., Bak F. and Conrad R. (1995) Competition for electron donors among nitrate reducers, ferric iron reducers, sulfate reducers, and methanogens in anoxic paddy soil. *Biol. Fertil. Soils* **19**, 65–72.
- Alewell C., Paul S., Lischeid G., Küsel K. and Gehre M. (2006) Characterizing the redox status in three different forested wetlands with geochemical data. *Environ. Sci. Technol.* **40**, 7609–7615.
- Alewell C., Paul S., Lischeid G. and Storck F. (2008) Co-regulation of redox processes in freshwater wetlands as a function of organic matter availability? *Sci. Total Environ.* **404**, 335–342.
- Amrhein C., Zahow M. F. and Suarez D. L. (1993) Calcite supersaturation in soil solutions. *Soil Sci.* **156**, 163–170.
- Augusto L., Ranger J., Turpault M.-P. and Bonnaud P. (2001) Experimental *in situ* transformation of vermiculites to study the weathering impact of tree species on the soil. *Eur. J. Soil Sci.* **52**, 81–92.
- Barré P., Velde B. and Abbadie L. (2007) Dynamic role of “illite-like” clay minerals in temperate soils: facts and hypotheses. *Biogeochemistry* **82**, 77–88.
- Bartlett R. J. and James B. R. (2000) Redox phenomena. In *Handbook of Soil Science* (ed. M. E. Sumner). CRC Press. Boca Raton, pp. B169–B194.
- Benner S. G., Hansel C. M., Wielinga B. W., Barber T. M. and Fendorf S. (2002) Reductive dissolution and biomineralization of iron hydroxide under dynamic flow conditions. *Environ. Sci. Technol.* **36**, 1705–1711.
- Benzine J., Shelobolina E., Xiong M. Y., Kennedy D. W., McKinley J. P., Lin X. and Roden E. E. (2013) Fe-phyllsilicate redox cycling organisms from a redox transition zone in Hanford 300 Area sediments. *Front. Microbiol.* **4**, 388.
- Bigham J. M., Fitzpatrick R. W. and Schulze D. G. (2002) Iron oxides. In *Soil mineralogy with environmental application* (eds. J. B. Dixon and D. G. Schulze). SSSA Inc. Madison Wis., 323–366.
- Bishop M. E., Jaisi D. P., Dong H., Kukkadapu R. K. and Ji J. (2010) Bioavailability of Fe(III) in loess sediments: an important source of electron acceptors. *Clays Clay Miner.* **58**, 542–557.
- Blakemore L. C., Searle P. L. and Darly B. K. (1987) Extractable iron, aluminum and silicon. In *Methods for Chemical Analysis of Soils* (ed. Blakemore L. C.). DISR. Lower Hutt, pp. 71–76.
- Bohn H. L. (1971) Redox potentials. *Soil Sci.* **112**, 39–45.
- Boivin P., Favre F., Hammecker C., Maeght J.-L., Delarivière J., Poussin J. C. and Wopereis M. C. S. (2002) Processes driving soil solution chemistry in a flooded rice-cropped vertisol: analysis of long-time monitoring data. *Geoderma* **110**, 87–107.
- Bonneville S., van Cappellen P. and Behrends T. (2004) Microbial reduction of iron(III) oxyhydroxides: effects of mineral solubility and availability. *Chem. Geol.* **212**, 255–268.

- Bonneville S., Behrends T. and van Cappellen P. (2009) Solubility and dissimilatory reduction kinetics of iron(III) oxyhydroxides: A linear free energy relationship. *Geochim. Cosmochim. Acta* **73**, 5273–5282.
- Bräuer T., Grootes P., Nadeau M.-J. and Andersen N. (2013) Downward carbon transport in a 2000-year rice paddy soil chronosequence traced by radiocarbon measurements. *Nucl. Instrum. Meth. B* **294**, 584–587.
- Bricker O. P., Godfrey A. E. and Cleaves E. T. (1968) Mineral–water intreractions during chemical weathering of silicates. *Adv. Chem.* **73**, 128–142.
- Brinkman R. (1969/1970) Ferrololysis, a hydromorphic soil forming process. *Geoderma* **3**, 199–206.
- Brümmer G. (1974) Redoxpotentiale und Redoxprozesse von Mangan-, Eisen- und Schwefelverbindungen in hydromorphen Böden und Sedimenten. *Geoderma* **12**, 207–222.
- Brunauer S., Emmett P. H. and Teller E. (1938) Adsorption of gases in multimolecular layers. *J. Am. Chem. Soc* **60**, 309–319.
- Bücher S. (2001). *Nitrogen and phosphorus availability in irrigated rice as influenced by soil drying during the fallow period, straw incorporation, and tillage*. ETH, Zürich.
- Canfield D. and Des Marais D. (1991) Aerobic sulfate reduction in microbial mats. *Science* **251**, 1471–1473.
- Cardile C. M., Johnston J. H. and Dickson D. P. E. (1986) Magnetic ordering at 4.2 and 1.3 K in nontronites of different iron contents: A  $^{57}\text{Fe}$  Mössbauer spectroscopic study. *Clays Clay Miner.* **34**, 233–238
- Carlson L. and Schwertmann U. (1990) The effect of  $\text{CO}_2$  and oxidation rate on the formation of goethite versus lepidocrocite from an Fe(II) system at pH 6 and 7. *Clay Miner.* **25**, 65–71.
- Cary L. and Trolard F. (2008) Metal mobility in the groundwater of a paddy field in Camargue (South eastern France). *J. Geochem. Explor.* **96**, 132–143.
- Catalano J. G., Fenter P., Park C., Zhang Z. and Rosso K. M. (2010) Structure and oxidation state of hematite surfaces reacted with aqueous Fe(II) at acidic and neutral pH. *Geochim. Cosmochim. Acta* **74**, 1498–1512.
- Chae G.-T., Kim K., Yun S.-T., Kim K.-H., Kim S.-O., Choi B.-Y., Kim H.-S. and Rhee C. W. (2004) Hydrogeochemistry of alluvial groundwaters in an agricultural area: an implication for groundwater contamination susceptibility. *Chemosphere* **55**, 369–378.
- Chae G.-T., Yun S.-T., Mayer B., Choi B.-Y., Kim K.-H., Kwon J.-S. and Yu S.-Y. (2009) Hydrochemical and stable isotopic assessment of nitrate contamination in an alluvial aquifer underneath a riverside agricultural field. *Agr. Water Manage.* **96**, 1819–1827.-
- Charlet L., Silvester E. and Liger E. (1998) N-compound reduction and actinide immobilisation in surficial fluids by Fe(II): the surface  $\equiv\text{Fe}^{\text{III}}\text{OFe}^{\text{II}}\text{OH}^\ominus$  species, as major reductant. *Chem. Geol.* **151**, 85–93.
- Chen C., Dynes J., Wang J., and Sparks D. L. (2014) Properties of Fe-organic matter associations via coprecipitation versus adsorption. *Environ. Sci. Technol.* **48**, 13751–13759.
- Chen C., Kukkadapu R., Sparks D. L. (2015) Influence of coprecipitated organic matter on  $\text{Fe}^{2+}_{(\text{aq})}$ -catalyzed transformation of ferrihydrite: Implications for carbon dynamics. *Environ. Sci. Technol.* **49**, 10927–10936.

- Chen L.-M., Zhang G.-L. and Effland W. R. (2011) Soil characteristic response times and pedogenic thresholds during the 1000-year evolution of a paddy soil chronosequence. *Soil Sci. Soc. Am. J.* **75**, 1807–1820.
- Chen S.-K. and Liu C.-W. (2002) Analysis of water movement in paddy rice fields (I) experimental studies. *J. Hydrol.* **260**, 206–215.
- Cheng Y.-Q., Yang L.-Z., Cao Z.-H., Ci E. and Yin S. (2009) Chronosequential changes of selected pedogenic properties in paddy soils as compared with non-paddy soils. *Geoderma* **151**, 31–41.
- Childers S. E., Ciuffo S. and Lovley D. R. (2002) *Geobacter metallireducens* accesses insoluble Fe(III) oxide by chemotaxis. *Nature* **416**, 767–769.
- Childs C. W. (1992) Ferrihydrite: A review of structure, properties and occurrence in relation to soils. *Z. Pflanzenernaehr. Bodenk.* **155**, 441–448.
- Childs C. W., Dickson D. P. E., Goodman B. A. and Lewis D. G. (1984) Mössbauer parameters for ferrihydrites at 4 K. *Aust. J. Soil Res* **22**, 149–154.
- Choi B.-Y., Yun S.-T., Kim K., Kim K.-H., Lee J.-H. and Han J.-S. (2013) A mesocosm study on biogeochemical role of rice paddy soils in controlling water chemistry and nitrate attenuation during infiltration. *Ecol. Eng.* **53**, 89–99.
- Chukrov F. V., Zvyagin B., Gorshkova I., Yermiloval P. and Balashov V. (1973) Ferrihydrite. *Izvestiya Akad. Nauk. SSSR Ser. Geol.* **4**, 23–33.
- Cismasu A. C., Michel F. M., Teaciu A. P., Tyliczszak T., Brown J. G. E. (2011) Composition and structural aspects of naturally occurring ferrihydrite. *C. R. Geosci.* **343**, 210–218.
- Cornell R. M. and Giovanoli R. (1985) Effect of solution conditions on the proportion and morphology of goethite formed from ferrihydrite. *Clays Clay Miner.* **33**, 424–432.
- Cornell R. M. and Schwertmann U. (2003) *The Iron Oxides*. Wiley-VCH, Weinheim.
- Cornell R. M., Giovanoli R. and Schneider W. (1989) Review of the hydrolysis of iron(III) and the crystallization of amorphous iron (III) hydroxide hydrate. *J. Chem. Technol. Biotechnol.* **46**, 115–134.
- Cornu S., Montagne D., Hubert F., Barré P. and Caner L. (2012) Evidence of short-term clay evolution in soils under human impact. *C. R. Geosci.* **344**, 747–757.
- Dong H., Kostka J. E. and Kim J. (2003a) Microscopic evidence for microbial dissolution of smectite. *Clay Miner.* **51**, 502–512.
- Dong H., Kukkadapu R. K., Fredrickson J. K., Zachara J. M., Kennedy D. W. and Kostandarites H. M. (2003b) Microbial reduction of structural Fe(III) in illite and goethite. *Environ. Sci. Technol.* **37**, 1268–1276.
- Drits V. A. and Manceau A. (2000) A model for the mechanism of Fe<sup>3+</sup> to Fe<sup>2+</sup> reduction in dioctahedral smectites. *Clays Clay Miner.* **48**, 185–195.
- Dyar M. D., Agresti D., Schaefer M. W., Grant C. and Sklute E. (2006) Mössbauer spectroscopy of earth and planetary materials. *Annu. Rev. Earth Planet. Sci.* **34**, 83–115.
- Eggleton A. (1977) Nontronite: chemistry and X-ray diffraction. *Clay Miner.* **12**, 181–194.
- Estop-Aragónés C., Knorr K.-H. and Blodau C. (2013) Belowground in situ redox dynamics and methanogenesis recovery in a degraded fen during dry-wet cycles and flooding. *Biogeosciences* **10**, 421–436.

- Eusterhues K., Rumpel C., Kleber M. and Kögel-Knabner I. (2003) Stabilisation of soil organic matter by interactions with minerals as revealed by mineral dissolution and oxidative degradation. *Org. Geochem.* **34**, 1591–1600.
- Eusterhues K., Rumpel C. and Kögel-Knabner I. (2005) Stabilization of soil organic matter isolated via oxidative degradation. *Org. Geochem.* **36**, 1567–1575.
- Eusterhues K., Wagner F. E., Häusler W., Hanzlik M., Knicker H., Totsche K. U., Kögel-Knabner I. and Schwertmann U. (2008) Characterization of ferrihydrite–soil organic matter coprecipitates by X-ray diffraction and Mössbauer spectroscopy. *Environ. Sci. Technol.* **42**, 7891–7897
- Eusterhues K., Rennert T., Knicker H., Kögel-Knabner I., Totsche K. U. and Schwertmann U. (2011) Fractionation of organic matter due to reaction with ferrihydrite: coprecipitation versus adsorption. *Environ. Sci. Technol.* **45**, 527–533.
- Eusterhues K., Hädrich A., Neidhardt J., Küsel K., Keller T. F., Jandt K. D., Totsche K. U. (2014) Reduction of ferrihydrite with adsorbed and coprecipitated organic matter: microbial reduction by *Geobacter bremensis* vs. abiotic reduction by Na-dithionite. *Biogeosciences* **11**, 4953–4966.
- Evangelou V. P. (1998) *Environmental soil and water chemistry*. Wiley-VCH, New York.
- FAO (2006) *Guidelines for soil description*. FAO, Rome.
- Favre F., Tessier D., Abdelmoula J. M., Génin W., Gates W. P. and Boivin P. (2002) Iron reduction and changes in cation exchange capacity in intermittently waterlogged soil. *Eur. J. Soil Sci.* **53**, 175–183.
- Favre F., Jaunet A. M., Pernes M., Badraoui M., Boivin P. and Tessier D. (2004) Changes in clay organization due to structural iron reduction in a flooded vertisol. *Clay Miner.* **39**, 123–134.
- Favre F., Stucki J. W. and Boivin P. (2006) Redox properties of structural Fe in ferroginous smectite. *Clays Clay Miner.* **54**, 466–472.
- Fiedler S. and Kalbitz K. (2003) Concentrations and properties of dissolved organic matter in forest soils as affected by the redox regime. *Soil Sci.* **168**, 793–801.
- Fiedler S., Verpraskas M. J. and Richardson J. L. (2007) Soil redox potential: importance, field measurements, and observations. *Adv. Agron.* **94**, 1–54.
- Fiedler S., Jungkunst H., Jahn R., Kleber M., Sommer M. and Stahr K. (2002) Linking soil classification and soil dynamics - pedological and ecological perspectives. *J. Plant Nutr. Soil Sci.* **165**, 517–529.
- Fischer W. R. (1987) Standard potentials ( $E_0$ ) of iron(III) oxides under reducing conditions. *Z. Pflanzenernaehr. Bodenk.* **150**, 286–289.
- Fitzpatrick R. W., Taylor R. M., Schwertmann U. and Childs C. W. (1985) Occurrence and properties of lepidocrocite in some soils of New Zealand, South Africa and Australia. *Aust. J. Soil Res.* **23**, 543.
- Fredrickson J. K., Zachara J. M., Kennedy D. W., Dong H., Onstott T. C., Hinman N. W. and Li S.-M. (1998) Biogenic iron mineralization accompanying the dissimilatory reduction of hydrous ferric oxide by a groundwater bacterium. *Geochim. Cosmochim. Acta* **62**, 3239–3257.

- Frenzel P., Bosse U. and Janssen P. H. (1999) Rice roots and methanogenesis in a paddy soil: ferric iron as an alternative electron acceptor in the rooted soil. *Soil Biol. Biochem.* **31**, 421–430.
- Gangas N. H. J., Wouterghem J. von, Mørup S. and Koch C. J. W. (1985) Magnetic bridging in nontronite by intercalated iron. *J. Phys. C: Solid State Phys.* **18**, 1011–1015.
- Gao S., Tanji K. K., Scardaci S. C. and Chow A. T. (2002) Comparison of redox indicators in a paddy soil during rice-growing season. *Soil Sci. Soc. Am. J.* **66**, 805–817.
- Gao S., Tanji K. K. and Scardaci S. C. (2004) Impact of rice straw incorporation on Soil redox status and sulfide toxicity. *Agron. J.* **96**, 70–76.
- Gates W. P., Slade P., Manceau A. and Lanson B. (2002) Site occupancies by iron in nontronites. *Clays Clay Miner.* **50**, 223–239.
- Gong Z.-T. (1983) Pedogenesis of paddy soil and its significance in soil classification. *Soil Sci.* **135**, 5–10.
- Gorski C. A., Aeschbacher M., Soltermann D., Voegelin A., Baeyens B., Marques Fernandes M., Hofstetter T. B. and Sander M. (2012a) Redox properties of structural Fe in clay minerals. 1. Electrochemical quantification of electron-donating and -accepting capacities of smectites. *Environ. Sci. Technol.* **46**, 9360–9368.
- Gorski C. A., Klüpfel L. E., Voegelin A., Sander M. and Hofstetter T. B. (2012b) Redox properties of structural Fe in clay minerals. 2. Electrochemical and spectroscopic characterization of electron transfer irreversibility in ferruginous smectite, SWa-1. *Environ. Sci. Technol.* **46**, 9369–9377.
- Gorski C. A., Klüpfel L. E., Voegelin A., Sander M. and Hofstetter T. B. (2013) Redox properties of structural Fe in clay minerals: 3. Relationships between smectite redox and structural properties. *Environ. Sci. Technol.* **47**, 13477–13485.
- Gotoh S. and Patrick W. H., Jr. (1974) Transformation of iron in a waterlogged soil as influenced by redox potential and pH. *Soil Sci. Soc. Am. J.* **38**, 66–71.
- Greenland D. J. (1997) *The sustainability of rice farming*. Cab International, Wallingford.
- Greppi M. (2004) Infiltration process and groundwater table raising in a paddy field area. *Paddy Water Environ* **2**, 171–179.
- GRiSP (Global Rice Science Partnership) (2013) *Rice almanac*. International Rice Research Institute, Los Baños.
- Grybos M., Davranche M., Gruau G., Petitjean P. and Pédrot M. (2009) Increasing pH drives organic matter solubilization from wetland soils under reducing conditions. *Geoderma* **154**, 13–19.
- Gupta R. K. and Abrol I. P. (1990) Salt-affected soils: Their reclamation and management for crop production. *Adv. Soil Sci.* **11**, 223–288.
- Hanke A., Cerli C., Muhr J., Borken W. and Kalbitz K. (2013) Redox control on carbon mineralization and dissolved organic matter along a chronosequence of paddy soils. *Eur. J. Soil Sci.* **64**, 476–487.
- Hanke A., Sauerwein M., Kaiser K. and Kalbitz K. (2014) Does anoxic processing of dissolved organic matter affect organic–mineral interactions in paddy soils? *Geoderma* **228–229**, 62–66.

- Hansel C. M., Benner S. G., Neiss J., Dohnalkova A., Kukkadapu R. K. and Fendorf S. (2003) Secondary mineralization pathways induced by dissimilatory iron reduction of ferrihydrite under advective flow. *Geochim. Cosmochim. Acta* **67**, 2977-2992.
- Hansel C. M., Benner S. G. and Fendorf S. (2005) Competing Fe(II)-induced mineralization pathways of ferrihydrite. *Environ. Sci. Technol.* **39**, 7147-7153.
- Hutchinson K. J. and Hesterberg D. (2004) Dissolution of phosphate in a phosphorus-enriched ultisol as affected by microbial reduction. *J. Environ. Qual.* **33**, 1793-1802.
- IRRI (1964) *Annual Report*. International Rice Research Institute, Los Baños.
- IUSS Working Group WRB (2007) World Reference Base for Soil Resources 2006. FAO, Rome.
- IUSS Working Group WRB (2014) World Reference Base for Soil Resources 2014. FAO, Rome.
- Jäckel U. and Schnell S. (2000) Suppression of methane emission from rice paddies by ferric iron fertilization. *Soil Biol. Biochem.* **32**, 1811-1814.
- Jäckel U., Russo S. and Schnell S. (2005) Enhanced iron reduction by iron supplement: A strategy to reduce methane emission from paddies. *Soil Biol. Biochem.* **37**, 2150-2154.
- Jaisi D. P., Kukkadapu R. K., Eberl D. D. and Dong H. (2005) Control of Fe(III) site occupancy on the rate and extent of microbial reduction of Fe(III) in nontronite. *Geochim. Cosmochim. Acta* **69**, 5429-5440.
- Jaisi D. P., Dong H. and Liu C. (2007a) Influence of biogenic Fe(II) on the extent of microbial reduction of Fe(III) in clay minerals nontronite, illite, and chlorite. *Geochim. Cosmochim. Acta* **71**, 1145-1158.
- Jaisi D. P., Dong H. and Liu C. (2007b) Kinetic analysis of microbial reduction of Fe(III) in nontronite. *Environ. Sci. Technol.* **41**, 2437-2444.
- Jaisi D. P., Dong H. and Morton J. P. (2008a) Partitioning of Fe(II) in reduced nontronite (NAu-2) to reactive sites: reactivity in terms of Tc(VII) reduction. *Clays Clay Miner.* **56**, 175-189.
- Jaisi D. P., Liu C., Dong H., Blake R. E. and Fein J. B. (2008b) Fe<sup>2+</sup> sorption onto nontronite (NAu-2). *Geochim. Cosmochim. Acta* **72**, 5361-5371.
- Janssen M. and Lennartz B. (2007) Horizontal and vertical water and solute fluxes in paddy rice fields. *Soil Till. Res.* **94**, 133-141.
- Jeon B.-H., Dempsey B. A., Burgos W. D. and Royer R. A. (2001) Reactions of ferrous iron with hematite. *Colloid Surface A* **191**, 41-55.
- Jeon B.-H., Dempsey B. A. and Burgos W. D. (2003) Kinetics and mechanisms for reactions of Fe(II) with iron(III) oxides. *Environ. Sci. Technol.* **37**, 3309-3315.
- Johnson C. E. (1969) Antiferromagnetism of gamma-FeOOH: A Mössbauer effect study. *J. Phys. C: Solid State Phys.* **2**, 1996-2002.
- Johnston A. E., Poulton P. R. and Coleman K. (2009) Soil organic matter. *Adv. Agron.* **101**, 1-57.
- Johnston J. H., Dickson D. P. E. and Cardile C. M. (1986) Magnetic ordering at 4.2 and 1.3 K in nontronites of different iron contents: A <sup>57</sup>Fe Mössbauer spectroscopic study. *Clays Clay Miner.* **34**, 233-238.

- Jones A. M., Collins R. N., Rose J. and Waite T. D. (2009) The effect of silica and natural organic matter on the Fe(II)-catalysed transformation and reactivity of Fe(III) minerals. *Geochim. Cosmochim. Acta* **73**, 4409–4422.
- Jugsujinda A. and Patrick W. H., Jr. (1996) Methane and water soluble iron production under controlled soil pH and redox conditions. *Commun. Soil Sci. Plant Anal.* **27**, 2221–2227.
- Kaiser K. and Guggenberger, Georg (2000) The role of DOM sorption to mineral surfaces in the preservation of organic matter in soils. *Org. Geochem.* **31**, 711–725.
- Kaiser K. and Guggenberger G. (2007) Sorptive stabilization of organic matter by microporous goethite: sorption into small pores vs. surface complexation. *Eur. J. Soil Sci.* **58**, 45–59.
- Kaiser K., Eusterhues K., Rumpel C., Guggenberger G. and Kögel-Knabner I. (2002) Stabilization of organic matter by soil minerals - investigations of density and particle-size fractions from two acid forest soils. *J. Plant Nutr. Soil Sci.* **165**, 451–459.
- Kalbitz K., Solinger S., Park J.-H., Michalzik B. and Matzner E. (2000) Controls on the dynamics of dissolved organic matter in soils: A review. *Soil Sci.* **165**, 277–304.
- Kalbitz K., Schwesig D., Rethemeyer J. and Matzner, E. (2007) Stabilization of dissolved organic matter by sorption to the mineral soil. *Soil Biol. Biochem.* **37**, 1319–1331.
- Kalbitz K., Kaiser K., Fiedler S., Kölbl A., Amelung W., Bräuer T., Cao Z.-H., Don A., Grootes P., Jahn R., Schwark L., Vogelsang V., Wissing L. and Kögel-Knabner I. (2013) The carbon count of 2000 years of rice cultivation. *Glob. Chang. Biol.* **19**, 1107–1113.
- Katoh M., Murase J. and Kimura M. (2004a) Sites and processes of nutrient accumulation in the subsoil through water percolation from the plow layer in a submerged paddy soil microcosm. *Soil Sci. Plant Nutr.* **50**, 731–738.
- Katoh M., Murase J., Hayashi M., Matsuya K. and Kimura M. (2004b) Nutrient leaching from the plow layer by water percolation and accumulation in the subsoil in an irrigated paddy field. *Soil Sci. Plant Nutr.* **50**, 721–729.
- Keeling J. L., Raven M. D. and Gates W. P. (2000) Geology and characterization of two hydrothermal nontronites from weathered metamorphic rocks at the Uley Graphite Mine, South Australia. *Clays Clay Miner.* **48**, 537–548.
- Kim J., Dong H., Seabaugh J., Newell S. W. and Eberl D. D. (2004) Role of microbes in the smectite-to-illite Reaction. *Science* **303**, 830–832.
- Kirk G. J. D. (2004) *The biogeochemistry of submerged soils*. Wiley-VCH, Chichester.
- Koch C., Mørup S., Madsen M. and Vistisen L. (1995) Iron-containing weathering products of basalt in a cold, dry climate. *Chem. Geol.* **122**, 109–119.
- Kögel-Knabner I., Guggenberger G., Kleber M., Kandeler E., Kalbitz K., Scheu S., Eusterhues K. and Leinweber P. (2008) Organo-mineral associations in temperate soils: integrating biology, mineralogy, and organic matter chemistry. *J. Plant Nutr. Soil Sci.* **171**, 61–82.
- Kögel-Knabner I., Amelung W., Cao Z.-H., Fiedler S., Frenzel P., Jahn R., Kalbitz K., Kölbl A. and Schloter M. (2010) Biogeochemistry of paddy soils. *Geoderma* **157**, 1–14.
- Kölbl A., Schad P., Jahn R., Amelung W., Bannert A., Cao Z., Fiedler S., Kalbitz K., Lehdorff E., Müller-Niggemann C., Schloter M., Schwark L., Vogelsang V., Wissing L. and Kögel-Knabner I. (2014) Accelerated soil formation due to paddy management on marshlands (Zhejiang Province, China). *Geoderma* **228-229**, 67–89.

- Komadel P., Lear P. R. and Stucki J. W. (1990) Reduction and reoxidation of nontronite: Extent of reduction and reaction rates. *Clays Clay Miner.* **38**, 203–208.
- Komlos J., Kukkadapu R. K., Zachara J. M. and Jaffé P. R. (2007) Biostimulation of iron reduction and subsequent oxidation of sediment containing Fe-silicates and Fe-oxides: Effect of redox cycling on Fe(III) bioreduction. *Water Res.* **41**, 2996–3004.
- Komlos J., Peacock A., Kukkadapu R. K. and Jaffé P. R. (2008) Long-term dynamics of uranium reduction/reoxidation under low sulfate conditions. *Geochim. Cosmochim. Acta* **72**, 3603–3615.
- Kostka J. E., Stucki J. W., Nealson K. H. and Wu J. (1996) Reduction of structural Fe(III) in smectite by a pure culture of *Shewanella putrefaciens* strain MR-1. *Clays Clay Miner.* **44**, 522–529.
- Kostka J. E., Haefele E., Viehweger R. and Stucki J. W. (1999a) Respiration and Dissolution of Iron(III)-Containing Clay Minerals by Bacteria. *Environ. Sci. Technol.* **33**, 3127–3133.
- Kostka J. E., Wu J., Nealson K. H. and Stucki J. W. (1999b) The impact of structural Fe(III) reduction by bacteria on the surface chemistry of smectite clay minerals. *Geochim. Cosmochim. Ac.* **63**, 3705–3713.
- Kralova M., Masscheleyn P. H., Lindau C. W. and Patrick W. H., Jr. (1992) Production of dinitrogen and nitrous oxide in soil suspensions as affected by redox potential. *Water Air Soil. Poll.* **61**, 37–45.
- Kukkadapu R. K., Zachara J. M., Fredrickson J. K. and Kennedy D. W. (2004) Biotransformation of two-line silica-ferrihydrite by a dissimilatory Fe(III)-reducing bacterium: formation of carbonate green rust in the presence of phosphate. *Geochim. Cosmochim. Acta* **68**, 2799–2814.
- Kyuma K. (2004) *Paddy soil science*. Kyoto University Press, Kyoto; Trans Pacific Press, Melbourne.
- Lavkulich M. L. (1981) *Methods Manual*. University of British Columbia, Vancouver.
- Lear P. R. and Stucki J. W. (1985) Role of structural hydrogen in the reduction and reoxidation of iron in nontronite. *Clays Clay Miner.* **33**, 539–545.
- Lee K., Kostka J. E. and Stucki J. W. (2006) Comparisons of structural Fe reduction in smectites by bacteria and dithionite: An infrared spectroscopic study. *Clays Clay Miner.* **54**, 195–208.
- Li Y.-L., Vali H., Sears S., Yang J., Deng B. and Zhang C. L. (2004) Iron reduction and alteration of nontronite NAu-2 by a sulfate-reducing bacterium. *Geochim. Cosmochim. Acta* **68**, 3251–3260.
- Li Z., Velde B. and Li D. (2003) Loss of K-bearing clay minerals in flood-irrigated, rice-growing soils in Jiangxi province, China. *Clays Clay Miner.* **51**, 75–82.
- Liang L., McCarthy J. F., Jolley L. W., McNabb J. A. and Mehlhorn T. L. (1993a) Iron dynamics: Transformation of Fe(II)/Fe(III) during injection of natural organic matter in a sandy aquifer. *Geochim. Cosmochim. Acta* **57**, 1987–1999.
- Liang L., McNabb J. A., Paulk J. M., Gu B. and McCarthy J. F. (1993b) Kinetics of iron(II) oxygenation at low partial pressure of oxygen in the presence of natural organic matter. *Environ. Sci. Technol.* **27**, 1864–1870.
- Liesack W., Schnell S. and Revsbech N. P. (2000) Microbiology of flooded rice paddies. *FEMS Microbiol. Rev.* **24**, 625–645.

- Liu H., Li P., Zhu M., Wei Y. and Sun Y. (2007) Fe(II)-induced transformation from ferrihydrite to lepidocrocite and goethite. *J. Solid State Chem.* **180**, 2121–2128.
- Liu S., Liu Y., Yang G., Qiao S., Li C., Zhu Z. and Shi X. (2012) Distribution of major and trace elements in surface sediments of Hangzhou Bay in China. *Acta Oceanol. Sin.* **31**, 89–100.
- Lovley D. R. (1991) Dissimilatory Fe(III) and Mn(IV) reduction. *Microbiol. Rev.* **55**, 259–287.
- Lovley D. R. and Blunt-Harris E. L. (1999) Role of humic-bound iron as an electron transfer agent in dissimilatory Fe(III) reduction. *Appl. Environ. Microbiol.* **65**, 4252–4254.
- Lovley D. R. and Phillips E. J. P. (1986) Availability of ferric iron for microbial reduction in bottom sediments of the freshwater tidal Potomac River. *Appl. Environ. Microbiol.* **52**, 751–757.
- Lovley D. R., Giovannoni S. J., White D. C., Champine J. E., Phillips E. J. P., Gorby Y. A. and Goodwin S. (1993) *Geobacter metallireducens* gen. nov. sp. nov., a microorganism capable of coupling the complete oxidation of organic compounds to the reduction of iron and other metals. *Arch. Microbiol.* **159**, 336–344.
- Lovley D. R., Coates J. D., Blunt-Harris E. L., Phillips E. J. P. and Woodward J. C. (1996) Humic substances as electron acceptors for microbial respiration. *Nature* **382**, 445–448.
- Lovley D. R., Fraga J. L., Blunt-Harris E. L., La Hayes, Phillips E. J. and Coates J. D. (1998) Humic substances as a mediator for microbially catalyzed metal reduction. *Acta Hydrochem. Hydrobiol.* **26**, 152–157.
- Lovley D. R., Holmes D. E. and Nevin K. P. (2004) Dissimilatory Fe(III) and Mn(IV) reduction. *Adv. Microbiol. Physiol.* **49**, 219–286.
- Majzlan J., Navrotsky A. and Schwertmann U. (2004) Thermodynamics of iron oxides: Part III. Enthalpies of formation and stability of ferrihydrite ( $\sim\text{Fe}(\text{OH})_3$ ), schwertmannite ( $\sim\text{FeO}(\text{OH})_{3/4}(\text{SO}_4)_{1/8}$ ), and  $\epsilon\text{-Fe}_2\text{O}_3$ . *Geochim. Cosmochim. Acta* **68**, 1049–1059.
- Manceau A. and Drits V. A. (1993) Local structure of ferrihydrite and feroxyhite by EXAFS spectroscopy. *Clay Miner.* **18**, 165–184.
- Manceau A., Drits V. A., Lanson B., Chateigner D., Wu J., Huo D., Gates W. P. and Stucki J. W. (2000a) Oxidation-reduction mechanism of iron in dioctahedral smectites: II. Crystal chemistry of reduced Garfield nontronite. *Am. Mineral.* **85**, 153–172.
- Manceau A., Lanson B., Drits V. A., Chateigner D., Gates W. P., Wu J., Huo D. and Stucki J. W. (2000b) Oxidation-reduction mechanism of iron in dioctahedral smectites: I. Crystal chemistry of oxidized reference nontronites. *Am. Mineral.* **85**, 133–152.
- Manceau A. (2009) Evaluation of the structural model for ferrihydrite derived from real-space modelling of high-energy X-ray diffraction data. *Clay Miner.* **44**, 19–34.
- Mansfeldt T. (2004) Redox potential of bulk soil and soil solution concentration of nitrate, manganese, iron, and sulfate in two Gleysols. *J. Plant Nutr. Soil Sci.* **167**, 7–16.
- Mansfeldt T., Schuth S., Häusler W., Wagner F. E., Kaufhold S. and Overesch M. (2012) Iron oxide mineralogy and stable iron isotope composition in a Gleysol with petroglycic properties. *J. Soils Sediments* **12**, 97–114.
- Marchand P. and Rancourt D. G. (2009) General model for the aqueous precipitation of rough-surface nanocrystals and application to ferrihydrite genesis. *Am. Mineral.* **94**, 1428–1439.

- Mehra O. P. and Jackson M. L. (1960) Iron oxide removal from soils and clays by dithionite-citrate system buffered with sodium bicarbonate. *Clays Clay Miner.* **7**, 317–327.
- Merola R. B. and McGuire M. M. (2009) Crystallographic site distribution and redox activity of Fe in nontronites determined by optical spectroscopy. *Clays Clay Miner.* **57**, 771–778.
- Mikutta C, Mikutta R., Bonneville S., Wagner F., Voegelin A., Christl I. and Kretzschmar R. (2008) Synthetic coprecipitates of exopolysaccharides and ferrihydrite. Part I: Characterization. *Geochim. Cosmochim. Acta* **72**, 1111–1127.
- Mikutta, C. (2011) X-ray absorption spectroscopy study on the effect of hydroxybenzoic acids on the formation and structure of ferrihydrite. *Geochim. Cosmochim. Acta* **75**, 5122–5139.
- Mikutta R., Kleber M., Kaiser K. and Jahn R. (2005) Review: Organic matter removal from soils using hydrogen peroxide, sodium hypochlorite, and disodium peroxodisulfate. *Soil Sci. Soc. Am. J.* **69**, 120–135.
- Mikutta R., Kleber M., Torn M. S. and Jahn R. (2006) Stabilization of soil organic matter: Association with minerals or chemical recalcitrance? *Biogeochemistry* **77**, 25–56.
- Mikutta R., Mikutta C., Kalbitz K., Scheel T., Kaiser K., Jahn R. (2007) Biodegradation of forest floor organic matter bound to minerals via different binding mechanisms. *Geochim. Cosmochim. Acta* **71**, 2569–2590.
- Mikutta R., Lorenz D., Guggenberger G., Haumaier L., and Freund A. (2014) Properties and reactivity of Fe-organic matter associations formed by coprecipitation versus adsorption: Clues from arsenate batch adsorption. *Geochim. Cosmochim. Acta* **144**, 258–276.
- Moore D. M. and Reynolds R. C. (1997) *X-ray diffraction and the identification and analysis of clay minerals*. Oxford Univ. Press, Oxford.
- Munch J. C. and Ottow J. C. G. (1980) Preferential reduction of amorphous to crystalline iron oxides by bacterial activity. *Soil Sci.* **129**, 15–21.
- Murad E. (1989) Poorly-crystalline minerals and complex mineral assemblages. *Hyperfine Interact.* **47**, 33–53.
- Murad E. (1988) The Mössbauer spectrum of "well"-crystallized Ferrihydrite. *J. Magn. Magn. Mater.* **74**, 153–157.
- Murad E. and Cashion J. (2004) *Mössbauer spectroscopy of environmental materials and their industrial utilization*. Kluwer Academic Publishers, Boston.
- Murad E. and Schwertmann U. (1984) The Influence of Crystallinity on the Mössbauer Spectrum of Lepidocrocite. *Mineralog. Mag.* **48**, 507–511.
- Murad E. and Schwertmann U. (1980) The Mössbauer spectrum of ferrihydrite and its relations to those of other iron oxides. *Am. Mineral.* **65**, 1044–1049.
- Murad E. and Wagner U. (1994) Mössbauer study of pure illite and its firing products. *Hyperfine Interact.* **91**, 685–688.
- Nevin K. P. and Lovley D. R. (2000) Lack of Production of Electron-Shuttling Compounds or solubilization of Fe(III) during reduction of insoluble Fe(III) oxide by *Geobacter metallireducens*. *Appl. Environ. Microbiol.* **66**, 2248–2251.
- Nevin K. P. and Lovley D. R. (2002) Mechanisms for Fe(III) Oxide Reduction in Sedimentary Environments. *Geomicrobiol. J.* **19**, 141–159.
- Newman D. K. and Kolter R. (2000) A role for excreted quinones in extracellular electron transfer. *Nature* **405**, 94–97.

- Nugent M. A., Brantley S. L., Pantano C. G. and Maurice P. A. (1998). *Nature* **395**, 588–591.
- O'Reilly S. E., Furukawa Y., Bickmore B., Kim J., Watkins J. and Newell S. W. (2005) Dissolution, precipitation, and Fe(III) reduction in experimental systems with nontronite (NAu-1) and *Shewanella oneidensis* MR-1. *Geochim. Cosmochim. Acta* **69**, A459.
- Oremland R. S. and Polcin S. (1982) Methanogenesis and sulfate reduction - competitive and noncompetitive substrates in estuarine sediments. *Appl. Environ. Microbiol.* **44**, 1270–1276.
- Pan G., Li L., Wu L. and Zhang X. (2003) Storage and sequestration potential of topsoil organic carbon in China's paddy soils. *Glob. Change Biol.* **10**, 79–92.
- Parfitt R. L., Childs C. W. (1988) Estimation of forms of Fe and Al: a review, and analysis of contrasting soils by dissolution and Moessbauer methods. *Aust. J. Soil Res.* **26**, 121–144.
- Patrick W. H., Jr. (1960) Nitrate reduction rates in a submerged soil as affected by redox potential. In *Transactions of 7th International Congress of Soil Science*, pp. 494–500.
- Patrick W. H., Jr. and DeLaune R. D. (1972) Characterization of the oxidised and reduced zones in flooded soils. *Soil Sci. Soc. Am. Proc.* **36**, 573–576.
- Patrick W. H., Jr. and Jugsujinda A. (1992) Sequential reduction and oxidation of inorganic nitrogen, manganese, and iron in flooded soil. *Soil Sci. Soc. Am. J.* **56**, 1071–1073.
- Patrick W. H., Jr. and Reddy K. R. (1978) Chemical changes in rice soils. In *Soils and rice* (ed. International Rice Research Institute). IRRI, Los Baños, pp. 361–379.
- Paul S., Küsel K. and Alewell C. (2006) Reduction processes in forest wetlands: Tracking down heterogeneity of source/sink functions with a combination of methods. *Soil Biol. Biochem.* **38**, 1028–1039.
- Pedersen H. D., Postma D., Jakobsen R. and Larsen O. (2005) Fast transformation of iron oxyhydroxides by the catalytic action of aqueous Fe(II). *Geochim. Cosmochim. Acta* **69**, 3967–3977.
- Peters V. and Conrad R. (1996) Sequential reduction processes and initiation of CH<sub>4</sub> production upon flooding of oxic upland soils. *Soil Biol. Biochem.* **28**, 371–382.
- Phillips E. J. P., Lovley D. R. and Roden E. E. (1993) Composition of non-microbially reducible Fe(III) in aquatic sediments. *Appl. Environ. Microbiol.* **59**, 2727–2729.
- Ponnamperuma F. N. (1972) The chemistry of submerged soils. *Adv. Agron.* **24**, 29–96.
- Ponnamperuma F. N., Martinez E. and Loy T. A. (1966) Influence of redox potential and partial pressure of carbon dioxide on pH values and the suspension effect on flooded soils. *Soil Sci.* **101**, 421–431.
- Quantin C., Grünberger O., Suvannang N. and Bourdon E. (2008) Land management effects on biogeochemical functioning of salt-affected paddy soils. *Pedosphere* **18**, 183–194.
- Rancourt D. G., McDonald A. M., Lalonde A. and Ping J. Y. (1993) Mössbauer absorber thicknesses for accurate site populations in Fe-bearing minerals. *Am. Mineral.* **78**, 1–7.
- Rancourt D. G., Thibault P. J., Mavrocordatos D. and Lamarche G. (2005) Hydrous ferric oxide precipitation in the presence of nonmetabolizing bacteria: Constraints on the mechanism of a biotic effect. *Geochim. Cosmochim. Acta* **69**, 553–577.
- Ranger J., Dambrine E., Robert M., Righi D. and Felix C. (1991) Study of current soil-forming processes using bags of vermiculite and resins placed within soil horizons. *Geoderma* **48**, 335–350.

- Ratering S. and Schnell S. (2000) Localization of iron-reducing activity in paddy soil by profile studies. *Biogeochemistry* **48**, 341–365.
- Reddy K. R. and DeLaune R. D. (2008) *Biogeochemistry of wetlands*. CRC Press, Boca Raton.
- Reddy K. R. and Patrick W. H., Jr. (1976) Effect of frequent changes in aerobic and anaerobic conditions on redox potential and nitrogen loss in a flooded soil. *Soil Biol. Biochem.* **8**, 491–495.
- Reddy K. R. and Patrick W. H., Jr. (1986) Denitrification losses in flooded rice fields. *Fertil. Res.* **9**, 99–116.
- Reguera G., McCarthy K. D., Mehta T., Nicoll J. S., Tuominen M. T. and Lovley D. R. (2005) Extracellular electron transfer via microbial nanowires. *Nature* **435**, 1098–1101.
- Ribeiro F. R., Fabris J. D., Kostka J. E., Komadel P. and Stucki J. W. (2009) Comparisons of structural iron reduction in smectites by bacteria and dithionite: II. A variable-temperature Mössbauer spectroscopic study of Garfield nontronite. *Pure Appl. Chem.* **81**, 1499–1509.
- Riedel T., Zak D., Biester H., Dittmar T. (2013) Iron traps terrestrially derived dissolved organic matter at redox interfaces. *Proc. Natl. Acad. Sci. USA* **110**, 10101–10105.
- Rietz D. N. and Haynes R. J. (2003) Effects of irrigation-induced salinity and sodicity on soil microbial activity. *Soil Biol. Biochem.* **35**, 845–854.
- Roden E. E. and Urrutia M. M. (2002) Influence of biogenic Fe(II) on bacterial crystalline Fe(III) oxide reduction. *Geomicrobiol. J.* **19**, 209–251.
- Roden E. E. and Zachara J. M. (1996) Microbial reduction of crystalline Iron(III) oxides: Influence of oxide surface area and potential for cell growth. *Environ. Sci. Technol.* **30**, 1618–1628.
- Roden E. E., Urrutia M. M. and Mann C. J. (2000) Bacterial reductive dissolution of crystalline Fe(III) oxide in continuous-flow column reactors. *Appl. Environ. Microbiol.* **66**, 1062–1065.
- Roth P. J., Lehdorff E., Cao Z.-H., Zhuang S., Bannert A., Wissing L., Schloter M., Kögel-Knabner I. and Amelung W. (2011) Accumulation of nitrogen and microbial residues during 2000 years of rice paddy and non-paddy soil development in the Yangtze River Delta, China. *Glob. Change Biol.* **17**, 3405–3417.
- Sahrawat K. L. (2003) Organic matter accumulation in submerged soils. *Adv. Agron.* **81**, 169–201.
- Sahrawat K. L. and Ponnamperna F. N. (1978) Measurement of exchangeable  $\text{NH}_4^+$  in tropical rice soils. *Soil Sci. Soc. Am. J.* **42**, 282–283.
- Sander T. and Gerke H. H. (2007) Preferential flow patterns in paddy fields using a dye tracer. *Vadose Zone J.* **6**, 105.
- Schaefer M. V., Gorski C. A. and Scherer M. M. (2011) Spectroscopic evidence for interfacial Fe(II)–Fe(III) electron transfer in a clay mineral. *Environ. Sci. Technol.* **45**, 540–545.
- Schneiders M. and Scherer H. W. (1998) Fixation and release of ammonium in flooded rice soils as affected by redox potential. *Eur. J. Agron.* **8**, 181–189.
- Schultz C. and Grundl T. (2004) pH dependence of ferrous sorption onto two smectite clays. *Chemosphere* **57**, 1301–1306.

- Schwartz R. and Miehlich G. (1993) Einsatz der Saugkerzentechnik in reduzierten Horizonten: Stoffausfällung im Fördersystem und methodische Verbesserungen. *Mitteilgn. Dtsch. Bodenkundl. Gesellsch.* **72**, 457–460.
- Schwertmann U. (1966) Inhibitory effect of soil organic matter on the crystallization of amorphous ferric hydroxide. *Nature* **212**, 645–646.
- Schwertmann U. (1964) Differenzierung der Eisenoxide des Bodens durch Extraktion mit Ammoniumoxalat-Lösung. *Z. Pflanzenernaehr. Dueng. Bodenk.* **105**, 194–202.
- Schwertmann U. and Fechter H. (1994) The formation of green rust and its transformation to Lepidocrocite. *Clay Miner.* **29**, 87–92.
- Schwertmann U. and Taylor R. M. (1972) The transformation of lepidocrocite to goethite. *Clays Clay Miner.* **20**, 151–158.
- Schwertmann U., Friedl J. and Stanjek H. (1999) From Fe(III) ions to ferrihydrite and then to hematite. *J. Colloid Interf. Sci.* **209**, 215–223.
- Schwertmann U., Wagner F.E., Knicker H. (2005) Ferrihydrite-humic associations. *Soil Sci. Soc. Am. J.* **69**, 1009–1015.
- Sexstone A. J., Revsbech N. P., Parkin T. B., Tiedje J. M. (1985) Direct measurement of oxygen profiles and denitrification rates in soil aggregates. *Soil Sci. Soc. Am. J.* **49**, 645–651.
- Smeck N. E., Bigham J. M., Guertal W. F. and Hall G. F. (2002) Spatial distribution of lepidocrocite in a soil hydrosequence. *Clay Miner.* **37**, 687–697.
- Smyth J. R. (1997) Crystal structure refinement and mössbauer spectroscopy of an ordered, triclinic clinocllore. *Clays Clay Miner.* **45**, 544–550.
- Sherman D. M. and Vergo N. (1988) Optical (diffusive reflectance) and Mössbauer spectroscopic study of nontronite and related Fe-bearing smectites. *Am. Mineral.* **73**, 1346–1354.
- Shimizu M., Zhou J., Schröder C., Obst M., Kappler A. and Borch T. (2013) Dissimilatory Fe reduction and transformation of ferrihydrite-humic acid coprecipitates. *Environ. Sci. Technol.* **47**, 13375–13384.
- Stucki J. W. (1988) *Iron in soils and clay minerals*. Reidel, Dordrecht.
- Stucki J. W. (2006) Properties and Behaviour of Iron in Clay Minerals. In *Handbook of Clay Science, Vol. 1* (eds. F. Bergaya, B. K. Theng and G. Lagaly). Elsevier, Oxford, Amsterdam, pp. 423–475.
- Stucki J. W. (2011) A review of the effects of iron redox cycles on smectite properties. *C. R. Geosci.* **343**, 199–209.
- Stucki J. W. and Kostka J. E. (2006) Microbial reduction of iron in smectite. *C. R. Geosci.* **338**, 468–475.
- Stucki J. W., Lee K., Zhang L. and Larson R. A. (2002) Effects of iron oxidation state on the surface and structural properties of smectites. *Pure Appl. Chem.* **74**, 2145–2158.
- Stucki J. W., Lee K., Goodman B. A. and Kostka J. E. (2007) Effects of in situ biostimulation on iron mineral speciation in a sub-surface soil. *Geochim. Cosmochim. Acta* **71**, 835–843.
- Stumm W. (1984) Interpretation and measurement of redox intensity in natural waters. *Schweiz. Z. Hydrologie* **46**, 291–296.
- Stumm W. and Morgan J. J. (1996) *Aquatic chemistry*. Wiley-VCH, New York.

- Stumm W. and Sulzberger B. (1992) The cycling of iron in natural environments: Considerations based on laboratory studies of heterogeneous redox processes. *Geochim. Cosmochim. Acta* **56**, 3233–3257.
- Su J. and Wang K. (1989) Changjiang river plume and suspended sediment transport in Hangzhou Bay. *Cont. Shelf Res.* **9**, 93–111.
- Suarez D. L. (1986) A soil water extractor that minimizes CO<sub>2</sub> degassing and pH errors. *Water Resour. Res.* **22**, 876–880.
- Suarez D. L. (1987) Prediction of pH errors in soil-water extractors due to degassing. *Soil Sci. Soc. Am. J.* **51**, 64–67.
- Tanwar K. S., Petitto S. C., Ghose S. K., Eng P. J. and Trainor T. P. (2009) Fe(II) adsorption on hematite (0001). *Geochim. Cosmochim. Acta* **73**, 4346–4365.
- Tanji K. K., Gao S., Scardaci S. C. and Chow A. T. (2003) Characterizing redox status of paddy soils with incorporated rice straw. *Geoderma* **114**, 333–353.
- Thamdrup B. (2000) Bacterial manganese and iron reduction in aquatic sediments. *Adv. Microbiol. Ecol.* **16**, 41–48.
- Thompson A., Chadwick O. A., Rancourt D. G. and Chorover J. (2006) Iron-oxide crystallinity increases during soil redox oscillations. *Geochim. Cosmochim. Acta* **70**, 1710–1727.
- Thompson A., Rancourt D. G., Chadwick O. A. and Chorover J. (2011) Iron solid-phase differentiation along a redox gradient in basaltic soils. *Geochim. Cosmochim. Acta* **75**, 119–133.
- Towe K. M. and Bradley W. F. (1967) Mineralogical constitution of colloidal "hydrous ferric oxides". *J. Colloid Interf. Sci.* **31**, 277–284.
- Trolard F. and Bourrié G. (2008) Geochemistry of green rusts and fougérite. *Adv. Agron.* **99**, 227–288.
- Urrutia M. M., Roden E. E., Fredrickson J. K. and Zachara J. M. (1998) Microbial and surface chemistry controls on reduction of synthetic Fe(III) oxide minerals by the dissimilatory iron-reducing bacterium *Shewanella alga*. *Geomicrobiol. J.* **15**, 269–291.
- van Asten P., van Zelfde J. 't, van der Zee S. and Hammecker C. (2004) The effect of irrigated rice cropping on the alkalinity of two alkaline rice soils in the Sahel. *Geoderma* **119**, 233–247.
- van Bodegom P. M.; Scholten J. C. M., Stams A. J. M. (2004) Direct inhibition of methanogenesis by ferric iron. *FEMS Microbiol. Ecol.* **49**, 261–268.
- van Breemen N. (1988) Effects of seasonal redox processes involving iron on the chemistry of periodically reduced soils. In *Iron in soils and clay minerals* (eds. J. W. Stucki, B. A. Goodman and U. Schwertmann). Springer. Amsterdam, pp. 797–809.
- van der Zee C., Roberts D. R., Rancourt D. G. and Slomp C. P. (2003) Nanogoethite is the dominant reactive oxyhydroxide phase in lake and marine sediments. *Geology* **31**, 993.
- Vepraskas M. and Faulkner S. P. (2001) Redox chemistry of hydric soils. In *Wetland soils* (eds. J. L. Richardson and M. J. Vepraskas). Lewis Publishers. Boca Raton, pp. 85–105.
- Vorenhout M., van der Geest H. G., van Marum D., Wattel K. and Eijsackers H. J. P. (2004) Automated and continuous redox potential measurements in soil. *J. Environ. Qual.* **33**, 1562–1567.

- Vogelsang V., Kaiser K., Wagner F. E., Fiedler S., Jahn R. (2016a) Transformation of clay-sized minerals in soils exposed to prolonged regular alternation of redox conditions. *Geoderma* **278**, 40–48.
- Vogelsang V., Fiedler S., Jahn R., Kaiser K. (2016b) *In-situ* transformation of iron-bearing minerals in paddy subsoils. *Eur. J. Soil Sci.* **67**, 676–685.
- Wang H., Yang Z., Wang Y., Saito Y. and Liu J. P. (2008) Reconstruction of sediment flux from the Changjiang (Yangtze River) to the sea since the 1860s. *J. Hydrol.* **349**, 318–332.
- Wang Y. T., Zhou X. D. and Wu J. J. (1992) Mössbauer study on the iron-oxide minerals of paddy soils derived from red soil in Fujian, China. *Hyperfine Interact.* **70**, 1037–1040.
- Weber K. A., Urrutia M. M., Churchill P. F., Kukkadapu R. K. and Roden E. E. (2006) Anaerobic redox cycling of iron by freshwater sediment microorganisms. *Environ. Microbiol.* **8**, 100–113.
- Wickham T. H. and Singh V. P. (1978) Water movement through wet soils. In *Soils and rice* (ed. International Rice Research Institute). IRRI Los Baños, Philippines, pp. 337–357.
- Williams A. G. B. and Scherer M. M. (2004) Spectroscopic evidence for Fe(II)–Fe(III) electron transfer at the iron oxide–water interface. *Environ. Sci. Technol.* **38**, 4782–4790.
- Wissing L., Kölbl A., Vogelsang V., Fu J.-R., Cao Z.-H. and Kögel-Knabner I. (2011) Organic carbon accumulation in a 2000-year chronosequence of paddy soil evolution. *Catena* **87**, 376–385.
- Wissing L., Kölbl A., Häusler W., Schad P., Cao Z.-H. and Kögel-Knabner I. (2013) Management-induced organic carbon accumulation in paddy soils: The role of organo–mineral associations. *Soil Till. Res.* **126**, 60–71.
- Wissing L., Kölbl A., Schad P., Bräuer T., Cao Z.-H. and Kögel-Knabner I. (2014) Organic carbon accumulation on soil mineral surfaces in paddy soils derived from tidal wetlands. *Geoderma* **228–229**, 90–103.
- Wright L. D. and Nittrouer C. A. (1995) Dispersal of river sediments in coastal seas: Six contrasting cases. *Estuaries* **18**, 494–508.
- Wu J. (2011) Carbon accumulation in paddy ecosystems in subtropical China: evidence from landscape studies. *Eur. J. Soil Sci.* **62**, 29–34.
- Wu J., Roth C. B. and Low P. F. (1988) Biological reduction of structural Fe in sodium-nontronite. *Soil Sci. Soc. Am. J.* **2**, 295–296.
- Xie D., Wang Z. and Gao S. V. H. J. de (2009) Modelling the tidal channel morphodynamics in a macro-tidal embayment, Hangzhou Bay, China. *Cont. Shelf Res.* **29**, 1757–1767.
- Xu H., Cai Z. C., Li X. P. and Tsuruta H. (2000) Effect of antecedent soil water regime and rice straw application time on CH<sub>4</sub> emission from rice cultivation. *Aust. J. Soil Res* **38**, 1–12.
- Yang J. (2010) *Effects of redox cycling of iron in nontronite on reduction of technetium*. Miami University, Miami.
- Yang J., Kukkadapu R. K., Dong H., Shelobolina E. S., Zhang J. and Kim J. (2012) Effects of redox cycling of iron in nontronite on reduction of technetium. *Chem. Geol.* **291**, 206–216.
- Yao H., Conrad R., Wassmann R. and Neue H.-U. (1999) Effect of soil characteristics on sequential reduction and methane production in sixteen rice paddy soils from China, the Philippines, and Italy. *Biogeochemistry* **47**, 269–295.

- Yee N., Shaw S., Benning L. G. and Nguyen T. H. (2006) The rate of ferrihydrite transformation to goethite via the Fe(II) pathway. *Am. Mineral.* **91**, 92–96.
- Yu J. Y., Park M. and Kim J. (2002) Solubilities of synthetic schwertmannite and ferrihydrite. *Geochem. J.* **36**, 119–132.
- Yu K. (2011) Redox Potential Control on cumulative global warming potentials from irrigated rice fields. In *Understanding greenhouse gas emissions from agricultural management* (eds. L. Guo et al.). American Chemical Society. Washington/DC, pp. 121–134.
- Zachara J. M., Kukkadapu R. K., Fredrickson J. K., Gorby Y. A. and Smith S. C. (2002) Biomineralization of poorly crystalline Fe(III) oxides by dissimilatory metal reducing bacteria (DMRB). *Geomicrobiol. J.* **19**, 179–207.
- Zeebe R. E. and Wolf-Gladrow D. A. (2001) *CO<sub>2</sub> in seawater*. Elsevier, Amsterdam.
- Zhang G.-L. and Gong Z.-T. (2003) Pedogenic evolution of paddy soils in different soil landscapes. *Geoderma* **115**, 15–29.
- Zhang M. and He Z. (2004) Long-term changes in organic carbon and nutrients of an Ultisol under rice cropping in southeast China. *Geoderma* **118**, 167–179.
- Zhang M., Lu H., Zhao X. J. and Li R. A. (2004) A comparative study of soil fertility change of upland soil in Cixi County. *Chinese J. Soil Sci.* **35**, 91–93.
- Zhang Y. S. and Lin X. Y. (2002) Relation between Fe-oxides transformation and phosphorus adsorption in the oxic and anoxic layers of two paddy soils as affected by flooding. *J. Zhejiang University* **28**, 485–491.
- Zhang Y. S., Lin X. Y. and Werner W. (2003) The effect of soil flooding on the transformation of Fe oxides and the adsorption/desorption behavior of phosphate. *J. Plant Nutr. Soil Sci.* **166**, 68–75.
- Zhi-Guang L. (1985) Oxidation-reduction potential. In *Physical chemistry of paddy soils* (ed. Y. Tian-ren). Springer. Berlin, pp. 1–26.
- Zhou W., He P., Li S., Lin B. (2005) Mineralization of organic sulfur in paddy soils under flooded conditions and its availability to plants. *Geoderma* **125**, 85–93.
- Zhu Y. and Elzinga E. J. (2014) Formation of layered Fe(II)-hydroxides during Fe(II) sorption onto clay and metal-oxide substrates. *Environ. Sci. Technol.* **48**, 4937–4945.
- Zong Y., Chen Z., Innes J. B., Chen C., Wang Z. and Wang H. (2007) Fire and flood management of coastal swamp enabled first rice paddy cultivation in east China. *Nature* **449**, 459–462.
- Zou P., Fu J.-R. and Cao Z.-H. (2011) Chronosequence of paddy soils and phosphorus sorption–desorption properties. *J. Soils Sediments* **11**, 249–259.

## A. Appendix: Soil profiles



**Figure A-1:** Images of the soil chronosequence of the marshland site (30 years) as well as the paddy (100, 700 and 2000 years) and respective non-paddy sites (100, 700 years) (modified from Kalbitz et al., 2013, and Koelbl et al., 2013). Soils were classified according to IUSS Working Group WRB (2007).

**Table A-1:** Field description of the study soils along the chronosequence of the marshland as well as paddy and non-paddy sites. Soil description was done according to FAO (2006) down to 1 m depth and classified according to IUSS Working Group WRB (2007) by R. Jahn and P. Schadt (DFG Research Group FOR 994 “Biogeochemistry of Paddy Soil Evolution”).

<b>Marshland 30 years</b>						
<b>Field description</b>	09.06.2008, during heavy rain, rainy since 2 days N: 30°18.819', E: 121°10.111' Gleyic Fluvisol (Calcaric, Hyposodic, Siltic)					
Depth cm	Horizon	Colour moist	Texture	CaCO <sub>3</sub> %	EC <sub>1:2.5</sub> mS cm <sup>-1</sup>	Eh V
0–13	n.a.	n.a.	n.a.	n.a.	n.a.	n.a.
13–30	n.a.	n.a.	n.a.	n.a.	n.a.	n.a.
<b>Paddy 100 years</b>						
<b>Field description</b>	05.06.2008, no rain during the last week N: 30°09.827', E: 121°20.971' Paddy, harvested Endogleyic Anthraquic Cambisol (Calcaric, Hyposodic, Siltic) Groundwater at 55 cm (1.66 mS cm <sup>-1</sup> )					
Depth cm	Horizon	Colour moist	Texture	CaCO <sub>3</sub> %	EC <sub>1:2.5</sub> mS cm <sup>-1</sup>	Eh V
0–9	(Alp1)	n.a.	n.a.	n.a.	n.a.	n.a.
9–15	(Alp2)	n.a.	n.a.	n.a.	n.a.	n.a.
0–15	Alp	10YR4/2	SiL	0	0.3	0.5
15–21	Ardp	10YR4/3	SiCL	2–5	0.3	0.6
21–30	Bwg1	10YR4/3.5	SiCL	2–5	0.3	0.6
30–50	Bwg2	10YR4.5/3	SiCL	2–5	0.3	0.5
50–75	Bwlg1	10YR4.5/3	SiCL	2–5	0.2	0.5
75–100	Bwlg2	10YR4.5/3	SiCL	2–5	0.1	0.4
<b>Paddy 700 years</b>						
<b>Field description</b>	04.06.2008, no rain during the last week N: 30°10.408', E: 121°09.180' Paddy (harvested) Endogleyic Hydragric Anthrosol (Hyposodic, Siltic, Thaptomollic)					
Depth cm	Horizon	Colour moist	Texture	CaCO <sub>3</sub> %	EC <sub>1:2.5</sub> mS cm <sup>-1</sup>	Eh V
0–10	Alp1	2.5Y3/2	n.a.	n.a.	n.a.	n.a.
10–16	Alp2	5Y2/2	n.a.	n.a.	n.a.	n.a.
16–22	Ardp	5Y3/2	n.a.	n.a.	n.a.	n.a.
22–45	Bg	2.5Y4/2	n.a.	n.a.	n.a.	n.a.
45–69	2Ahgb	2.5Y3/1	n.a.	n.a.	n.a.	n.a.
69–106	2Blg1	5Y4/1	n.a.	n.a.	n.a.	n.a.

n.a. not analysed

Table A-1 (continued)

<b>Paddy 2000 years</b>						
<b>Field description</b> 05.06.2008 Paddy (since 1 month flooded, for last 4 days flooding interrupted) Endogleyic Hydragric Anthrosol (Eutric, Siltic) Ground-/ irrigation water (0.86 mS cm <sup>-1</sup> )						
Depth cm	Horizon	Colour moist	Texture	CaCO <sub>3</sub> %	EC <sub>1:2.5</sub> mS cm <sup>-1</sup>	Eh V
0–15	Alp	2.5Y4/1	L	0	0.0	0.1
15–20	Ar(d)p	2.5Y4/1	L	0	0.0	0.1
20–27	Bdg	2.5Y5/2	SiCL	0	0.1	0.5
27–35	2AhgB	2.5y4/1	SiCL	0	0.0	0.5
35–50	2Bg1	2.5Y5/1	SiCL	0	0.0	0.6
50–70	2Bg2	2.5Y6/2	SiCL	0	0.4	0.6
70–100	2Blg	2.5Y4/2	SiCL	0	0.0	0.5

<b>Non-Paddy 100 years</b>						
<b>Field description</b> 12.06.2008, rain since afternoon of 7th June, last night without rain N: 30°11.884', E: 121°21.196' Field cropping, actually melons Endogleyic Cambisol (Calcaric, Siltic) Groundwater at 58 cm (3.34 mS cm <sup>-1</sup> )						
Depth cm	Horizon	Colour moist	Texture	CaCO <sub>3</sub> %	EC <sub>1:2.5</sub> mS cm <sup>-1</sup>	Eh V
0–14	Ap1	10YR3/3	SiL	0–2	0.2	0.4
14–25	Ap2	10YR4/3	SiL	2–5	0.2	0.4
25–30	Bw	10YR4/3	SiL	2–5	0.3	0.4
30–38	BCwg1	10YR4/4	SiL	2–5	n.a.	n.a.
38–70	BCwg2	10YR4/4	SiL	2–5	0.3	0.4
70–100	BCwlg	10YR4/4	SiL	2–5	0.5	0.2

<b>Non-Paddy 700 years</b>						
<b>Field description</b> 07.06.2008, no rain during the last week, rain since some hours N: 30°10.967', E: 121°08.706' Field cropping, actually cotton (harvested) after rape seed Haplic Cambisol (Eutric, Siltic)						
Depth cm	Horizon	Colour moist	Texture	CaCO <sub>3</sub> %	EC <sub>1:2.5</sub> mS cm <sup>-1</sup>	Eh V
0–11	Ap1	10YR3.5/3	SiL	0	0.1	0.6
11–17	Ap2	7.5YR4/3	SiL	0–2	0.1	0.6
17–23	Bw1	7.5YR4/3	SiL	0–2	0.1	0.6
23–45	Bw2	7.5YR4/3	SiL	2–10	0.1	0.4
45–70	Bw11	7.5YR4/3	SiL	2–10	0.2	0.5
70–100	Bw12	7.5YR4/3	SiL	2–10	0.2	0.4

n.a. not analysed

## B. Appendix: Soil properties

**Table B-1:** Total carbon ( $C_{\text{total}}$ ) and total nitrogen ( $N_{\text{total}}$ ) concentrations in the clay fractions of paddy (P) and non-paddy sites (NP). Organic carbon (OC) was calculated by subtracting total inorganic carbon (IC) from  $C_{\text{total}}$ . The marshland site (ML30) is given as point zero of soil evolution.

Site	Depth cm	$C_{\text{total}}$ g $\text{kg}_{\text{clay}}^{-1}$	$N_{\text{total}}$ g $\text{kg}_{\text{clay}}^{-1}$	C/N-ratio	IC g $\text{kg}_{\text{clay}}^{-1}$	OC g $\text{kg}_{\text{clay}}^{-1}$
<b>ML30</b>	0–13	15.9	1.2	13.0	n.d.	15.9
	13–30	14.6	1.0	14.2	n.d.	14.6
<b>P100</b>	0–9	36.5	4.2	9.2	n.d.	36.5
	9–15	33.1	4.0	8.7	n.d.	33.1
	15–21	16.6	1.8	10.0	n.d.	16.6
	21–30	9.3	0.6	15.0	n.d.	9.3
	30–50	6.4	0.8	7.8	n.d.	6.4
	50–75	6.2	0.8	7.5	n.d.	6.2
	70–100	7.0	0.9	8.2	n.d.	7.0
<b>P700</b>	0–10	41.6	4.3	10.5	n.d.	41.6
	10–16	24.8	2.5	10.7	n.d.	24.8
	16–22	22.6	2.4	10.1	n.d.	22.6
	22–45	12.0	1.1	11.4	n.d.	12.0
	45–69	9.3	0.9	10.9	n.d.	9.3
	69–106	4.9	0.7	7.1	n.d.	4.9
<b>P2000</b>	0–15	55.2	6.4	9.1	n.d.	55.2
	15–20	42.5	4.8	9.4	n.d.	42.5
	20–27	15.1	1.4	11.7	n.d.	15.1
	27–35	8.4	0.9	9.7	n.d.	8.4
	35–50	5.3	0.6	9.5	n.d.	5.3
	50–70	3.7	0.6	6.3	n.d.	3.7
	70–100	3.5	0.5	7.2	n.d.	3.5

n.d. = not detectable

**Table B-2:** Total carbon ( $C_{total}$ ) and total nitrogen ( $N_{total}$ ) concentrations in the clay fractions of non-paddy sites (NP). The marshland site (ML30) is given as point zero of soil evolution. Organic carbon (OC) was calculated by subtracting total inorganic carbon (IC) from  $C_{total}$ .

Site	Depth cm	$C_{total}$ g kg <sub>clay</sub> <sup>-1</sup>	$N_{total}$ g kg <sub>clay</sub> <sup>-1</sup>	C/N-ratio	IC g kg <sub>clay</sub> <sup>-1</sup>	OC g kg <sub>clay</sub> <sup>-1</sup>
<b>ML30</b>	0–13	15.9	1.2	13.0	n.d.	15.9
	13–30	14.6	1.0	14.2	n.d.	14.6
<b>NP100</b>	0–14	14.2	1.6	9.2	n.d.	14.2
	14–25	15.7	1.8	9.1	n.d.	15.7
	25–30	14.7	1.4	11.4	n.d.	14.7
	30–38	7.7	1.0	7.9	n.d.	7.7
	38–70	8.0	1.0	8.6	n.d.	8.0
	70–100	8.4	1.0	8.2	n.d.	8.4
<b>NP700</b>	0–12	29.7	3.3	9.6	n.d.	29.7
	12–17	18.0	2.1	9.1	n.d.	18.0
	17–23	11.0	1.3	8.7	n.d.	11.0
	23–45	7.6	1.2	6.8	n.d.	7.6
	45–70	6.4	0.9	7.8	n.d.	6.4
	70–100	5.9	0.8	7.6	n.d.	5.9

n.d. = not detectable

**Table B-3:** Cation exchange capacity ( $CEC_{pH7}$ ), exchangeable cations and base saturation (BS) of non-paddy (NP) clay fractions. The marshland site (ML30) is given as point zero of soil evolution.

Site	Depth cm	$CEC_{pH7}$	$Na^+$	$K^+$	$Ca^{2+}$	$Mg^{2+}$	BS %
			mmol <sub>c</sub> kg <sub>clay</sub> <sup>-1</sup>				
<b>ML30</b>	0–13	187.7	2.6	7.3	136.3	41.5	100
	13–30	201.0	6.0	5.4	147.6	42.0	100
<b>NP100</b>	0–14	482.9	2.3	9.4	377.5	65.8	94
	14–25	529.6	1.4	9.3	396.4	76.4	91
	25–30	501.8	1.0	9.3	396.6	59.4	93
	30–38	463.5	1.7	8.9	346.9	53.3	89
	38–70	462.0	2.1	9.7	353.2	97.1	100
	70–100	474.7	2.3	8.9	331.5	71.8	87
<b>NP700</b>	0–12	627.3	0.6	10.2	343.8	110.7	74
	12–17	653.6	1.3	9.1	369.5	132.6	78
	17–23	592.8	0.4	7.9	340.6	127.6	80
	23–45	490.6	0.9	8.3	341.5	89.6	90
	45–70	503.9	0.7	7.7	342.7	74.3	84
	70–100	453.9	1.2	9.1	349.8	93.8	100

**Table B-4:** Total element concentrations in the clay fractions of paddy (P) sites, determined with XRF.

Site	Depth cm	Al <sub>t</sub>	Ca <sub>t</sub>	Fe <sub>t</sub>	K <sub>t</sub>	Mg <sub>t</sub>	Mn <sub>t</sub> g kg <sub>clay</sub> <sup>-1</sup>	Na <sub>t</sub>	P <sub>t</sub>	S <sub>t</sub>	Si <sub>t</sub>	Ti <sub>t</sub>
<b>P100</b>	0–9	106.6	6.8	68.7	29.8	16.2	0.8	2.9	1.8	1.4	196.5	6.1
	9–15	106.7	7.7	76.9	31.9	15.7	0.9	3.0	1.7	1.2	194.7	6.1
	15–21	103.2	7.7	75.7	32.7	16.4	1.3	3.6	1.4	0.6	207.8	6.8
	21–30	108.2	9.5	84.3	34.9	15.7	1.5	2.7	1.1	0.4	204.8	6.8
	30–50	110.4	10.6	77.4	32.5	16.4	1.4	2.7	0.9	0.2	210.7	5.8
	50–75	107.2	10.9	89.4	34.5	15.6	1.8	2.1	1.1	0.3	201.9	6.4
	70–100	110.7	10.4	76.2	32.1	16.4	1.4	3.0	1.0	0.3	208.0	5.9
<b>P700</b>	0–10	103.2	9.4	70.4	28.3	14.5	1.0	2.6	2.4	1.4	191.3	5.9
	10–16	107.5	9.9	77.4	32.5	15.4	0.9	2.5	1.6	0.9	198.4	5.9
	16–22	106.6	7.2	73.2	30.3	16.3	0.9	3.6	1.2	0.6	201.2	6.2
	22–45	110.1	6.3	74.4	32.8	16.2	1.3	3.7	1.2	0.4	206.1	6.7
	45–69	117.4	4.9	70.2	32.5	14.0	0.5	3.3	0.4	0.4	207.0	6.8
	69–106	105.7	4.0	107.9	33.6	14.1	0.8	2.8	0.8	0.2	200.6	6.2
<b>P2000</b>	0–15	111.2	6.4	51.1	24.8	8.7	0.5	2.6	2.3	1.8	196.2	7.1
	15–20	109.1	7.2	59.3	25.7	9.1	0.5	2.7	2.0	1.4	198.4	7.4
	20–27	117.5	5.8	89.0	24.2	9.7	1.0	3.3	0.8	0.4	199.1	6.7
	27–35	119.7	6.0	68.5	27.9	9.3	1.0	2.7	0.4	0.2	207.1	8.7
	35–50	112.4	5.4	101.3	27.6	10.7	0.9	1.7	0.5	0.2	185.6	7.9
	50–70	113.6	5.7	87.9	29.4	14.2	0.9	2.5	0.6	0.2	204.0	7.3
	70–100	112.7	6.0	86.3	30.6	15.1	1.5	3.1	0.8	0.1	205.9	6.8

*Appendix B*

**Table B-5:** Total element concentrations in the clay fractions of non-paddy sites (NP), determined with XRF. The marshland site (ML30) is given as point zero of soil evolution.

Site	Depth cm	Al <sub>t</sub>	Ca <sub>t</sub>	Fe <sub>t</sub>	K <sub>t</sub>	Mg <sub>t</sub>	Mn <sub>t</sub> g kg <sub>clay</sub> <sup>-1</sup>	Na <sub>t</sub>	P <sub>t</sub>	S <sub>t</sub>	Si <sub>t</sub>	Ti <sub>t</sub>
<b>ML30</b>	0–13	119.3	8.7	63.2	29.6	19.0	1.8	4.1	0.2	0.2	207.3	5.8
	13–30	117.5	10.3	67.2	29.4	20.9	1.6	4.0	0.2	0.2	206.6	6.3
<b>NP100</b>	0–14	106.1	11.1	74.4	32.5	15.9	1.5	2.7	1.7	0.6	207.4	6.0
	14–25	109.4	10.9	72.0	31.1	16.3	1.6	2.7	1.6	0.7	201.4	5.8
	25–30	108.1	11.6	77.3	33.2	16.3	1.6	2.8	1.8	0.7	204.3	6.3
	30–38	110.5	10.2	79.9	33.5	15.4	1.6	2.4	1.1	0.4	205.4	6.1
	38–70	109.9	10.7	75.3	32.5	16.7	1.6	2.7	1.1	0.3	207.7	5.8
	70–100	110.5	9.7	76.7	33.3	16.1	1.5	2.6	1.1	0.3	207.4	6.1
<b>NP700</b>	0–12	104.4	9.6	73.4	30.3	17.0	2.1	2.5	2.3	1.0	196.0	6.0
	12–17	104.0	9.4	74.8	30.5	17.4	2.2	3.0	1.5	0.6	203.5	6.0
	17–23	105.6	9.8	81.9	32.2	17.0	2.4	2.9	1.4	0.5	207.3	5.9
	23–45	109.0	10.9	80.7	32.0	16.8	1.4	2.4	1.1	0.3	206.1	5.7
	45–70	109.3	9.9	82.2	31.6	15.8	1.9	2.3	1.0	0.3	206.9	5.6
	70–100	108.8	11.3	81.6	31.8	16.5	2.2	2.5	1.0	0.2	207.1	6.2

### C. Appendix: X-ray diffraction

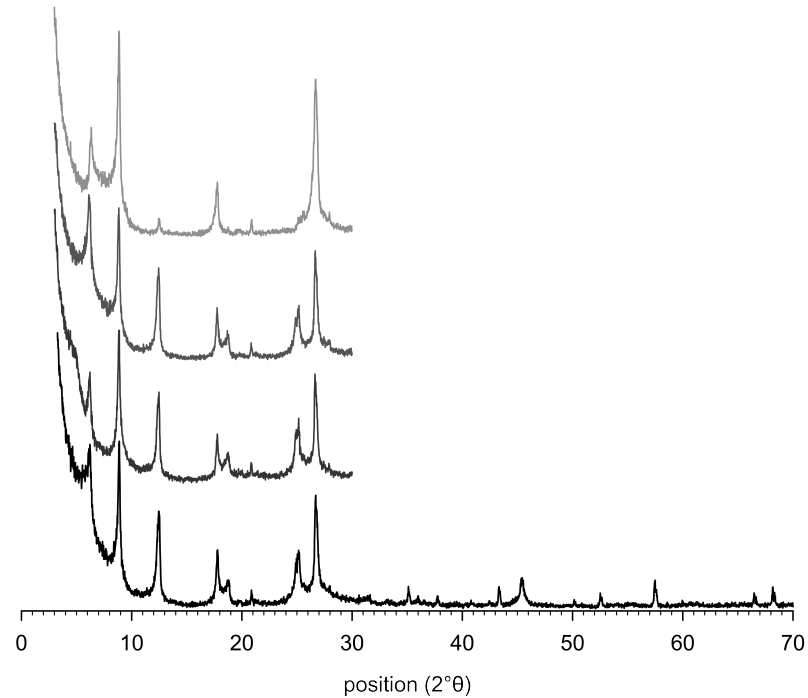


**Figure C-1:** X-ray diffraction (XRD) patterns (oriented texture specimens, Cu K $\alpha$  radiation) of the clay fraction in the uppermost horizon (0–13 cm) of the 30 year marshland site (ML 30); patterns from bottom to top: Ca<sup>2+</sup> saturated, ethylene glycol solvated, K<sup>+</sup> saturated and K<sup>+</sup> saturated specimen heated to 550 °C.

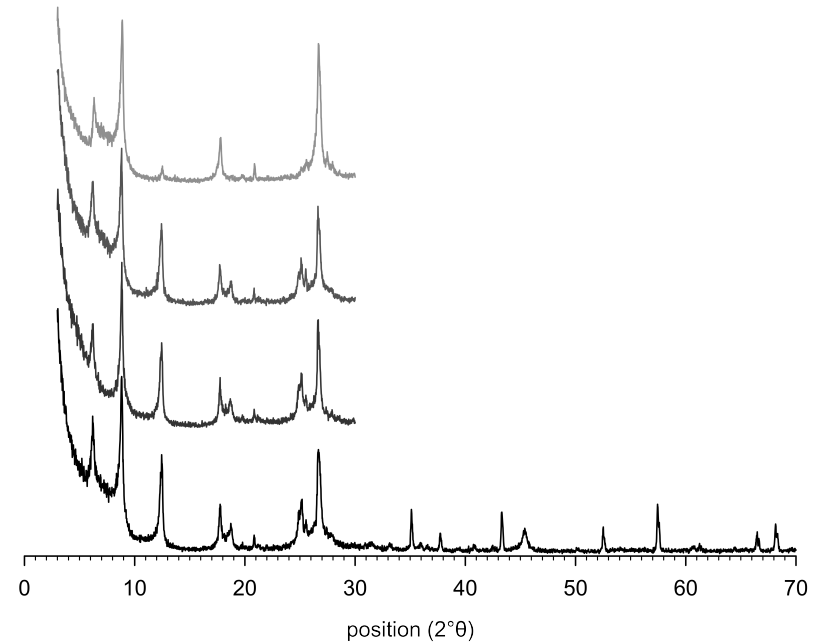


**Figure C-2:** XRD patterns (oriented texture specimens, Cu K $\alpha$  radiation) of the clay fraction in the second horizon (13–30 cm) of the 30 year marshland site (ML 30); patterns from bottom to top: Ca<sup>2+</sup> saturated, ethylene glycol solvated, K<sup>+</sup> saturated and K<sup>+</sup> saturated specimen heated to 550 °C.

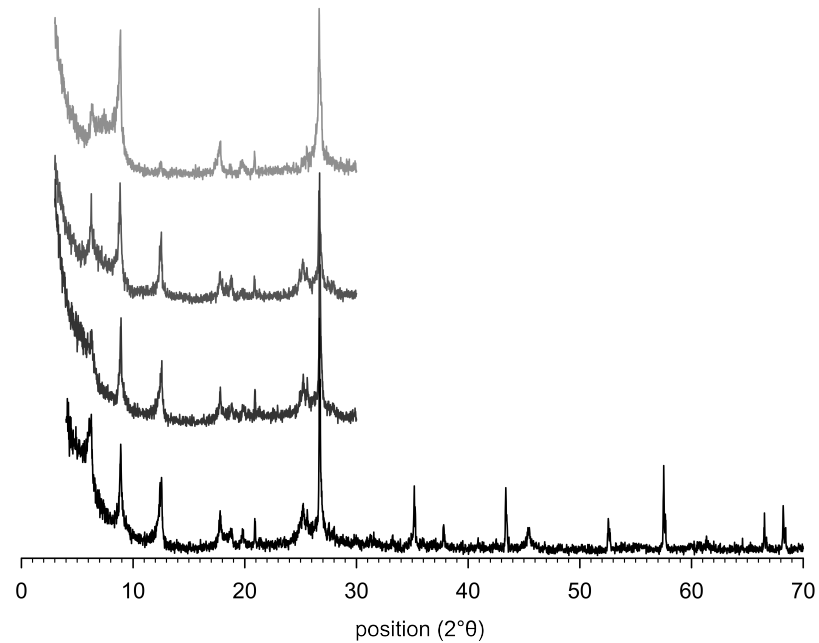


**Figure C-3:** XRD patterns (oriented texture specimens, Cu K $\alpha$  radiation) of the clay fraction in the Alp2 horizon (9–15 cm) of the 100 year paddy site (P100); patterns from bottom to top: Ca<sup>2+</sup> saturated, ethylene glycol solvated, K<sup>+</sup> saturated and K<sup>+</sup> saturated specimen heated to 550 °C.

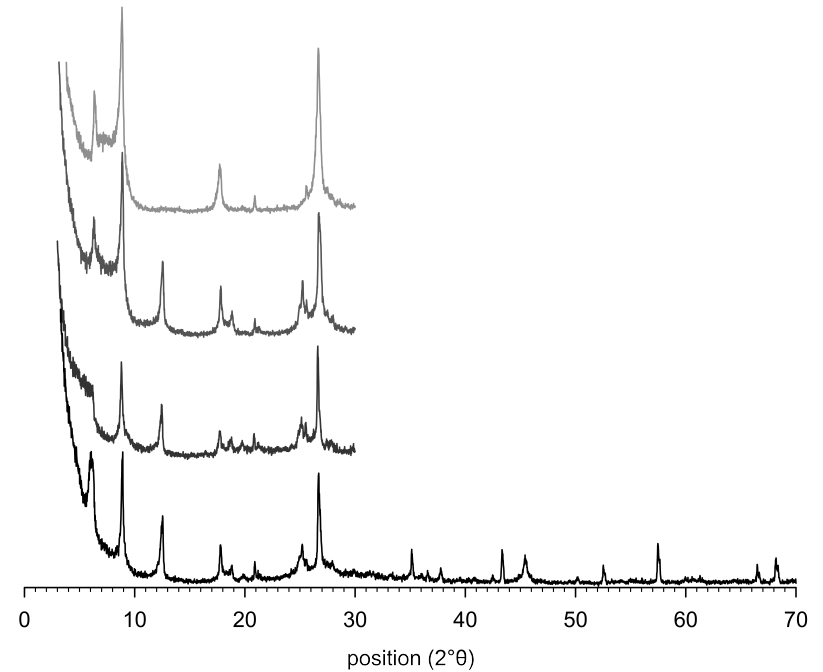


**Figure C-4:** XRD patterns (oriented texture specimens, Cu K $\alpha$  radiation) of the clay fraction in the Ardp horizon (15–21 cm) of the 100 year paddy site (P100); patterns from bottom to top: Ca<sup>2+</sup> saturated, ethylene glycol solvated, K<sup>+</sup> saturated and K<sup>+</sup> saturated specimen heated to 550 °C.

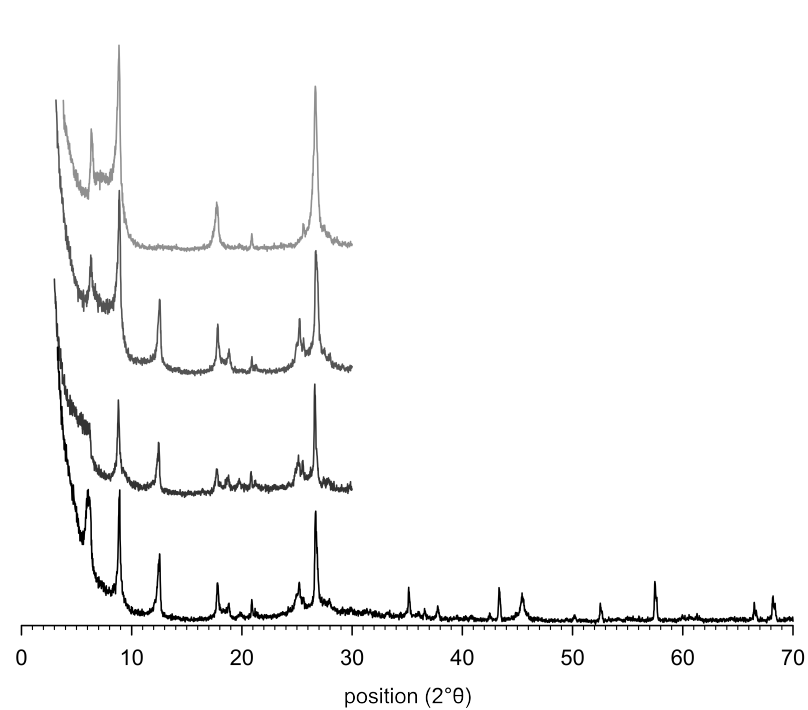


**Figure C-5:** XRD patterns (oriented texture specimens, Cu  $K\alpha$  radiation) of the clay fraction in the Bwg1 horizon (21–31 cm) of the 100 year paddy site (P100); patterns from bottom to top:  $\text{Ca}^{2+}$  saturated, ethylene glycol solvated,  $\text{K}^+$  saturated and  $\text{K}^+$  saturated specimen heated to 550 °C.

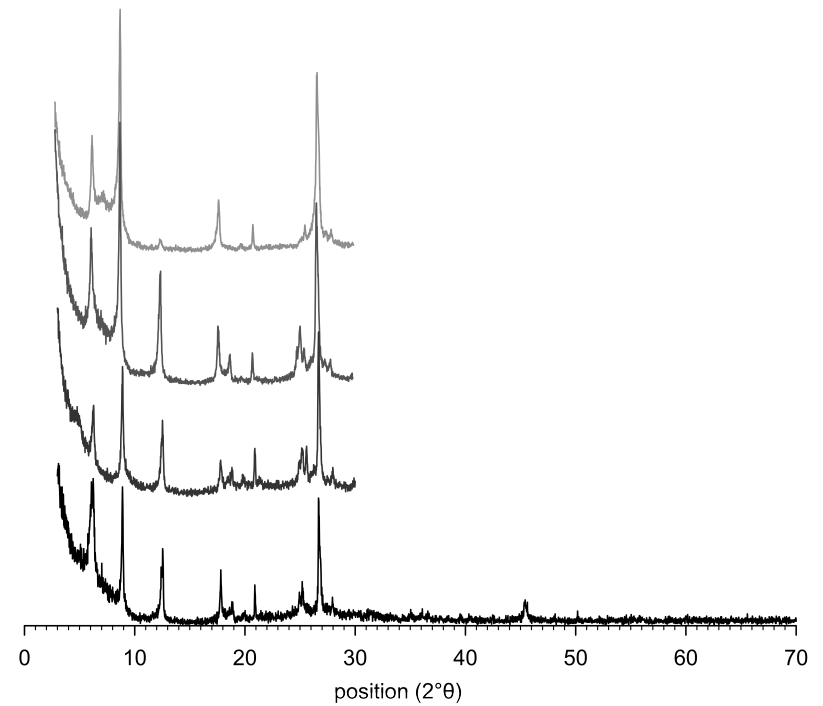


**Figure C-6:** XRD patterns (oriented texture specimens, Cu  $K\alpha$  radiation) of the clay fraction in the Bwg2 horizon (30–50 cm) of the 100 year paddy site (P100); patterns from bottom to top:  $\text{Ca}^{2+}$  saturated, ethylene glycol solvated,  $\text{K}^+$  saturated and  $\text{K}^+$  saturated specimen heated to 550 °C.

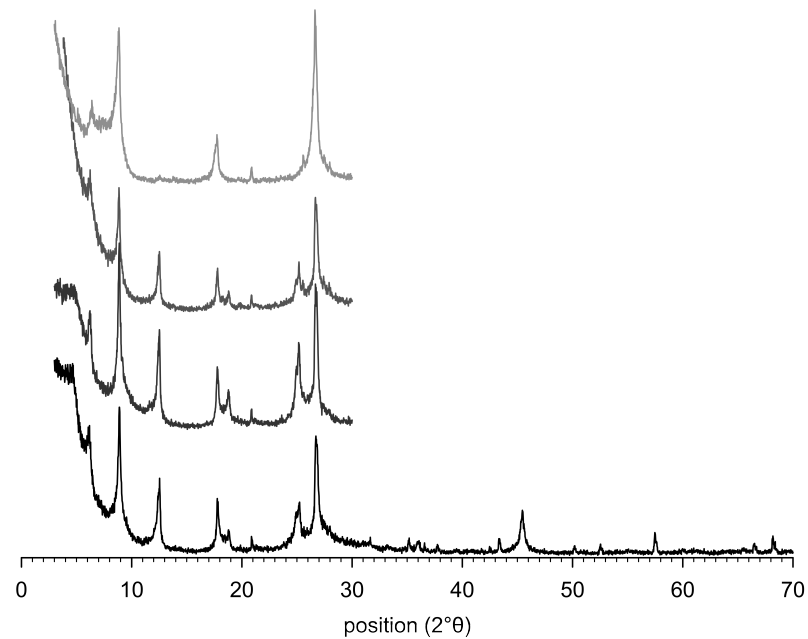


**Figure C-7:** XRD patterns (oriented texture specimens, Cu K $\alpha$  radiation) of the clay fraction in the Bwlg1 horizon (50–75 cm) of the 100 year paddy site (P100); patterns from bottom to top: Ca<sup>2+</sup> saturated, ethylene glycol solvated, K<sup>+</sup> saturated and K<sup>+</sup> saturated specimen heated to 550 °C.

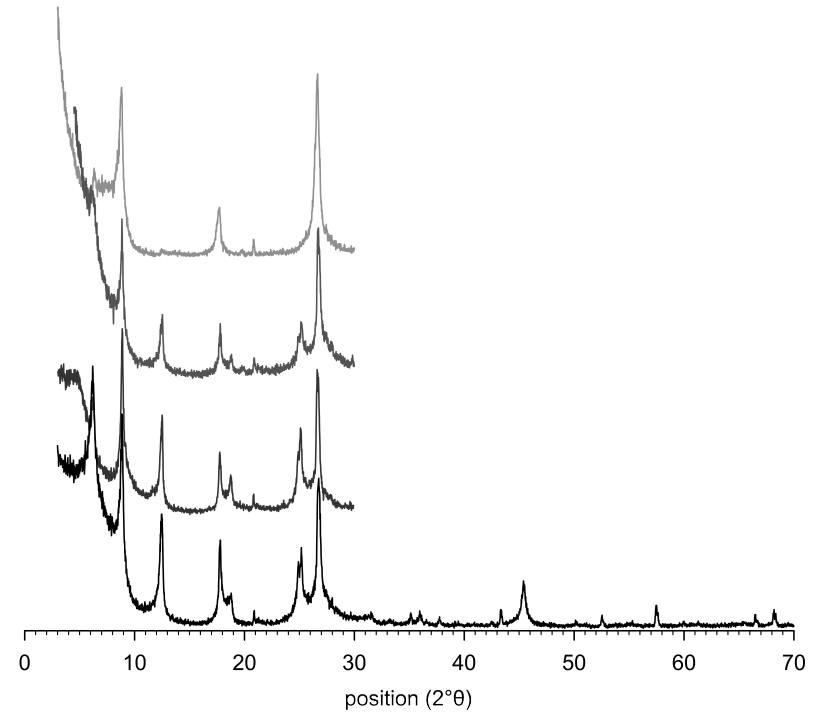


**Figure C-8:** XRD patterns (oriented texture specimens, Cu K $\alpha$  radiation) of the clay fraction in the Bwlg2 horizon (70–100 cm) of the 100 year paddy site (P100); patterns from bottom to top: Ca<sup>2+</sup> saturated, ethylene glycol solvated, K<sup>+</sup> saturated and K<sup>+</sup> saturated specimen heated to 550 °C.

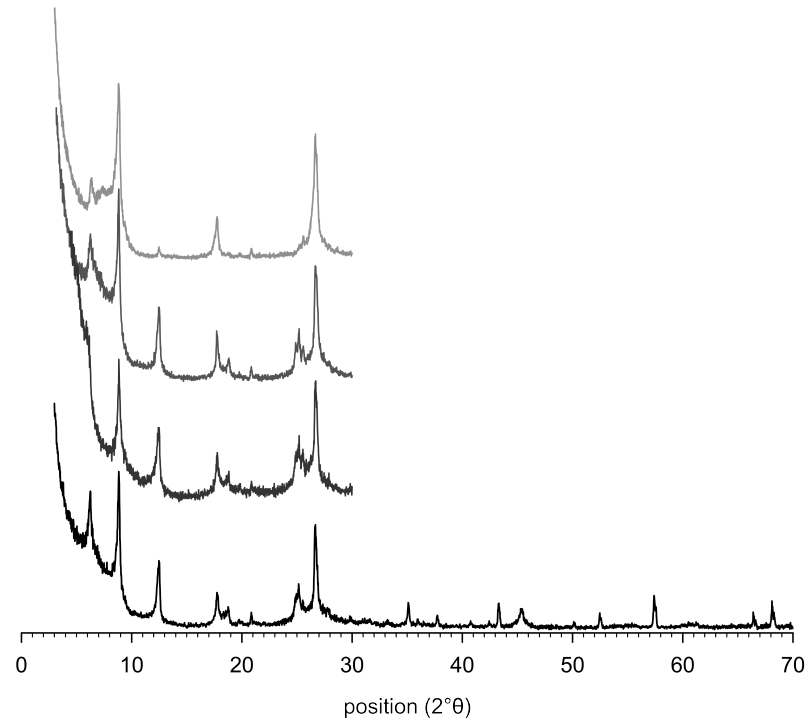


**Figure C-9:** XRD patterns (oriented texture specimens, Cu K $\alpha$  radiation) of the clay fraction in the Alp1 horizon (0–10 cm) of the 700 year paddy site (P700); patterns from bottom to top: Ca<sup>2+</sup> saturated, ethylene glycol solvated, K<sup>+</sup> saturated and K<sup>+</sup> saturated specimen heated to 550 °C.

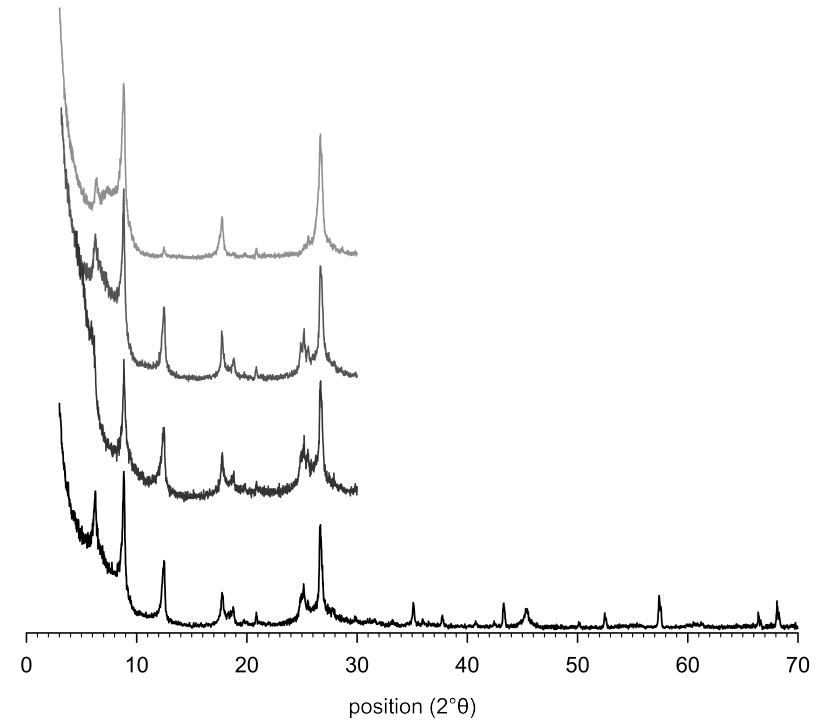


**Figure C-10:** XRD patterns (oriented texture specimens, Cu K $\alpha$  radiation) of the clay fraction in the Alp2 horizon (10–16 cm) of the 700 year paddy site (P700); patterns from bottom to top: Ca<sup>2+</sup> saturated, ethylene glycol solvated, K<sup>+</sup> saturated and K<sup>+</sup> saturated specimen heated to 550 °C.

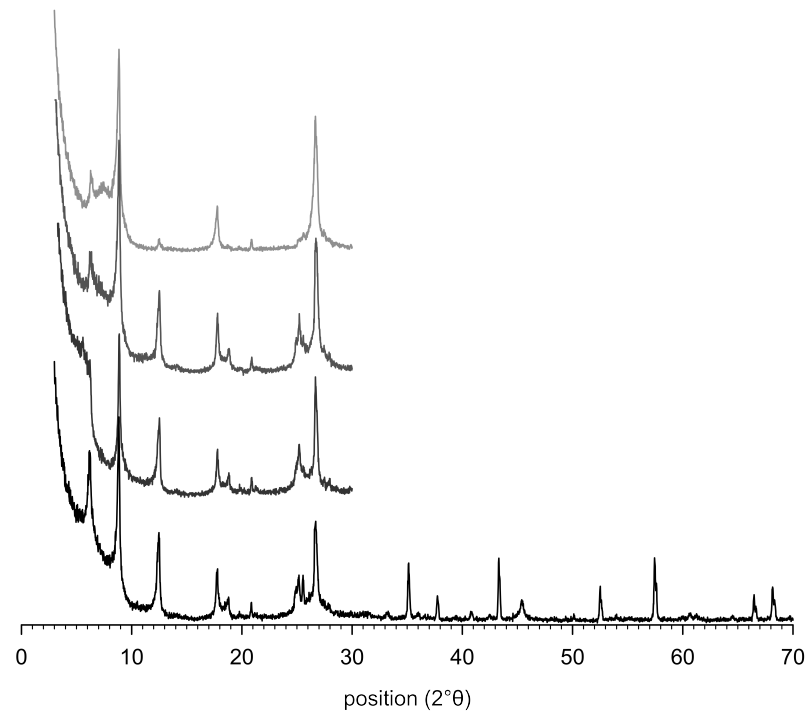


**Figure C-11:** XRD patterns (oriented texture specimens, Cu K $\alpha$  radiation) of the clay fraction in the Ardp horizon (16–22 cm) of the 700 year paddy site (P700); patterns from bottom to top: Ca<sup>2+</sup> saturated, ethylene glycol solvated, K<sup>+</sup> saturated and K<sup>+</sup> saturated specimen heated to 550 °C.

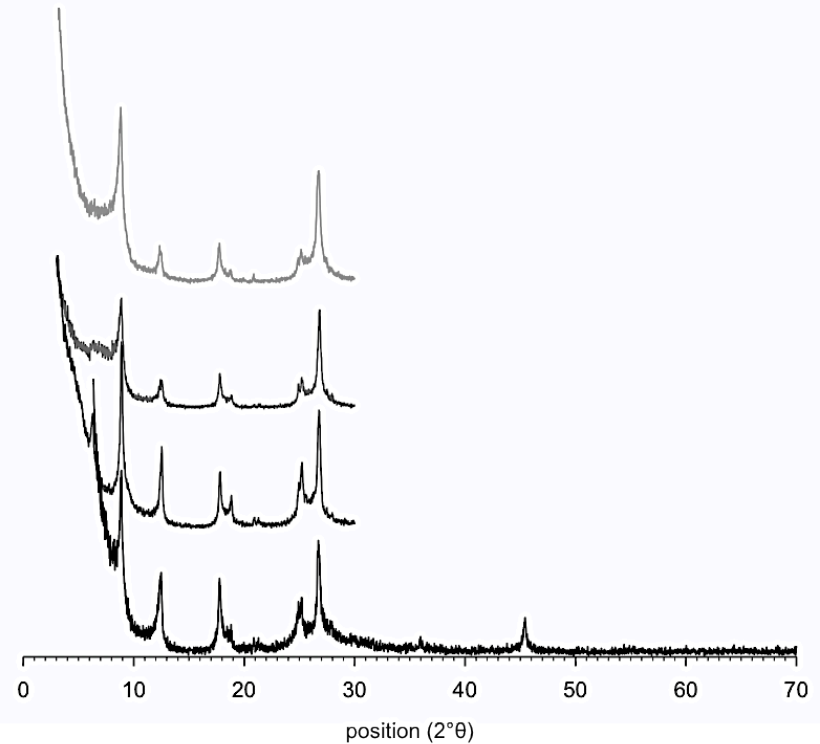


**Figure C-12:** XRD patterns (oriented texture specimens, Cu K $\alpha$  radiation) of the clay fraction in the Bg horizon (22–45 cm) of the 700 year paddy site (P700); patterns from bottom to top: Ca<sup>2+</sup> saturated, ethylene glycol solvated, K<sup>+</sup> saturated and K<sup>+</sup> saturated specimen heated to 550 °C.

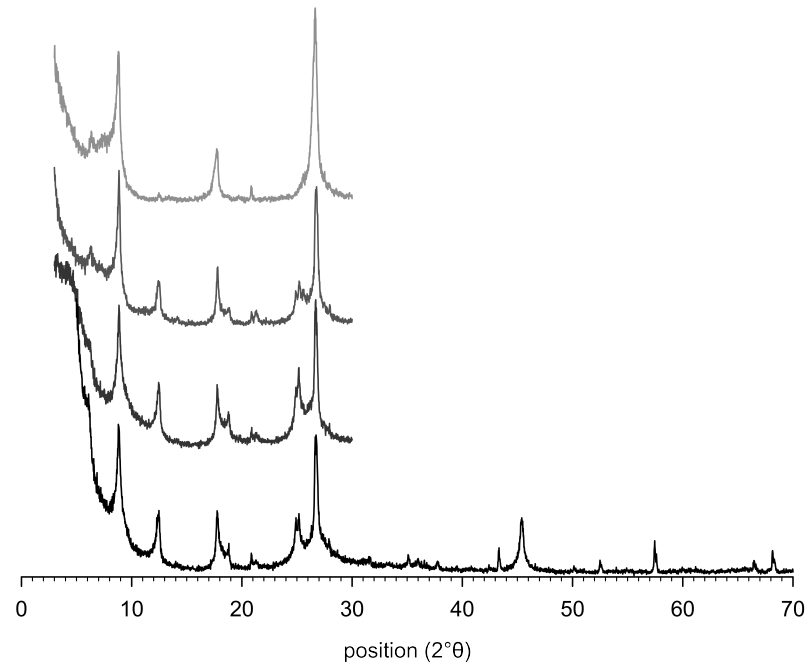


**Figure C-13:** XRD patterns (oriented texture specimens, Cu K $\alpha$  radiation) of the clay fraction in the 2Ahgb horizon (45–69 cm) of the 700 year paddy site (P700); patterns from bottom to top: Ca<sup>2+</sup> saturated, ethylene glycol solvated, K<sup>+</sup> saturated and K<sup>+</sup> saturated specimen heated to 550 °C.

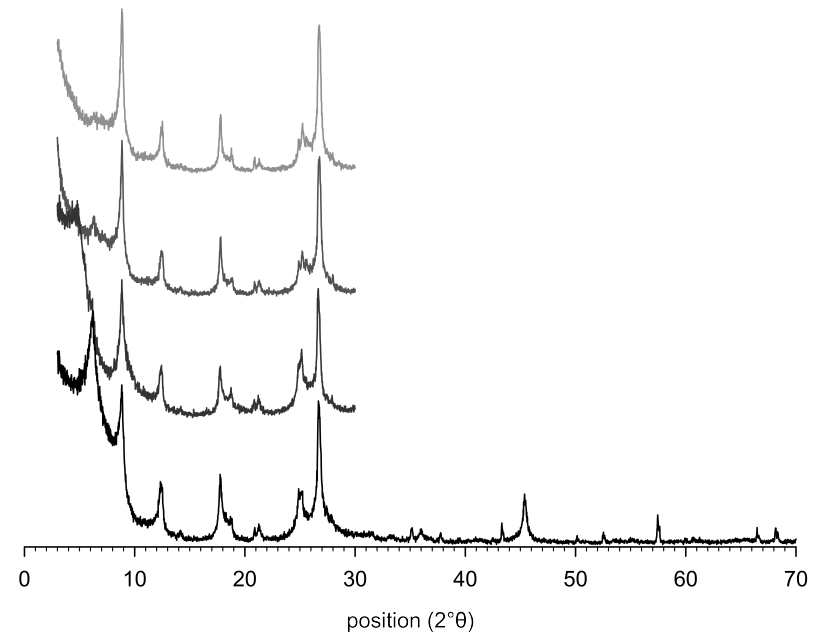


**Figure C-14:** XRD patterns (oriented texture specimens, Cu K $\alpha$  radiation) of the clay fraction in the 2Blg1 horizon (69–106 cm) of the 700 year paddy site (P700); patterns from bottom to top: Ca<sup>2+</sup> saturated, ethylene glycol solvated, K<sup>+</sup> saturated and K<sup>+</sup> saturated specimen heated to 550 °C.

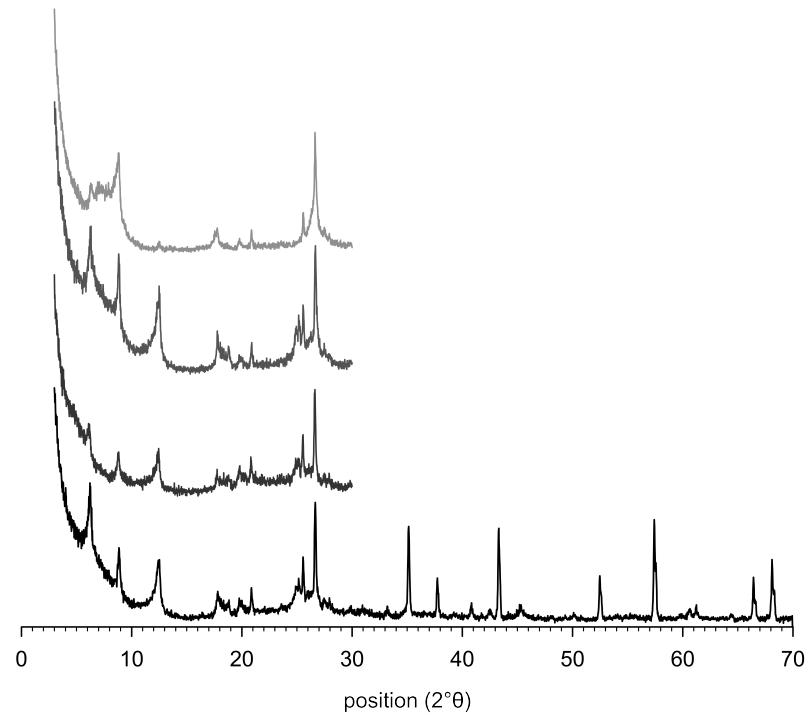


**Figure C-15:** XRD patterns (oriented texture specimens, Cu K $\alpha$  radiation) of the clay fraction in the Alp horizon (0–15 cm) of the 2000 year paddy site (P2000); patterns from bottom to top: Ca<sup>2+</sup> saturated, ethylene glycol solvated, K<sup>+</sup> saturated and K<sup>+</sup> saturated specimen heated to 550 °C.

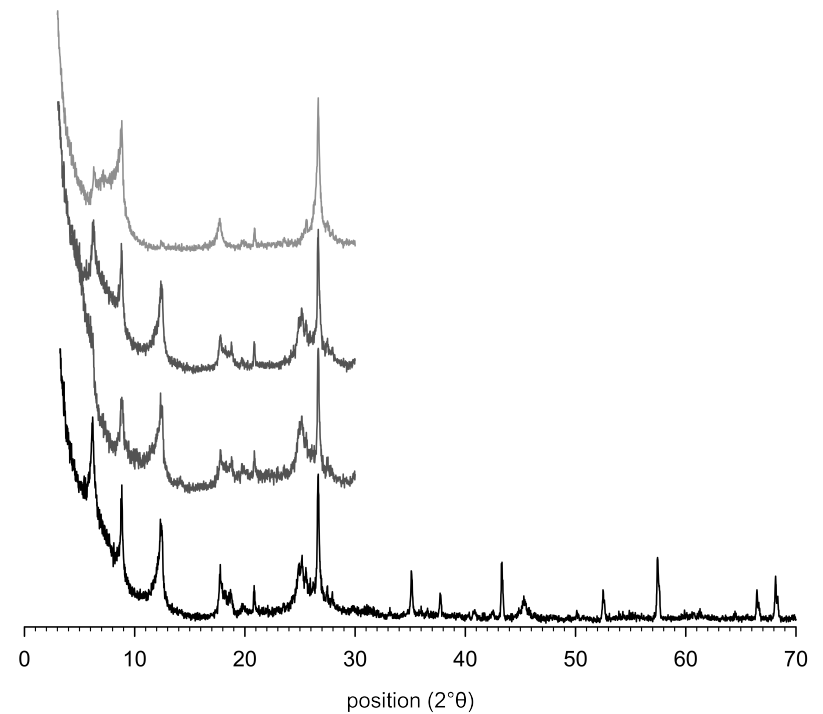


**Figure C-16:** XRD patterns (oriented texture specimens, Cu K $\alpha$  radiation) of the clay fraction in the Ardp horizon (15–20 cm) of the 2000 year paddy site (P2000); patterns from bottom to top: Ca<sup>2+</sup> saturated, ethylene glycol solvated, K<sup>+</sup> saturated and K<sup>+</sup> saturated specimen heated to 550 °C.

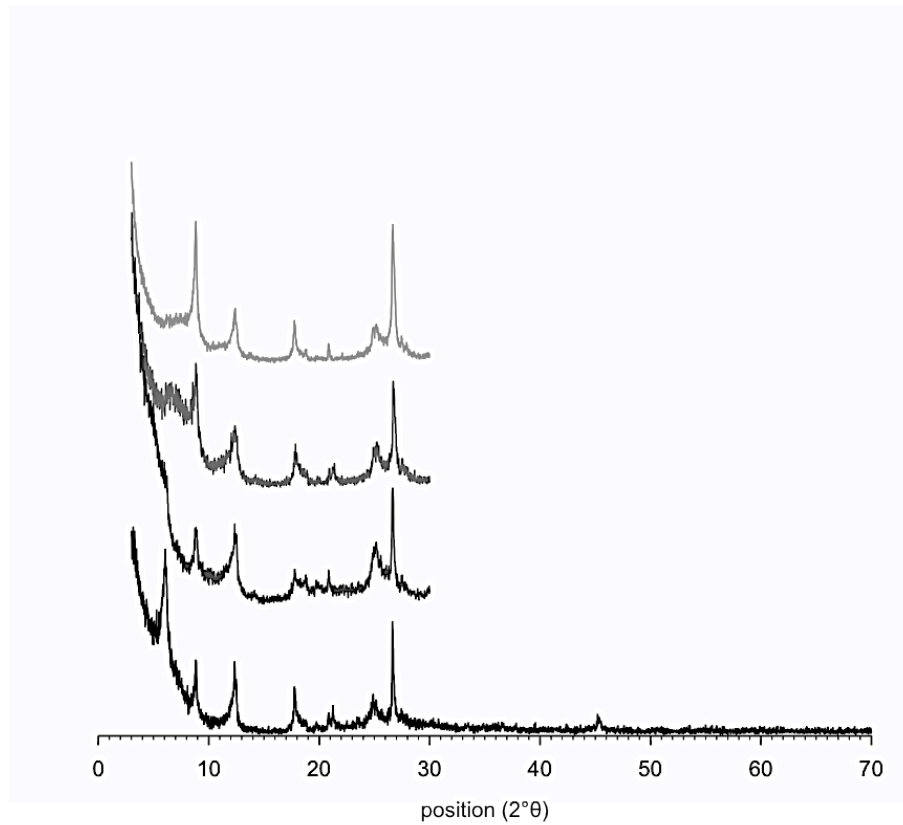


**Figure C-17:** XRD patterns (oriented texture specimens, Cu K $\alpha$  radiation) of the clay fraction in the Bdg horizon (20–27 cm) of the 2000 year paddy site (P2000); patterns from bottom to top: Ca<sup>2+</sup> saturated, ethylene glycol solvated, K<sup>+</sup> saturated and K<sup>+</sup> saturated specimen heated to 550 °C.

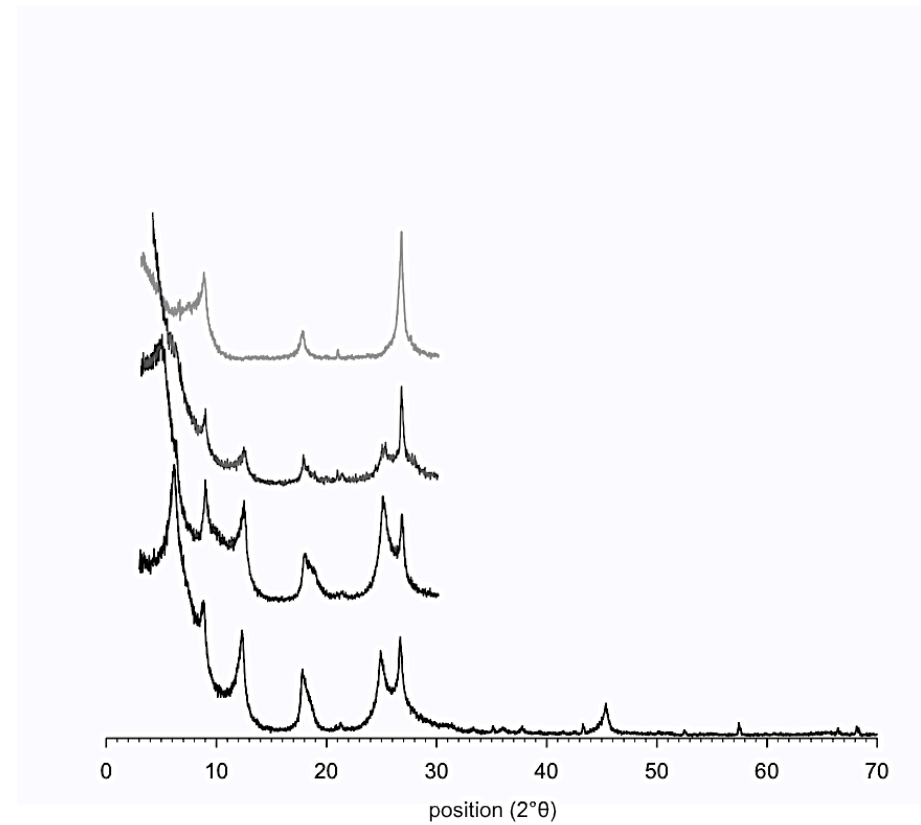


**Figure C-18:** XRD patterns (oriented texture specimens, Cu K $\alpha$  radiation) of the clay fraction in the 2AhgB horizon (27–35 cm) of the 2000 year paddy site (P2000); patterns from bottom to top: Ca<sup>2+</sup> saturated, ethylene glycol solvated, K<sup>+</sup> saturated and K<sup>+</sup> saturated specimen heated to 550 °C.

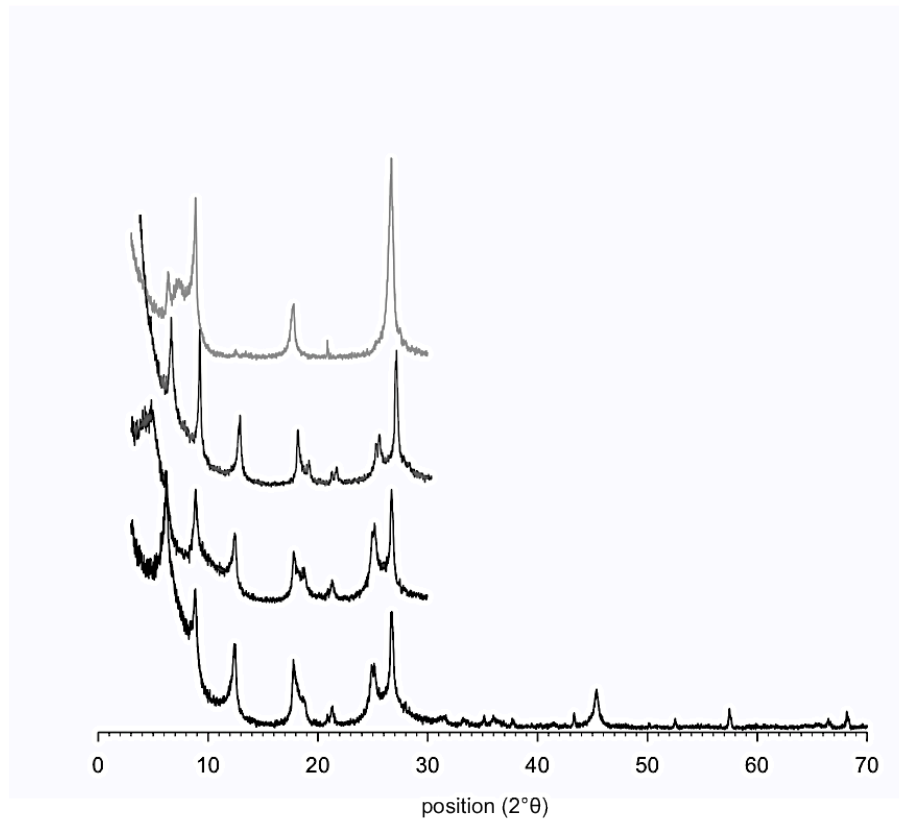


**Figure C-19:** XRD patterns (oriented texture specimens, Cu K $\alpha$  radiation) of the clay fraction in the 2Bg1 horizon (35–50 cm) of the 2000 year paddy site (P2000); patterns from bottom to top: Ca<sup>2+</sup> saturated, ethylene glycol solvated, K<sup>+</sup> saturated and K<sup>+</sup> saturated specimen heated to 550 °C.

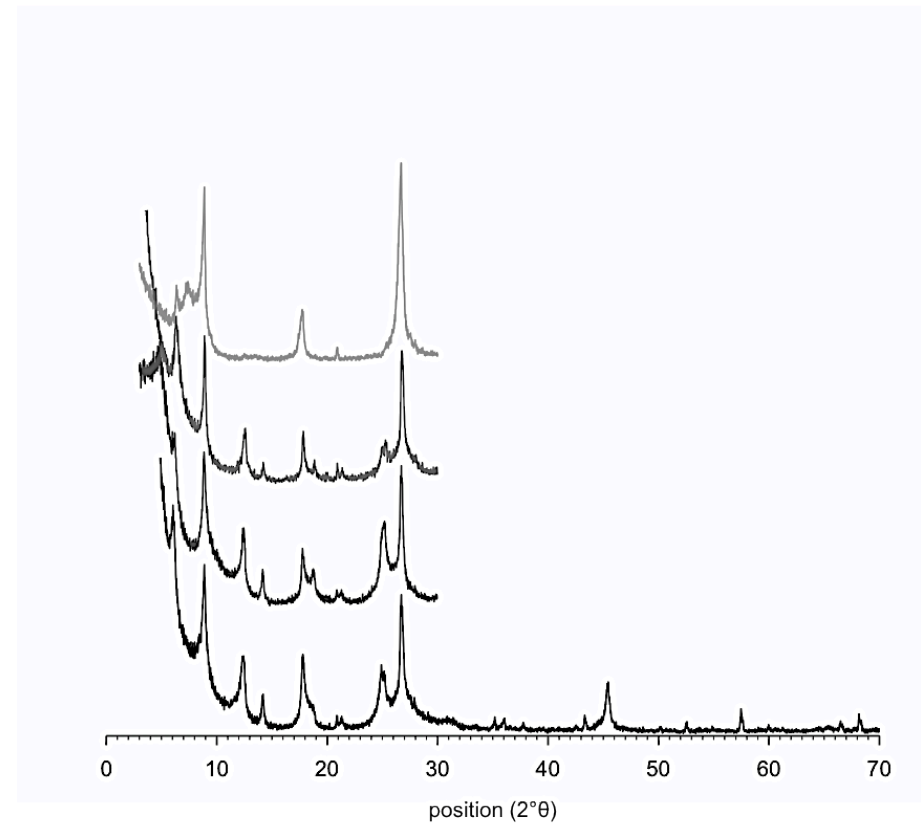


**Figure C-20:** XRD patterns (oriented texture specimens, Cu K $\alpha$  radiation) of the clay fraction in the 2Bg2 horizon (50–70 cm) of the 2000 year paddy site (P2000); patterns from bottom to top: Ca<sup>2+</sup> saturated, ethylene glycol solvated, K<sup>+</sup> saturated and K<sup>+</sup> saturated specimen heated to 550 °C.

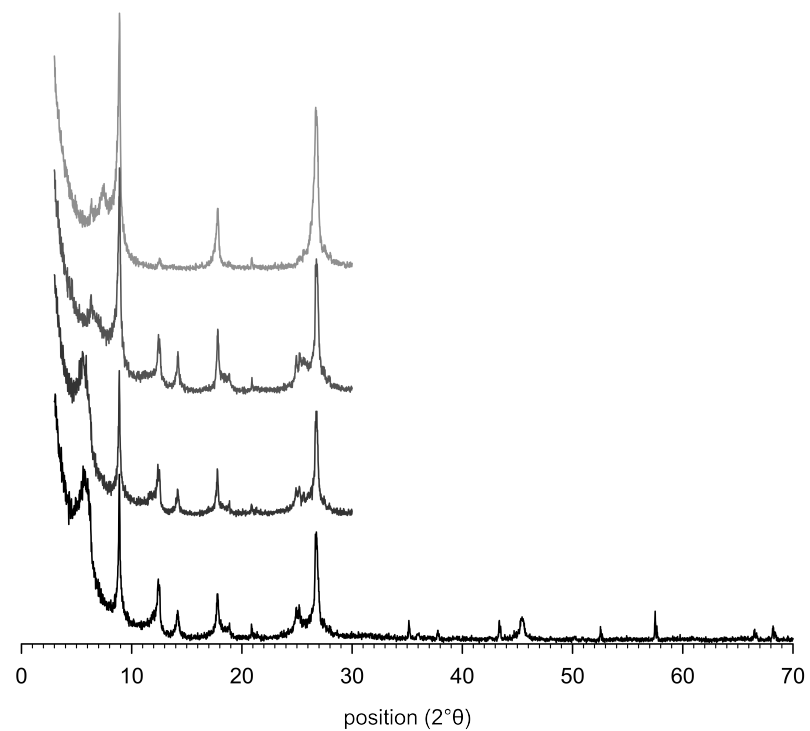


**Figure C-21:** XRD patterns (oriented texture specimens, Cu  $K\alpha$  radiation) of the clay fraction in the 2B1g horizon (70–100 cm) of the 2000 year paddy site (P2000); patterns from bottom to top:  $\text{Ca}^{2+}$  saturated, ethylene glycol solvated,  $\text{K}^{+}$  saturated and  $\text{K}^{+}$  saturated specimen heated to 550 °C.

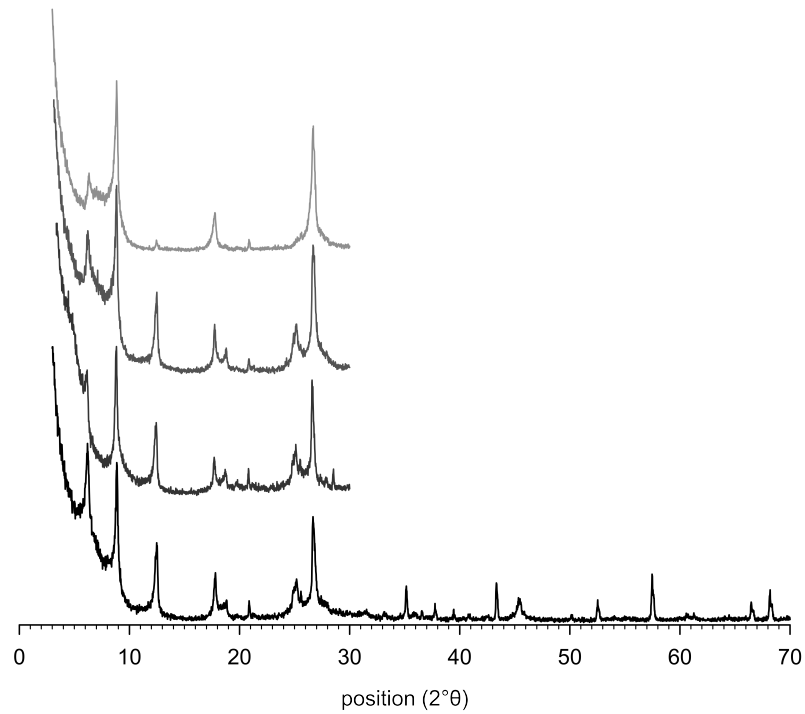


**Figure C-22:** XRD patterns (oriented texture specimens, Cu K $\alpha$  radiation) of the clay fraction in the Ap1 horizon (0–14 cm) of the 100 year non-paddy site (NP100); patterns from bottom to top: Ca<sup>2+</sup> saturated, ethylene glycol solvated, K<sup>+</sup> saturated and K<sup>+</sup> saturated specimen heated to 550 °C.

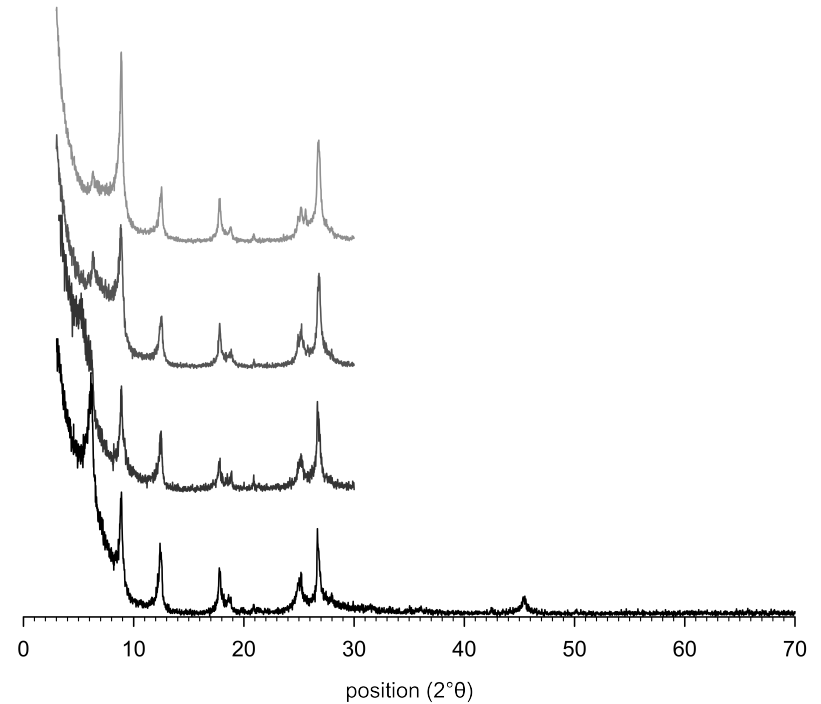


**Figure C-23:** XRD patterns (oriented texture specimens, Cu K $\alpha$  radiation) of the clay fraction in the Ap2 horizon (14–25 cm) of the 100 year non-paddy site (NP100); patterns from bottom to top: Ca<sup>2+</sup> saturated, ethylene glycol solvated, K<sup>+</sup> saturated and K<sup>+</sup> saturated specimen heated to 550 °C.

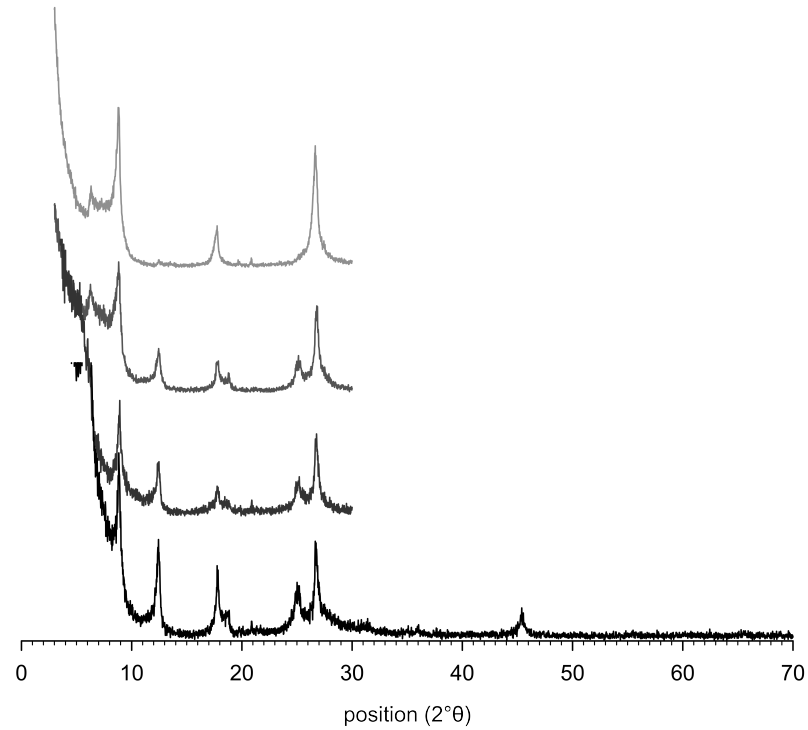


**Figure C-24:** XRD patterns (oriented texture specimens, Cu K $\alpha$  radiation) of the clay fraction in the Bw horizon (25–30 cm) of the 100 year non-paddy site (NP100); patterns from bottom to top: Ca<sup>2+</sup> saturated, ethylene glycol solvated, K<sup>+</sup> saturated and K<sup>+</sup> saturated specimen heated to 550 °C.

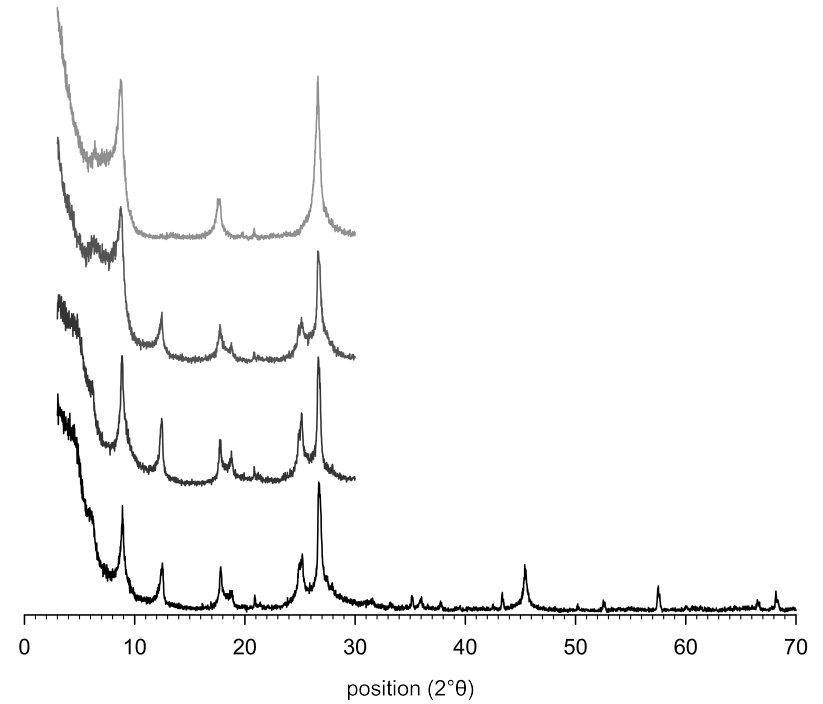


**Figure C-25:** XRD patterns (oriented texture specimens, Cu K $\alpha$  radiation) of the clay fraction in the BCwg1 horizon (30–38 cm) of the 100 year non-paddy site (NP100); patterns from bottom to top: Ca<sup>2+</sup> saturated, ethylene glycol solvated, K<sup>+</sup> saturated and K<sup>+</sup> saturated specimen heated to 550 °C.

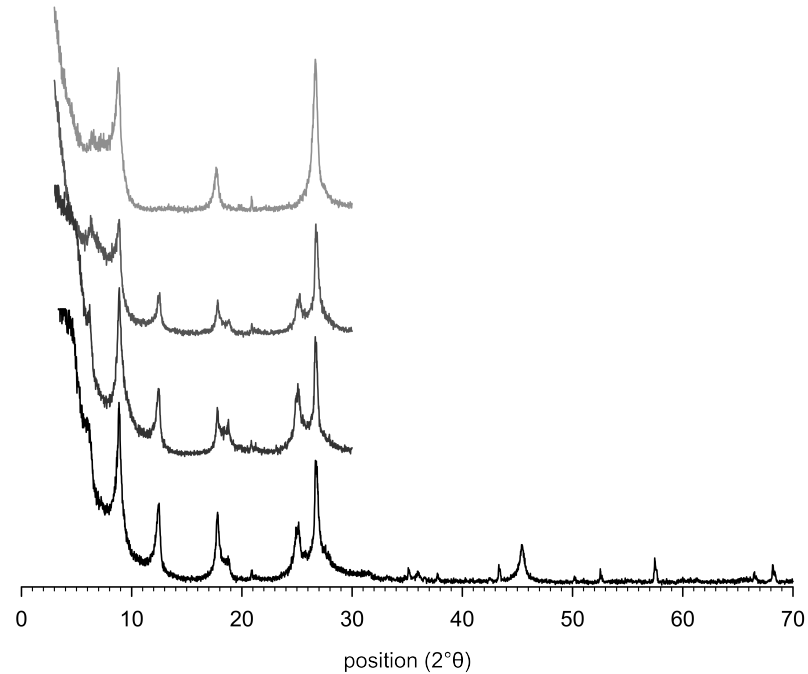


**Figure C-26:** XRD patterns (oriented texture specimens, Cu K $\alpha$  radiation) of the clay fraction in the BCwg2 horizon (38–70 cm) of the 100 year non-paddy site (NP100); patterns from bottom to top: Ca<sup>2+</sup> saturated, ethylene glycol solvated, K<sup>+</sup> saturated and K<sup>+</sup> saturated specimen heated to 550 °C.

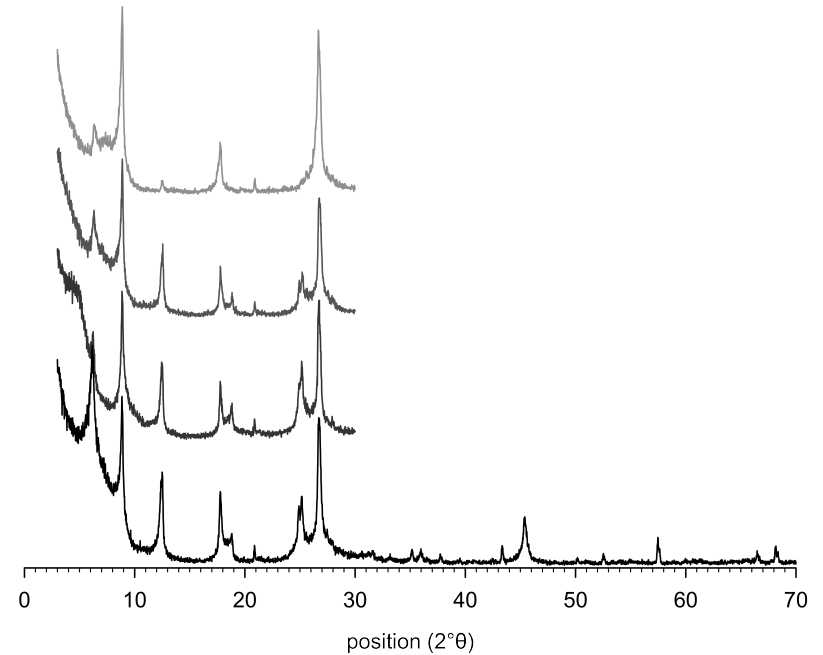


**Figure C-27:** XRD patterns (oriented texture specimens, Cu K $\alpha$  radiation) of the clay fraction in the BCwg3 horizon (70–100 cm) of the 100 year non-paddy site (NP100); patterns from bottom to top: Ca<sup>2+</sup> saturated, ethylene glycol solvated, K<sup>+</sup> saturated and K<sup>+</sup> saturated specimen heated to 550 °C.

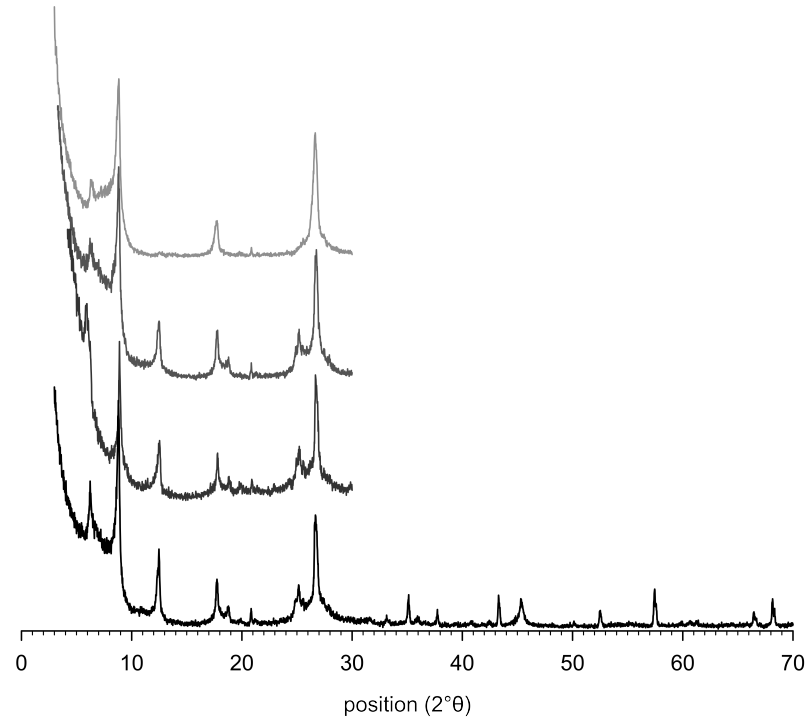


**Figure C-28:** XRD patterns (oriented texture specimens, Cu K $\alpha$  radiation) of the clay fraction in the Ap1 horizon (0–12 cm) of the 700 year non-paddy site (NP700); patterns from bottom to top: Ca<sup>2+</sup> saturated, ethylene glycol solvated, K<sup>+</sup> saturated and K<sup>+</sup> saturated specimen heated to 550 °C.

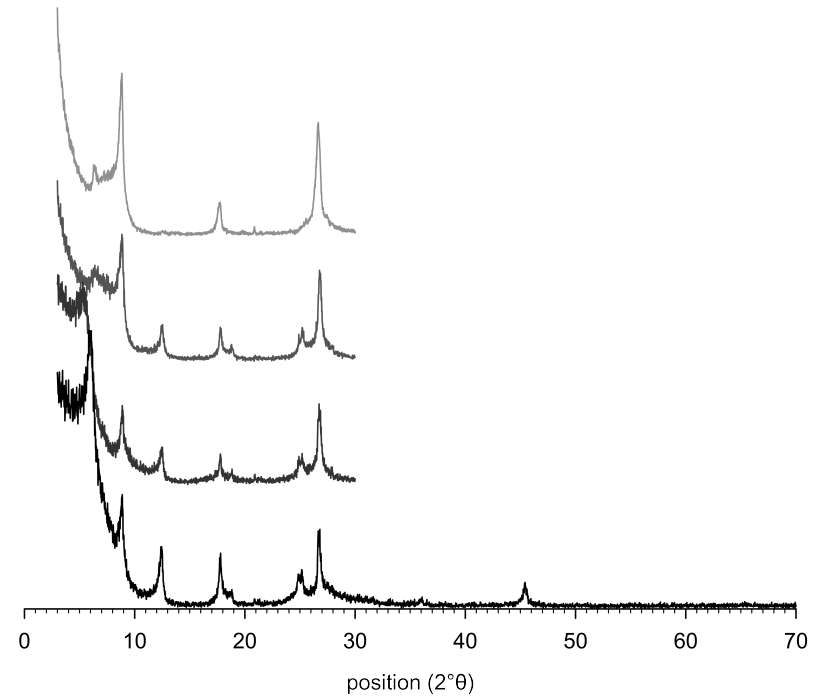


**Figure C-29:** XRD patterns (oriented texture specimens, Cu K $\alpha$  radiation) of the clay fraction in the Ap2 horizon (12–17 cm) of the 700 year non-paddy site (NP700); patterns from bottom to top: Ca<sup>2+</sup> saturated, ethylene glycol solvated, K<sup>+</sup> saturated and K<sup>+</sup> saturated specimen heated to 550 °C.

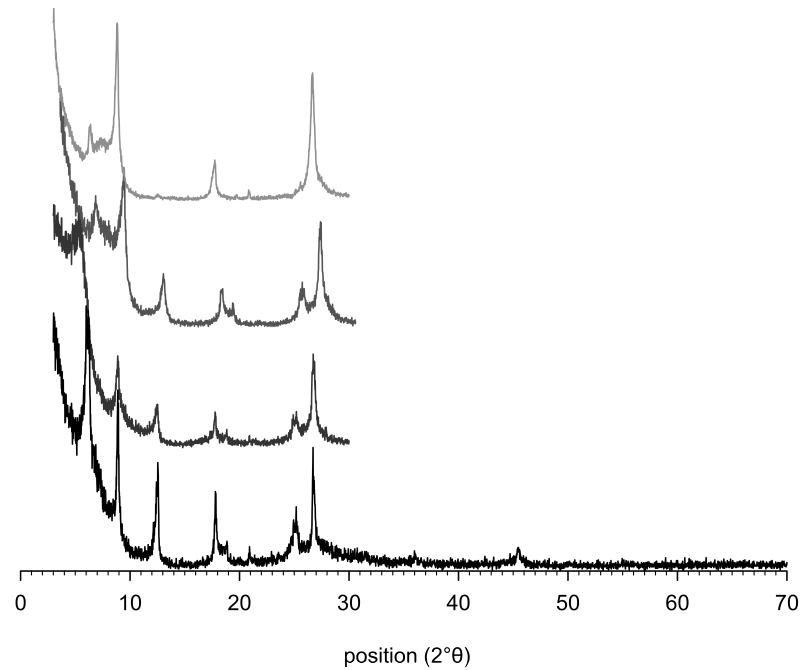


**Figure C-30:** XRD patterns (oriented texture specimens, Cu K $\alpha$  radiation) of the clay fraction in the Bw1 horizon (17–23 cm) of the 700 year non-paddy site (NP700); patterns from bottom to top: Ca<sup>2+</sup> saturated, ethylene glycol solvated, K<sup>+</sup> saturated and K<sup>+</sup> saturated specimen heated to 550 °C.

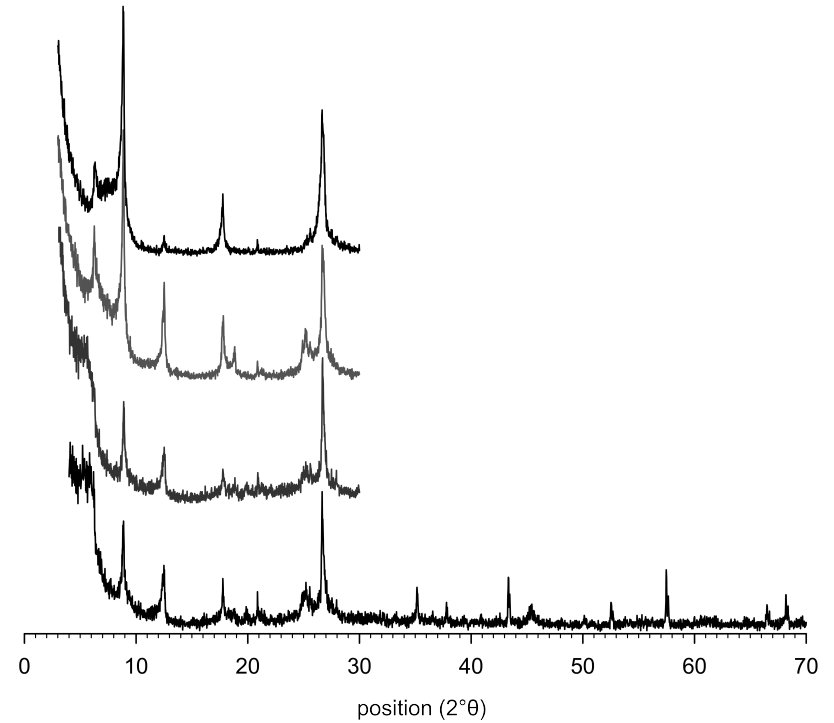


**Figure C-31:** XRD patterns (oriented texture specimens, Cu K $\alpha$  radiation) of the clay fraction in the -Bw2 horizon (23–45 cm) of the 700 year non-paddy site (NP700); patterns from bottom to top: Ca<sup>2+</sup> saturated, ethylene glycol solvated, K<sup>+</sup> saturated and K<sup>+</sup> saturated specimen heated to 550 °C.

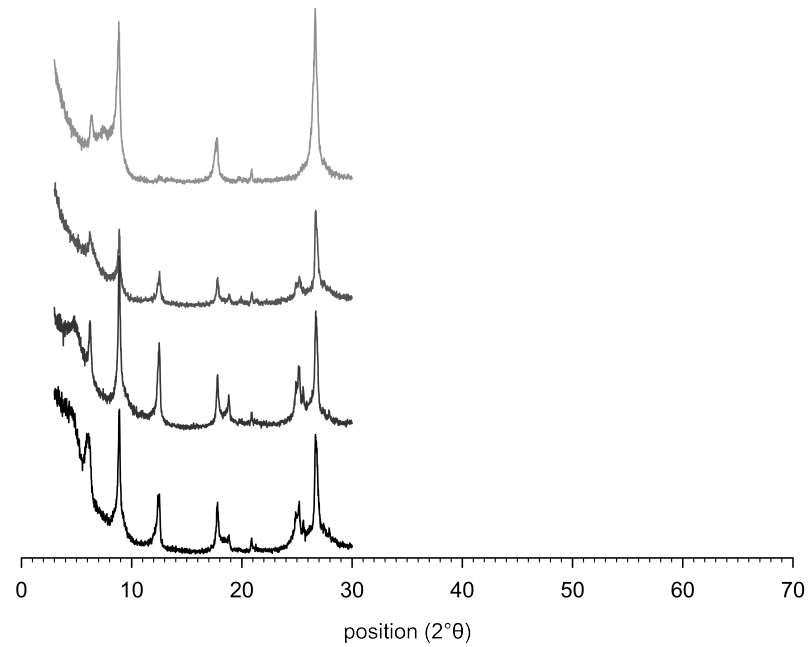


**Figure C-32:** XRD patterns (oriented texture specimens, Cu K $\alpha$  radiation) of the clay fraction in the Bw11 horizon (45–70 cm) of the 700 year non-paddy site (NP700); patterns from bottom to top: Ca<sup>2+</sup> saturated, ethylene glycol solvated, K<sup>+</sup> saturated and K<sup>+</sup> saturated specimen heated to 550 °C.

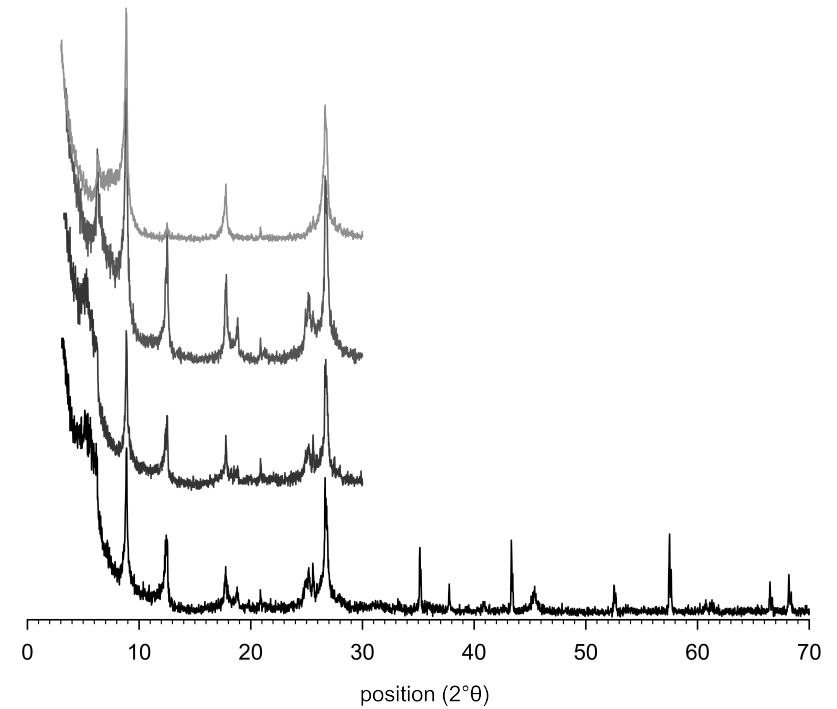


**Figure C-33:** XRD patterns (oriented texture specimens, Cu K $\alpha$  radiation) of the clay fraction in the Bw12 horizon (70–100 cm) of the 700 year non-paddy site (NP700); patterns from bottom to top: Ca<sup>2+</sup> saturated, ethylene glycol solvated, K<sup>+</sup> saturated and K<sup>+</sup> saturated specimen heated to 550 °C.

## D. Appendix: Mössbauer spectroscopy

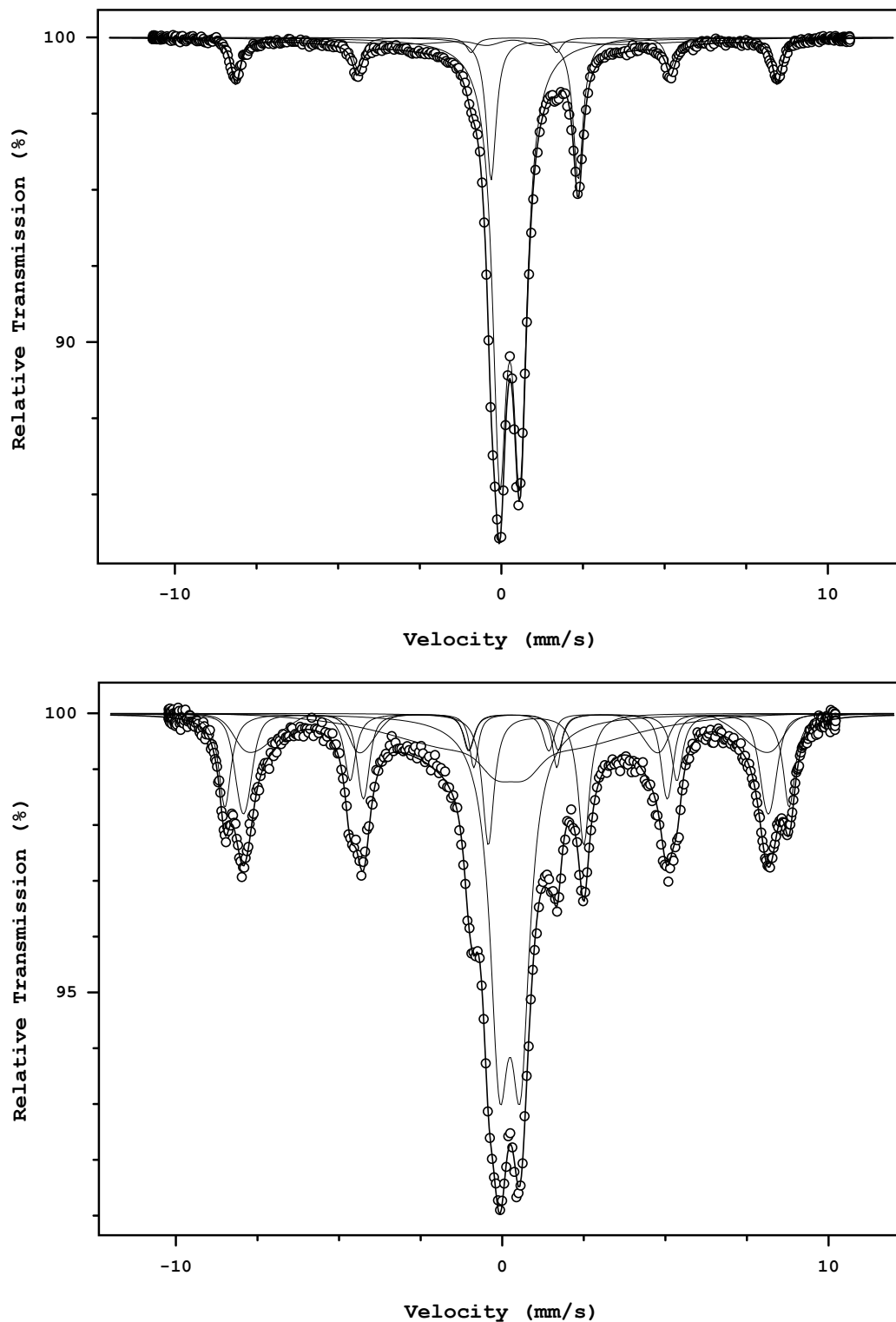


**Figure D-1:**  $^{57}\text{Fe}$  Mössbauer spectra at 298 K (top) and 4.2 K (bottom) of the clay fraction of the upper horizon (0–13 cm) of the marshland site (ML30). The solid black line drawn through the data points is the calculated fit. Corresponding Mössbauer parameters can be found in Table D-2 and Table D-4.

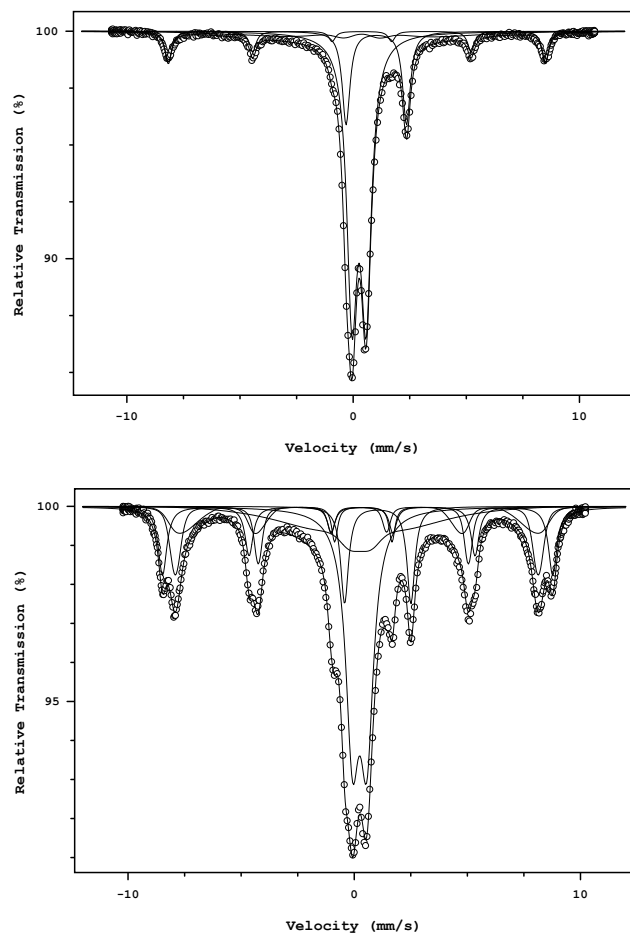


**Figure D-2:**  $^{57}\text{Fe}$  Mössbauer spectra at 298 K (top) and 4.2 K (bottom) of the clay fraction of the lower horizon (13–30 cm) of the marshland site (ML30). The solid black line drawn through the data points is the calculated fit. Corresponding Mössbauer parameters can be found in Table D-2 and Table D-4.

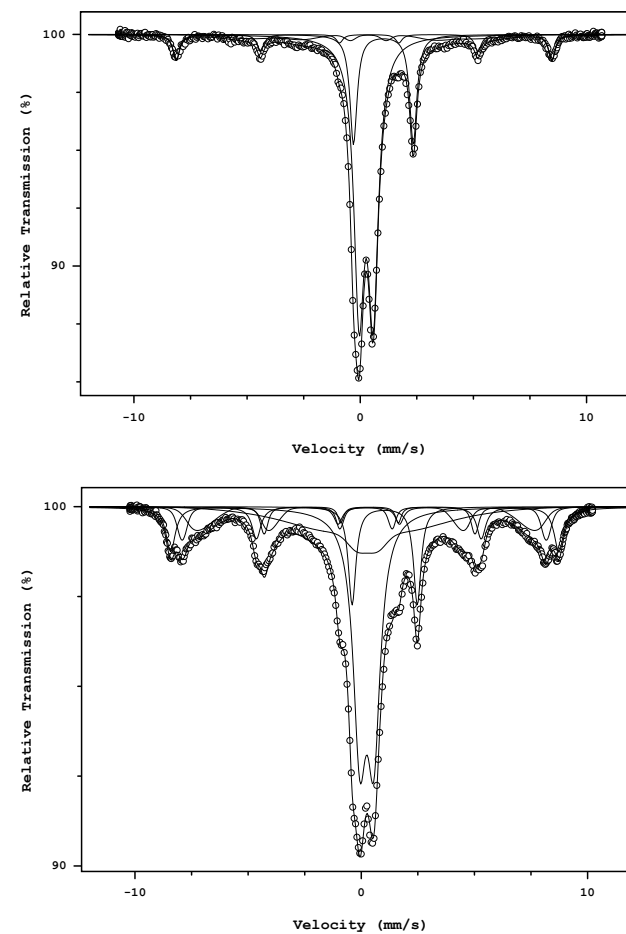


**Figure D-3:**  $^{57}\text{Fe}$  Mössbauer spectra at 298 K (top) and 4.2 K (bottom) of the clay fraction of the Alp1 horizon (0–9 cm) of the 100 year paddy site (P100). The solid black line drawn through the data points is the calculated fit. Corresponding Mössbauer parameters can be found in Table D-1 and Table D-3.

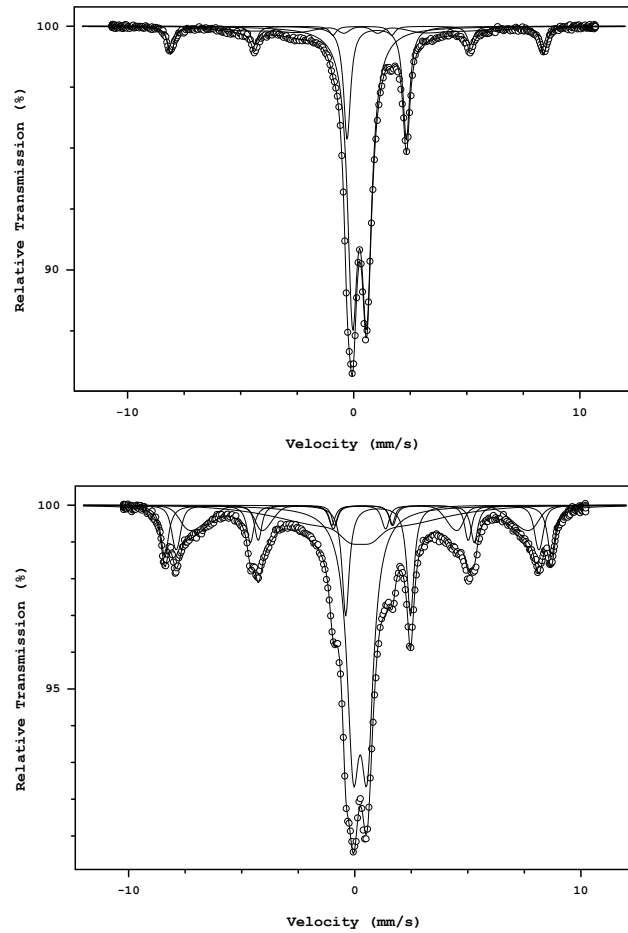


**Figure D-4:**  $^{57}\text{Fe}$  Mössbauer spectra at 298 K (top) and 4.2 K (bottom) of the clay fraction of the Alp2 horizon (9–15 cm) of the 100 year paddy site (P100). The solid black line drawn through the data points is the calculated fit. Corresponding Mössbauer parameters can be found in Table D-1 and Table D-3.

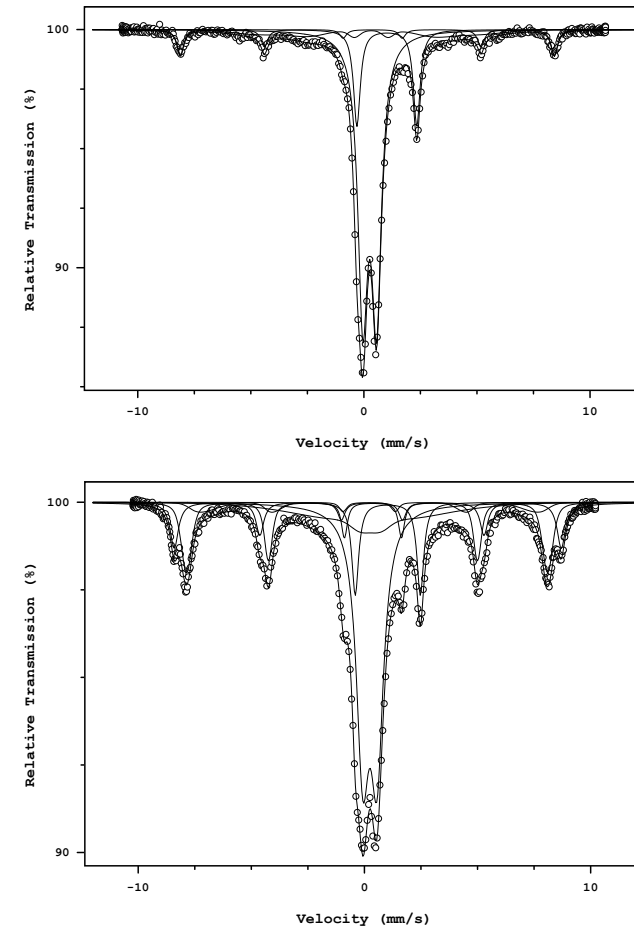


**Figure D-5:**  $^{57}\text{Fe}$  Mössbauer spectra at 298 K (top) and 4.2 K (bottom) of the clay fraction of the Ardp horizon (15–21 cm) of the 100 year paddy site (P100). The solid black line drawn through the data points is the calculated fit. Corresponding Mössbauer parameters can be found in Table D-1 and Table D-3.

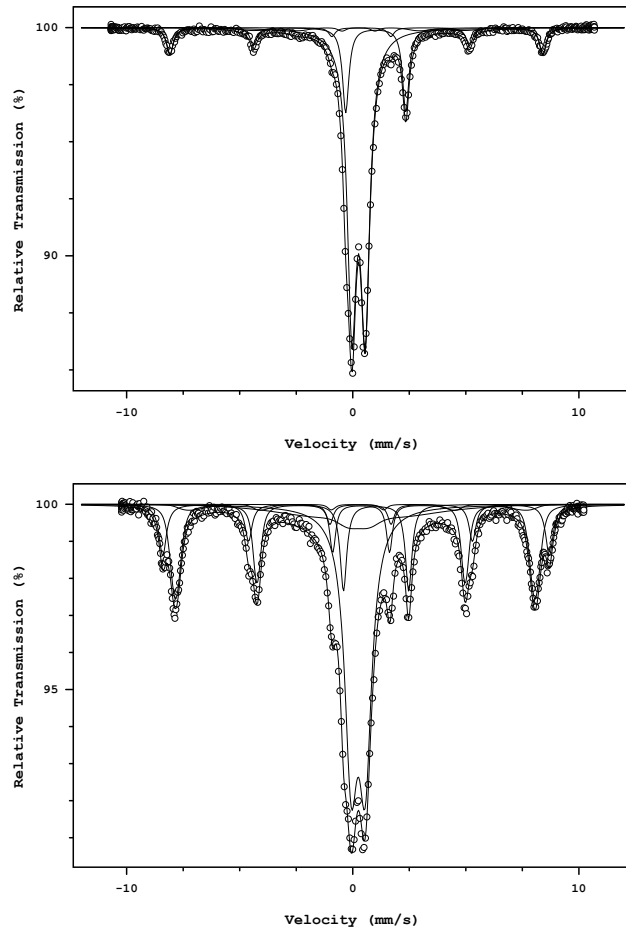


**Figure D-6:**  $^{57}\text{Fe}$  Mössbauer spectra at 298 K (top) and 4.2 K (bottom) of the clay fraction of the Bwg1 horizon (21–30 cm) of the 100 year paddy site (P100). The solid black line drawn through the data points is the calculated fit. Corresponding Mössbauer parameters can be found in Table D-1 and Table D-3.

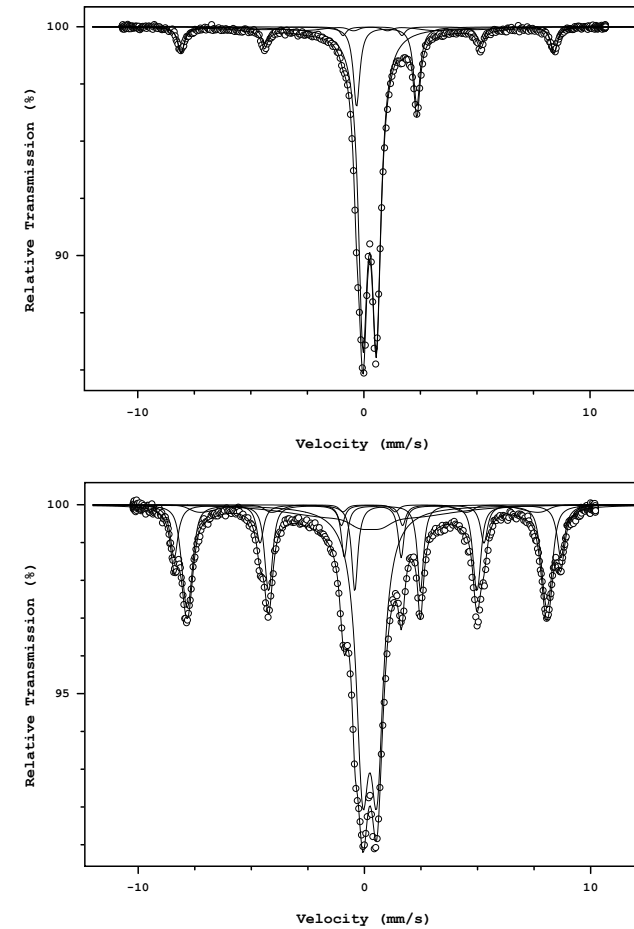


**Figure D-7:**  $^{57}\text{Fe}$  Mössbauer spectra at 298 K (top) and 4.2 K (bottom) of the clay fraction of the Bwg2 horizon (30–50 cm) of the 100 year paddy site (P100). The solid black line drawn through the data points is the calculated fit. Corresponding Mössbauer parameters can be found in Table D-1 and Table D-3.

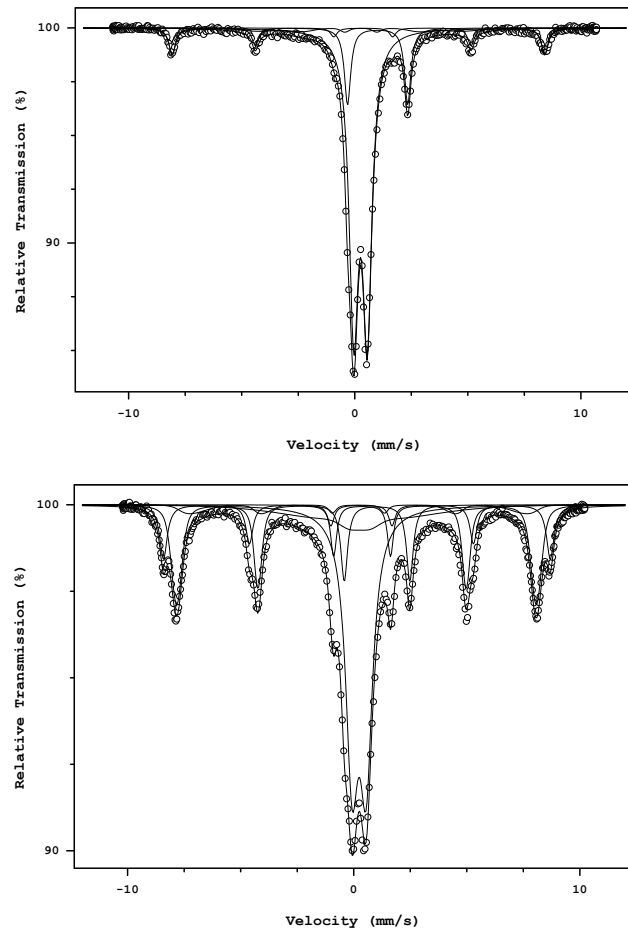


**Figure D-8:**  $^{57}\text{Fe}$  Mössbauer spectra at 298 K (top) and 4.2 K (bottom) of the clay fraction of the Bwlg1 horizon (50–75 cm) of the 100 year paddy site (P100). The solid black line drawn through the data points is the calculated fit. Corresponding Mössbauer parameters can be found in Table D-1 and Table D-3.

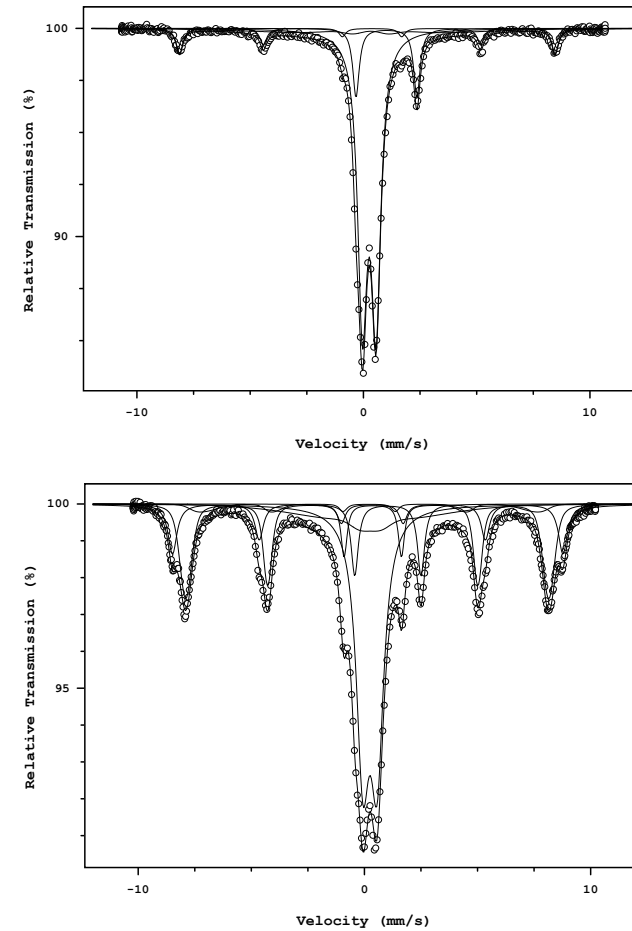


**Figure D-9:**  $^{57}\text{Fe}$  Mössbauer spectra at 298 K (top) and 4.2 K (bottom) of the clay fraction of the Bwlg2 horizon (75–100 cm) of the 100 year paddy site (P100). The solid black line drawn through the data points is the calculated fit. Corresponding Mössbauer parameters can be found in Table D-1 and Table D-3.

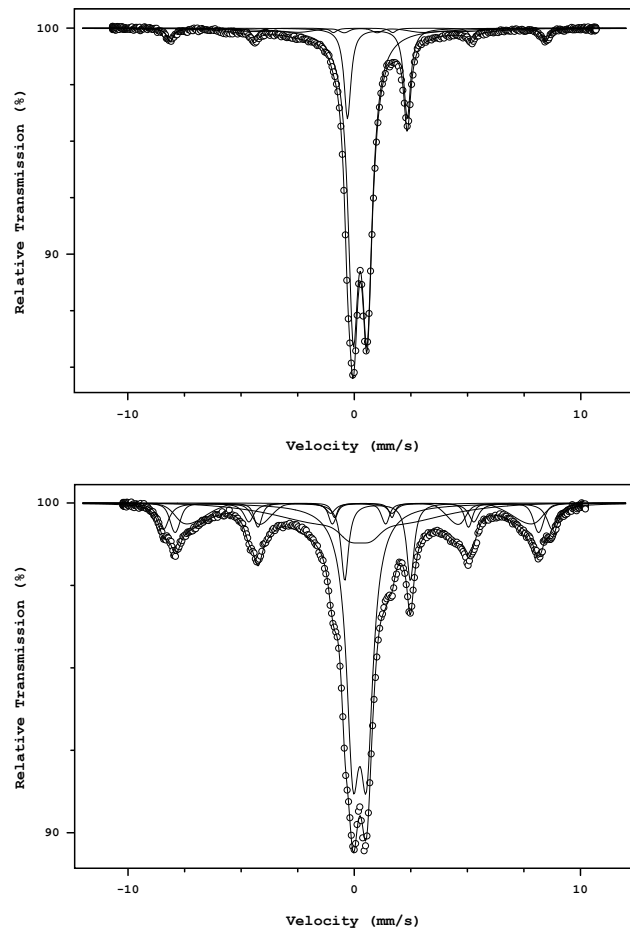


**Figure D-10:**  $^{57}\text{Fe}$  Mössbauer spectra at 298 K (top) and 4.2 K (bottom) of the clay fraction of the Alp1 horizon (0–10 cm) of the 700 year paddy site (P700). The solid black line drawn through the data points is the calculated fit. Corresponding Mössbauer parameters can be found in Table D-1 and Table D-3.

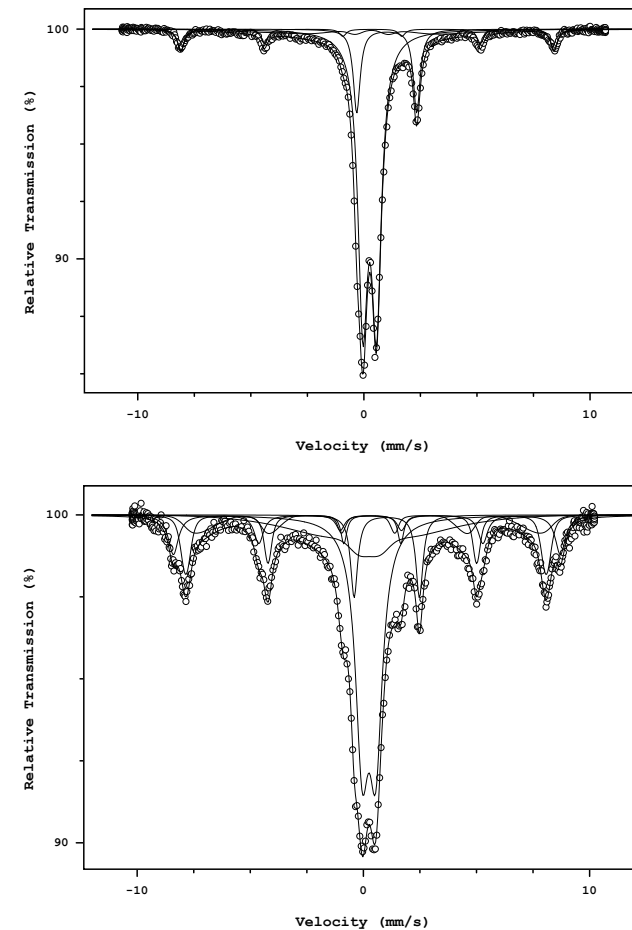


**Figure D-11:**  $^{57}\text{Fe}$  Mössbauer spectra at 298 K (top) and 4.2 K (bottom) of the clay fraction of the Alp2 horizon (10–16 cm) of the 700 year paddy site (P700). The solid black line drawn through the data points is the calculated fit. Corresponding Mössbauer parameters can be found in Table D-1 and Table D-3.

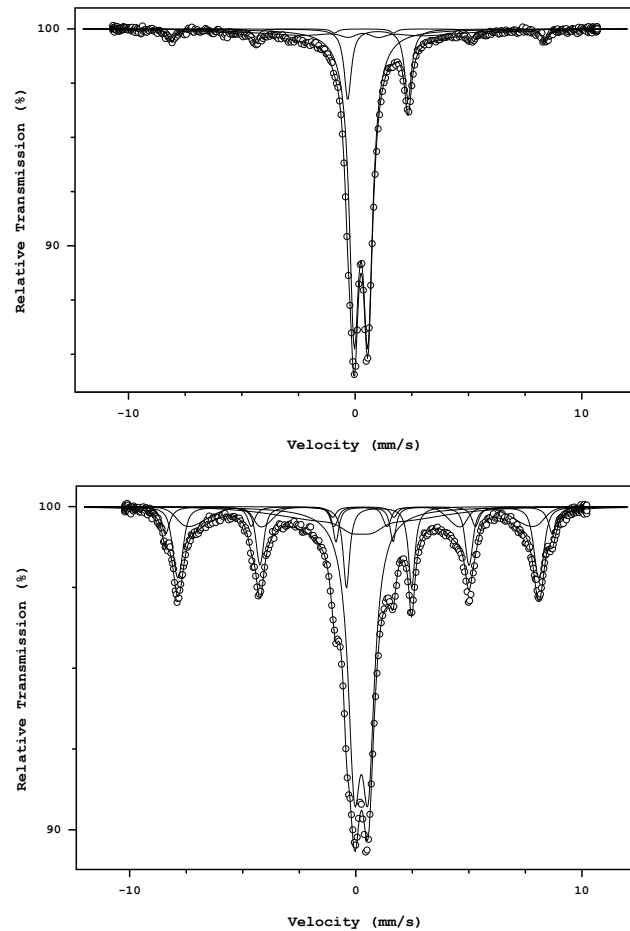


**Figure D-12:**  $^{57}\text{Fe}$  Mössbauer spectra at 298 K (top) and 4.2 K (bottom) of the clay fraction of the Ardp horizon (16–22 cm) of the 700 year paddy site (P700). The solid black line drawn through the data points is the calculated fit. Corresponding Mössbauer parameters can be found in Table D-1 and Table D-3.

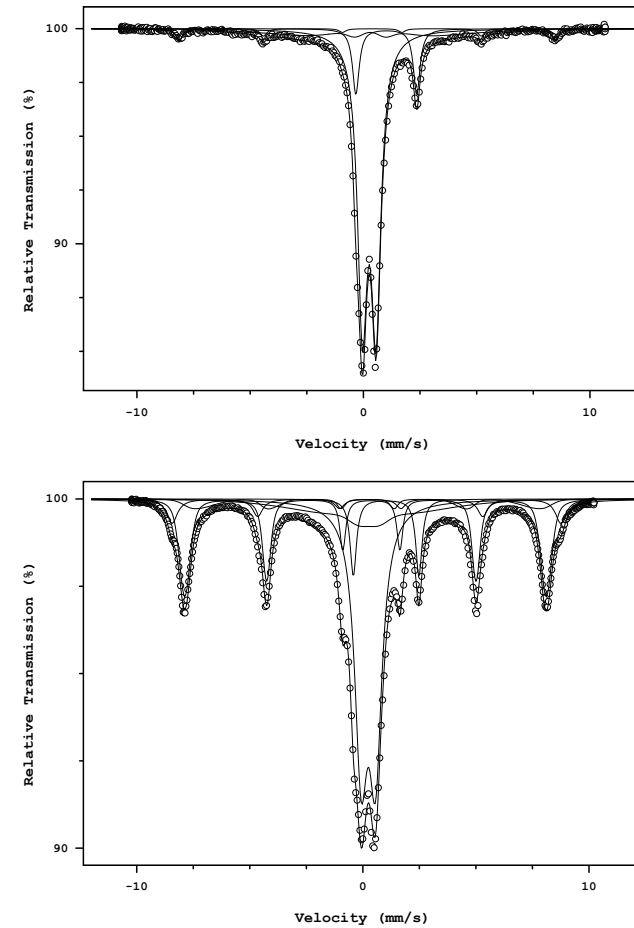


**Figure D-13:**  $^{57}\text{Fe}$  Mössbauer spectra at 298 K (top) and 4.2 K (bottom) of the clay fraction of the Bg horizon (22–45 cm) of the 700 year paddy site (P700). The solid black line drawn through the data points is the calculated fit. Corresponding Mössbauer parameters can be found in Table D-1 and Table D-3.

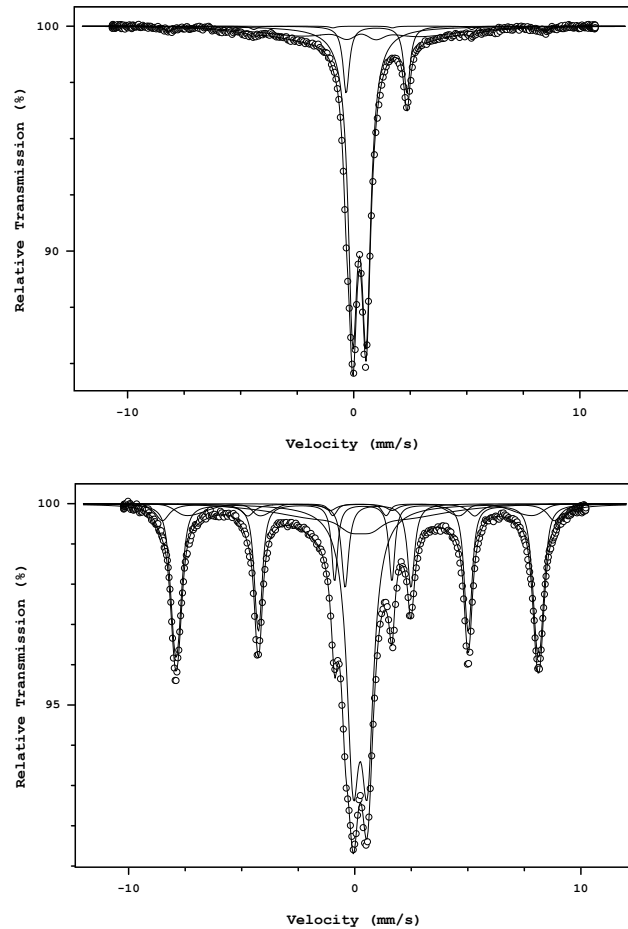


**Figure D-14:**  $^{57}\text{Fe}$  Mössbauer spectra at 298 K (top) and 4.2 K (bottom) of the clay fraction of the 2Ahgb horizon (45–69 cm) of the 700 year paddy site (P700). The solid black line drawn through the data points is the calculated fit. Corresponding Mössbauer parameters can be found in Table D-1 and Table D-3.

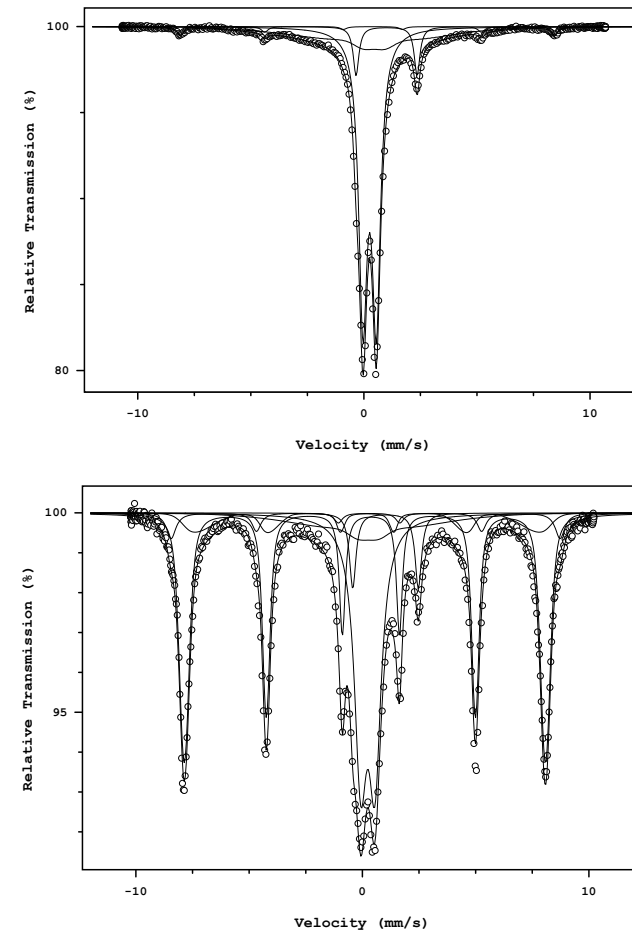


**Figure D-15:**  $^{57}\text{Fe}$  Mössbauer spectra at 298 K (top) and 4.2 K (bottom) of the clay fraction of the 2Blg1 horizon (69–106 cm) of the 700 year paddy site (P700). The solid black line drawn through the data points is the calculated fit. Corresponding Mössbauer parameters can be found in Table D-1 and Table D-3.

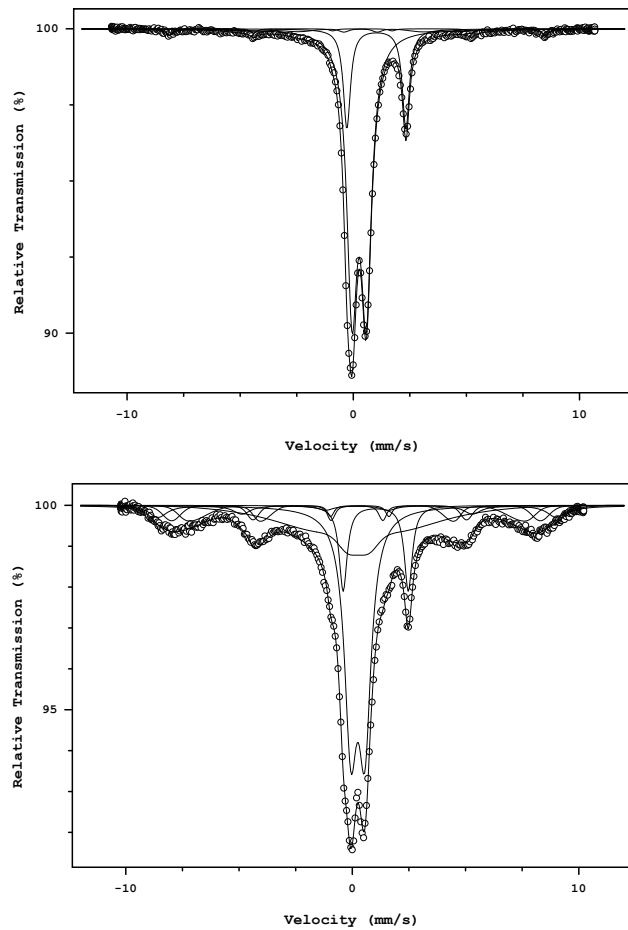


**Figure D-16:**  $^{57}\text{Fe}$  Mössbauer spectra at 298 K (top) and 4.2 K (bottom) of the clay fraction of the Alp horizon (0–15 cm) of the 2000 year paddy site (P2000). The solid black line drawn through the data points is the calculated fit. Corresponding Mössbauer parameters can be found in Table D-1 and Table D-3.

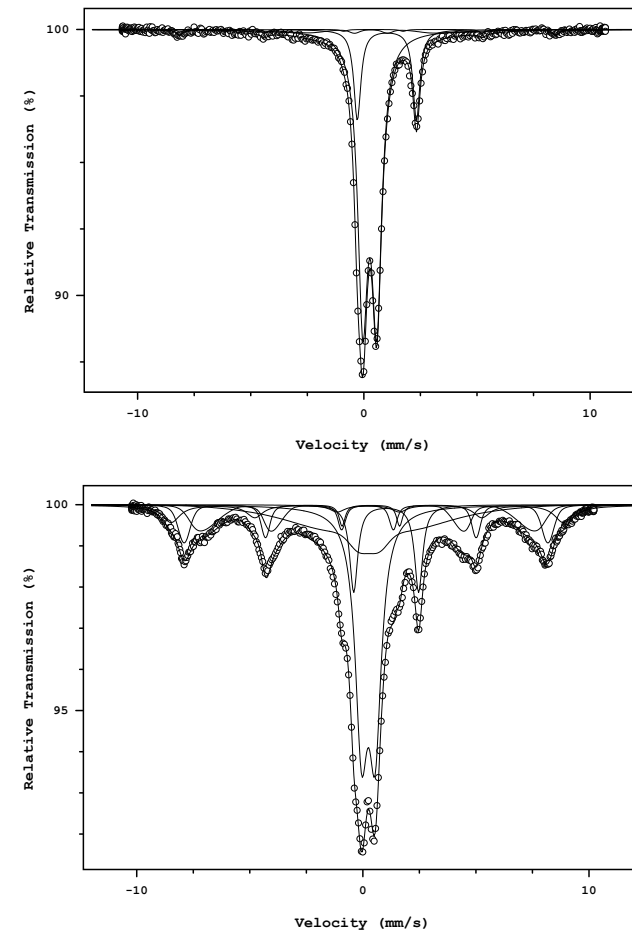


**Figure D-17:**  $^{57}\text{Fe}$  Mössbauer spectra at 298 K (top) and 4.2 K (bottom) of the clay fraction of the Ardp horizon (15–20 cm) of the 2000 year paddy site (P2000). The solid black line drawn through the data points is the calculated fit. Corresponding Mössbauer parameters can be found in Table D-1 and Table D-3.

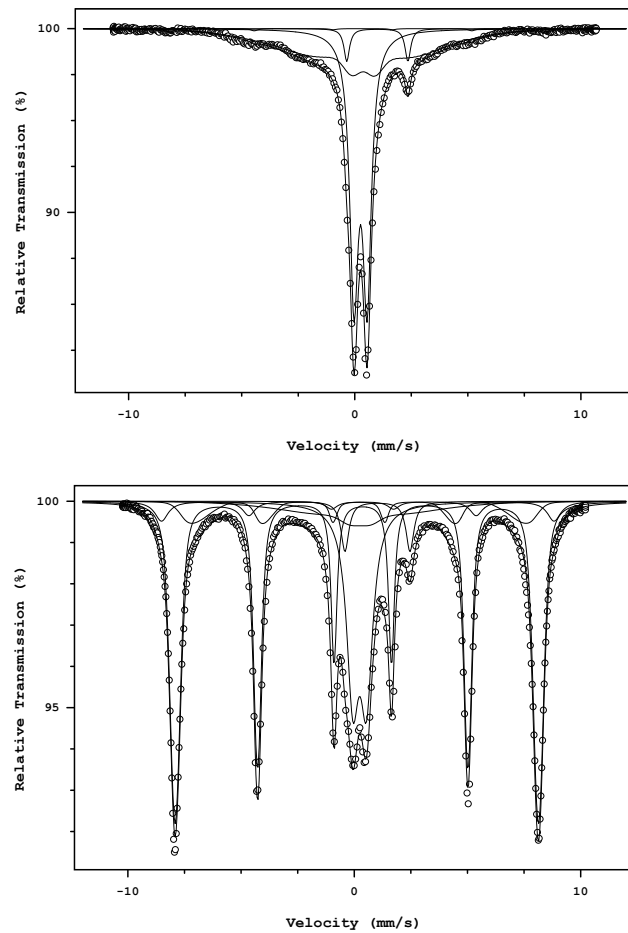


**Figure D-18:**  $^{57}\text{Fe}$  Mössbauer spectra at 298 K (top) and 4.2 K (bottom) of the clay fraction of the Bdg horizon (20–27 cm) of the 2000 year paddy site (P2000). The solid black line drawn through the data points is the calculated fit. Corresponding Mössbauer parameters can be found in Table D-1 and Table D-3.

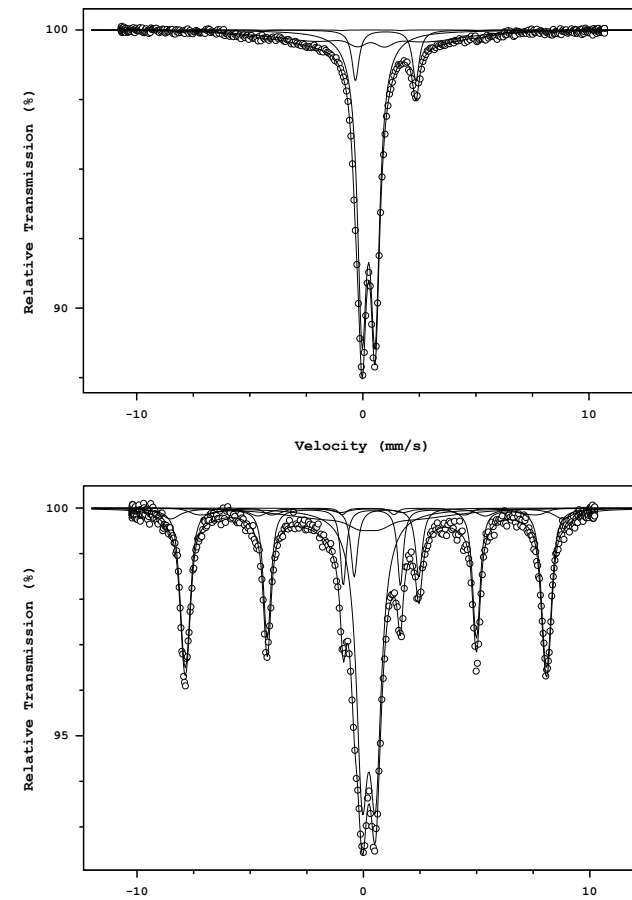


**Figure D-19:**  $^{57}\text{Fe}$  Mössbauer spectra at 298 K (top) and 4.2 K (bottom) of the clay fraction of the 2AhgB horizon (27–35 cm) of the 2000 year paddy site (P2000). The solid black line drawn through the data points is the calculated fit. Corresponding Mössbauer parameters can be found in Table D-1 and Table D-3.

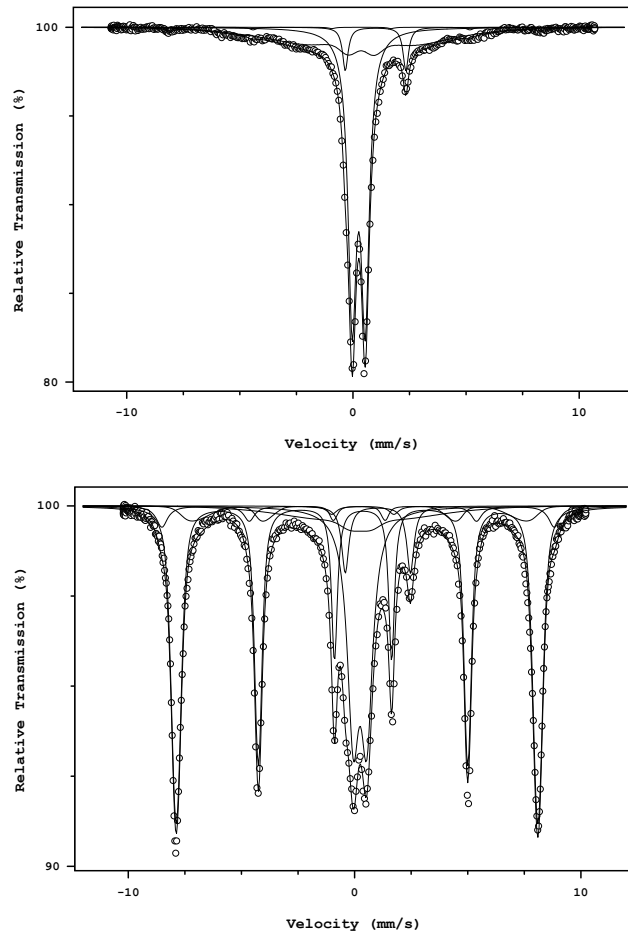


**Figure D-20:**  $^{57}\text{Fe}$  Mössbauer spectra at 298 K (top) and 4.2 K (bottom) of the clay fraction of the 2Bg1 horizon (35–50 cm) of the 2000 year paddy site (P2000). The solid black line drawn through the data points is the calculated fit. Corresponding Mössbauer parameters can be found in Table D-1 and Table D-3.

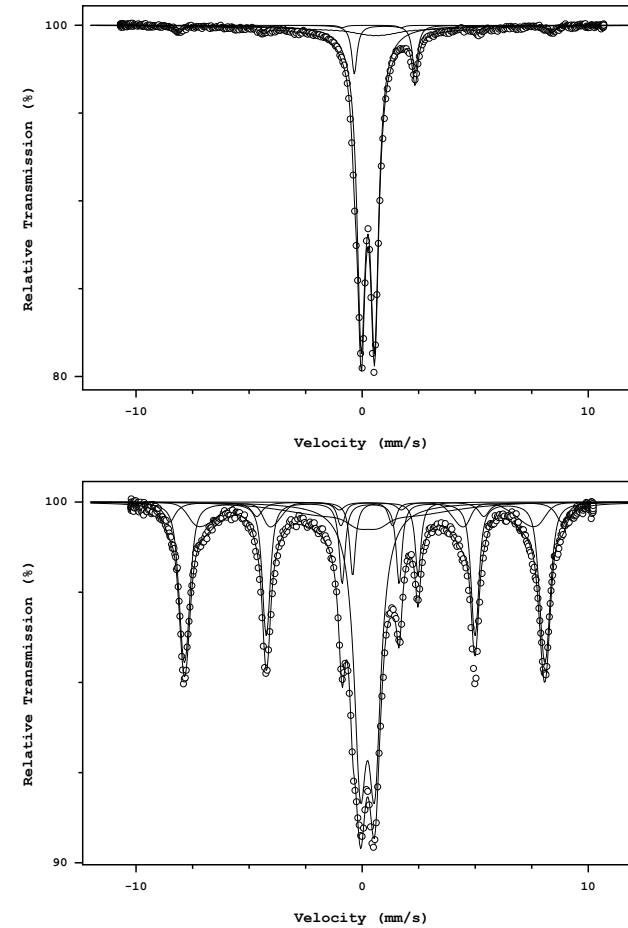


**Figure D-21:**  $^{57}\text{Fe}$  Mössbauer spectra at 298 K (top) and 4.2 K (bottom) of the clay fraction of the 2Bg2 horizon (50–70 cm) of the 2000 year paddy site (P2000). The solid black line drawn through the data points is the calculated fit. Corresponding Mössbauer parameters can be found in Table D-1 and Table D-3.

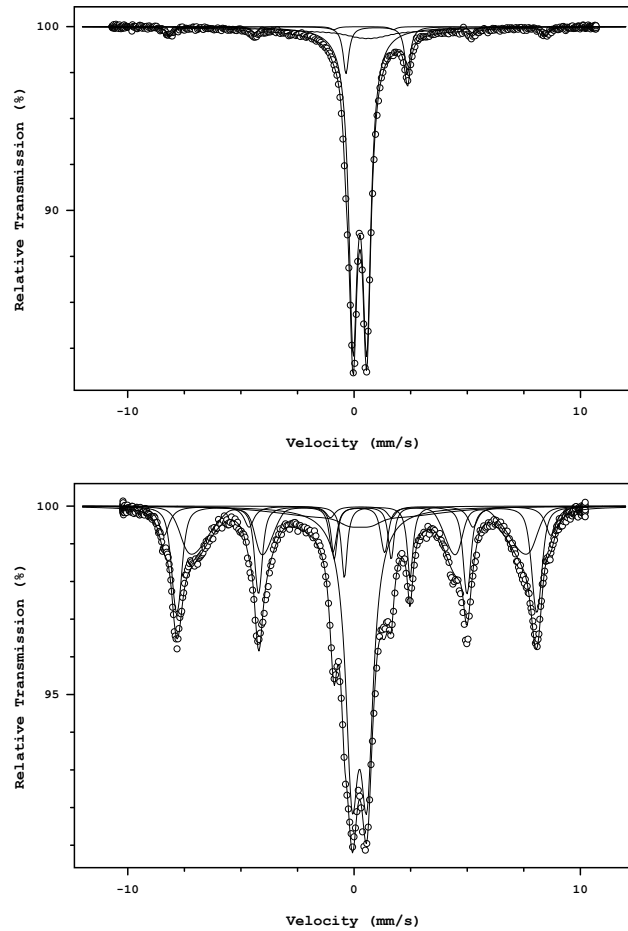


**Figure D-22:**  $^{57}\text{Fe}$  Mössbauer spectra at 298 K (top) and 4.2 K (bottom) of the clay fraction of the 2Blg horizon (70–100 cm) of the 2000 year paddy site (P2000). The solid black line drawn through the data points is the calculated fit. Corresponding Mössbauer parameters can be found in Table D-1 and Table D-3.

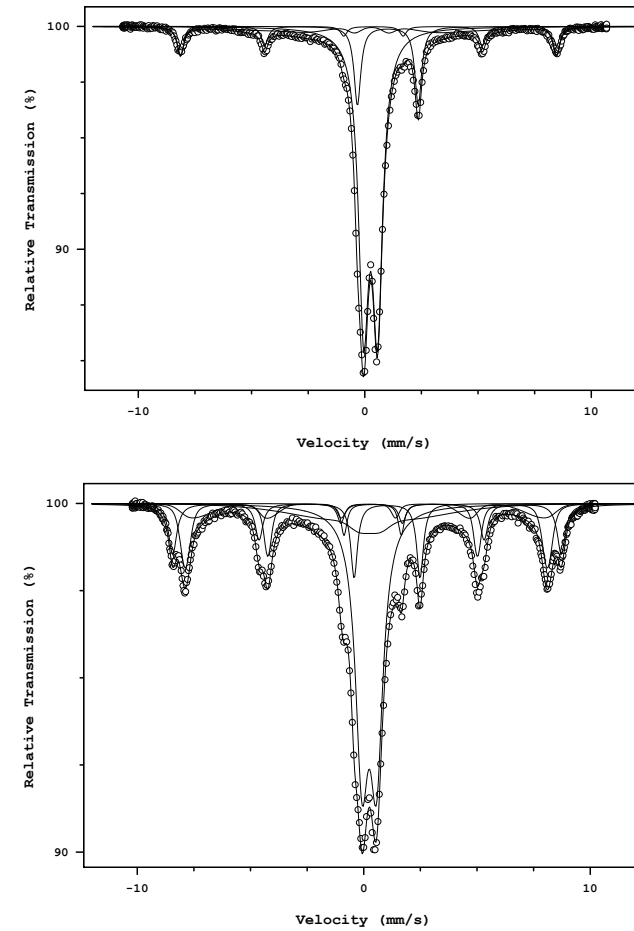


**Figure D-23:**  $^{57}\text{Fe}$  Mössbauer spectra at 298 K (top) and 4.2 K (bottom) of the clay fraction of the Ap1 horizon (0–14 cm) of the 100 year non-paddy site (NP100). The solid black line drawn through the data points is the calculated fit. Corresponding Mössbauer parameters can be found in Table D-2 and Table D-4.

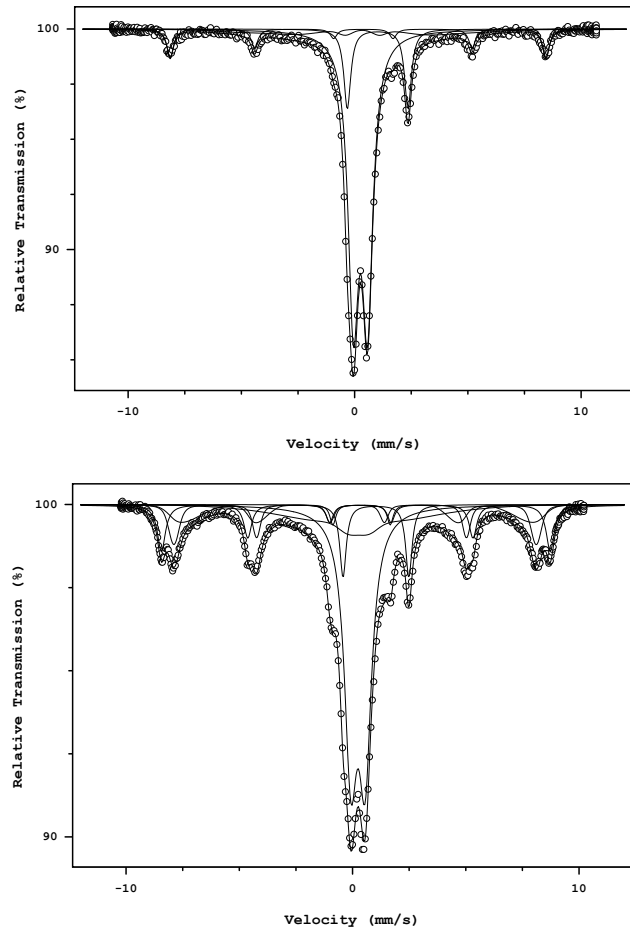


**Figure D-24:**  $^{57}\text{Fe}$  Mössbauer spectra at 298 K (top) and 4.2 K (bottom) of the clay fraction of the Ap2 horizon (14–25 cm) of the 100 year non-paddy site (NP100). The solid black line drawn through the data points is the calculated fit. Corresponding Mössbauer parameters can be found in Table D-2 and Table D-4.

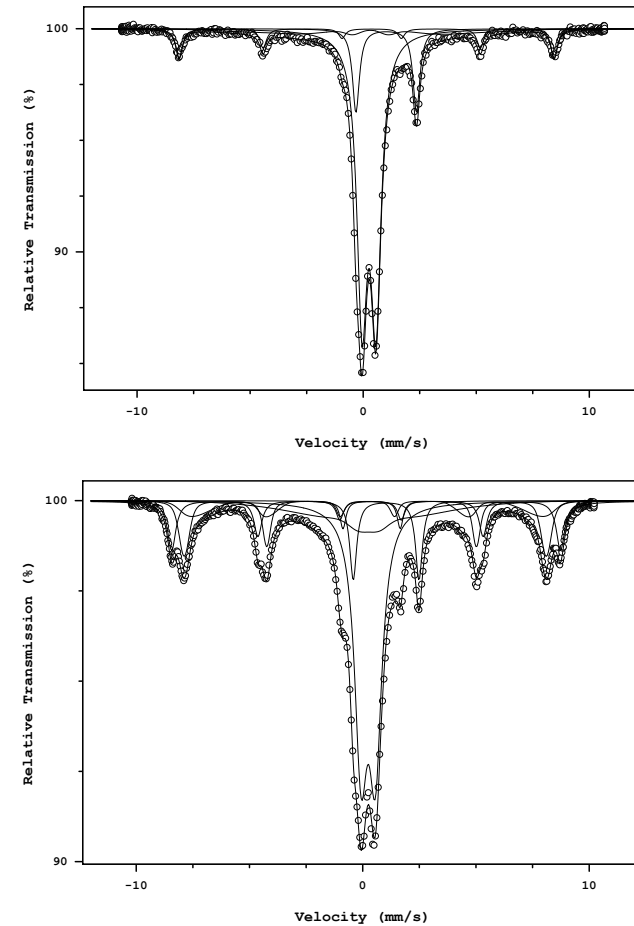


**Figure D-25:**  $^{57}\text{Fe}$  Mössbauer spectra at 298 K (top) and 4.2 K (bottom) of the clay fraction of the Bw horizon (25–30 cm) of the 100 year non-paddy site (NP100). The solid black line drawn through the data points is the calculated fit. Corresponding Mössbauer parameters can be found in Table D-2 and Table D-4.

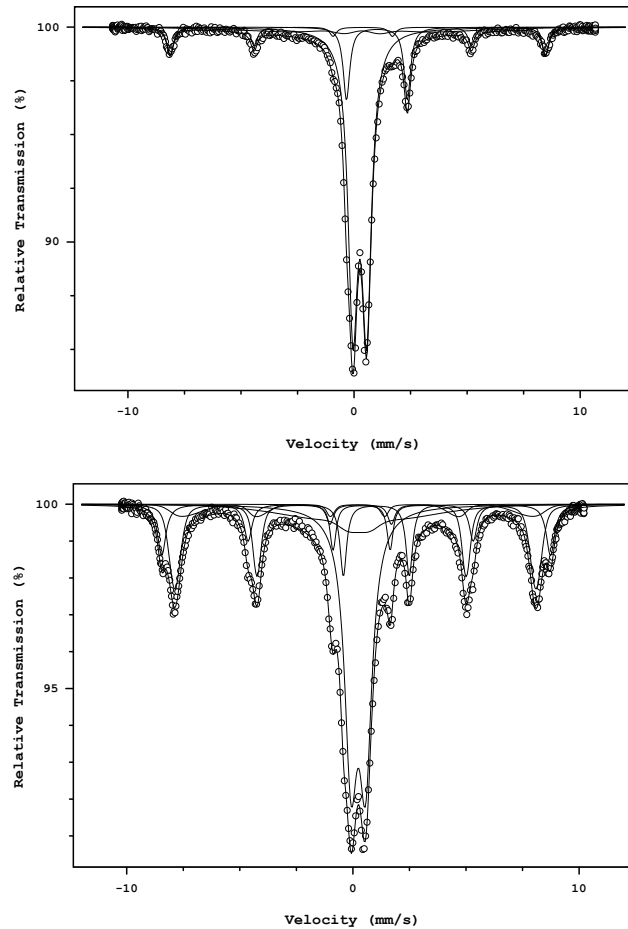


**Figure D-26:**  $^{57}\text{Fe}$  Mössbauer spectra at 298 K (top) and 4.2 K (bottom) of the clay fraction of the BCwg1 horizon (30–38 cm) of the 100 year non-paddy site (NP100). The solid black line drawn through the data points is the calculated fit. Corresponding Mössbauer parameters can be found in Table D-2 and Table D-4.

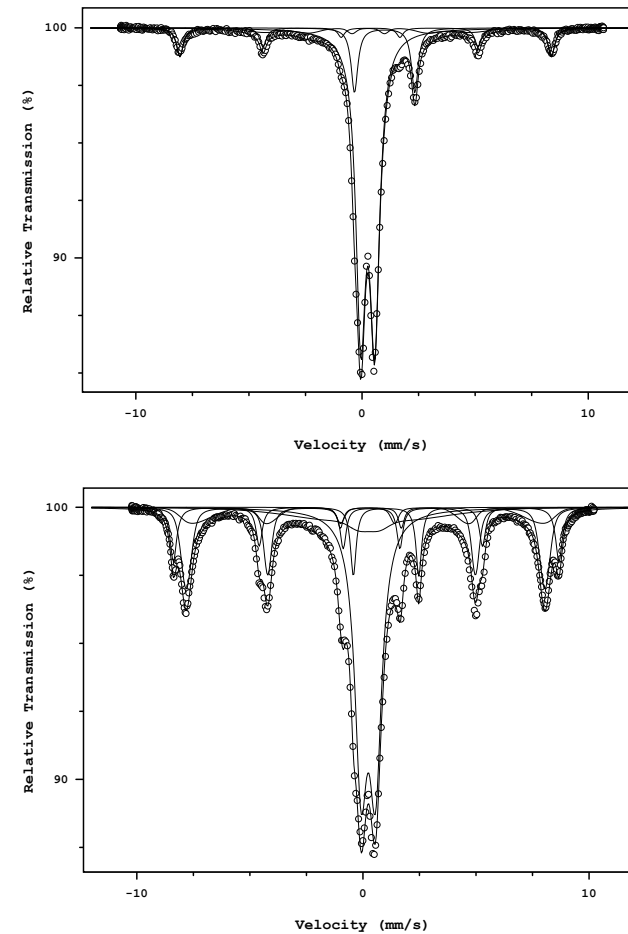


**Figure D-27:**  $^{57}\text{Fe}$  Mössbauer spectra at 298 K (top) and 4.2 K (bottom) of the clay fraction of the BCwg2 horizon (38–70 cm) of the 100 year non-paddy site (NP100). The solid black line drawn through the data points is the calculated fit. Corresponding Mössbauer parameters can be found in Table D-2 and Table D-4.

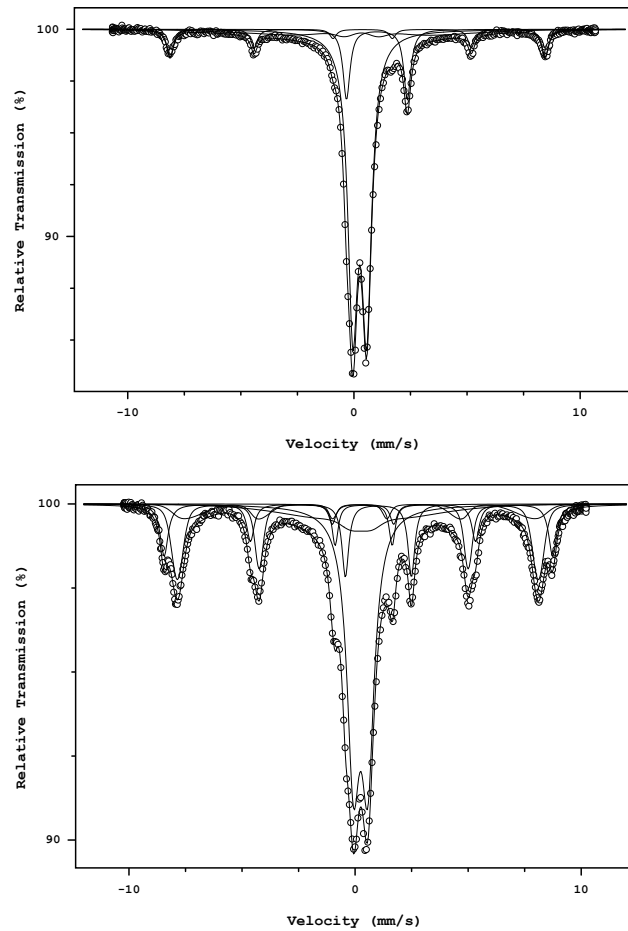


**Figure D-28:**  $^{57}\text{Fe}$  Mössbauer spectra at 298 K (top) and 4.2 K (bottom) of the clay fraction of the BCwlg horizon (70–100 cm) of the 100 year non-paddy site (NP100). The solid black line drawn through the data points is the calculated fit. Corresponding Mössbauer parameters can be found in Table D-2 and Table D-4.

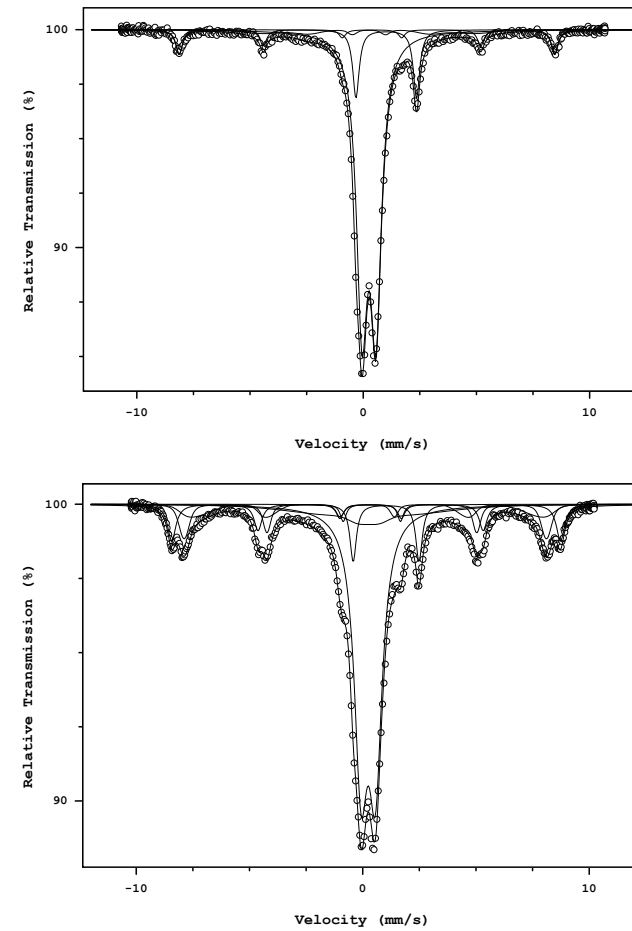


**Figure D-29:**  $^{57}\text{Fe}$  Mössbauer spectra at 298 K (top) and 4.2 K (bottom) of the clay fraction of the Ap1 horizon (0–11 cm) of the 700 year non-paddy site (NP700). The solid black line drawn through the data points is the calculated fit. Corresponding Mössbauer parameters can be found in Table D-2 and Table D-4.

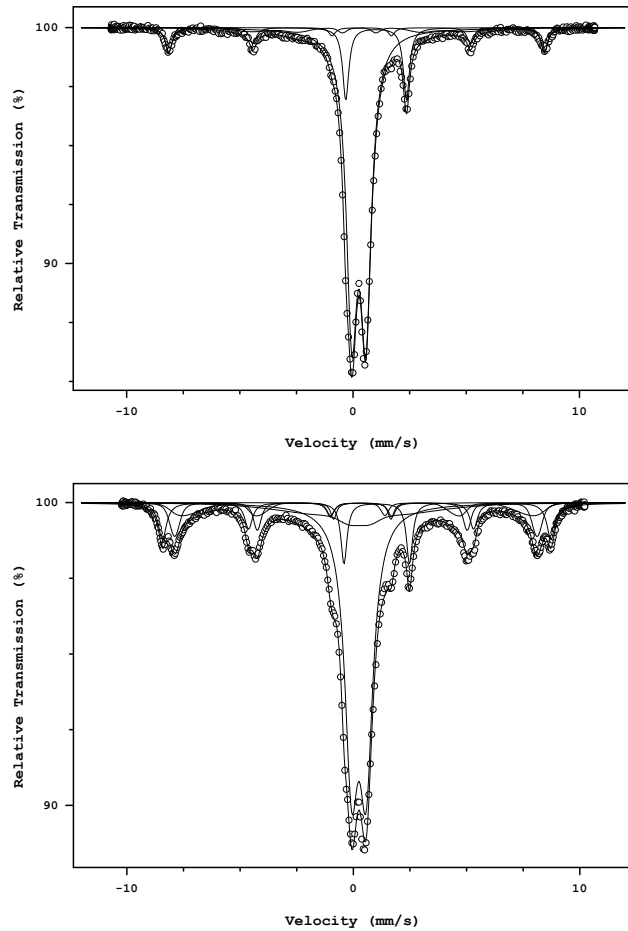


**Figure D-30:**  $^{57}\text{Fe}$  Mössbauer spectra at 298 K (top) and 4.2 K (bottom) of the clay fraction of the Ap2 horizon (11–17 cm) of the 700 year non-paddy site (NP700). The solid black line drawn through the data points is the calculated fit. Corresponding Mössbauer parameters can be found in Table D-2 and Table D-4.

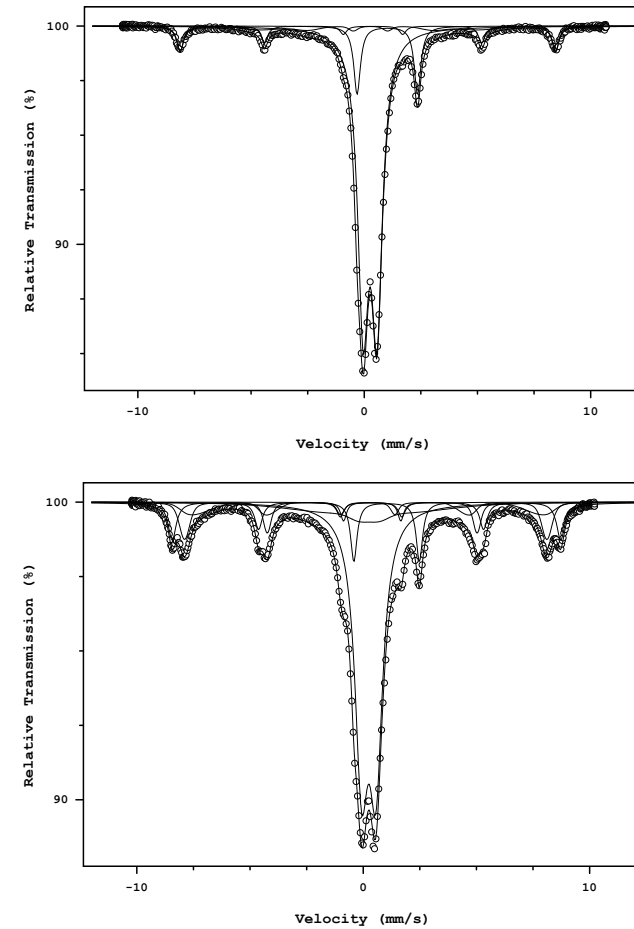


**Figure D-31:**  $^{57}\text{Fe}$  Mössbauer spectra at 298 K (top) and 4.2 K (bottom) of the clay fraction of the Bw1 horizon (17–23 cm) of the 700 year non-paddy site (NP700). The solid black line drawn through the data points is the calculated fit. Corresponding Mössbauer parameters can be found in Table D-2 and Table D-4.

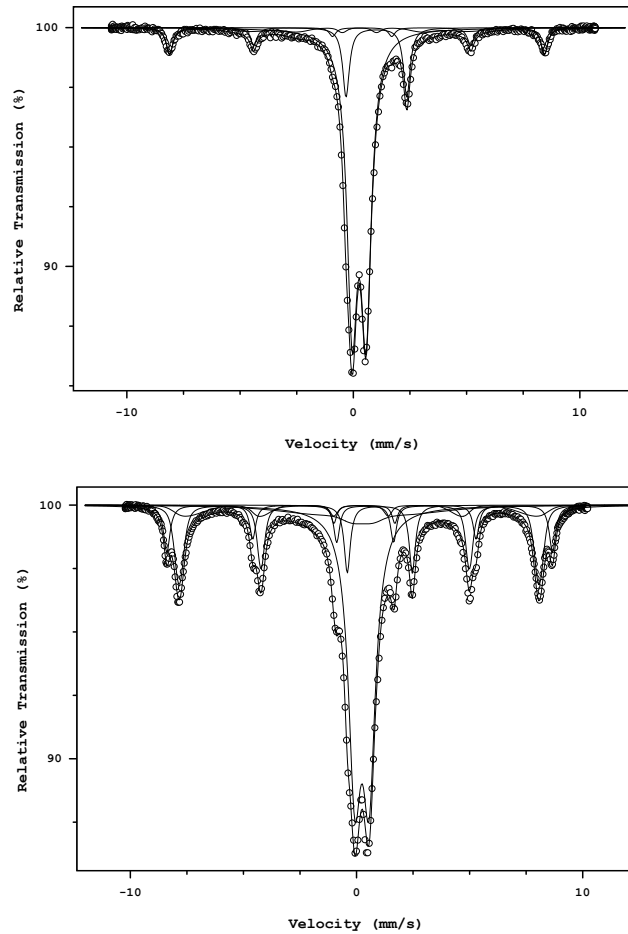


**Figure D-32:**  $^{57}\text{Fe}$  Mössbauer spectra at 298 K (top) and 4.2 K (bottom) of the clay fraction of the Bw2 horizon (23–45 cm) of the 700 year non-paddy site (NP700). The solid black line drawn through the data points is the calculated fit. Corresponding Mössbauer parameters can be found in Table D-2 and Table D-4.

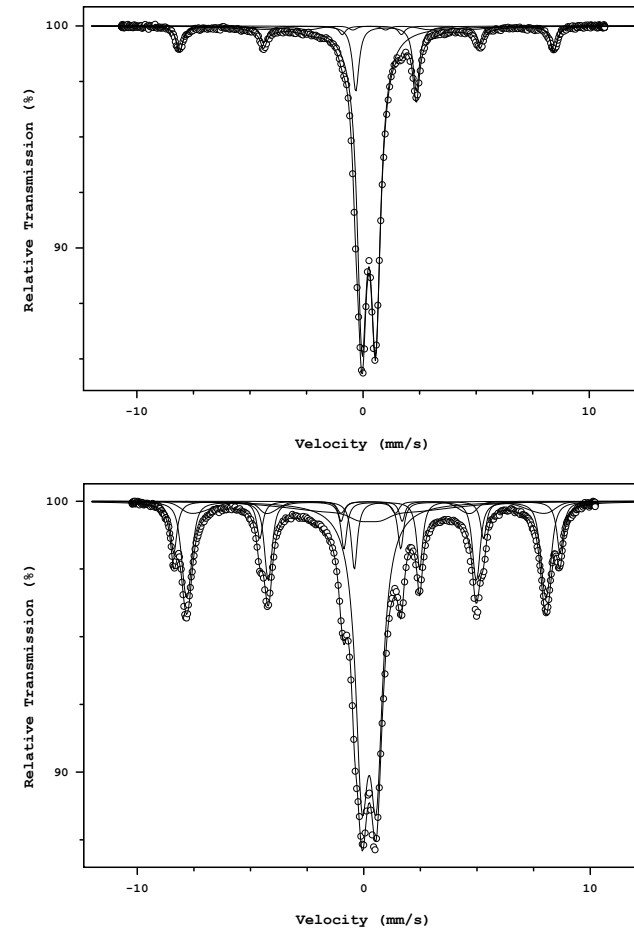


**Figure D-33:**  $^{57}\text{Fe}$  Mössbauer spectra at 298 K (top) and 4.2 K (bottom) of the clay fraction of the Bw11 horizon (45–70 cm) of the 700 year non-paddy site (NP700). The solid black line drawn through the data points is the calculated fit. Corresponding Mössbauer parameters can be found in Table D-2 and Table D-4.

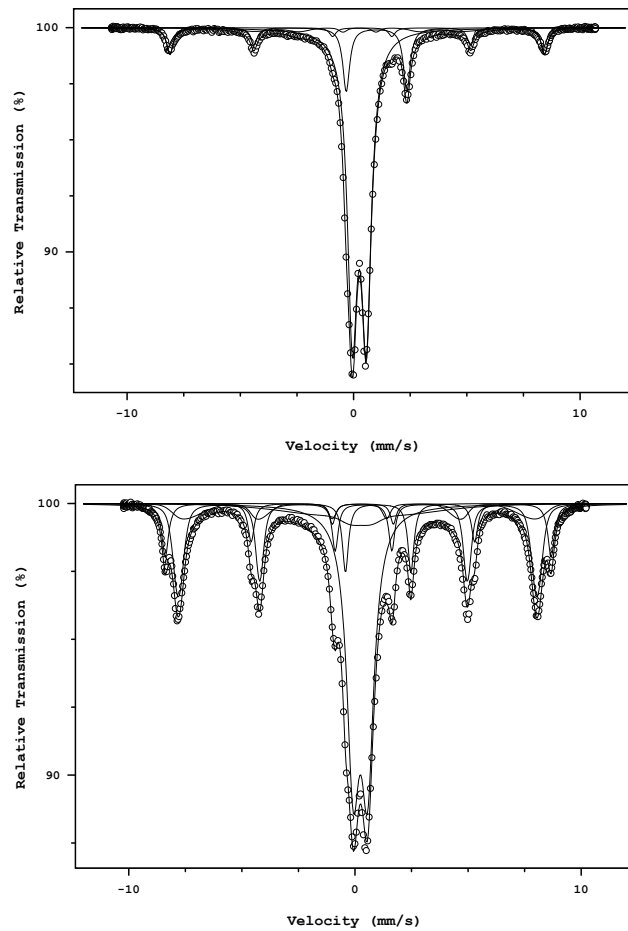


**Figure D-34:**  $^{57}\text{Fe}$  Mössbauer spectra at 298 K (top) and 4.2 K (bottom) of the clay fraction of the Bw12 horizon (70–100 cm) of the 700 year non-paddy site (NP700). The solid black line drawn through the data points is the calculated fit. Corresponding Mössbauer parameters can be found in Table D-2 and Table D-4.

**Table D-1:**  $^{57}\text{Fe}$  Mössbauer parameters, isomer shift (IS), quadrupole splitting (QS) and hyperfine field ( $B_{\text{hf}}$ ), of the spectra taken of paddy (P) clay fractions at room temperature (298 K).

Site	Depth cm	Total Area	S3-FeOx		S2		Hm			GtB							
			Area %	IS <sup>a</sup> mm s <sup>-1</sup>	QS mm s <sup>-1</sup>	Area %	IS <sup>a</sup> mm s <sup>-1</sup>	QS mm s <sup>-1</sup>	Area %	IS <sup>a</sup> mm s <sup>-1</sup>	QS mm s <sup>-2</sup>	$B_{\text{hf}}$ T	Area %	IS <sub>mean</sub> <sup>a, b</sup> mm s <sup>-1</sup>	QS <sub>mean</sub> mm s <sup>-2</sup>	$B_{\text{hf-mean}}$ T	$B_{\text{hf-sdev}}$ T
<b>P100</b>	0-9	0.188	65.2	0.263	0.627	19.1	1.023	2.642	8.3	0.283	-0.225	51.5	7.4	0.250	-0.209	31.1	6.7
	9-15	0.180	64.0	0.261	0.625	18.8	1.018	2.620	8.7	0.269	-0.229	51.1	8.5	0.250	-0.123	29.3	7.0
	15-21	0.182	65.5	0.257	0.610	16.1	1.014	2.648	8.4	0.270	-0.235	51.1	10.0	0.250	-0.150	29.1	7.5
	21-30	0.167	71.3	0.257	0.590	15.0	1.017	2.659	9.9	0.270	-0.222	51.1	3.8	0.250	-0.007	28.6	4.3
	30-50	0.170	71.1	0.255	0.598	14.1	1.009	2.667	9.5	0.272	-0.218	51.1	5.3	0.250	-0.089	29.3	6.5
	50-75	0.181	72.3	0.257	0.600	13.3	1.011	2.660	9.6	0.269	-0.210	51.1	4.8	0.250	-0.037	27.7	4.9
	70-100	0.191	70.5	0.257	0.603	11.8	1.017	2.689	8.9	0.276	-0.209	51.4	8.8	0.250	-0.151	30.3	14.2
<b>P700</b>	0-10	0.180	73.7	0.260	0.615	16.2	1.020	2.639	4.6	0.274	-0.236	51.4	5.5	0.250	-0.686	28.5	5.8
	10-16	0.177	70.0	0.256	0.602	14.9	1.009	2.653	7.4	0.265	-0.216	51.2	7.6	0.250	-0.180	28.4	9.5
	16-22	0.185	71.1	0.259	0.606	13.3	1.005	2.664	4.3	0.269	-0.240	51.1	11.3	0.250	-0.205	25.2	11.5
	22-45	0.185	72.7	0.257	0.605	11.6	1.009	2.689	3.9	0.284	-0.216	51.5	11.7	0.250	-0.109	26.2	11.1
	45-69	0.177	69.3	0.255	0.592	11.3	1.010	2.689	1.8	0.273	-0.250	51.6	17.3	0.250	-0.181	24.2	11.7
	69-106	0.222	66.3	0.254	0.591	7.7	1.003	2.699	3.1	0.280	-0.248	51.3	22.9	0.250	-0.408	17.8	14.5
<b>P2000</b>	0-15	0.128	74.5	0.260	0.630	19.3	1.022	2.610	2.2	0.291	-0.228	51.5	3.9	0.250	-0.147	28.9	5.5
	15-20	0.143	75.3	0.262	0.620	17.8	1.018	2.614	2.0	0.298	-0.252	51.6	4.9	0.250	-0.129	28.6	6.2
	20-27	0.245	52.1	0.256	0.580	4.3	0.998	2.704	1.0	0.260	-0.210	51.5	42.6	0.250	-0.260	19.1	13.0
	27-35	0.141	69.3	0.254	0.576	9.6	1.008	2.674	0.6	0.270	-0.210	51.3	20.4	0.250	-0.212	22.3	12.4
	35-50	0.226	61.0	0.254	0.576	6.3	1.000	2.677	1.4	0.270	-0.210	51.3	31.3	0.250	-0.225	21.2	13.2
	50-70	0.190	77.5	0.254	0.592	8.4	1.000	2.687	3.0	0.288	-0.275	51.1	11.1	0.250	-0.753	16.0	20.1
	70-100	0.189	76.1	0.257	0.605	8.3	1.000	2.719	3.7	0.291	-0.257	51.5	12.0	0.250	-0.743	14.7	20.5

<sup>a</sup> given with respect to the  $^{57}\text{Co}$ -Rh source; to refer to  $\alpha$ -Fe add  $0.24 \text{ mm} \cdot \text{s}^{-1}$ ; <sup>b</sup> fixed value

**Table D-2:**  $^{57}\text{Fe}$  Mössbauer parameters, isomer shift (IS), quadrupole splitting (QS) and hyperfine field ( $B_{\text{hf}}$ ), of the spectra taken of marshland (ML) and non-paddy (NP) clay fractions at room temperature (298 K).

Site	Depth cm	Total Area	S3-FeOx		S2		Hm			GtB							
			Area %	IS <sup>a</sup> mm s <sup>-1</sup>	QS mm s <sup>-1</sup>	Area %	IS <sup>a</sup> mm s <sup>-1</sup>	QS mm s <sup>-1</sup>	Area %	IS <sup>a</sup> mm s <sup>-1</sup>	QS mm s <sup>-2</sup>	$B_{\text{hf}}$ T	IS <sub>mean</sub> <sup>a,b</sup> mm s <sup>-1</sup>	QS <sub>mean</sub> mm s <sup>-2</sup>	$B_{\text{hf-mean}}$ T	$B_{\text{hf-sdev}}$ T	
<b>ML30</b>	0-13	0.206	65.1	0.258	0.621	16.6	1.020	2.665	10.1	0.271	-0.223	51.4	8.2	0.250	-0.220	31.1	12.1
	13-30	0.200	64.3	0.261	0.627	16.7	1.023	2.671	9.6	0.275	-0.223	51.7	9.4	0.250	-0.263	30.5	13.2
<b>NP100</b>	0-14	0.197	69.2	0.256	0.615	12.9	1.017	2.686	9.3	0.273	-0.219	51.5	8.7	0.250	-0.110	29.5	8.6
	14-25	0.201	69.4	0.258	0.625	13.2	1.016	2.680	9.1	0.268	-0.231	51.4	8.3	0.250	-0.186	29.2	9.4
	25-30	0.196	68.1	0.259	0.618	14.0	1.017	2.677	9.3	0.264	-0.224	51.4	8.6	0.250	-0.140	30.6	10.8
	30-38	0.194	68.9	0.255	0.609	12.1	1.011	2.691	9.4	0.275	-0.217	51.5	9.6	0.250	-0.197	29.5	14.5
	38-70	0.178	72.8	0.253	0.617	11.2	1.000	2.668	9.7	0.268	-0.217	50.9	6.3	0.250	-0.049	28.1	4.8
	70-100	0.206	68.4	0.257	0.613	12.2	1.015	2.689	9.1	0.274	-0.224	51.4	10.4	0.250	-0.158	29.5	12.9
<b>NP700</b>	0-12	0.196	75.8	0.255	0.618	10.9	1.017	2.676	8.0	0.275	-0.223	51.4	5.3	0.250	-0.004	28.7	5.1
	12-17	0.183	75.5	0.256	0.621	11.0	1.018	2.681	8.0	0.270	-0.226	51.5	5.5	0.250	-0.045	29.0	4.9
	17-23	0.195	75.2	0.257	0.613	11.2	1.019	2.671	8.3	0.273	-0.228	51.4	5.3	0.250	-0.048	29.7	5.1
	23-45	0.175	74.0	0.256	0.614	11.7	1.020	2.683	8.9	0.275	-0.229	51.3	5.4	0.250	-0.038	29.6	5.0
	45-70	0.178	75.2	0.254	0.606	11.4	1.014	2.675	9.2	0.272	-0.230	51.3	4.2	0.250	-0.044	28.3	4.1
	70-100	0.180	74.9	0.255	0.617	11.4	1.013	2.674	9.1	0.271	-0.222	51.3	4.6	0.250	-0.021	28.6	4.2

<sup>a</sup> given with respect to the  $^{57}\text{Co}$ -Rh source; to refer to  $\alpha$ -Fe add  $0.24 \text{ mm} \cdot \text{s}^{-1}$ ; <sup>b</sup> fixed value

**Table D-3:**  $^{57}\text{Fe}$  Mössbauer parameters, isomer shift (IS), quadrupole splitting (QS), hyperfine field ( $B_{\text{hf}}$ ) and asymmetry (asym), of the spectra taken of paddy (P) clay fractions at liquid helium temperature (4.2 K).

Site	Depth cm	Total Area	S3		S2		Hm				$B_{\text{hf}}$	
			Area %	IS <sup>a</sup> $\text{mm s}^{-1}$	QS $\text{mm s}^{-1}$	Area %	IS <sup>a</sup> $\text{mm s}^{-1}$	QS $\text{mm s}^{-1}$	Area %	IS <sup>a</sup> $\text{mm s}^{-1}$		QS $\text{mm s}^{-1}$
<b>P100</b>	0-9	0.223	38.5	0.243	0.618	9.8	1.036	2.881	11.4	0.243	-0.180	53.2
	9-15	0.215	38.7	0.241	0.611	10.5	1.033	2.866	10.7	0.240	-0.191	53.0
	15-21	0.219	43.8	0.242	0.628	8.8	1.033	2.878	10.6	0.240	-0.183	53.1
	21-30	0.208	44.1	0.241	0.620	7.8	1.031	2.883	10.6	0.244	-0.197	53.0
	30-50	0.211	42.6	0.238	0.632	7.1	1.025	2.905	10.9	0.237	-0.197	53.0
	50-75	0.231	42.6	0.239	0.622	6.8	1.031	2.902	10.9	0.241	-0.202	53.0
	70-100	0.223	41.9	0.246	0.629	6.6	1.037	2.930	11.6	0.246	-0.202	53.5
<b>P700</b>	0-10	0.222	43.6	0.245	0.600	8.4	1.032	2.899	8.2	0.238	-0.155	53.3
	10-16	0.244	39.3	0.246	0.599	7.7	1.034	2.886	10.7	0.242	-0.177	53.0
	16-22	0.231	43.8	0.244	0.608	7.4	1.031	2.887	6.3	0.239	-0.192	53.1
	22-45	0.223	43.8	0.242	0.634	6.6	1.028	2.902	7.1	0.241	-0.165	53.3
	45-69	0.220	36.7	0.242	0.630	7.2	1.030	2.911	5.6	0.225	-0.128	53.7
	69-106	0.266	30.5	0.238	0.630	4.9	1.021	2.895	4.9	0.218	-0.153	53.2
<b>P2000</b>	0-15	0.172	41.7	0.243	0.616	10.3	1.035	2.876	6.7	0.215	0.002	54.5
	15-20	0.195	36.5	0.242	0.599	9.4	1.031	2.871	8.4	0.216	-0.049	53.8
	20-27	0.270	21.2	0.238	0.605	3.7	1.024	2.871	5.1	0.260	-0.210	53.8
	27-35	0.175	38.9	0.241	0.588	6.2	1.023	2.856	5.6	0.260	-0.210	53.8
	35-50	0.301	24.3	0.240	0.598	4.7	1.027	2.878	4.7	0.260	-0.210	53.8
	50-70	0.257	35.5	0.237	0.636	4.8	1.026	2.894	5.4	0.260	-0.210	53.8
	70-100	0.246	37.2	0.240	0.655	4.8	1.023	2.906	7.1	0.227	-0.161	53.0

<sup>a</sup> given with respect to the  $^{57}\text{Co}$ -Rh source; to refer to  $\alpha$ -Fe add  $0.24 \text{ mm} \cdot \text{s}^{-1}$ ; <sup>b</sup> fixed value

Table D-3 (continued)

Site	Gt			HFO							FeB					
	Depth cm	Area %	IS <sup>a</sup> mm s <sup>-1</sup>	QS mm s <sup>-1</sup>	B <sub>hf</sub>	Area %	IS <sub>mean</sub> <sup>a,b</sup> mm s <sup>-1</sup>	QS <sub>mean</sub> <sup>b</sup> mm s <sup>-1</sup>	B <sub>hf-mean</sub> <sup>b</sup> T	B <sub>hf-sdev</sub> <sup>b</sup> T	Asym <sup>b</sup> mm s <sup>-1</sup>	Area %	IS <sub>mean</sub> <sup>b</sup> mm s <sup>-1</sup>	QS <sub>mean</sub> <sup>b</sup> mm s <sup>-1</sup>	B <sub>hf-mean</sub> <sup>b</sup> T	B <sub>hf-sdev</sub> <sup>b</sup> T
<b>P100</b>	0-9	7.4	0.249	-0.236	49.9	11.9	0.209	0.000	45.1	2.4	-0.5	20.9	0.260	0.000	17.0	14.8
	9-15	9.3	0.249	-0.250	49.7	12.9	0.209	0.000	45.1	2.4	-0.5	17.9	0.260	0.000	17.0	14.8
	15-21	17.1	0.247	-0.259	49.5	5.2	0.209	0.000	45.1	2.4	-0.5	14.5	0.260	0.000	17.0	14.8
	21-30	22.9	0.240	-0.257	49.3	3.1	0.209	0.000	45.1	2.4	-0.5	11.4	0.260	0.000	17.0	14.8
	30-50	24.3	0.242	-0.253	49.3	3.8	0.209	0.000	45.1	2.4	-0.5	11.2	0.260	0.000	17.0	14.8
	50-75	23.8	0.246	-0.248	49.3	4.5	0.209	0.000	45.1	2.4	-0.5	11.5	0.260	0.000	17.0	14.8
	70-100	24.0	0.247	-0.243	49.8	4.0	0.209	0.000	45.1	2.4	-0.5	12.0	0.260	0.000	17.0	14.8
<b>P700</b>	0-10	7.3	0.258	-0.281	49.8	12.8	0.210	0.000	45.8	2.4	-0.5	19.7	0.260	0.000	17.0	14.8
	10-16	13.2	0.255	-0.280	49.4	10.2	0.210	0.000	45.8	2.4	-0.5	18.9	0.260	0.000	17.0	14.8
	16-22	17.2	0.251	-0.268	49.5	11.9	0.210	0.000	45.8	2.4	-0.5	13.3	0.260	0.000	17.0	14.8
	22-45	24.3	0.246	-0.258	49.6	5.6	0.210	0.000	45.8	2.4	-0.5	12.7	0.260	0.000	17.0	14.8
	45-69	32.2	0.245	-0.264	49.7	6.0	0.210	0.000	45.8	2.4	-0.5	12.3	0.260	0.000	17.0	14.8
	69-106	42.3	0.242	-0.266	49.4	8.2	0.210	0.000	45.8	2.4	-0.5	9.3	0.260	0.000	17.0	14.8
<b>P2000</b>	0-15	6.3	0.248	-0.166	50.5	9.4	0.206	0.000	44.6	2.4	-0.5	25.6	0.260	0.000	17.0	14.8
	15-20	10.0	0.246	-0.213	49.9	13.7	0.206	0.000	44.6	2.4	-0.5	22.1	0.260	0.000	17.0	14.8
	20-27	53.8	0.243	-0.263	49.8	8.3	0.206	0.000	44.6	2.4	-0.5	7.9	0.260	0.000	17.0	14.8
	27-35	35.5	0.241	-0.261	49.5	3.6	0.206	0.000	44.6	2.4	-0.5	10.2	0.260	0.000	17.0	14.8
	35-50	52.1	0.241	-0.265	49.6	5.8	0.206	0.000	44.6	2.4	-0.5	8.4	0.260	0.000	17.0	14.8
	50-70	32.4	0.244	-0.264	49.4	11.1	0.206	0.000	44.6	2.4	-0.5	10.7	0.260	0.000	17.0	14.8
	70-100	21.0	0.251	-0.263	49.3	21.7	0.206	0.000	44.6	2.4	-0.5	8.2	0.260	0.000	17.0	14.8

<sup>a</sup> given with respect to the <sup>57</sup>Co–Rh source; to refer to  $\alpha$ -Fe add 0.24 mm s<sup>-1</sup>; <sup>b</sup> fixed value

**Table D-4:**  $^{57}\text{Fe}$  Mössbauer parameters, isomer shift (IS), quadrupole splitting (QS) hyperfine field ( $B_{\text{hf}}$ ) and asymmetry (asym), of the spectra taken of marshland (ML30) and non-paddy (NP) clay fractions at liquid helium temperature (4.2 K).

Site	Depth cm	S3		S2		Hm		$B_{\text{hf}}$				
		Total Area	Area %	IS <sup>a</sup> $\text{mm s}^{-1}$	QS $\text{mm s}^{-1}$	Area %	IS <sup>a</sup> $\text{mm s}^{-1}$		QS $\text{mm s}^{-1}$			
<b>ML30</b>	0-13	0.239	33.1	0.238	0.640	8.4	1.038	2.927	12.6	0.247	-0.199	53.5
	13-30	0.239	34.1	0.239	0.632	8.7	1.037	2.933	13.5	0.247	-0.196	53.5
<b>NP100</b>	0-14	0.222	44.2	0.241	0.641	6.8	1.029	2.909	11.4	0.245	-0.201	53.2
	14-25	0.220	45.7	0.241	0.630	6.7	1.033	2.907	11.1	0.245	-0.200	53.2
	25-30	0.213	43.6	0.243	0.633	7.5	1.033	2.903	11.5	0.247	-0.195	53.2
	30-38	0.219	42.1	0.238	0.643	6.2	1.035	2.915	11.2	0.242	-0.201	53.3
	38-70	0.283	44.1	0.236	0.638	5.3	1.022	2.894	10.0	0.246	-0.206	52.9
	70-100	0.238	42.6	0.244	0.636	6.5	1.030	2.920	11.0	0.248	-0.202	53.3
<b>NP700</b>	0-12	0.222	54.9	0.243	0.637	5.5	1.032	2.908	9.9	0.249	-0.197	53.2
	12-17	0.220	54.1	0.244	0.643	6.0	1.034	2.893	9.7	0.245	-0.194	53.2
	17-23	0.223	54.4	0.245	0.634	6.1	1.033	2.894	9.9	0.244	-0.203	53.2
	23-45	0.282	49.5	0.239	0.633	6.2	1.029	2.876	9.0	0.243	-0.208	52.9
	45-70	0.282	45.6	0.238	0.636	5.7	1.027	2.887	9.4	0.243	-0.208	52.9
	70-100	0.282	44.0	0.239	0.637	5.6	1.026	2.896	9.6	0.246	-0.208	52.9

<sup>a</sup> given with respect to the  $^{57}\text{Co}$ -Rh source; to refer to  $\alpha$ -Fe add  $0.24 \text{ mm} \cdot \text{s}^{-1}$ ; <sup>b</sup> fixed value

Table D-4 (continued)

Site	Depth cm	Gt			HFO				FeB							
		Area %	IS <sup>a</sup> mm s <sup>-1</sup>	QS mm s <sup>-1</sup>	B <sub>hf</sub>	Area %	IS <sub>mean</sub> <sup>a</sup> mm s <sup>-1</sup>	QS <sub>mean</sub> <sup>b</sup> mm s <sup>-1</sup>	B <sub>hf-mean</sub> <sup>b</sup> T	B <sub>hf-sdev</sub> <sup>b</sup> T	Asym <sup>b</sup> mm s <sup>-1</sup>	Area %	IS <sub>mean</sub> <sup>a</sup> mm s <sup>-1</sup>	QS <sub>mean</sub> <sup>b</sup> mm s <sup>-1</sup>	B <sub>hf-mean</sub> <sup>b</sup> T	B <sub>hf-sdev</sub> <sup>b</sup> T
ML30	0-13	15.1	0.258	-0.289	49.9	12.3	0.202	0.000	47.9	2.4	-0.5	18.6	0.260	0.000	17.0	14.8
	13-30	14.1	0.257	-0.289	49.7	12.1	0.202	0.000	47.9	2.4	-0.5	17.5	0.260	0.000	17.0	14.8
NP100	0-14	15.1	0.253	-0.278	49.6	8.5	0.206	0.000	46.7	2.4	-0.5	14.0	0.260	0.000	17.0	14.8
	14-25	10.2	0.254	-0.285	49.6	11.1	0.206	0.000	46.7	2.4	-0.5	15.2	0.260	0.000	17.0	14.8
	25-30	13.4	0.251	-0.280	49.6	9.3	0.206	0.000	46.7	2.4	-0.5	14.8	0.260	0.000	17.0	14.8
	30-38	21.0	0.247	-0.274	49.5	6.8	0.206	0.000	46.7	2.4	-0.5	12.7	0.260	0.000	17.0	14.8
	38-70	19.7	0.249	-0.266	49.2	9.5	0.206	0.000	46.7	2.4	-0.5	11.5	0.260	0.000	17.0	14.8
	70-100	19.2	0.251	-0.258	49.5	8.3	0.206	0.000	46.7	2.4	-0.5	12.3	0.260	0.000	17.0	14.8
NP700	0-12	9.6	0.258	-0.289	49.6	8.5	0.197	0.000	46.8	2.4	-0.5	11.1	0.260	0.000	17.0	14.8
	12-17	9.2	0.253	-0.281	49.6	8.6	0.197	0.000	46.8	2.4	-0.5	12.5	0.260	0.000	17.0	14.8
	17-23	10.4	0.252	-0.285	49.6	8.3	0.197	0.000	46.8	2.4	-0.5	10.9	0.260	0.000	17.0	14.8
	23-45	19.0	0.247	-0.268	49.3	6.8	0.197	0.000	46.8	2.4	-0.5	9.5	0.260	0.000	17.0	14.8
	45-70	22.8	0.247	-0.263	49.2	6.9	0.197	0.000	46.8	2.4	-0.5	9.6	0.260	0.000	17.0	14.8
	70-100	22.2	0.240	-0.260	49.2	8.6	0.197	0.000	46.8	2.4	-0.5	10.1	0.260	0.000	17.0	14.8

<sup>a</sup> given with respect to the <sup>57</sup>Co–Rh source; to refer to  $\alpha$ -Fe add 0.24 mm s<sup>-1</sup>; <sup>b</sup> fixed value

## E. Appendix: Soil redox potentials and soil solution composition

**Table E-1:** Soil redox potential (Eh) determined at 10 cm (10), 35 cm (35) and 55 cm (55) below surface at the 100 year paddy site (P100).

Site	Date	daf	m.Eh 10	sd.Eh 10	n.Eh 10	m.Eh 35	sd.Eh 35	n.Eh 35	m.Eh 55	sd.Eh 55	n.Eh 55
			--- mV ---			--- mV ---			--- mV ---		
P100	24.03.09				0	-146	119	5	-190	25	5
P100	25.03.09				0	-146	114	5	-188	25	5
P100	22.04.09				0	-198	33	5	-205	16	5
P100	23.04.09				0	-197	33	5	-204	17	5
P100	27.05.09				0	592	31	5	493	197	5
P100	28.05.09				0	588	30	5	494	195	5
P100	29.05.09		241	166	4	588	32	5	487	201	5
P100	30.05.09		215	217	4	588	32	5	482	211	5
P100	31.05.09		197	237	4	591	27	5	459	230	5
P100	01.06.09		181	282	4	591	26	4	404	272	4
P100	02.06.09		241	298	4	596	27	5	510	129	5
P100	03.06.09		-4	132	4	602	30	5	394	328	5
P100	04.06.09				0	597	32	0			0
P100	05.06.09		-41	200	4	594	30	5	386	327	5
P100	06.06.09		-34	191	4	583	29	5	375	322	5
P100	07.06.09				0			0			0
P100	08.06.09		47	355	4	575	31	5	338	312	5
P100	09.06.09		83	352	4	577	31	5	282	316	5
P100	10.06.09		-39	268	4	586	30	5	252	300	5
P100	11.06.09		-56	243	4	576	31	5	240	297	5
P100	12.06.09	-1	-96	186	4	570	31	5	228	292	5
P100	13.06.09	0			0			0			0
	<i>flooding</i>										
P100	14.06.09	1	-143	138	4	547	36	5	192	279	5

daf = days after flooding, m = mean, sd = standard deviation, n = number of samples

Table E-1 (continued)

Site	Date	daf	m.Eh 10	sd.Eh 10	n.Eh 10	m.Eh 35	sd.Eh 35	n.Eh 35	m.Eh 55	sd.Eh 55	n.Eh 55
			--- mV ---			--- mV ---			--- mV ---		
P100	15.06.09	2	-144	101	4	520	40	5	48	252	5
P100	16.06.09	3	-161	83	4	467	64	5	18	252	5
P100	17.06.09	4	-165	72	4	314	186	5	1	231	5
P100	18.06.09	5	-165	59	4	191	240	5	-26	163	5
P100	19.06.09	6	-167	57	4	97	221	5	-65	90	5
P100	20.06.09	7	-166	76	4	38	194	5	2	60	5
P100	21.06.09	8	-167	76	4	-1	178	5	-123	61	5
P100	22.06.09	9	-168	67	4	-32	135	5	-126	60	5
P100	23.06.09	10	-171	60	4			5	-130	80	5
P100	24.06.09	11	-176	51	4	-93	82	5	-157	44	5
P100	25.06.09	12	-177	48	4	-119	54	5	-168	35	5
P100	26.06.09	13	-179	46	4	-146	35	5	-176	29	5
P100	27.06.09	14	-182	44	4	-169	31	5	-185	22	5
P100	28.06.09	15	-185	40	4	-181	27	5	-191	15	5
P100	03.07.09	20			0	-191	17	5	-207	23	5
P100	09.07.09	26			0	-192	17	5	-209	24	5
P100	10.07.09	27			0	-187	17	5	-207	23	5
P100	16.07.09	33			0	-203	18	5	-216	30	5
P100	17.07.09	34			0	-200	19	5	-213	30	5
P100	23.07.09	40			0	-199	16	5	-196	63	5
P100	24.07.09	41			0	-187	11	5	-194	54	5
P100	11.08.09	59			0	-180	17	5	-193	36	5
P100	12.08.09	60			0	-179	12	5	-183	41	5
P100	26.08.09	74			0	-183	23	5	-147	124	5
P100	27.08.09	75			0	-183	22	5	-145	128	5
P100	10.09.09	89			0	-182	28	5	-140	142	5
P100	11.09.09	90			0	-190	27	5	-141	141	5
P100	28.09.09	107			0	-163	40	5	-160	77	5
P100	29.09.09	108			0	-154	42	5	-142	67	5
P100	11.10.09 <i>drainage</i>	120			0			0			0

Appendix E

Table E-1 (continued)

Site	Date	daf	m.Eh 10 --- mV ---	sd.Eh 10	n.Eh 10	m.Eh 35 --- mV ---	sd.Eh 35	n.Eh 35	m.Eh 55 --- mV ---	sd.Eh 55	n.Eh 55
P100	12.10.09	121			0	-151	13	5	-177	47	5
P100	13.10.09	122			0	-167	25	5	-177	43	5
P100	24.10.09 <i>harvest</i>	133			0			0			0
P100	29.10.09				0	458	177	5	326	244	5
P100	30.10.09				0	517	120	5	336	246	5
P100	31.10.09		541	23	4	508	105	5	356	245	5
P100	01.11.09		311	98	4	532	87	5	366	246	5
P100	02.11.09		350	140	4	553	78	5	389	247	5
P100	03.11.09		526	88	4	553	78	5	374	242	5
P100	05.11.09		564	78	4	586	64	5	394	241	5
P100	06.11.09		544	66	4	583	59	5	398	245	5
P100	07.11.09		572	90	4	593	57	5	416	248	5
P100	10.11.09		393	99	4	580	61	5	419	250	5
P100	11.11.09		324	101	4	576	58	5	414	252	5
P100	12.11.09		272	83	4	575	60	5	411	254	5
P100	13.11.09		244	77	4	558	71	5	418	259	5
P100	14.11.09		222	79	4	500	108	5	373	247	5
P100	15.11.09		202	95	4	425	167	5	364	254	5
P100	16.11.09		187	106	4	378	151	5	366	265	5
P100	17.11.09		174	114	4	304	196	5	356	270	5
P100	18.11.09		159	118	4	219	218	5	334	278	5
P100	26.11.09				0	46	283	5	258	272	5
P100	28.12.09				0	-120	132	5	11	344	5
P100	29.12.09				0	-125	134	5	4	341	5
P100	28.01.10				0	297	354	5	137	356	5
P100	29.01.10				0	293	362	5	141	357	5
P100	24.02.10				0	-81	228	5	23	234	5
P100	25.02.10				0	-83	215	5	16	228	5

Appendix E

**Table E-2:** Soil redox potential (Eh) determined at 10 cm (10), 35 cm (35) and 55 cm (55) below surface at the 700 year paddy site (P700).

Site	Date	daf	m.Eh 10	sd.Eh 10	n.Eh 10	m.Eh 35	sd.Eh 35	n.Eh 35	m.Eh 55	sd.Eh 55	n.Eh 55
			--- mV ---			--- mV ---			--- mV ---		
P700	24.03.09				0	-176	19	5	-49	157	5
P700	25.03.09				0	-179	19	5	-58	153	5
P700	22.04.09				0	-198	33	5	-205	16	5
P700	23.04.09				0	-197	33	5	-204	17	5
P700	27.05.09				0	513	211	5	559	72	5
P700	28.05.09				0	513	209	5	569	116	5
P700	29.05.09				0	518	201	5	544	108	5
P700	30.05.09				0	535	176	5	546	116	5
P700	31.05.09				0	528	164	5	542	115	5
P700	01.06.09				0	536	165	5	553	119	5
P700	02.06.09				0	555	178	5	522	184	5
P700	03.06.09				0	571	140	5	563	88	5
P700	04.06.09				0			0			0
P700	05.06.09				0	572	99	5	543	94	5
P700	06.06.09		13	95	4	577	88	5	545	100	5
P700	07.06.09				0			0			0
P700	08.06.09 <i>flooding</i>	0	-56	142	3	532	164	5	574	40	5
P700	09.06.09	1	-76	144	3	461	171	5	577	57	5
P700	10.06.09	2	-87	118	4	410	172	5	574	60	5
P700	11.06.09	3	-117	112	4	366	157	5	559	67	5
P700	12.06.09	4	-132	102	4	333	158	5	554	81	5
P700	13.06.09	5	-148	94	4	318	154	5	497	126	5
P700	14.06.09	6	-161	82	4	293	159	5	320	303	5
P700	15.06.09	7	-161	74	4	266	171	5	222	376	5
P700	16.06.09	8	-151	47	4	233	186	5	197	380	5
P700	17.06.09	9	-177	64	4	149	233	5	183	377	5
P700	18.06.09	10	-182	71	4	84	227	5	166	370	5
P700	19.06.09	11	-186	60	4	67	235	5	142	354	5
P700	20.06.09	12	-185	57	4	61	243	5	97	310	5

daf = days after flooding, m = mean, sd = standard deviation, n = number of samples

Appendix E

Table E-2 (continued)

Site	Date	daf	m.Eh 10	sd.Eh 10	n.Eh 10	m.Eh 35	sd.Eh 35	n.Eh 35	m.Eh 55	sd.Eh 55	n.Eh 55
			--- mV ---			--- mV ---			--- mV ---		
P700	21.06.09	13	-191	50	4	39	231	5	-87	182	5
P700	22.06.09	14			0	-9	209	5	-118	149	5
P700	23.06.09	15	-196	33	4	-29	206	5	-128	138	5
P700	24.06.09	16	-199	16	4	-67	198	5	-130	132	5
P700	25.06.09	17	-199	16	4	-67	198	5	-130	132	5
P700	26.06.09	18	-207	16	4	-81	217	5	-143	127	5
P700	27.06.09	19	-201	33	4	-93	203	5	-162	117	5
P700	28.06.09	20	-194	32	4	-92	197	5	-161	110	5
P700	03.07.09	25			0	-189	29	5	-203	69	5
P700	09.07.09	31			0	-197	28	5	-219	52	5
P700	10.07.09	32			0	-189	29	5	-209	50	5
P700	16.07.09	38			0	-202	31	5	-223	47	5
P700	17.07.09	39			0	-179	45	5	-216	45	5
P700	23.07.09	45			0	-198	32	5	-216	47	5
P700	24.07.09	46			0	-198	32	5	-215	47	5
P700	11.08.09	64			0	-210	29	5	-222	53	5
P700	12.08.09	65			0	-211	29	5	-221	54	5
P700	26.08.09	79			0	-183	23	5	-147	124	5
P700	27.08.09	80			0	-183	22	5	-145	128	5
P700	10.09.09	94			0	-204	30	5	-214	57	5
P700	11.09.09	95			0	-210	31	5	-220	57	5
P700	28.09.09	112			0	-197	44	5	-198	77	5
P700	29.09.09	113			0	-196	45	5	-216	58	5
P700	11.10.09	125			0			0			0
P700	12.10.09	126			0	-213	27	5	-218	56	5
P700	13.10.09	127			0	-205	27	5	-215	54	5
P700	17.10.09	131			0			0			0
P700	24.10.09	138			0			0			0
P700	27.10.09	141			0			0			0
P700	<i>drainage</i>				0			0			0
P700	29.10.09	143			0	-210	14	5	-231	35	5

Appendix E

Table E-2 (continued)

Site	Date	daf	m.Eh 10 --- mV ---	sd.Eh 10	n.Eh 10	m.Eh 35 --- mV ---	sd.Eh 35	n.Eh 35	m.Eh 55 --- mV ---	sd.Eh 55	n.Eh 55
P700	30.10.09	144			0	-212	16	5	-236	44	5
P700	31.10.09	145	58	42	4	-210	16	5	-241	44	5
P700	01.11.09	146	-135	45	4	-145	45	5	-235	43	5
P700	02.11.09	147	-172	38	4	-202	20	5	-242	42	5
P700	03.11.09	148	-167	32	4	-203	18	5	-238	47	5
P700	05.11.09	150	-155	84	4	-203	17	5	-242	44	5
P700	06.11.09 <i>harvest</i>	151			0			0			0
P700	07.11.09		-6	326	4	-200	15	5	-238	43	5
P700	10.11.09				0			0			0
P700	11.11.09		-102	271	4	-191	20	5	-232	34	5
P700	12.11.09		-92	214	4	-197	14	5	-233	30	5
P700	13.11.09		-134	214	4	-205	13	5	-249	23	5
P700	14.11.09		-235	33	3	-203	16	5	-237	37	5
P700	15.11.09		-226	34	4	-210	22	5	-237	38	5
P700	16.11.09		-157	113	3	-214	27	5	-243	36	5
P700	17.11.09				0			0			0
P700	18.11.09		150	365	4	-194	16	5	-238	43	5
P700	26.11.09				0	-185	19	5	-232	44	5
P700	28.12.09				0	-167	22	5	-237	42	5
P700	29.12.09				0	-176	22	5	-245	50	5
P700	28.01.10				0	-173	17	5	-232	53	5
P700	29.01.10				0	-176	16	5	-237	52	5
P700	24.02.10				0	-163	14	5	-224	57	5
P701	25.02.10				0	-179	16	5	-235	55	5

Appendix E

**Table E-3:** Soil redox potential (Eh) determined at 10 cm (10), 35 cm (35) and 55 cm (55) below surface at the 2000 year paddy site (P2000).

Site	Date	daf	10			35			55			75		
			m.Eh	sd.Eh	n.Eh									
			--- mV ---			--- mV ---			--- mV ---			--- mV ---		
P2000	24.03.09				0	-54	184	5	58	140	5	177	257	5.00
P2000	25.03.09				0	-55	184	5	53	134	5	174	255	5
P2000	22.04.09				0	-119	93	5	-80	57	5	-50	95	5
P2000	23.04.09				0	-126	92	5	-82	54	5	-51	95	5
P2000	27.05.09				0	579	120	5	653	13	5	668	41	5
P2000	28.05.09	0			0	568	135	5	646	15	5	664	50	5
	<i>flooding</i>													
P2000	29.05.09	1			0	550	132	5	642	23	5	659	53	5
P2000	30.05.09	2			0	545	141	5	642	22	5	664	48	5
P2000	31.05.09	3			0	483	183	5	636	22	5	654	38	5
P2000	01.06.09	4			0	404	182	5	636	26	5	663	30	5
P2000	02.06.09	5	-3	121	4	203	185	5	598	80	5	647	23	5
P2000	03.06.09	6	-31	104	4	66	235	5	614	31	5	632	41	5
P2000	04.06.09	7	-46	103	4	9	137	5	621	33	5	655	31	5
P2000	05.06.09	8	-69	88	4	-21	108	5	611	25	5	652	21	5
P2000	06.06.09	9	-63	91	4	-57	81	5	616	25	5	659	20	5
P2000	07.06.09	10			0			0			0			0
P2000	08.06.09	11	-79	91	4	-107	38	5	610	24	5	652	19	5
P2000	09.06.09	12	-112	78	4	-134	36	5	594	27	5	616	49	5
P2000	10.06.09	13	-108	76	4	-134	36	5	593	33	5	639	24	5
P2000	11.06.09	14			0			0			0			0
P2000	12.06.09	15	-127	64	4	-146	26	5	590	32	5	638	33	5
P2000	13.06.09	16	-121	62	4	-134	16	5	593	37	5	644	34	5
P2000	14.06.09	17			1			0			0			0
P2000	15.06.09	18	-142	55	4	-151	13	5	575	45	5	630	35	5
P2000	16.06.09	19	-153	54	4	-154	11	5	568	51	5	626	37	5
P2000	17.06.09	20			0			0			0			0
P2000	18.06.09	21			0			0			0			0
P2000	19.06.09	22	-165	39	4	-162	15	5	543	58	5	593	41	5
P2000	20.06.09	23	-174	37	4	-170	17	5	517	73	5	587	40	5

daf = days after flooding, m = mean, sd = standard deviation, n = number of samples

Appendix E

Table E-3 (continued)

Site	Date	daf	m.Eh 10 --- mV ---	sd.Eh 10	n.Eh 10	m.Eh 35 --- mV ---	sd.Eh 35	n.Eh 35	m.Eh 55 --- mV ---	sd.Eh 55	n.Eh 55	m.Eh 75 --- mV ---	sd.Eh 75	n.Eh 75
P2000	21.06.09	24			0			0			0			0
P2000	22.06.09	25			0			0			0			0
P2000	23.06.09	26	-174	35	4	-169	20	5	233	322	5	427	345	5
P2000	24.06.09	27	-173	31	4	-171	20	5	176	365	5	566	90	5
P2000	25.06.09	28			0			0			0			0
P2000	26.06.09	29			0			0			0			0
P2000	27.06.09	30	-181	39	4	-174	17	5	137	374	5	499	182	5
P2000	28.06.09	31			0	-172	18	5	122	375	5	470	235	5
P2000	03.07.09	36			0	-172	51	5	-81	181	5	320	306	5
P2000	09.07.09	42			0	-195	41	5	-157	36	5	-22	166	5
P2000	10.07.09	43			0	-182	34	5	-144	34	5	-23	155	5
P2000	16.07.09	49			0	-192	35	5	-163	22	5	-124	33	5
P2000	17.07.09	50			0	-190	35	5	-174	29	5	-123	33	5
P2000	23.07.09	56			0	-186	63	5	-191	12	5	-140	35	5
P2000	24.07.09	57			0	-188	65	5	-193	15	5	-138	34	5
P2000	11.08.09	75			0	-172	50	5	-189	4	5	-111	80	5
P2000	12.08.09	76			0	-175	52	5	-193	8	5	-109	80	5
P2000	26.08.09	90			0	-198	41	5	-189	34	5	-171	48	5
P2000	27.08.09	91			0	-191	44	5	-185	34	5	-140	44	5
P2000	10.09.09	105			0	-201	66	5	-151	16	5	-137	64	5
P2000	11.09.09	106			0	-193	64	5	-163	20	5	-135	72	5
P2000	28.09.09	123			0	-211	50	5	-147	44	5	-140	75	5
P2000	29.09.09	124			0	-185	54	5	-139	40	5	-127	83	5
P2000	11.10.09	136			0			0			0			0
P2000	12.10.09	137			0	-224	34	5	-142	73	5	-123	83	5
P2000	13.10.09	138			0	-216	30	5	-125	74	5	-123	65	5
P2000	17.10.09 <i>drainage</i>	142			0			0			0			0
P2000	24.10.09	149			0			0			0			0
P2000	27.10.09	152			0			0			0			0
P2000	29.10.09	154			0	-91	158	5	8	176	5	-111	34	5

Appendix E

Table E-3 (continued)

Site	Date	daf	m.Eh 10	sd.Eh 10	n.Eh 10	m.Eh 35	sd.Eh 35	n.Eh 35	m.Eh 55	sd.Eh 55	n.Eh 55	m.Eh 75	sd.Eh 75	n.Eh 75
			--- mV ---			--- mV ---			--- mV ---			--- mV ---		
P2000	30.10.09	155			0	-47	193	5	33	203	5	-106	48	5
P2000	31.10.09	156	201	123	4	1	245	5	229	321	5	-155	42	5
P2000	01.11.09	157	32	184	4	48	260	5	284	339	5	-121	66	5
P2000	02.11.09	158	22	211	4	53	289	5	309	350	5	-99	76	5
P2000	03.11.09	159	0	250	4	79	288	5	323	340	5	-89	82	5
P2000	05.11.09 <i>harvest</i>	161	-28	247	4	159	292	5	504	131	5	246	251	5
P2000	06.11.09	2	-26	243	4	168	292	5	485	141	5	402	245	5
P2000	07.11.09	3	-42	241	4	192	300	5	584	39	5	521	166	5
P2000	10.11.09	6	16	292	4	217	304	5	598	27	5	597	66	5
P2000	11.11.09	7	-68	192	4	214	294	5	620	14	5	605	49	5
P2000	12.11.09	8	-155	86	4	180	267	5	577	40	5	619	38	5
P2000	13.11.09	9	-167	63	4	108	214	5	602	18	5	611	63	5
P2000	14.11.09	10	-184	49	4	33	156	5	583	23	5	589	58	5
P2000	15.11.09	11	-176	42	4	10	133	5	592	32	5	603	68	5
P2000	16.11.09	12	-183	39	4	-5	118	5	-158	28	5	576	78	5
P2000	17.11.09	13	-187	38	4	-29	113	5	576	37	5	580	79	5
P2000	18.11.09	14	-183	34	4	-91	70	5	553	74	5	582	53	5
P2000	26.11.09				0	-158	62	5	479	127	5	553	126	5
P2000	28.12.09				0	-200	45	5	-95	39	5	35	164	5
P2000	29.12.09				0	-197	51	5	-114	49	5	46	150	5
P2000	28.01.10				0	201	345	5	490	258	5	166	101	5
P2000	29.01.10				0	199	353	5	471	294	5	159	101	5
P2000	24.02.10				0	87	295	5	22	69	5	35	120	5
P2000	25.02.10				0	119	344	5	-29	92	5	19.8	122	5

Appendix E

**Table E-4:** Soil redox potential (Eh) determined at 10 cm (10), 35 cm (35) and 55 cm (55) below surface at the 100 year non-paddy site (NP100).

Site	Date	m.Eh 10	sd.Eh 10	n.Eh 10	m.Eh 35	sd.Eh 35	n.Eh 35	m.Eh 55	sd.Eh 55	n.Eh 55
		--- mV ---			--- mV ---			--- mV ---		
NP100	24.03.09			0.00	586	33	5	575	68	5
NP100	25.03.09			0	588	33	5	580	64	5
NP100	22.04.09			0	578	40	5	586	71	5
NP100	23.04.09			0	582	33	5	586	68	5
NP100	27.05.09			0	590	33	5	593	65	5
NP100	28.05.09			0	589	33	5	587	76	5
NP100	29.05.09			0	593	33	5	586	81	5
NP100	30.05.09			0	589	33	5	611	61	5
NP100	31.05.09			0	591	34	5	589	63	5
NP100	01.06.09			0			0			0
NP100	02.06.09			0			0			0
NP100	03.06.09			0	589	32	5	588	67	5
NP100	04.06.09			0			0			0
NP100	05.06.09			0	586	34	5	585	69	5
NP100	06.06.09	517	55	4	589	34	5	588	66	5
NP100	07.06.09			0			0			0
NP100	08.06.09	511	88	4	589	32	5	582	67	4
NP100	09.06.09	523		3	575	30	5	573	61	5
NP100	10.06.09	457	147	4	569	40	5	575	61	5
NP100	11.06.09	382	160	4	565	44	5	569	67	5
NP100	12.06.09	458	153	4	572	41	5	571	73	5
NP100	13.06.09			0			0			0
NP100	14.06.09	482	137	4	572	38	5	565	71	5
NP100	15.06.09	537	33	4	575	42	5	564	80	5
NP100	16.06.09	525	17	4	555	47	5	555	76	5
NP100	17.06.09			0			0			0
NP100	18.06.09			0			0			0
NP100	19.06.09	525	9	4	556	49	5	551	69	5
NP100	20.06.09	512	3	4	557	43	5	537	76	5

m = mean, sd = standard deviation, n = number of samples

Appendix E

**Table E-4 (continued)**

Site	Date	m.Eh 10	sd.Eh 10	n.Eh 10	m.Eh 35	sd.Eh 35	n.Eh 35	m.Eh 55	sd.Eh 55	n.Eh 55
		--- mV ---			--- mV ---			--- mV ---		
NP100	21.06.09			0			0			0
NP100	22.06.09			0			0			0
NP100	23.06.09	517	18	4	556	41	5	546	67	5
NP100	24.06.09	514	22	4	553	45	5	549	62	5
NP100	25.06.09			0			0			0
NP100	26.06.09			0			0			0
NP100	27.06.09	468	42	4	557	38	5	553	56	5
NP100	28.06.09	481	55	4	557	40	5	553	59	5
NP100	03.07.09			0	549	48	5	544	60	5
NP100	09.07.09			0	554	44	5	535	66	5
NP100	10.07.09			0	560	39	5	533	66	5
NP100	16.07.09			0	558	31	5	546	63	5
NP100	17.07.09			0	561	32	5	545	61	5
NP100	23.07.09			0	557	27	5	544	58	5
NP100	24.07.09			0	546	31	5	535	56	5
NP100	11.08.09			0	451	34	4	483	61	5
NP100	12.08.09			0	428	22	4	473	59	5
NP100	26.08.09			0	612	22	5	580	53	5
NP100	27.08.09			0	611	21	5	582	53	5
NP100	10.09.09			0	608	31	5	580	59	5
NP100	11.09.09			0	604	31	5	578	60	5
NP100	28.09.09			0	601	32	5	573	71	5
NP100	29.09.09			0	596	35	5	574	71	5
NP100	11.10.09			0			0			0
NP100	12.10.09			0	607	32	5	590	73	5
NP100	13.10.09			0	606	33	5	592	71	5
NP100	17.10.09			0			0			0
NP100	24.10.09			0			0			0
NP100	27.10.09			0			0			0
NP100	29.10.09			0	598	57	5	599	68	5
NP100	30.10.09			0	602	56	5	604	66	5

Table E-4 (continued)

Site	Date	m.Eh 10	sd.Eh 10	n.Eh 10	m.Eh 35	sd.Eh 35	n.Eh 35	m.Eh 55	sd.Eh 55	n.Eh 55
		--- mV ---			--- mV ---			--- mV ---		
NP100	31.10.09			0	595	55	5	598	64	5
NP100	01.11.09			0	615	34	5	614	67	5
NP100	02.11.09			0	601	54	5	604	65	5
NP100	03.11.09			0	603	57	5	606	67	5
NP100	05.11.09			0	600	60	5	606	67	5
NP100	06.11.09			0			0			0
NP100	07.11.09			0	594	58	5	601	68	5
NP100	10.11.09			0	402	137	5	633	28	5
NP100	11.11.09	333	126	4	522	154	5	602	67	5
NP100	12.11.09	317	123	4	596	57	5	603	66	5
NP100	13.11.09	361	117	4	596	58	5	594	80	5
NP100	14.11.09	390	126	4	597	63	5	603	66	5
NP100	15.11.09	388	100	4	586	61	5	603	66	5
NP100	16.11.09	382	92	4	581	60	5	604	68	5
NP100	17.11.09			0			0			0
NP100	18.11.09	386	112	4	587	66	5	593	71	5
NP100	26.11.09			0	574	66	5	592	67	5
NP100	28.12.09			0	584	60	5	581	67	5
NP100	29.12.09			0	588	59	5	586	65	5
NP100	28.01.10			0	593	50	5	592	60	5
NP100	29.01.10			0	596	51	5	593	60	5
NP100	24.02.10			0	592	36	5	584	92	5
NP100	25.02.10			0	592	37	5	585	91	5

Appendix E

**Table E-5:** Soil redox potential determined at 10 cm (10), 35 cm (35) and 55 cm (55) below surface at the 700 year non-paddy site (NP700).

Site	Date	m.Eh 10	sd.Eh 10	n.Eh 10	m.Eh 35	sd.Eh 35	n.Eh 35	m.Eh 55	sd.Eh 55	n.Eh 55
		--- mV ---			--- mV ---			--- mV ---		
NP700	24.03.09			0	615	32	5	557	98	5
NP700	25.03.09			0	616	33	5	557	102	5
NP700	22.04.09			0	622	28	5	561	94	5
NP700	23.04.09			0	618	28	5	553	87	5
NP700	27.05.09			0	613	32	5	560	92	5
NP700	28.05.09			0	620	33	5	546	81	5
NP700	29.05.09			0	618	31	5	550	87	5
NP700	30.05.09			0	612	29	5	550	83	5
NP700	31.05.09			0	617	30	5	543	77	5
NP700	01.06.09			0	536	165	5	553	119	5
NP700	02.06.09			0	555	178	5	522	184	5
NP700	03.06.09			0	571	140	5	563	88	5
NP700	04.06.09			0			0			0
NP700	05.06.09			0	597	32	5	530	139	4
NP700	06.06.09	409	238	4	595	54	5	587	85	5
NP700	07.06.09			0			0			0
NP700	08.06.09	489	126	4	608	30	5	567	60	5
NP700	09.06.09	546	30	4	595	30	5	556	60	5
NP700	10.06.09	527	45	4	595	31	5	556	57	5
NP700	11.06.09	546	40	4	595	31	5	556	54	5
NP700	12.06.09	574	47	4	605	30	5	568	52	5
NP700	13.06.09	567	48	4	601	30	5	581	81	5
NP700	14.06.09	577	58	4	599	30	5	561	51	5
NP700	15.06.09	580	62	4	603	30	5	569	48	5
NP700	16.06.09	571	63	4	594	30	5	557	51	5
NP700	17.06.09			0			0			0
NP700	18.06.09			0			0			0
NP700	19.06.09	588	63	4	611	30	5	582	43	5
NP700	20.06.09	574	65	4	588	31	5	540	43	5
NP700	21.06.09			0			0			0

m = mean, sd = standard deviation, n = number of samples

Appendix E

Table E-5 (continued)

Site	Date	m.Eh 10	sd.Eh 10	n.Eh 10	m.Eh 35	sd.Eh 35	n.Eh 35	m.Eh 55	sd.Eh 55	n.Eh 55
		--- mV ---			--- mV ---			--- mV ---		
NP700	22.06.09			0			0			0
NP700	23.06.09	579	68	4	595	32	5	564	41	5
NP700	24.06.09	619	59	4	638	34	5	602	39	5
NP700	25.06.09			0			0			0
NP700	26.06.09			0			0			0
NP700	27.06.09	587	59	4	593	34	5	537	40	5
NP700	28.06.09	589	59	4	594	33	5	561	38	5
NP700	03.07.09			0	590	32	5	560	37	5
NP700	09.07.09			0	588	33	5	563	31	5
NP700	10.07.09			0	590	31	5	569	32	5
NP700	16.07.09			0	591	34	5	572	25	5
NP700	17.07.09			0	589	32	5	571	26	5
NP700	23.07.09			0	597	40	5	576	39	5
NP700	24.07.09			0	618	34	5	571	36	5
NP700	11.08.09			0	569	28	5	555	26	5
NP700	12.08.09			0	569	32	5	552	27	5
NP700	26.08.09			0	595	38	5	504	165	5
NP700	27.08.09			0	578	40	5	568	30	5
NP700	10.09.09			0	565	27	5	554	20	5
NP700	11.09.09			0	555	27	5	539	27	5
NP700	28.09.09			0	555	26	5	543	15	5
NP700	29.09.09			0	539	30	5	527	25	5
NP700	11.10.09			0			0			0
NP700	12.10.09			0	530	26	5	521	51	5
NP700	13.10.09			0	528	34	5	515	47	5
NP700	17.10.09			0			0			0
NP700	24.10.09			0			0			0
NP700	27.10.09			0			0			0
NP700	29.10.09			0	612	24	5	614	74	5
NP700	30.10.09			0	617	23	5	626	85	5
NP700	31.10.09			0	620	25	5	639	78	5

Appendix E

Table E-5 (continued)

Site	Date	m.Eh 10	sd.Eh 10	n.Eh 10	m.Eh 35	sd.Eh 35	n.Eh 35	m.Eh 55	sd.Eh 55	n.Eh 55
		--- mV ---			--- mV ---			--- mV ---		
NP700	01.11.09			0	618	26	5	587	18	5
NP700	02.11.09			0	606	23	5	572	18	5
NP700	03.11.09			0	619	15	5	595	20	5
NP700	05.11.09			0	601	21	5	569	22	5
NP700	06.11.09			0			0			0
NP700	07.11.09			0	636	42	5	597	24	5
NP700	10.11.09			0			0			0
NP700	11.11.09	469	94	4	600	27	5	571	26	5
NP700	12.11.09	441	125	4	582	25	5	555	26	5
NP700	13.11.09	430	120	4	590	24	5	553	32	5
NP700	14.11.09	479	121	4	575	17	5	552	22	5
NP700	15.11.09	405	204	4	575	23	5	559	32	5
NP700	16.11.09	503	139	4	568	15	5	536	29	5
NP700	17.11.09			0			0			0
NP700	18.11.09	539	84	4	566	18	5	558	15	5
NP700	26.11.09			0	610	65	5	654	109	5
NP700	28.12.09			0	604	50	5	553	38	5
NP700	29.12.09			0	620	32	5	576	73	5
NP700	28.01.10			0	595	15	5	552	10	5
NP700	29.01.10			0	604	22	5	571	33	5
NP700	24.02.10			0	592	36	5	584	92	5
NP700	25.02.10			0	592	37	5	585	91	5

**Table E–6:** pH values and alkalinity (alk) determined in the soil solution of the 100 year paddy soil (P100).

Site	Depth cm	daf	m.pH ---/---	sd.pH	n.pH	m.alk --- mmol l <sup>-1</sup> ---	sd.alk	n.alk
P100	35	2	8.2	0.3	4	2.89	1.25	4
		3	8.3	0.3	4	2.45	1.60	4
		4	7.9	0.5	4	2.60	1.58	4
		5	7.6	0.9	4	2.99	1.57	4
		6	8.3	0.3	4	2.56	0.91	4
		7	8.1	0.1	4	2.80	1.76	4
		8	7.7	1.0	4	3.49	0.81	4
		9	8.2	0.5	4	3.23	1.01	4
		10	8.2	0.4	4	3.31	0.88	2
		11	8.3	0.2	4	3.43	1.41	4
		12	8.0	0.7	4	4.29	0.50	3
		13	8.4	0.3	4	3.70	0.70	3
		14	8.3	0.7	3	4.18	0.80	4
		15	8.1	0.1	3	4.48	0.59	3
		21	8.2	0.5	2	4.11		1
		27	9.1	0.4	3	2.66	1.72	3
34	9.3	0.5	3	4.81	0.01	3		
41	8.4	0.6	3	5.99	0.42	3		
60	9.3	0.5	3	6.55	0.67	3		
P100	55	2	8.0	0.5	4	4.94	1.14	4
		3	8.4	0.2	4	4.07	1.64	4
		4	8.2	0.4	4	5.46	0.89	4
		5	8.1	0.2	4	4.14	0.31	4
		6	8.5	0.4	4	3.93	1.85	4
		7	8.8	0.2	4	3.59	0.48	4
		8	8.3	0.2	4	4.45	0.20	4
		9	8.5	0.4	4	4.65	1.11	3
		10	8.6	0.2	4	3.39		1
		11	8.6	0.0	4	4.30	0.78	4
		12	7.9	0.7	4	5.41	0.56	3
		13	8.3	0.2	4	3.86	0.16	3
		14	8.5	0.4	4	4.48	0.31	4
		15	8.1	0.3	4	4.13	1.22	4
		21	8.7	0.1	2	3.91	1.10	2
		27	9.4	0.2	3	3.07	0.65	3
34	9.2	0.5	2	4.30	0.13	2		
41	8.3	0.4	3	4.89	0.42	3		
60	9.0	0.1	3	3.77	2.75	3		

daf = days after flooding, m = mean, sd = standard deviation, n = number of samples

**Table E-7:** pH values and alkalinity (alk) determined in the soil solution of the 700 year paddy soil (P700).

site	depth cm	daf	m.pH --	sd.pH	n.pH	m.alk --- mmol l <sup>-1</sup> ---	sd.alk	n.alk
P700	35	0	9.1	0.1	2	0.66	0.55	2
		1	8.4	0.6	4	0.41	0.36	3
		2	8.7	0.2	3	1.57	0.71	3
		3	8.9	0.2	4	1.48	0.51	3
		4	8.9	0.2	3	1.60	0.32	3
		5	8.2	0.7	4	2.59	0.41	4
		6	8.7	0.2	4	1.84	0.55	4
		7	8.2	0.3	4	1.59	0.36	4
		8	7.8	0.4	3	2.02	0.72	3
		9	8.4	0.8	3	2.11	1.05	3
		10	8.9	0.4	4	1.30		1
		11	8.1	0.6	4	2.86	0.85	4
		12	7.8	0.2	3	2.83	0.39	3
		13	8.9	0.3	4	1.86	0.23	3
		14	8.6	0.8	4	2.29	0.53	3
		15	7.9	0.5	4	3.77	0.87	4
		20	8.5	0.7	3	3.65	0.72	2
26	8.3		1	4.07	0.51	2		
32	9.4	0.4	3	1.94	1.75	3		
39	9.4	0.0	3	4.82	0.47	3		
65	9.3	0.4	3	6.94	1.68	3		
P700	55	0	8.9		1	0.00		1
		1	8.3	0.8	4	0.55	0.34	2
		2	8.6	0.4	4	1.71	0.93	4
		3	8.6	0.5	4	1.20	0.72	4
		4	8.8	0.1	4	1.25	0.51	4
		5	8.5	0.5	4	2.12	0.44	4
		6	8.5	0.5	4	1.80	0.52	3
		7	8.4	0.8	4	1.50	0.36	4
		8	7.9	0.6	4	1.71	0.58	4
		9	8.5	0.6	3	2.94	0.99	3
		10	8.3	0.6	4	1.34	0.79	4
		11	7.8	0.7	4	2.76	0.72	4
		12	7.8	0.2	4	2.59	0.93	3
		13	8.7	0.5	4	1.38	0.78	4
		14	8.3	0.5	4	2.24	0.61	4
		15	8.0	0.1	4	3.55	0.77	4
		20	8.0	0.7	4	2.87	0.19	4
26	8.5	0.2	2	3.04	0.59	2		
32	9.1	0.1	3	2.83	0.59	3		
39	9.5	0.1	3	2.78	1.44	3		
65	9.4	0.2	3	6.75	1.02	3		

daf = days after flooding, m = mean, sd = standard deviation, n = number of samples

**Table E-8:** pH values and alkalinity determined in the soil solution of the 2000 year paddy soil (P2000).

Site	Depth	daf	m.pH ---/---	sd.pH	n.pH	m.alk --- mmol l <sup>-1</sup> ---	sd.alk	n.Alk
P2000	35	0			0			0
		1	6.9	0.1	3	0.28	0.39	3
		2	7.2	0.3	4	0.06	0.08	4
		3	7.2	0.4	4	0.96	0.31	4
		4	7.0	0.2	4	0.28	0.23	4
		7	6.9	0.4	2	1.31	0.11	2
		8	7.3	0.5	3	0.82	0.25	3
		9	7.3	0.2	2	1.31	0.40	3
		11	8.4	0.1	3	1.12	0.21	3
		12	7.7	0.6	4	1.47	0.14	4
		13	7.9	0.4	4	1.75	0.16	4
		16	7.2	1.0	3	1.59	1.62	3
		19	7.7	0.1	4	2.09	0.46	4
		27	7.5	0.2	4	1.98	0.25	4
		31	7.8	0.9	4	1.80	0.55	4
		37	8.1	0.7	2	2.39	0.13	2
43	8.2	1.1	3	2.49	0.44	3		
57	8.0	0.8	3	3.43	0.41	2		
P2000	55	0			0			0
		1	6.9	0.2	3	0.22	0.33	3
		2	7.1	0.3	4	0.29	0.36	4
		3	7.0	0.2	4	0.69	0.56	4
		4	7.0	0.2	4	0.14	0.12	4
		7	7.4	0.3	3	0.30	0.06	2
		8	7.2	0.2	4	0.82	0.11	4
		9	7.5	0.4	4	1.30	0.58	4
		11	8.4	0.7	4	1.45	0.27	3
		12	8.1	0.6	4	1.70	0.30	4
		13	7.1	0.6	4	1.72	0.23	4
		16	7.7	0.3	4	4.53	0.93	4
		19	8.1	0.7	4	1.84	0.32	4
		27	8.1	0.6	4	1.69	0.40	4
		31	7.4	0.9	3	1.90	0.51	3
		37	8.3	0.2	2	2.43	0.18	2
43	8.9	0.5	3	2.24	0.31	3		
57	8.0	0.6	3	3.30	0.17	3		

daf = days after flooding, m = mean, sd = standard deviation, n = number of samples

**Table E-9:** Electric conductivity (EC), sodium adsorption ratio (SAR) and chloride (Cl<sup>-</sup>) contents determined in the soil solution of the 100 year paddy soil (P100).

Site	Depth cm	daf	m.EC	sd.EC	n.EC	m.SAR	sd.SAR	n.SAR	m.Cl <sup>-</sup>	n.Cl <sup>-</sup>	sd.Cl <sup>-</sup>
			--- $\mu\text{S cm}^{-1}$ ---			---/---			--- $\text{mmol l}^{-1}$ ---		
P100	35	2	805	113	4	2.39	0.54	4	2.95	4	0.59
		3	850	230	4	2.17	0.59	4	3.43	4	1.37
		4	1018	252	4	2.65	0.87	4	4.15	4	1.63
		5	672	191	4	1.78	0.58	4	2.49	4	1.35
		6	797	130	4	2.33	0.57	4	3.21	4	0.94
		7	777	251	4	2.51	0.91	4	3.33	4	1.56
		8	782	224	4	2.36	0.91	4	3.21	4	1.36
		9	625	212	4	1.97	0.80	4	2.67	4	1.21
		10	925	183	4	2.76	0.54	4	3.96	2	2.01
		11	595	178	4	2.01	0.86	4	2.47	4	1.11
		12	637	285	4	1.49	0.03	3	2.70	4	1.85
		13	600	247	4	2.21	1.05	3	2.57	4	1.60
		14	548	132	4	1.84	0.63	4	2.20	4	0.74
		15	621	165	3	1.89	0.52	3	2.32	3	0.86
		21	926	123	2	3.34	0.26	2	3.63	1	
		27	723	259	3	2.88	1.30	3	3.07	3	1.08
		34	552	185	3	1.91	0.67	3	1.88	3	0.72
		41	639	81	3	2.19	0.39	3	2.62	3	0.40
60	580	184	3	1.93	0.67	3	1.98	3	0.70		

daf = days after flooding, m = mean, sd = standard deviation, n = number of samples

Appendix E

Table E-9 (continued)

Site	Depth cm	daf	m.EC	sd.EC	n.EC	m.SAR	sd.SAR	n.SAR	m.Cl <sup>-</sup>	n.Cl <sup>-</sup>	sd.Cl <sup>-</sup>
			--- $\mu\text{S cm}^{-1}$ ---			---/---			--- $\text{mmol l}^{-1}$ ---		
P100	55	2	1179	255	4	3.57	0.56	4	5.08	4	1.14
		3	1042	245	4	2.79	0.66	4	4.50	4	1.26
		4	955	252	4	2.72	0.84	4	3.95	4	1.25
		5	822	190	4	2.49	0.55	4	3.45	4	1.07
		6	1128	231	4	3.43	0.66	4	5.10	4	1.43
		7	986	313	4	2.93	0.79	4	4.27	4	1.71
		8	841	58	4	2.58	0.30	4	3.45	4	0.62
		9	850	241	4	2.21	0.54	3	3.53	4	1.23
		10	957	106	4	2.76	0.20	4	4.04	3	1.02
		11	799	74	3	2.24	0.81	4	2.64	4	1.08
		12	611	147	3	1.70	0.67	3	1.82	4	0.96
		13	790	258	4	2.26	0.87	3	2.87	3	1.59
		14	866	263	4	2.52	0.65	4	3.62	4	1.55
		15	753	46	4	2.40	0.25	4	3.03	4	0.33
		21	1027	336	2	3.26	1.02	2	4.60	2	1.88
		27	1095	322	3	3.96	0.61	3	4.63	3	1.65
		34	557	226	2	2.14	1.07	2	1.88	2	0.91
41	923	64	3	2.85	0.14	3	3.27	3	0.23		
60	707	253	3	2.11	1.02	3	2.59	3	1.05		

**Table E-10:** Electric conductivity (EC), sodium adsorption ratio (SAR) and chloride (Cl<sup>-</sup>) contents determined in the soil solution of the 700 year paddy soil (P700).

Site	Depth cm	daf	m.EC	sd.EC	n.EC	m.SAR	sd.SAR	n.SAR	m.Cl <sup>-</sup>	sd.Cl <sup>-</sup>	n.Cl <sup>-</sup>
			--- $\mu\text{S cm}^{-1}$ ---			---/---			--- $\text{mmol l}^{-1}$ ---		
P700	35	0	913		1	4.62	0.03	2	4.99	0.11	2
		1	1015	105	4	4.01	0.36	4	4.80	0.74	3
		2	653	26	3	2.58	0.62	3	2.51	0.29	3
		3	564	14	4	2.32	0.40	4	2.28	0.23	3
		4	625	146	3	2.63	0.52	3	2.52	0.74	3
		5	720	232	4	2.95	0.95	4	3.06	1.22	4
		6	735	260	3	3.12	0.91	4	3.60	1.46	4
		7	792	185	4	3.31	0.55	4	3.50	1.09	4
		8	835	243	3	3.31	0.80	3	3.87	1.38	3
		9	966	165	3	3.96	0.35	3	4.48	0.93	3
		10	916	15	3	4.09		1	4.52	0.09	3
		11	828	85	4	3.66	0.62	4	3.78	0.71	4
		12	815	223	4	3.39	1.09	3	3.74	1.26	4
		13	799	305	3	3.28	1.02	4	3.89	1.92	3
		14	634	189	2	3.09	0.97	4	2.74	0.63	3
		15	988	87	4	4.19	0.15	4	4.62	0.31	4
		20	703	270	3	3.23	1.23	4	2.32	0.49	2
26	1093		1	3.81	0.40	2	4.43	1.32	2		
32	952	98	3	4.48	0.25	3	4.73	0.24	3		
39	675	220	3	2.87	0.99	3	2.78	0.91	3		
65	823	193	3	2.98	0.62	3	3.30	0.61	3		

daf = days after flooding, m = mean, sd = standard deviation, n = number of samples

Table E-10 (continued)

Site	Depth cm	daf	m.EC	sd.EC	n.EC	m.SAR	sd.SAR	n.SAR	m.Cl <sup>-</sup>	sd.Cl <sup>-</sup>	n.Cl <sup>-</sup>
			--- $\mu\text{S cm}^{-1}$ ---			---/---			--- $\text{mmol l}^{-1}$ ---		
P700	55	0	956		1	4.29		1	4.83		1
		1	937	95	4	3.12	0.11	2	4.11	0.61	4
		2	660	135	4	2.55	0.47	4	2.72	0.59	4
		3	714	168	4	2.81	0.55	4	2.98	0.88	4
		4	773	161	4	3.18	0.81	4	3.38	1.13	4
		5	778	117	4	3.07	0.65	4	3.27	0.78	4
		6	798	225	3	2.22	0.86	3	2.90	1.58	4
		7	690	159	4	2.83	0.85	4	3.02	1.11	4
		8	650	232	4	2.41	0.72	4	2.62	1.12	4
		9	828	221	3	3.37	0.41	3	3.48	1.13	3
		10	898	119	4	3.74	0.37	4	4.18	0.95	4
		11	674	143	4	2.85	0.34	4	2.72	0.52	4
		12	869	228	4	3.88	0.86	3	4.17	1.45	4
		13	1056	55	3	4.24	0.36	4	5.10	0.27	4
		14	750	213	4	3.03	0.87	4	3.47	1.33	4
		15	886	174	4	3.71	0.56	4	4.05	0.95	4
		20	579	119	4	2.37	0.39	4	2.25	0.50	4
		26	1093		1	4.00	0.30	2	4.46	0.89	2
		32	993	34	3	3.67	1.04	3	4.65	0.58	3
		39	634	152	3	2.61	1.12	3	2.68	0.63	3
65	682	82	3	2.38	0.33	3	2.49	0.35	3		

**Table E-11:** Electric conductivity (EC), sodium adsorption ratio (SAR) and chloride (Cl<sup>-</sup>) contents determined in the soil solution of the 2000 year paddy soil (P2000).

Site	Depth	daf	m.EC	sd.EC	n.EC	m.SAR	sd.SAR	n.SAR	m.Cl <sup>-</sup>	sd.Cl <sup>-</sup>	n.Cl <sup>-</sup>
			--- $\mu\text{S cm}^{-1}$ ---			---/---			--- $\text{mmol l}^{-1}$ ---		
P2000	35	0			0	1.31		1			0
		1	640	99	2	1.54	0.08	3	1.97	0.28	3
		2	665	74	4	1.59	0.05	4	2.09	0.29	4
		3	675	63	4	1.53	0.15	4	2.08	0.25	4
		4	714		1	1.57	0.10	4	2.11	0.27	4
		7			0	1.47	0.07	3	2.01	0.03	2
		8			0	1.60	0.09	3	2.06	0.07	3
		9			0	1.42	0.18	4	1.79	0.17	3
		11	459	64	3	1.15	0.12	3	1.21	0.15	3
		12	508	67	4	1.31	0.56	4	1.45	0.54	4
		13	589	61	4	1.51	0.13	4	1.94	0.17	4
		16	449	105	3	1.17	0.30	3	1.29		1
		19	427	73	4	0.92	0.34	4	1.00	0.47	4
		27	350	53	4	1.00	0.21	4	1.08	0.23	4
		31	275	29	3	0.80	0.41	4	0.86	0.24	3
		37	407	0	2	1.40	0.24	2	1.42	0.23	2
		43	419	57	3	1.68	0.06	3	1.63	0.13	3
57	356	57	3	1.19	0.31	2	1.27	0.34	3		

daf = days after flooding, m = mean, sd = standard deviation, n = number of samples

Table E-11 (continued)

Site	Depth cm	daf	m.EC	sd.EC	n.EC	m.SAR	sd.SAR	n.SAR	m.Cl <sup>-</sup>	sd.Cl <sup>-</sup>	n.Cl <sup>-</sup>
			--- $\mu\text{S cm}^{-1}$ ---			---/---			--- $\text{mmol l}^{-1}$ ---		
P2000	55	0			0	1.16		1			0
		1	681		1	1.55	0.09	4	2.02	0.14	3
		2	633	68	4	1.42	0.15	4	2.03	0.26	4
		3	622	73	4	1.54	0.06	4	1.93	0.24	4
		4	658	89	4	1.52	0.13	4	2.07	0.31	4
		7	640	63	3	1.62	0.19	4	2.09	0.31	3
		8			0	1.57	0.17	4	2.06	0.21	4
		9	646	46	3	1.47	0.13	4	2.05	0.18	4
		11	572	85	4	1.34	0.28	3	1.73	0.42	4
		12	582	87	4	1.43	0.30	4	1.78	0.40	4
		13	533	67	4	1.20	0.29	4	1.45	0.42	4
		16	485	86	4	1.18	0.21	4	0.53	0.05	4
		19	402	71	4	0.86	0.24	4	0.92	0.31	4
		27	337	48	4	0.93	0.19	4	1.02	0.23	4
		31	316	68	3	1.63	1.34	4	0.97	0.38	3
		37	475	64	2	1.59	0.09	2	1.68	0.16	2
43	378	42	3	1.69	0.12	3	1.56	0.18	3		
57	384	37	3	1.13	0.25	3	1.38	0.39	3		

**Table E–12:** Concentrations of earth alkali/alkali elements determined in the soil solution of the 100 year paddy soil (P100).

Site	Depth cm	daf	m.Ca	sd.Ca	n.Ca	m.K	sd.K	n.K	m.Mg	sd.Mg	n.Mg	m.Na	sd.Na	n.Na
			--- mmol l <sup>-1</sup> ---			--- mmol l <sup>-1</sup> ---			--- mmol l <sup>-1</sup> ---			--- mmol l <sup>-1</sup> ---		
P100	35	2	2.26	0.05	4	0.03	0.01	4	0.78	0.18	4	2.96	0.75	4
		3	2.75	0.43	4	0.04	0.02	4	0.97	0.29	4	3.00	1.00	4
		4	2.69	0.11	4	0.05	0.03	4	1.19	0.39	4	3.74	1.31	4
		5	2.42	0.14	4	0.04	0.02	4	0.73	0.23	4	2.27	0.86	4
		6	2.38	0.24	4	0.04	0.01	4	0.95	0.24	4	3.03	0.81	4
		7	2.16	0.29	4	0.04	0.02	4	0.86	0.29	4	3.13	1.29	4
		8	2.48	0.37	4	0.05	0.02	4	0.94	0.39	4	3.16	1.39	4
		9	2.22	0.25	4	0.03	0.01	4	0.69	0.17	4	2.40	1.03	4
		10	2.71	0.31	4	0.07	0.05	4	1.17	0.29	4	3.87	0.86	4
		11	2.11	0.50	4	0.04	0.02	4	0.68	0.20	4	2.35	0.91	4
		12	2.22	0.24	3	0.04	0.02	4	0.59	0.04	3	2.50	1.46	4
		13	1.95	0.44	3	0.05	0.03	3	0.79	0.34	3	2.65	1.46	3
		14	2.18	0.46	4	0.03	0.02	4	0.67	0.14	4	2.21	0.80	4
		15	2.33	0.40	3	0.03	0.01	3	0.78	0.32	3	2.39	0.87	3
		21	1.93	0.12	2	0.07	0.03	2	1.18	0.39	2	4.19	0.67	2
		27	1.34	0.58	2	0.07	0.02	3	0.90	0.54	3	3.00	1.93	3
		34	2.01	0.19	3	0.04	0.01	3	0.79	0.20	3	2.29	0.93	3
41	2.29	0.23	3	0.06	0.02	3	0.93	0.10	3	2.79	0.55	3		
60	2.36	0.31	3	0.05	0.02	3	1.01	0.27	3	2.52	0.88	3		

daf = days after flooding, m = mean, sd = standard deviation, n = number of samples

Table E-12 (continued):

Site	Depth cm	daf	m.Ca --- mmol l <sup>-1</sup> ---	sd.Ca	n.Ca	m.K --- mmol l <sup>-1</sup> ---	sd.K	n.K	m.Mg --- mmol l <sup>-1</sup> ---	sd.Mg	n.Mg	m.Na --- mmol l <sup>-1</sup> ---	sd.Na	n.Na
P100	55	2	2.45	0.14	4	0.07	0.03	4	1.65	0.47	4	5.16	1.16	4
		3	2.83	0.37	4	0.06	0.01	4	1.57	0.37	4	4.16	1.07	4
		4	2.59	0.08	4	0.05	0.02	4	1.35	0.39	4	3.87	1.36	4
		5	2.46	0.16	4	0.04	0.01	4	1.12	0.23	4	3.36	0.88	4
		6	2.30	0.29	4	0.07	0.03	4	1.65	0.40	4	4.86	1.13	4
		7	2.49	0.22	4	0.05	0.01	4	1.48	0.57	4	4.18	1.41	4
		8	2.69	0.21	4	0.04	0.01	4	1.17	0.11	4	3.60	0.48	4
		9	2.92	0.42	3	0.04	0.02	3	1.15	0.45	3	3.17	0.92	3
		10	2.87	0.40	4	0.05	0.02	4	1.47	0.34	4	4.06	0.39	4
		11	2.44	0.26	4	0.04	0.02	4	0.98	0.36	4	2.97	1.15	4
		12	2.73	0.13	3	0.03	0.01	4	0.79	0.29	3	2.00	0.99	4
		13	2.25	0.30	3	0.03	0.01	3	0.96	0.46	3	2.94	1.50	3
		14	2.58	0.19	4	0.05	0.03	4	1.18	0.47	4	3.50	1.16	4
		15	2.36	0.65	4	0.04	0.01	4	0.99	0.05	4	3.09	0.19	4
		21	2.45	0.21	2	0.06	0.02	2	1.49	0.54	2	4.62	1.63	2
		27	1.33	0.33	3	0.11	0.02	3	1.50	0.42	3	4.77	1.32	3
		34	1.97	0.86	2	0.04	0.03	2	0.81	0.25	2	2.45	0.99	2
41	2.21	0.64	3	0.09	0.02	3	1.24	0.08	3	3.73	0.21	3		
60	2.57	0.02	2	0.04	0.03	3	0.89	0.48	3	3.64	0.79	2		

**Table E–13:** Concentrations of the earth alkali/alkali elements determined in the soil solution of the 700 year paddy soil (P700).

site	depth cm	daf	m.Ca	sd.Ca	n.Ca	m.K	sd.K	n.K	m.Mg	sd.Mg	n.Mg	m.Na	sd.Na	n.Na
			--- mmol l <sup>-1</sup> ---			--- mmol l <sup>-1</sup> ---			--- mmol l <sup>-1</sup> ---			--- mmol l <sup>-1</sup> ---		
P700	35	0	1.16	0.31	2	0.08	0.02	2	0.99	0.01	2	4.79	0.33	2
		1	1.44	0.22	4	0.07	0.01	4	1.02	0.12	4	4.46	0.45	4
		2	1.33	0.27	3	0.04	0.01	3	0.66	0.06	3	2.56	0.47	3
		3	1.29	0.33	4	0.03	0.00	4	0.61	0.04	4	2.24	0.24	4
		4	1.37	0.20	3	0.04	0.01	3	0.68	0.14	3	2.69	0.70	3
		5	1.45	0.21	4	0.04	0.02	4	0.76	0.21	4	3.16	1.23	4
		6	1.46	0.21	4	0.05	0.02	4	0.90	0.29	4	3.45	1.22	4
		7	1.42	0.29	4	0.05	0.00	2	0.88	0.21	4	3.57	0.90	4
		8	1.46	0.26	3	0.06	0.02	3	0.96	0.29	3	3.69	1.19	3
		9	1.52	0.38	3	0.07	0.02	3	1.07	0.11	3	4.51	0.62	3
		10	1.30		1	0.07		1	0.92		1	4.32		1
		11	1.41	0.19	4	0.06	0.02	4	0.88	0.09	4	3.92	0.61	4
		12	1.30	0.11	3	0.05	0.02	3	0.84	0.27	3	3.54	1.34	3
		13	1.61	0.30	4	0.06	0.02	4	1.01	0.34	4	3.86	1.49	4
		14	1.45	0.09	4	0.05	0.01	4	0.79	0.23	4	3.32	1.21	4
		15	1.68	0.31	4	0.07	0.01	4	1.14	0.12	4	4.98	0.38	4
		20	1.69	0.34	4	0.05	0.02	4	0.89	0.32	4	3.74	1.62	4
		26	1.69	0.01	2	0.06	0.02	2	1.18	0.24	2	4.58	0.69	2
		32	1.05	0.09	3	0.11	0.00	3	1.14	0.02	3	4.70	0.19	3
		39	1.57	0.09	3	0.06	0.02	3	0.91	0.22	3	3.23	1.19	3
65	1.90	0.32	3	0.06	0.02	3	1.22	0.36	3	3.75	0.92	3		

daf = days after flooding, m = mean, sd = standard deviation, n = number of samples

Table E-13 (continued)

site	depth cm	daf	m.Ca	sd.Ca	n.Ca	m.K	sd.K	n.K	m.Mg	sd.Mg	n.Mg	m.Na	sd.Na	n.Na
			--- mmol l <sup>-1</sup> ---			--- mmol l <sup>-1</sup> ---			--- mmol l <sup>-1</sup> ---			--- mmol l <sup>-1</sup> ---		
P700	55	0	1.04		1	0.06		1	0.95		1	4.29		1
		1	1.49	0.23	2	0.06	0.01	2	0.90	0.02	2	3.42	0.03	2
		2	1.29	0.16	4	0.04	0.01	4	0.73	0.12	4	2.58	0.59	4
		3	1.34	0.11	4	0.04	0.02	4	0.77	0.16	4	2.91	0.67	4
		4	1.37	0.06	4	0.06	0.01	4	0.88	0.23	4	3.41	1.02	4
		5	1.41	0.13	4	0.05	0.01	4	0.85	0.15	4	3.28	0.71	4
		6	1.40	0.22	3	0.03	0.01	3	0.68	0.30	3	2.34	1.20	3
		7	1.27	0.08	4	0.05	0.02	4	0.82	0.21	4	2.92	1.00	4
		8	1.31	0.18	4	0.06	0.05	4	0.78	0.26	4	2.51	0.98	4
		9	1.43	0.20	3	0.06	0.02	3	0.91	0.17	3	3.67	0.74	3
		10	1.39	0.17	4	0.07	0.02	4	1.01	0.17	4	4.13	0.63	4
		11	1.21	0.20	4	0.05	0.02	4	0.71	0.07	4	2.82	0.50	4
		12	1.42	0.07	3	0.07	0.01	3	1.10	0.31	3	4.40	1.21	3
		13	1.46	0.25	4	0.08	0.02	4	1.21	0.09	4	4.90	0.27	4
		14	1.56	0.26	4	0.07	0.03	4	0.87	0.26	4	3.41	1.20	4
		15	1.53	0.20	4	0.09	0.04	4	0.99	0.21	4	4.21	0.93	4
		20	1.35	0.10	4	0.04	0.01	4	0.67	0.09	4	2.40	0.49	4
		26	1.35	0.08	2	0.08	0.00	2	1.09	0.11	2	4.44	0.50	2
		32	0.90	0.42	3	0.09	0.04	3	1.00	0.43	3	4.67	0.21	2
39	0.99	0.18	3	0.05	0.03	3	0.86	0.29	3	2.57	1.26	3		
65	2.03	0.25	3	0.06	0.01	3	1.12	0.18	3	2.98	0.29	3		

**Table E–14:** Concentrations of the earth alkali/alkali elements determined in the soil solution of the 2000 year paddy soil (P2000).

Site	Depth cm	daf	m.Ca	sd.Ca	n.Ca	m.K	sd.K	n.K	m.Mg	sd.Mg	n.Mg	m.Na	sd.Na	n.Na
			--- mmol l <sup>-1</sup> ---			--- mmol l <sup>-1</sup> ---			--- mmol l <sup>-1</sup> ---			--- mmol l <sup>-1</sup> ---		
P2000	35	0	1.75		1	0.02		1	0.69		1	1.45		1
		1	1.42	0.11	3	0.01	0.00	3	0.65	0.03	3	1.57	0.05	3
		2	1.67	0.27	4	0.03	0.02	4	0.71	0.05	4	1.74	0.16	4
		3	1.68	0.23	4	0.04	0.02	4	0.72	0.06	4	1.68	0.17	4
		4	1.71	0.12	4	0.02	0.02	4	0.72	0.07	4	1.74	0.18	4
		7	1.94	0.05	3	0.02	0.02	3	0.79	0.01	3	1.72	0.08	3
		8	1.71	0.31	3	0.03	0.02	3	0.72	0.05	3	1.76	0.05	3
		9	1.72	0.27	4	0.02	0.01	4	0.68	0.02	4	1.55	0.12	4
		11	1.21	0.14	3	0.01	0.01	3	0.50	0.07	3	1.06	0.15	3
		12	1.38	0.19	4	0.01	0.00	4	0.55	0.13	4	1.29	0.53	4
		13	1.48	0.17	4	0.02	0.01	4	0.66	0.06	4	1.57	0.16	4
		16	1.20	0.09	3	0.01	0.00	3	0.51	0.09	3	1.09	0.34	3
		19	1.44	0.15	4	0.01	0.00	4	0.45	0.09	4	0.90	0.35	4
		27	1.17	0.13	4	0.01	0.00	4	0.43	0.08	4	0.90	0.21	4
		31	0.87	0.27	4	0.01	0.00	4	0.35	0.09	4	0.63	0.32	4
		37	1.11	0.11	2	0.01	0.00	2	0.57	0.03	2	1.28	0.20	2
43	0.94	0.23	3	0.03	0.01	3	0.66	0.07	3	1.50	0.09	3		
57	1.31	0.00	2	0.01	0.01	2	0.66	0.15	2	1.19	0.36	2		

daf = days after flooding, m = mean, sd = standard deviation, n = number of samples

Table E-14 (continued)

Site	Depth cm	daf	m.Ca --- mmol l <sup>-1</sup> ---	sd.Ca	n.Ca	m.K --- mmol l <sup>-1</sup> ---	sd.K	n.K	m.Mg --- mmol l <sup>-1</sup> ---	sd.Mg	n.Mg	m.Na --- mmol l <sup>-1</sup> ---	sd.Na	n.Na
P2000	55	0	1.44		1	0.01		1	0.58		1	1.17		1
		1	1.53	0.18	4	0.02	0.01	4	0.68	0.04	4	1.64	0.14	4
		2	1.67	0.16	4	0.02	0.01	4	0.76	0.06	4	1.57	0.23	4
		3	1.45	0.20	4	0.02	0.00	4	0.72	0.09	4	1.61	0.16	4
		4	1.62	0.28	4	0.02	0.01	4	0.77	0.11	4	1.67	0.25	4
		7	1.61	0.15	4	0.02	0.01	4	0.78	0.07	4	1.78	0.29	4
		8	1.68	0.14	4	0.02	0.01	4	0.78	0.04	4	1.74	0.24	4
		9	1.67	0.16	4	0.02	0.01	4	0.80	0.07	4	1.64	0.17	4
		11	1.42	0.07	3	0.02	0.01	3	0.64	0.09	3	1.37	0.34	3
		12	1.49	0.20	4	0.02	0.01	4	0.70	0.12	4	1.50	0.34	4
		13	1.50	0.09	4	0.02	0.01	4	0.61	0.12	4	1.24	0.31	4
		16	1.36	0.11	4	0.01	0.01	4	0.57	0.09	4	1.17	0.27	4
		19	1.38	0.16	4	0.01	0.01	4	0.50	0.11	4	0.84	0.25	4
		27	1.06	0.18	4	0.01	0.00	4	0.43	0.08	4	0.81	0.20	4
		31	1.13	0.42	4	0.04	0.06	4	0.64	0.43	4	0.82	0.33	3
		37	1.11	0.18	2	0.02	0.00	2	0.68	0.04	2	1.51	0.18	2
43	0.78	0.22	3	0.03	0.01	3	0.65	0.04	3	1.43	0.12	3		
57	1.35	0.08	3	0.02	0.02	3	0.64	0.12	3	1.13	0.28	3		

**Table E-15:** Concentrations of redox sensitive elements and compounds, respectively, determined in the soil solution of the 100 year paddy soil (P100).

Site	Depth cm	daf	m.NO <sub>2/3</sub> <sup>-1</sup> --- mmol l <sup>-1</sup> ---	sd.NO <sub>2/3</sub> <sup>-1</sup>	n.NO <sub>2/3</sub> <sup>-1</sup>	m.NH <sub>4</sub> <sup>+</sup> --- mmol l <sup>-1</sup> ---	sd.NH <sub>4</sub> <sup>+</sup>	n.NH <sub>4</sub> <sup>+</sup>	m.Mn --- mmol l <sup>-1</sup> ---	sd.Mn	n.Mn	m.Fe --- mmol l <sup>-1</sup> ---	sd.Fe	n.Fe
P100	35	2	0.008	0.006	4	0.014	0.003	4	0.001	0.00	4	0.000	0.000	4
		3	0.004	0.006	4	0.022	0.000	4	0.001	0.00	4	0.000	0.000	4
		4	0.008	0.008	4	0.014	0.004	4	0.002	0.00	4	0.000	0.000	4
		5	0.003	0.004	4	0.017	0.006	4	0.003	0.00	4	0.000	0.000	4
		6	0.004	0.007	4	0.017	0.005	4	0.003	0.00	4	0.001	0.001	4
		7	0.004	0.005	4	0.016	0.004	4	0.003	0.00	4	0.001	0.001	4
		8	0.004	0.007	4	0.016	0.009	4	0.003	0.00	4	0.002	0.002	4
		9	0.002	0.003	4	0.028	0.006	4	0.005	0.00	4	0.002	0.002	4
		10	0.003	0.004	4	0.024	0.019	4	0.005	0.00	4	0.003	0.003	4
		11	0.003	0.003	4	0.023	0.006	4	0.004	0.00	4	0.002	0.002	4
		12	0.001	0.001	4	0.022	0.009	4	0.005	0.00	4	0.002	0.003	4
		13	0.002	0.002	4	0.021	0.012	4	0.004	0.00	3	0.001	0.002	3
		14	0.001	0.001	4	0.018	0.014	4	0.006	0.00	4	0.003	0.003	4
		15	0.002	0.002	3	0.019	0.002	3	0.008	0.01	3	0.002	0.002	3
		21	0.003		1	0.036		1	0.009	0.00	2	0.005	0.002	2
		27	0.003	0.001	3	0.026	0.020	2	0.006	0.00	3	0.006	0.005	3
		34	0.001	0.000	3	0.017	0.013	3	0.010	0.01	3	0.007	0.005	3
41	0.004	0.003	3	0.021	0.013	2	0.024	0.01	3	0.022	0.023	3		
60	0.003	0.002	3	0.023	0.024	3	0.030	0.02	3	0.026	0.026	3		

daf = days after flooding, m = mean, sd = standard deviation, n = number of samples

Table E-15 (continued):

Site	Depth cm	daf	m.NO <sub>2/3</sub> <sup>-1</sup> --- mmol l <sup>-1</sup> ---	sd.NO <sub>2/3</sub> <sup>-1</sup>	n.NO <sub>2/3</sub> <sup>-1</sup>	m.NH <sub>4</sub> <sup>+</sup> --- mmol l <sup>-1</sup> ---	sd.NH <sub>4</sub> <sup>+</sup>	n.NH <sub>4</sub> <sup>+</sup>	m.Mn --- mmol l <sup>-1</sup> ---	sd.Mn	n.Mn	m.Fe --- mmol l <sup>-1</sup> ---	sd.Fe	n.Fe
P100	55	2	0.016	0.009	4	0.014	0.003	4	0.000	0.00	4	0.000	0.000	4
		3	0.011	0.003	4	0.017	0.006	4	0.000	0.00	4	0.000	0.000	4
		4	0.011	0.001	4	0.014	0.001	4	0.000	0.00	4	0.000	0.000	4
		5	0.009	0.004	4	0.014	0.004	4	0.000	0.00	4	0.000	0.000	4
		6	0.009	0.004	4	0.011	0.002	4	0.000	0.00	4	0.000	0.000	4
		7	0.008	0.005	4	0.011	0.002	4	0.000	0.00	4	0.000	0.000	4
		8	0.006	0.002	4	0.010	0.002	4	0.000	0.00	4	0.000	0.000	4
		9	0.005	0.002	4	0.010	0.003	4	0.001	0.00	3	0.000	0.000	3
		10	0.005	0.002	4	0.009	0.003	2	0.001	0.00	4	0.000	0.000	4
		11	0.003	0.001	4	0.017	0.003	4	0.001	0.00	4	0.000	0.000	4
		12	0.002	0.001	4	0.014	0.003	4	0.002	0.00	4	0.000	0.000	4
		13	0.002	0.002	4	0.010	0.001	4	0.001	0.00	3	0.000	0.000	3
		14	0.002	0.002	4	0.010	0.004	4	0.001	0.00	4	0.000	0.000	4
		15	0.001	0.001	4	0.023	0.003	4	0.002	0.00	4	0.000	0.000	4
		21	0.001	0.001	2	0.015	0.005	2	0.008	0.00	2	0.003	0.001	2
		27	0.004	0.004	3	0.011	0.004	3	0.004	0.00	3	0.004	0.003	3
		34	0.002	0.001	2	0.014	0.003	2	0.005	0.00	2	0.005	0.003	2
41	0.002	0.000	3	0.010	0.001	3	0.005	0.00	3	0.006	0.002	3		
60	0.003	0.002	3	0.012	0.002	3	0.003	0.00	3	0.004	0.002	3		

**Table E–16:** Concentrations of redox sensitive elements and compounds, respectively, determined in the soil solution of the 700 year paddy soil (P700).

Site	Depth cm	daf	m.NO <sub>2/3</sub> <sup>-1</sup>	sd.NO <sub>2/3</sub> <sup>-1</sup>	n.NO <sub>2/3</sub> <sup>-1</sup>	m.NH <sub>4</sub> <sup>+</sup>	sd.NH <sub>4</sub> <sup>+</sup>	n.NH <sub>4</sub> <sup>+</sup>	m.Mn	sd.Mn	n.Mn	m.Fe	sd.Fe	n.Fe
			--- mmol l <sup>-1</sup> ---			--- mmol l <sup>-1</sup> ---			--- mmol l <sup>-1</sup> ---			--- mmol l <sup>-1</sup> ---		
P700	35	0	0.089	0.021	2	0.025	0.002	2	0.000	0.00	2	0.000	0.000	2
		1	0.045	0.044	4	0.015	0.005	4	0.000	0.00	4	0.000	0.000	4
		2	0.011	0.011	3	0.019	0.004	3	0.000	0.00	3	0.000	0.000	3
		3	0.004	0.004	4	0.014	0.003	4	0.001	0.00	4	0.000	0.000	4
		4	0.000	0.000	3	0.016	0.003	3	0.002	0.00	3	0.000	0.000	3
		5	0.001	0.000	4	0.016	0.005	4	0.003	0.00	4	0.001	0.000	4
		6	0.002	0.001	4	0.017	0.006	4	0.003	0.00	4	0.001	0.000	4
		7	0.001	0.001	4	0.022	0.004	4	0.004	0.00	4	0.001	0.001	4
		8	0.002	0.003	3	0.024	0.009	3	0.004	0.00	3	0.002	0.000	3
		9	0.000	0.000	3	0.021	0.010	3	0.004	0.00	3	0.002	0.001	3
		10	0.000	0.000	4	0.035	0.008	4	0.005		1	0.003		1
		11	0.002	0.000	4	0.028	0.005	4	0.006	0.00	4	0.003	0.001	4
		12	0.001	0.001	4	0.028	0.010	4	0.004	0.00	3	0.003	0.001	3
		13	0.000	0.000	3	0.045	0.016	3	0.007	0.00	4	0.003	0.001	4
		14	0.001	0.001	4	0.044	0.013	4	0.007	0.00	4	0.003	0.000	4
		15	0.002	0.002	4	0.031	0.007	4	0.009	0.00	4	0.004	0.001	4
		20	0.000	0.000	3	0.026	0.006	3	0.013	0.00	4	0.005	0.002	4
		26	0.003	0.004	2	0.037	0.023	2	0.019	0.00	2	0.014	0.006	2
		32	0.002	0.002	3	0.027	0.001	3	0.012	0.00	3	0.008	0.004	3
		39	0.003	0.001	3	0.030	0.010	3	0.027	0.00	3	0.015	0.002	3
65	0.007	0.003	3	0.017	0.002	3	0.041	0.01	3	0.023	0.001	3		

daf = days after flooding, m = mean, sd = standard deviation, n = number of samples

Table E-16 (continued)

Site	Depth cm	daf	m.NO <sub>2/3</sub> <sup>-1</sup> --- mmol l <sup>-1</sup> ---	sd.NO <sub>2/3</sub> <sup>-1</sup> ---	n. NO <sub>2/3</sub> <sup>-1</sup>	m.NH <sub>4</sub> <sup>+</sup> --- mmol l <sup>-1</sup> ---	sd.NH <sub>4</sub> <sup>+</sup> ---	n.NH <sub>4</sub> <sup>+</sup>	m.Mn --- mmol l <sup>-1</sup> ---	sd.Mn ---	n.Mn	m.Fe --- mmol l <sup>-1</sup> ---	sd.Fe ---	n.Fe
P700	55	0	0.108		1	0.023		1	0.000		1	0.000		1
		1	0.035	0.018	4	0.034	0.020	4	0.000	0.00	2	0.000	0.000	2
		2	0.010	0.011	4	0.030	0.010	4	0.000	0.00	4	0.000	0.000	4
		3	0.004	0.003	4	0.030	0.010	4	0.001	0.00	4	0.000	0.000	4
		4	0.001	0.001	4	0.028	0.007	4	0.002	0.00	4	0.001	0.001	4
		5	0.001	0.000	4	0.025	0.006	4	0.002	0.00	4	0.001	0.000	4
		6	0.002	0.003	4	0.022	0.010	4	0.002	0.00	3	0.001	0.000	3
		7	0.001	0.001	4	0.029	0.008	4	0.002	0.00	4	0.001	0.000	4
		8	0.001	0.000	4	0.028	0.009	4	0.003	0.00	4	0.002	0.001	4
		9	0.001	0.000	3	0.024	0.007	3	0.003	0.00	3	0.001	0.001	3
		10	0.001	0.000	4	0.042	0.007	4	0.003	0.00	4	0.002	0.001	4
		11	0.003	0.001	4	0.031	0.005	4	0.003	0.00	4	0.002	0.002	4
		12	0.001	0.001	4	0.038	0.014	4	0.003	0.00	3	0.002	0.001	3
		13	0.001	0.001	4	0.045	0.008	4	0.003	0.00	4	0.003	0.001	4
		14	0.001	0.001	4	0.045	0.012	4	0.005	0.00	4	0.007	0.007	4
		15	0.001	0.000	4	0.028	0.007	4	0.006	0.01	4	0.006	0.005	4
		20	0.000	0.000	4	0.025	0.005	4	0.009	0.01	4	0.008	0.005	4
		26	0.004	0.003	2	0.039	0.008	2	0.012	0.01	2	0.013	0.007	2
32	0.004	0.003	3	0.025	0.004	3	0.008	0.00	3	0.011	0.004	3		
39	0.005	0.003	3	0.028	0.008	3	0.010	0.00	3	0.011	0.004	3		
65	0.005	0.001	3	0.022	0.004	3	0.044	0.02	3	0.039	0.017	3		

Appendix E

**Table E–17:** Concentrations of redox sensitive elements and compounds, respectively, determined in the soil solution of the 2000 year paddy soil (P2000).

Site	Depth cm	daf	m.NO <sub>2/3</sub> <sup>-</sup>	sd.NO <sub>2/3</sub> <sup>-</sup>	n.NO <sub>2/3</sub> <sup>-</sup>	m.NH <sub>4</sub> <sup>+</sup>	sd.NH <sub>4</sub> <sup>+</sup>	n.NH <sub>4</sub> <sup>+</sup>	m.Mn	sd.Mn	n.Mn	m.Fe	sd.Fe	n.Fe
			--- mmol l <sup>-1</sup> ---			--- mmol l <sup>-1</sup> ---			--- mmol l <sup>-1</sup> ---			--- mmol l <sup>-1</sup> ---		
P2000	35	0	0.044		1	0.029		1	0.00		1	0.000		1
		1	0.020	0.001	3	0.023	0.008	3	0.00	0.00	3	0.000	0.000	3
		2	0.003	0.002	4	0.019	0.004	4	0.00	0.00	4	0.000	0.000	4
		3	0.002	0.001	4	0.018	0.002	4	0.00	0.01	4	0.002	0.003	4
		4	0.000	0.000	4	0.015	0.005	4	0.00	0.00	4	0.002	0.002	4
		7	0.000	0.000	3	0.012	0.003	3	0.011	0.01	3	0.014	0.014	3
		8	0.000	0.000	3	0.013	0.002	3	0.011	0.01	3	0.014	0.016	3
		9	0.000	0.000	4	0.014	0.005	4	0.012	0.01	4	0.020	0.030	4
		11	0.001	0.001	3	0.025	0.009	3	0.004	0.00	3	0.004	0.004	3
		12	0.002	0.000	4	0.025	0.005	4	0.008	0.01	4	0.019	0.020	4
		13	0.001	0.000	4	0.015	0.007	4	0.009	0.01	4	0.014	0.015	4
		16	0.000	0.000	3	0.013	0.001	3	0.005	0.00	3	0.008	0.004	3
		19	0.001	0.001	4	0.016	0.002	4	0.009	0.01	4	0.017	0.019	4
		27	0.000	0.000	4	0.023	0.006	4	0.009	0.00	4	0.013	0.011	4
		31	0.001	0.001	4	0.013	0.004	4	0.007	0.00	4	0.013	0.011	4
		37	0.003	0.001	2	0.014	0.002	2	0.010	0.00	2	0.016	0.008	2
		43	0.003	0.002	3	0.016	0.003	3	0.008	0.00	3	0.016	0.004	3
57	0.002	0.001	3	0.024	0.011	3	0.013	0.00	2	0.023	0.008	2		

daf = days after flooding, m = mean, sd = standard deviation, n = number of samples

Appendix E

Table E-17 (continued)

Site	Depth cm	daf	m.NO <sub>2/3</sub> <sup>-</sup> --- mmol l <sup>-1</sup> ---	sd.NO <sub>2/3</sub> <sup>-</sup>	n.NO <sub>2/3</sub> <sup>-</sup>	m.NH <sub>4</sub> <sup>+</sup> --- mmol l <sup>-1</sup> ---	sd.NH <sub>4</sub> <sup>+</sup>	n.NH <sub>4</sub> <sup>+</sup>	m.Mn --- mmol l <sup>-1</sup> ---	sd.Mn	n.Mn	m.Fe --- mmol l <sup>-1</sup> ---	sd.Fe	n.Fe
P2000	55	0	0.030		1	0.014		1	0.000		1	0.000		1
		1	0.021	0.011	3	0.018	0.002	3	0.001	0.00	4	0.000	0.000	4
		2	0.010	0.003	4	0.018	0.002	4	0.000	0.00	4	0.000	0.000	4
		3	0.005	0.002	4	0.016	0.002	4	0.001	0.00	4	0.000	0.000	4
		4	0.002	0.004	4	0.019	0.002	4	0.001	0.00	4	0.001	0.001	4
		7	0.001	0.001	4	0.019	0.002	4	0.002	0.00	4	0.001	0.001	4
		8	0.001	0.001	4	0.010	0.001	4	0.003	0.00	4	0.001	0.001	4
		9	0.001	0.000	4	0.015	0.004	4	0.003	0.00	4	0.001	0.001	4
		11	0.000	0.000	4	0.014	0.002	4	0.002	0.00	3	0.001	0.001	3
		12	0.003	0.000	4	0.023	0.002	4	0.004	0.00	4	0.003	0.003	4
		13	0.001	0.000	4	0.015	0.005	4	0.004	0.00	4	0.003	0.002	4
		16	0.000	0.000	4	0.015	0.004	4	0.003	0.00	4	0.003	0.002	4
		19	0.000	0.000	4	0.022	0.011	4	0.003	0.00	4	0.002	0.001	4
		27	0.001	0.000	4	0.024	0.004	4	0.004	0.00	4	0.010	0.009	4
		31	0.001	0.000	3	0.022	0.004	3	0.006	0.00	4	0.012	0.007	4
		37	0.003	0.003	2	0.022	0.001	2	0.005	0.00	2	0.009	0.002	2
43	0.002	0.001	3	0.010	0.003	3	0.004	0.00	3	0.013	0.003	3		
57	0.003	0.004	3	0.023	0.014	3	0.009	0.00	3	0.016	0.009	3		

**Table E–18:** Concentration of the redox sensitive elements and compounds, respectively, determined in the soil solution of the 100 year paddy soil (P100).

Site	depth cm	daf	m.S --- mmol l <sup>-1</sup> ---	sd.S	n.S	m.SO <sub>4</sub> <sup>2-</sup> --- mmol l <sup>-1</sup> ---	sd.SO <sub>4</sub> <sup>2-</sup>	n.SO <sub>4</sub> <sup>2-</sup>	m.DIC --- mg l <sup>-1</sup> ---	sd.DIC	n.DIC	m.DOC --- mg l <sup>-1</sup> ---	sd.DOC	n.DOC
P100	35	2	1.61	0.37	4	2.08	0.45	4	27.06	9.36	4	10.51	2.73	4
		3	2.13	0.63	4	2.19	0.77	4	20.64	8.80	3	9.35	5.24	3
		4	1.68	0.49	4	2.39	0.64	4	36.63	9.59	3	8.85	5.32	3
		5	1.46	1.00	4	1.56	0.67	4	27.20	8.04	4	9.34	4.62	4
		6	1.29	0.26	4	1.75	0.34	4	36.43	10.90	3	10.83	5.57	3
		7	2.15	1.27	4	1.66	0.66	4	31.93	5.75	4	11.49	5.48	4
		8	1.33	0.54	4	1.54	0.51	4	29.33	0.24	2	10.47	0.90	2
		9	1.12	0.08	4	1.18	0.46	4	36.30	7.71	4	10.34	6.14	4
		10	1.39	0.16	4	1.49	0.33	3	30.36		1	14.61		1
		11	0.80	0.25	4	1.00	0.35	4	33.46	13.01	3	8.71	1.62	2
		12	0.67	0.19	3	0.92	0.50	4	28.88	12.23	4	9.45	5.55	4
		13	0.73	0.32	3	0.82	0.43	4	32.18	11.58	3	11.53	7.74	3
		14	0.57	0.13	4	0.65	0.23	4	31.69	5.40	4	8.74	2.16	4
		15	0.65	0.29	3	0.80	0.45	3	40.10	1.46	2	9.97	2.54	2
		21	0.90	0.34	2	1.13	0.52	2			0			0
		27	0.63	0.55	3	0.74	0.73	3	45.71	6.18	3	13.44	4.73	3
		34	0.81	0.44	3	0.67	0.45	3	26.69	13.48	3	9.36	3.83	3
41	0.74	0.52	3	0.44	0.45	3	59.71	4.68	3	15.07	6.30	3		
60	0.49	0.37	3	0.40	0.46	3	51.44	20.39	3	12.73	5.86	3		

daf = days after flooding, m = mean, sd = standard deviation, n = number of samples

Table E-18 (continued):

Site	depth cm	daf	m.S --- mmol l <sup>-1</sup> ---	sd.S	n.S	m.SO <sub>4</sub> <sup>2-</sup> --- mmol l <sup>-1</sup> ---	sd.SO <sub>4</sub> <sup>2-</sup>	n.SO <sub>4</sub> <sup>2-</sup>	m.DIC --- mg l <sup>-1</sup> ---	sd.DIC	n.DIC	m.DOC --- mg l <sup>-1</sup> ---	sd.DOC	n.DOC
P100	55	2	1.59	0.39	4	2.29	0.55	4	54.24	10.36	4	9.24	3.46	3
		3	1.86	1.23	4	2.11	0.76	4	40.15	3.65	4	7.29	5.08	4
		4	1.35	0.45	4	1.88	0.64	4	46.76	13.32	3	6.69	2.43	3
		5	1.17	0.27	4	1.52	0.37	4	39.95	10.87	4	5.62	0.39	4
		6	1.60	0.34	4	2.27	0.54	4	46.86	8.80	4	8.67	3.32	4
		7	1.45	0.43	4	1.96	0.62	4	36.10	6.81	3	7.13	0.89	3
		8	1.34	0.38	4	1.62	0.15	4	48.60	4.97	2	4.03	0.16	2
		9	0.98	0.28	3	1.66	0.51	4	35.03	3.44	3	6.62	2.09	3
		10	1.43	0.29	4	1.80	0.24	4	27.49	6.84	2	5.73		1
		11	0.98	0.39	4	1.31	0.59	4	31.29	10.05	4	4.37	0.67	2
		12	0.77	0.28	3	0.85	0.47	4	29.97	12.25	4	4.82	0.85	4
		13	1.00	0.48	3	1.38	0.61	4	38.14	4.30	3	5.19	0.37	3
		14	1.35	0.58	4	1.51	0.42	4	36.19	10.93	2	3.45	2.04	2
		15	1.40	0.70	4	1.29	0.24	4	40.12	5.99	3	5.08	1.74	3
		21	1.36	0.22	2	1.78	0.50	2			0			0
		27	1.33	0.55	3	1.61	0.76	3	42.32	11.23	2	17.62		1
		34	0.83	0.07	2	0.66	0.10	2	35.95	15.24	2	10.11	1.56	2
		41	1.07	0.32	3	1.30	0.47	3	48.75	4.76	3	12.14	2.56	3
60	0.92	0.55	3	1.07	0.50	3	40.50	2.29	3	8.55	3.74	3		

Appendix E

**Table E–19:** Concentration of the redox sensitive elements and compounds, respectively, determined in the soil solution of the 700 year paddy soil (P700).

Site	Depth cm	daf	m.S	sd.S	n.S	m.SO <sub>4</sub> <sup>2-</sup>	sd. SO <sub>4</sub> <sup>2-</sup>	n. SO <sub>4</sub> <sup>2-</sup>	m.DIC	sd.DIC	n.DIC	m.DOC	sd.DOC	n.DOC
			--- mmol l <sup>-1</sup> ---			--- mmol l <sup>-1</sup> ---			--- mmol l <sup>-1</sup> ---			--- mg l <sup>-1</sup> ---		
P700	35	0	1.72	0.74	2	1.82	0.29	2	11.25	0.16	2	50.05	22.02	2
		1	1.62	0.13	4	2.03	0.27	4	19.11	4.15	3	25.01	7.33	3
		2	1.10	0.05	3	1.42	0.09	3	37.43	27.46	2	11.16	6.33	2
		3	0.93	0.10	4	1.23	0.18	3	16.88	2.31	3	16.97	7.55	3
		4	0.98	0.24	3	1.31	0.38	3			0			0
		5	1.14	0.34	4	1.40	0.50	4	16.53	2.89	4	17.78	11.58	4
		6	1.20	0.45	4	1.54	0.53	4	23.18	0.15	2	13.63	2.81	2
		7	1.05	0.23	4	1.45	0.43	4	27.95	7.54	4	17.34	4.98	4
		8	1.12	0.16	3	1.50	0.36	3	21.56	5.16	3	13.71	5.12	3
		9	1.41	0.42	3	1.80	0.46	3	28.31	8.67	3	14.58	1.88	3
		10	1.23	0.20	4	1.71	0.22	3	26.95	5.73	3	15.19	5.05	3
		11	1.27	0.43	4	1.29	0.12	4	23.88	5.96	4	17.08	8.41	4
		12	1.04	0.33	3	1.25	0.26	4	23.61	0.27	2	6.08	0.01	2
		13	1.91	0.83	4	1.37	0.49	3	28.51	8.29	4	22.93	16.23	4
		14	0.80	0.21	4	0.98	0.24	3	30.35	7.72	3	20.67	15.71	3
		15	1.06	0.08	4	1.37	0.14	4	33.57	8.75	4	21.24	11.42	4
		20	0.99	0.40	4	0.63	0.13	2	41.67	12.45	3	24.82	15.53	3
		26	0.89	0.07	2	0.96	0.27	2			0			0
		32	0.90	0.19	3	0.88	0.23	3	44.07	7.57	3	19.97	5.99	3
		39	0.66	0.26	3	0.42	0.27	3	43.89	16.45	3	19.53	3.26	3
65	0.60	0.02	3	0.48	0.01	3	56.20	12.67	3	16.11	5.42	3		

daf = days after flooding, m = mean, sd = standard deviation, n = number of samples

Table E-19 (continued)

Site	Depth cm	daf	m.S	sd.S	n.S	m.SO <sub>4</sub> <sup>2-</sup>	sd. SO <sub>4</sub> <sup>2-</sup>	n. SO <sub>4</sub> <sup>2-</sup>	m.DIC	sd.DIC	n.DIC	m.DOC	sd.DOC	n.DOC
			--- mmol l <sup>-1</sup> ---			--- mmol l <sup>-1</sup> ---			--- mmol l <sup>-1</sup> ---			--- mg l <sup>-1</sup> ---		
P700	55	0	1.42		1	1.70		1	15.67		1	18.63		1
		1	1.37	0.04	2	1.90	0.08	4	14.58		1	17.84		1
		2	1.06	0.25	4	1.41	0.36	4	17.46	4.68	3	13.40	1.19	3
		3	1.08	0.29	4	1.51	0.43	4	16.77	1.45	2	14.04	0.73	2
		4	1.42	0.51	3	1.57	0.20	4	20.40	4.58	2	11.84	3.52	2
		5	1.20	0.34	4	1.52	0.21	4	18.15	2.62	3	12.04	2.89	3
		6	0.98	0.47	3	1.25	0.56	4	19.27		1	6.81		1
		7	0.91	0.15	4	1.23	0.24	4	24.88	5.65	4	12.67	3.39	4
		8	0.87	0.40	4	1.19	0.62	4	24.18	3.41	4	10.26	1.51	4
		9	1.10	0.26	3	1.58	0.53	3	28.33	6.82	3	11.72	1.57	3
		10	1.14	0.29	4	1.60	0.49	4	32.66	6.56	4	15.75	6.75	4
		11	1.23	0.61	4	1.05	0.31	4	22.64	6.39	4	11.03	1.72	4
		12	1.76	0.70	4	1.40	0.59	4	27.82	3.55	3	12.90	3.93	3
		13	1.34	0.18	4	1.77	0.31	4	33.34	4.23	4	18.11	3.17	4
		14	0.86	0.20	4	1.20	0.35	4	32.42	13.15	4	12.83	3.81	4
		15	0.91	0.08	4	1.19	0.11	4	33.24	12.44	4	13.90	4.89	4
		20	0.55	0.14	4	0.65	0.23	4	33.33	0.21	3	9.91	0.36	3
		26	0.76	0.31	2	0.96	0.27	2			0			0
		32	0.76	0.38	3	0.83	0.25	3	48.98	1.02	3	17.81	2.04	3
		39	0.57	0.28	3	0.37	0.19	3	37.91	7.39	3	16.29	1.77	3
65	0.35	0.09	3	0.19	0.09	3	56.09	6.84	3	13.11	2.68	3		

Appendix E

**Table E–20:** Concentration of the redox sensitive elements and compounds, respectively, determined in the soil solution of the 2000 year paddy soil (P2000).

Site	Depth cm	daf	m.S      sd.S      n.S			m.SO <sub>4</sub> <sup>2-</sup> sd. SO <sub>4</sub> <sup>2-</sup> n. SO <sub>4</sub> <sup>2-</sup>			m.DIC    sd.DIC    n.DIC			m.DOC    sd.DOC    n.DOC		
			--- mmol l <sup>-1</sup> ---			--- mmol l <sup>-1</sup> ---			--- mg l <sup>-1</sup> ---			--- mg l <sup>-1</sup> ---		
P2000	35	0	1.53		1			0			0			0
		1	1.41	0.13	3	1.98	0.37	3	7.03	1.29	3	17.59	0.98	3
		2	1.64	0.28	4	2.16	0.32	4	8.07	1.17	4	15.39	2.89	4
		3	1.72	0.17	4	2.16	0.25	4	8.54	0.81	3	13.98	1.43	3
		4	1.71	0.26	4	2.10	0.22	4	10.12	2.05	2	19.11	3.74	2
		7	1.44	0.09	3	1.81	0.18	2	13.08	2.10	3	13.92	0.76	3
		8	1.62	0.49	3	1.84	0.24	3	10.97		1	15.20		1
		9	1.20	0.11	4	1.60	0.20	3	16.69	2.43	4	12.03	1.45	4
		11	1.01	0.20	3	1.27	0.31	3	12.39	1.75	3	11.71	1.14	3
		12	1.41	0.45	4	1.36	0.16	4	12.95	4.15	4	12.71	1.44	4
		13	1.92	0.88	4	1.43	0.28	4	15.82	2.53	3	12.21	0.46	3
		16	1.63	0.56	3	1.03	0.13	2			0	15.73		1
		19	1.95	0.69	4	0.94	0.14	4	15.31	2.84	2	10.72	1.89	2
		27	0.62	0.15	4	0.50	0.16	4			0			0
		31	0.33	0.07	4	0.27	0.14	4	21.98	0.73	2	15.26	3.48	3
		37	0.46	0.02	2	0.39	0.02	2			0			0
43	0.54	0.05	3	0.38	0.08	3	27.51	10.14	3	23.64	6.04	3		
57	0.36	0.01	2	0.20	0.04	3	32.83	16.26	3	17.45	4.40	3		

daf = days after flooding, m = mean, sd = standard deviation, n = number of samples

Appendix E

Table E-20 (continued)

Site	Depth cm	daf	m.S --- mmol l <sup>-1</sup> ---	sd.S	n.S	m.SO <sub>4</sub> <sup>2-</sup> --- mmol l <sup>-1</sup> ---	sd. SO <sub>4</sub> <sup>2-</sup>	n. SO <sub>4</sub> <sup>2-</sup>	m.DIC --- mg l <sup>-1</sup> ---	sd.DIC	n.DIC	m.DOC --- mg l <sup>-1</sup> ---	sd.DOC	n.DOC
P2000	55	0	1.85		1			0			0			0
		1	1.52	0.18	4	2.07	0.19	3	7.27	1.42	4	17.20	3.43	4
		2	1.44	0.16	4	2.00	0.28	4	8.29	1.69	4	12.79	1.93	3
		3	1.45	0.19	4	1.93	0.27	4	9.71	1.30	4	12.40	2.45	4
		4	1.52	0.23	4	2.05	0.35	4	10.78	0.93	2	17.60		1
		7	1.90	0.45	4	1.96	0.22	3	10.45	0.61	4	12.77	1.35	4
		8	1.62	0.29	4	1.87	0.13	4	13.08	2.02	4	13.93	1.68	4
		9	1.37	0.08	4	1.82	0.10	4	15.26	1.14	3	12.06	1.21	3
		11	1.29	0.25	3	1.59	0.20	4	13.59	2.97	4	13.27	2.18	4
		12	1.36	0.25	4	1.57	0.21	4	14.64	3.44	4	12.53	1.78	4
		13	1.71	0.81	4	1.36	0.17	4	18.54	3.72	3	8.98	1.34	3
		16	2.02	0.28	4	0.18	0.06	4			0			0
		19	1.16	0.34	4	1.02	0.13	4	13.05	1.59	2	10.44	0.56	2
		27	0.51	0.08	4	0.55	0.10	4	15.24	5.44	2	16.53	6.88	2
		31	0.60	0.41	4	0.36	0.05	3	28.26	10.07	3	22.60	10.92	3
		37	0.55	0.15	2	0.47	0.12	2			0			0
43	0.50	0.08	3	0.31	0.10	3	23.55	1.16	3	21.28	1.64	3		
57	0.39	0.06	3	0.25	0.07	3	31.74	3.62	3	18.02	1.22	3		

**Table E–21:** Concentrations of the matrix elements Si and Al determined in the soil solution of the 100 year paddy soil (P100).

Site	Depth cm	daf	m.Al	sd.Al	n.Al	m.Si	sd.Si	n.Si
			--- mmol l <sup>-1</sup> ---			--- mmol l <sup>-1</sup> ---		
P100	35	2	0.001	0.000	4	0.08	0.02	4
		3	0.003	0.001	4	0.08	0.02	4
		4	0.003	0.000	4	0.09	0.01	4
		5	0.002	0.001	4	0.07	0.04	4
		6	0.003	0.001	4	0.10	0.01	4
		7	0.002	0.001	4	0.09	0.01	4
		8	0.003	0.000	4	0.10	0.01	4
		9	0.002	0.001	4	0.08	0.02	4
		10	0.003	0.001	4	0.13	0.03	4
		11	0.001	0.001	4	0.09	0.03	4
		12	0.002	0.000	4	0.11	0.01	4
		13	0.002	0.000	3	0.09	0.01	3
		14	0.002	0.001	4	0.13	0.03	4
		15	0.002	0.001	3	0.09	0.02	3
		21	0.002	0.000	2	0.13	0.05	2
		27	0.002	0.001	3	0.10	0.05	3
		34	0.002	0.000	3	0.14	0.03	3
41	0.003	0.001	3	0.16	0.03	3		
60	0.003	0.001	3	0.13	0.02	3		
P100	55	2	0.002	0.000	4	0.14	0.01	4
		3	0.003	0.001	4	0.15	0.02	4
		4	0.003	0.000	4	0.14	0.04	4
		5	0.002	0.000	4	0.13	0.01	4
		6	0.002	0.000	4	0.13	0.05	4
		7	0.002	0.000	4	0.12	0.04	4
		8	0.003	0.000	4	0.13	0.03	4
		9	0.003	0.000	3	0.17	0.03	3
		10	0.003	0.000	4	0.16	0.03	4
		11	0.002	0.001	4	0.12	0.03	4
		12	0.003	0.001	4	0.16	0.04	4
		13	0.002	0.000	3	0.10	0.02	3
		14	0.002	0.000	4	0.15	0.03	4
		15	0.003	0.001	4	0.11	0.03	4
		21	0.003	0.000	2	0.15	0.03	2
		27	0.002	0.000	3	0.18	0.00	3
		34	0.002	0.001	2	0.15	0.01	2
41	0.003	0.001	3	0.18	0.01	3		
60	0.002	0.001	3	0.13	0.08	3		

daf = days after flooding, m = mean, sd = standard deviation, n = number of samples

**Table E–22:** Concentrations of the matrix elements Si and Al determined in the soil solution of the 700 year paddy soil (P700).

Site	Depth cm	daf	m.Al    sd.Al    n.Al			m.Si    sd.Si    n.Si		
			--- mmol l <sup>-1</sup> ---			--- mmol l <sup>-1</sup> ---		
P700	35	0	0.001	0.001	2	0.16	0.03	2
		1	0.001	0.000	4	0.14	0.03	4
		2	0.000	0.001	3	0.12	0.04	3
		3	0.001	0.000	4	0.13	0.03	4
		4	0.001	0.000	3	0.13	0.03	3
		5	0.001	0.000	4	0.14	0.04	4
		6	0.001	0.000	4	0.14	0.02	4
		7	0.001	0.001	4	0.14	0.03	4
		8	0.001	0.000	3	0.15	0.05	3
		9	0.001	0.001	3	0.15	0.03	3
		10	0.001		1	0.17		1
		11	0.001	0.001	4	0.17	0.02	4
		12	0.001	0.000	3	0.19	0.02	3
		13	0.002	0.000	4	0.13	0.05	4
		14	0.001	0.000	4	0.16	0.03	4
		15	0.001	0.001	4	0.17	0.03	4
		20	0.001	0.001	4	0.17	0.04	4
26	0.014	0.017	2	0.19	0.07	2		
32	0.001	0.000	3	0.19	0.03	3		
39	0.002	0.000	3	0.19	0.02	3		
65	0.003	0.000	3	0.19	0.03	3		
P700	55	0	0.001		1	0.13		1
		1	0.002	0.001	2	0.13	0.01	2
		2	0.001	0.000	4	0.14	0.03	4
		3	0.001	0.000	4	0.16	0.02	4
		4	0.003	0.002	4	0.17	0.05	4
		5	0.001	0.001	4	0.16	0.04	4
		6	0.002	0.000	3	0.17	0.03	3
		7	0.001	0.001	4	0.16	0.03	4
		8	0.002	0.000	4	0.13	0.02	4
		9	0.000	0.000	3	0.13	0.03	3
		10	0.001	0.001	4	0.15	0.03	4
		11	0.000	0.000	4	0.14	0.02	4
		12	0.001	0.001	3	0.18	0.02	3
		13	0.001	0.000	4	0.15	0.04	4
		14	0.002	0.001	4	0.17	0.05	4
		15	0.004	0.005	4	0.18	0.03	4
		20	0.002	0.002	4	0.16	0.01	4
26	0.003	0.001	2	0.17	0.01	2		
32	0.002	0.001	3	0.15	0.08	3		
39	0.003	0.001	3	0.16	0.05	3		
65	0.003	0.000	3	0.19	0.03	3		

daf = days after flooding, m = mean, sd = standard deviation, n = number of samples

**Table E–23:** Concentrations of the matrix elements Si and Al determined in the soil solution of the 2000 year paddy soil (P2000).

Site	Depth cm	daf	m.Al    sd.Al    n.Al			m.Si    sd.Si    n.Si		
			--- mmol l <sup>-1</sup> ---			--- mmol l <sup>-1</sup> ---		
P2000	35	0	0.002		1	0.13		1
		1	0.000	0.000	3	0.10	0.04	3
		2	0.001	0.001	4	0.08	0.02	4
		3	0.001	0.001	4	0.09	0.03	4
		4	0.002	0.001	4	0.12	0.02	4
		7	0.002	0.000	3	0.13	0.04	3
		8	0.002	0.001	3	0.15	0.06	3
		9	0.002	0.000	4	0.12	0.03	4
		11	0.000	0.001	3	0.13	0.02	3
		12	0.001	0.000	4	0.17	0.02	4
		13	0.001	0.001	4	0.17	0.03	4
		16	0.000	0.001	3	0.12	0.01	2
		19	0.001	0.000	4	0.17	0.02	4
		27	0.001	0.000	4	0.17	0.02	4
		31	0.001	0.000	4	0.11	0.02	4
37	0.001	0.000	2	0.13	0.01	2		
43	0.001	0.000	3	0.14	0.01	3		
57	0.002	0.000	2	0.17	0.01	2		
P2000	55	0	0.002		1	0.16		1
		1	0.001	0.001	4	0.06	0.01	3
		2	0.001	0.001	4	0.09	0.03	4
		3	0.000	0.000	4	0.10	0.02	4
		4	0.001	0.001	4	0.08	0.05	4
		7	0.002	0.001	4	0.09	0.01	4
		8	0.002	0.001	4	0.16	0.01	4
		9	0.001	0.001	4	0.14	0.03	4
		11	0.001	0.000	3	0.16	0.01	3
		12	0.001	0.001	4	0.17	0.01	4
		13	0.001	0.001	4	0.16	0.04	4
		16	0.001	0.001	4	0.18	0.01	4
		19	0.001	0.001	4	0.19	0.01	4
		27	0.006	0.010	4	0.15	0.01	4
		31	0.001	0.001	4	0.12	0.03	4
37	0.001	0.000	2	0.18	0.04	2		
43	0.002	0.001	3	0.16	0.01	3		
57	0.002	0.000	3	0.18	0.03	3		

daf = days after flooding, m = mean, sd = standard deviation, n = number of samples

**Eidesstattliche Erklärung / *Declaration under Oath***

Ich erkläre an Eides statt, dass ich die Arbeit selbstständig und ohne fremde Hilfe verfasst, keine anderen als die von mir angegebenen Quellen und Hilfsmittel benutzt und die den benutzten Werken wörtlich oder inhaltlich entnommenen Stellen als solche kenntlich gemacht habe.

*I declare under penalty of perjury that this thesis is my own work entirely and has been written without any help from other people. I used only the sources mentioned and included all the citations correctly both in word or content.*

15.06.2017  
Datum / *Date*

gez. Vogelsang  
Unterschrift / *Signature*

---

## Lebenslauf

Name: Vanessa Vogelsang  
Geburtstag: 04.03.1980 in Berlin

### Wissenschaftlicher Werdegang

---

- 06/13 – 04/17 Doktorandin, Naturwissenschaftliche Fakultät III, Institut für Geowissenschaften, Martin-Luther-Universität Halle-Wittenberg, betreuender Hochschullehrer: Prof. Dr. Reinhold Jahn
- 04/12 – 08/13 wissenschaftliche Mitarbeiterin an der Professur für Bodengeographie (Prof. Dr. Sabine Fiedler), Institut für Geographie, Johannes Gutenberg-Universität Mainz
- 04/08 – 09/11 wissenschaftliche Mitarbeiterin an der Professur für Bodenkunde und Bodenschutz (Prof. Dr. Reinhold Jahn) im Rahmen der DFG-Forschergruppe FOR 995 „Biogeochemistry of Paddy Soil Evolution“/Teilprojekt 1, Institut für Agrar- und Ernährungswissenschaften, Martin-Luther-Universität Halle-Wittenberg
- 10/00 – 10/07 Studium der Umweltwissenschaften (Diplom) Leuphana Universität Lüneburg, Vertiefungsfächer: Umweltchemie und Ökologie  
Thema Diplomarbeit: „Kennzeichnung der Elementassoziationen in kontaminierten Auenlehmproben der Mittelelbe und Mulde durch chemische Extraktionsverfahren“, ausgeführt am Institut für Umwelttechnik und Energiewirtschaft der Technischen Universität Hamburg-Harburg
- 06/99 Abitur, Marie-Curie-Gymnasium, Berlin

15.06.2017  
Datum / Date

gez. Vogelsang  
Unterschrift / Signature

---